Development and optimization of mechanical polishing process for superconducting accelerating cavities

Oleksandr Hryhorenko

université PARIS-SACLAY

UNIVERSITÉ PARIS SUD
Comprendre le monde, construire l'avenir

NNT : 2019SACLS566

Thèse de doctorat

Development and Optimization of Mechanical Polishing Process for Superconducting Accelerating Cavities

Thèse de doctorat de l'Université Paris-Saclay
préparée à l'Université Paris-Sud

Ecole doctorale n°576 particules hadrons énergie et noyau : instrumentation, image, cosmos et simulation (PHENIICS)
Spécialité de doctorat : physique des accélérateurs

Thèse présentée et soutenue à Orsay, le 13 décembre 2019, par

OLEKSANDR HRYHORENKO

Composition du Jury :

Anne Lafosse Professeur des Universités, Institut des Sciences Moléculaires d'Orsay (ISMO)	Président
Joel Rech Professeur des Universités, École nationale d'ingénieurs de Saint-Étienne (ENISE)	Rapporteur
Sergio Calatroni Directeur de Recherche, CERN	Rapporteur
David Longuevergne Chargé de Recherche, Institut de Physique Nucléaire d'Orsay (IPNO)	Examinateur
Marin Chabot Directeur de Recherche, Institut de Physique Nucléaire d'Orsay (IPNO)	Directeur de thèse

université PARIS-SACLAY | ÉCOLE DOCTORALE PHENIICS

Titre : Développement et optimisation d'un procédé de polissage mécanique pour les cavités accélératrices supraconductrices

Mots clés : cavité accéleratrice, supraconductivité, radiofréquence, traitment de surface, polissage

Résumé :
La production de masse de cavités accélératrices supraconductrices en régime radiofréquence (SRF) est un réel défi industriel non seulement du fait du nombre croissant de cavité pour les futurs grands projets mais également de par les besoins en terme de fiabilité, reproductibilité et performances demandées très proches des limites physiques du Niobium. De nos jours, XFEL (DESY) et le LHC (CERN) sont les deux accélérateurs les plus importants utilisant la technologie supraconductrice. Des projets accélérateurs encore plus ambitieux, tels que l'ILC (International Linear Collider) et FCC (Future Circular Collider) sont en cours d'étude. Pour de tels projets, il est encore nécessaire d'améliorer les performances et de réduire les coûts de fabrication et d'opération avant d'engager la phase d'industrialisation. Une voie d'amélioration des performances et de réduction des coûts a été étudiée. Ceci consiste à améliorer les procédés de nettoyage des surfaces. En effet, la pollution et les dommages causés à la structure cristalline durant la fabrication d'une cavité supraconductrice doivent être impérativement retirés afin de garantir des performances optimales. Cette régénération des surfaces est couramment réalisée à l'aide de deux types de polissages chimiques : par BCP (Buffered Chemical Polishing) ou par électro-polissage (EP). Cependant, ces techniques utilisent des acides très concentrés qui entrainent des coûts d'opération très conséquents du fait des problèmes de sécurité. Une voie d'amélioration pouvant rendre possible la construction de telles machines serait de remplacer totalement ou partiellement l'utilisation des acides par des techniques de polissage alternatives. Le polissage mécanique a été étudié durant des décennies et plus spécifiquement les techniques par centrifugation (CBP). Cette technique permet d'atteindre des rugosités de surface bien meilleures et est bien plus efficace pour retirer certains défauts de surface comparé aux procédés chimiques. Cependant, cette technique n'est pas envisageable comme solution alternative à cause des fortes pollutions de surface et des durées de traitement très longues. La première partie de la thèse a consisté à reproduire l'état de l'art, comprendre les limitations réelles de cette technique et essayer d'améliorer le procédé en réduisant la pollution de surface générée par le piégeage des abrasifs en surface ainsi que la durée de traitement (réduction du nombre d'étapes intermédiaires). Il a été conclu que ce procédé ne peut pas être considéré comme alternatif mais complémentaire aux traitements chimiques. La deuxième partie du travail de thèse s'est concentrée sur la méthode de polissage métallographique. Cette dernière ne peut s'appliquer que sur plaques et non sur des géométries complexes, cependant elle retire très efficacement toutes les impuretés et dommages cristallins formés durant la fabrication des tôles de Niobium. Un procédé optimisé à 2 étapes, inspiré des techniques conventionnelles (typiquement 5-6 étapes) a été développé avec succès et optimisé pour les contraintes particulières du Niobium pour les applications SRF. Ce procédé permet non seulement d'obtenir une rugosité de surface incomparable mais préserve également la structure cristalline. Des études complémentaires sont encore requises afin d'améliorer les techniques de formage des tôles ou même caractériser des solutions alternatives permettant des limiter les dégâts en surface et de préserver la qualité du matériau. Finalement, ce travail mené est d'une importance capitale pour le futur des cavités accélératrices supraconductrices, c'est-à-dire l'utilisation de nouveaux matériaux supraconducteurs sous forme de couche mince. La qualité des couches minces de ces matériaux alternatifs dépend très fortement de l'état de surface du substrat (typiquement niobium ou cuivre poly cristallin).

Université Paris-Saclay
Espace Technologique / Immeuble Discovery
Route de l'Orme aux Merisiers RD 128 / 91190 Saint-Aubin, France

université PARIS-SACLAY | ÉCOLE DOCTORALE PHENIICS

Title : Development and optimization of mechanical polishing process for superconducting accelerating cavities

Keywords : accelerating cavity, superconductivity, radiofrequency, surface treatment, polishing

Abstract : Large-scale production of superconducting radio-frequency (SRF) cavities is an industrial challenge, not only because of the increasing number of unit for future projects but also because of requirements in term of reliability, reproducibility and performances very close to the physical limit of polycrystalline bulk Niobium. Nowadays, XFEL (DESY) and LHC (CERN) are the largest existing accelerators which are based on SRF technology. Even more challenging SRF accelerator projects like ILC (International Linear Collider) and FCC (Future Circular Collider) are being studied. For such large-scale facilities, higher performances, reduction in fabrication and operation costs are required and essential to proceed with industrialization. A pathway to reduce these costs and improve performances has been studied in this work. It consists in optimizing the cleaning process of cavity surfaces. Indeed, pollution and crystal defects on the surface created during fabrication steps of a SRF cavity have to be removed to ensure optimal superconducting performances. In order to get rid of impurities and to recover crystal structure, two polishing techniques are routinely used : the buffered chemical polishing (BCP) and electro-polishing (EP). However, these techniques involve highly concentrated acids, which lead to high operation costs and safety concerns. A way to overcome the aforementioned drawbacks and make the construction of future accelerators possible would be to replace or complement the conventional chemical polishing by alternative polishing techniques. Mechanical polishing has already been applied in SRF-community for decades by using centrifugal barrel polishing (CBP). This technique could provide a better surface roughness and could be more efficient at removing some surface defects compared to EP and BCP. However, this process does not satisfy requirements for large-scale production due to strong surface pollution and an extremely long processing time. The first part of the PhD work consisted in reproducing the state of the art, understanding its limitations and optimizing the recipe by the reduction of the surface pollution (embedded abrasives) and processing time (reduction of intermediate steps). As a conclusion to this first study, CBP could only be a complementary polishing technique to chemical treatments. The second part of the work focused on metallographic flat polishing. This technique cannot be directly applied on enclosed geometries however, it can remove efficiently surface defects (impurities and crystal damages) created during the fabrication of Niobium sheet. A 2-step process, inspired from metallographic techniques (typically 5-6 steps) has been successfully developed and optimized on Niobium for SRF applications. This process provides not only an improved roughness compared to conventional chemical treatments but also preserve the crystal quality underneath the surface, over the field penetration depth. Additional studies have to be now carried out to optimize conventional forming process or characterize alternative techniques to limit surface damages and preserve material quality as much as possible. Last but not least, the work done is of first importance for the future of SRF cavities meaning the use of new superconducting materials as thin films. The quality of thin-films of alternative superconductors depends strongly on the surface state of the substrate, typically polycrystalline bulk Niobium or Copper.

Université Paris-Saclay
Espace Technologique / Immeuble Discovery
Route de l'Orme aux Merisiers RD 128 / 91190 Saint-Aubin, France

Dedication

"They didn't know it was impossible so they did it."
Mark Twain

This thesis is dedicated to my family who has supported me doing my PhD thesis.

Contents

List of Figures

List of Tables

Acknowledgements

I would like to thank many people who surrounded and helped me to complete my thesis during these three years. This scientific work is patience, hard-working, impact and strong support of people I worked with.

I would like to express my sincere gratitude to my supervisor Marin Chabot for the discussions, proof-reading, ideas, the administrative help and monitoring of my doctoral process in the university. I am grateful for his great scientific supervision.

My deep gratitude goes to David Longuevergne, I'm grateful for his help to integrate me in accelerator science. Firstly he invited me to IPNO for internship, to study the mechanical polishing, in particular centrifugal barrel polishing, secondly he involved me in R&D of lab and at last, but not at least he was my guide and support during all my PhD. He is a great person, researcher and teacher, so I'm happy that I had opportunity to work with him. Merci pour ton encouragement.

Many thanks to my colleagues from the SUPRAtech for their high quality help in the experiments, useful discussions and suggestions during my study. Working at SUPRATech has been tremendously interesting and I would like to thank all my colleagues for the great time we shared. Author would like to thank the persons listed below: Fetra Rabehasy, Thierry Pepin-Donat, Antoine Luboz, Guillaume Olry, Guillaume Martinet, Didier Grolet, Wladimir Sarlin, Virginie Quipourt, Sylvie Durand, Natacha Bippus, Sarra Bira, David Ledrean, Yosra Gargouri, Soukaina Gulnar, Nathalie Leon and Richard Martret. I am very grateful for them for the friendly atmosphere during working days and definitely I was lucky to work together with them.

Thanks a lot to Fetra Rabehasy for unfailing help with the damaged layer study of Niobium samples after mechanical polishing, strong support with buffered chemical etching and shared moments "after work" together. Thanks to him I gained not only knowing how to do the BCP but how to build muscles also.

I would like to acknowledge the help of Thierry Pepin-Donat, who helped me a lot with 3D-printing and prepared plenty of supports for my polishing study. Also without him, I could not have gained such invaluable experience in tennis games during breaks. Merci beaucop.

Also I would like to say thanks to Antoine Luboz for sharing office together, ideas, time and his efforts to improve my climbing skills. I will never forget his kindness.

My deep thanks to Wladimir Sarlin, who dedicated a lot of time to speak with me in English and for his advises with "Code de la Route" and prepared me (at least mentally) to run a marathon.

I must thank the administrative staff of accelerator department of IPNO, Virginie Quipourt and Sylvie Durand for their kind support in administrative questions and making all my missions stuff such a bliss.

I would like to thank Guillaume Olry and Guillaume Martinet for their all the encouragements and wise advices during meetings which were dedicated to PhD students in our department.

Also I want to thank the workshop mechanician Didier Grolet for his efficiency in the production of all required tools for my thesis research. Thanks also to François Brisset (ICMMO lab) for his professional assistance in the damaged layer characterizations of cross-sections and polished faces of Nb by means of an EBSD analysis. Many thanks to Gael Sattonnay (LAL) and Suheyla Bilgen (LAL) for their advises, professional support and time dedicated during characterization of damaged layer by means of a XRD analysis. Thanks to them I became an independent user of diffractometer.

I highly appreciate the fruitful collaboration with CEA/DRF/IRFU at Saclay. I personally acknowledge the support from C.Z. Antoine for her assistance, patience and excellent cooperation in the surface investigations. She is an example of an incredible woman in science, who knows everything about materials, which are used in accelerators. Based on her knowledge and David's control I made a huge step towards becoming an independent scientist. Besides Claire from CEA, I would like to thank to F. Éozénou for the private conversations and all details about the electro-polishing process.

I would like to express my very great appreciations to the following companies

and to my native university for their assistance and for their contribution to this R&D:

- LAM PLAN (J.M. Jeoffroy, Gaillard, France),
- Plasotec (Tobias Weise, Rathenow, Germany),
- V.N. Karazin National University (Aleksey Migal, Kharkiv, Ukraine).

Moreover, Mr. Jean-Michel Jeoffroy deserves special attention. Eventhough that he represents commercial duty at LAM PLAN, during working with him I gained a lot of experience and gain valuable knowledge in the metallographic field. Mr. Jeoffroy taught me a lot and always guided me on the right way. Je vous remercie beaucoup pour votre gentillesse et assistance. Besides Jean-Michel from LAM PLAN, I would like to thank for the great and high quality work of Guillaume Carrey on a lapping process.

Also, I would like to thank Paul Welander working in the Accelerator Technology Research Department from SLAC for the RF test of our prepared samples allowing us to have RF results ready for this thesis.

Nobody has been more important to me than the members of my family. I would like to thank my parents, whose support, guidance and love are with me no matter what.

Also, I have to mention all those who surrounded me during this time in Chandon's house: Leonid Burmistrov, Dmytro Hohov and many other students (Ivanka, Andrii, Olya, Vladyk, Katya, Denys...). Without them, this difficult period of my life could not be complete. They have become more than just neighbours, some of them have become even more than just friends for me. Thank them for everything, I will never forget this friendly and lovely atmosphere. You are the greatest happiness during my PhD period.

Of course, many thanks to reviewers and editors of this manuscript. They made possible to bring this thesis into an academically qualitative shape. Merci beaucoup and grazie mille.

However except all huge amount of help and support from people whom I mentioned above, this work would not have been possible without the financial support of the European Nuclear Science and Applications Research 2 (ENSAR 2) under

grant agreement n°654002 of the Work Package 15 (TecHIBA - Technologies for High Intensity Beams and Applications).

Acronyms and List of Symbols

A	Surface area.
$ASTM$	American Society for Testing and Materials.
A_l	Elongation.
E	Young's modulus.
EDS	Energy-dispersive X-Ray spectrometry.
G	Shear modulus.
HV	Vickers hardness.
K	Bulk modulus.
L	Final length.
L_0	Initial length.
R	2D linear roughness.
R_s	Surface Resistance.
S	3D surface area roughness.
S_a	Average surface roughness.
S_p	Maximum peak height.
S_q	Root mean square surface roughness.
S_v	Deepest valley of the height distribution.
S_z	Maximum height fluctuation of the surface profile.
S_{al}	Horizontal length of the auto-correlation function.
S_{dq}	Root mean square slope.
S_{dr}	Developed area ratio.
S_{ku}	Kurtosis of the surface texture.
S_{pc}	Mean peak curvature.
S_{pd}	Mean peak density.
S_{sk}	Skewness of the surface texture.
S_{td}	Texture direction.

S_{tr}	Texture aspect ratio parameter.
Z	Height deviation.
μm	1 Micrometer = 10^{-6} meter.
ν	Poisson's coefficient.
σ	Normal stress of the material.
σ_U	Ultimate tensile strength.
σ_Y	Yield strength.
σ_x	Stress in the x direction.
σ_y	Stress in the y direction.
τ	Shear stress of the material.
τ_{xy}	Vertical shear stress.
τ_{yx}	Horizontal shear stress.
ε	Strain of the material.
ε_x	Strain in the x direction.
ε_y	Strain in the y direction.
d_g	Grain size.
n	Strain hardening coefficient.
pH	Capacity of Hydrogen.
ACF	Auto-correlation function.
Al_2O_3	Aluminium Oxide (Alumina).
B_4C	Boron Carbide.
BCP	Buffered Chemical Polishing.
BCS	Bardeen-Cooper-Schrieffer.
CBP	Centrifugal Barrel Polishing.
CEA/Irfu	Commissariat à l'énergie atomique et aux énergies alternatives/Institut de recherche sur les lois fondamentales de l'Univers.
CeO_2	Cerium Oxide.
CESR	Cornell Electron Storage Ring.
CLIC	Compact Linear Collider.
CMP	Chemical Mechanical Polishing.
Cu	Copper.
CW	Continuous Wave.

DESY	Deutsches Elektronen-Synchrotron.
DTL	Drift Tube Linac.
EBSD	Electron Backscatter Diffraction.
EP	Electro-Polishing.
EPP	Electrolytic plasma polishing.
ESS	European Spallation Source.
F_f	Frictional Force.
F_N	Normal Force.
FCC	Future Circular Collider.
Fermilab	Fermi National Accelerator Laboratory.
H_2O_2	Oxygen peroxide.
H_2SO_4	Sulfuric Acid.
H_3PO_4	Phosphoric Acid.
HF	Hydrofluoric Acid.
HNO_3	Nitric Acid.
ILC	International Linear Collider.
INFN/LNL	Italian Insitute of Nuclear Physics/Laboratori Nazionali di Legnaro.
IPNO	Institut de Physique Nucléaire d'Orsay.
JLAB	Jefferson Laboratory.
KEK	Koh Ene Ken (From Japanese: High Energy Accelerator Research Organization).
LHC	Large Hadron Collider.
LINAC	Linear Accelerator.
MP	Mechanical Polishing.
MRP	Magnetorheological Polishing.
MRR	Material Removal Rate.
MYRRHA	Multi-purpose hYbrid Research Reactor for High-tech Applications.

Nb	Niobium.
NC	Normal Conducting.
NH_4OH	Ammoniac.
nm	1 Nanometer = 10^{-9} meter.
PE	Plasma etching.
PIP-2	Proton Improvement Plan 2.
PS	Proton Synchrotron.
RFQ	Radio Frequency Quadrupole.
RPM	Rotations per Minute.
SiC	Silicon Carbide.
SIMS	Secondary Ion Mass Spectrometry.
SiO_2	Silica Colloidal (Silica).
SLAC	Stanford Linear Accelerator Center.
SPS	Super Proton Synchrotron.
SRF	Superconducting Radio-Frequency.
SW	Standing Wave.
TeV	Tera Electron Volt = 10^{12} eV.
TW	Travelling Wave.
XFEL	X-Ray Free Electron Laser.
XRD	X-Ray Diffraction.

Synthèse en français

Cette thèse a été faite à l'Institut de Physique Nucléaire d'Orsay (IPNO) en collaboration avec l'Institut de recherche sur les lois fondamentales de l'Univers (CEA/IRFU). Ces travaux ont été financés par le projet européen : European Nuclear Science and Applications Research - 2 (ENSAR-2) dans le cadre de la convention de subvention n° 654002 (Workpackage 15 - TecHIBA) [1, 2].

L'objectif de ce travail de thèse est l'amélioration des cavités accélératrices supraconductrices en remplaçant ou en réduisant fortement l'utilisation des techniques de polissage chimique (électropolissage, abrasion chimique) en raison de la complexité de mise en œuvre, des problèmes de sécurité et de recyclage et de certaines limitations observées en ce qui concerne les propriétés supraconductrices en régime radiofréquence.

En outre, compte tenu de la demande importante et croissante de cavités supraconductrices à radiofréquence (SRF), la réduction des coûts de fonctionnement et de fabrication ainsi que l'amélioration des performances sont cruciales non seulement pour les futurs accélérateurs de particules à haute énergie mais également pour d'autres applications (médicales, sociétales et science des matériaux). De plus, afin d'anticiper la construction des futurs grands projets accélérateurs supraconducteurs (ILC, FCC, ...), la technique alternative de polissage doit répondre aux exigences d'industrialisation en termes de répétabilité, de fiabilité et de durée de traitement afin de permettre une production à grande échelle. Les exigences physiques et techniques de ces futurs projets accélérateurs sont très ambitieuses en terme d'énergie et puissance faisceau, rendant certaines solutions techniques obsolètes ou non compétitives. Il est à noter que le nombre de cavités supraconductrices nécessaires à la construction de l'ILC est vingt fois le nombre de cavités qui a été nécessaires pour la construction de l'un des plus grand accélérateur linéaire supraconducteur XFEL.

Dans le Chapitre 2 est donnée une brève introduction sur les différents types d'accélérateurs de particules, le phénomène de la supraconductivité notamment en régime radiofréquence (SRF). Afin de comprendre les principaux avantages, défis et limites, différents effets, modèles et théories (effet Meissner, théorie de Londres, modèle de Ginsburg-Landau, théorie BCS) sont présentés. Enfin, les différents types de structures accélératrices ainsi que l'avenir de la technologie SRF sont discutés.

Dans le Chapitre 3 sont présentées les techniques de traitement de surface alternatives et sont définies les exigences physiques et techniques de la surface finale afin d'obtenir de bonnes performances supraconductrices pour la technologie SRF. La qualité de surface du matériau supraconducteur est un enjeu clé pour obtenir les performances requises des cavités accélératrices supraconductrices. Il est primordial de se débarrasser de l'ensemble des défauts de surface crées lors de la fabrication des tôles de Niobium et des cavités (cf figure 1 ci-dessous).

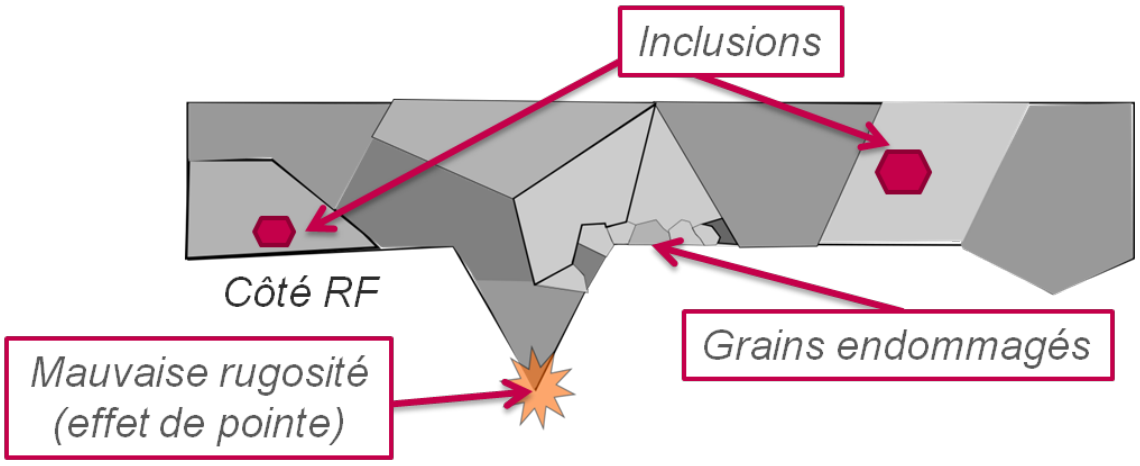

Figure 1: Représentation d'une surface endommagée par les procédés de fabrication conventionnels.

Dans le cadre de ces travaux de thèse, différents types de travaux expérimentaux sur des équipements de recherche ont été réalisés. Le Chapitre 4 se décompose en deux parties. La première partie est consacrée à la description des dispositifs de polissage et des outils/consommables qui ont été utilisés pour les procédés de polissage. Une centrifugeuse satellitaire à axes obliques ainsi qu'une polisseuse métallographique ont été utilisées pour le développement et l'optimisation des recettes de polissage pour le Niobium polycristallin (cf. figure 2 ci-dessous).

La deuxième partie concerne les outils utilisés pour la caractérisation de la qualité de surface des échantillons (rugosité, composition chimique, pollution et structure cristalline) après chaque étape de polissage. La surface a été caractérisée

(a) machine de polissage centrifuge (b) machine de polissage métallographique

Figure 2: (a) Centrifugeuse satellitaire fournie par ABC Swisstech. (b) Polisseuse métallographique approvisionnée chez LAM PLAN.

par plusieurs techniques ou dispositifs: notamment microscope confocal laser, SIMS (Spectromètre de masse ionique secondaire), GIDRX (Grazing Incidence Diffractomètre à rayons X), MEB (microscope électronique à balayage) et EBSD (diffraction électronique rétrodiffusée).

Dans cette thèse, le travail a consisté principalement à évaluer la propreté chimique, la qualité cristallographique de la surface, la nanorugosité, le taux d'abrasion, tout en simplifiant les techniques conventionnelles de polissage mécanique par centrifugation (CBP) et de polissage métallographique afin que ces procédés répondent aux exigences d'industrialisation. Le Chapitre 5 présente tous les résultats expérimentaux des études de polissage CBP et métallographique. L'inspection optique, la caractérisation de la pollution et l'analyse cristallographique sont également présentées. De plus, afin de simplifier la caractérisation des données (reconnaissance des schémas SIMS et description de la dépollution statistique), plusieurs scripts ont été écrits en language Python, voir le Chapitre A.

Cette technique n'est pas adaptée pour la production à grande échelle en raison de très fortes limitations techniques comme il sera affiché dans présenté dans le Chapitre 5.

Par conséquent, une voie alternative pour la production de cavités pourrait être envisagée en inversant les étapes de formage et de polissage. En d'autres termes, il s'agit de premièrement polir les tôles de Niobium par la technique de polissage métallographique puis dans une deuxième temps de procéder à la fabrication de la cavité (cf. figure 3 ci-dessous) [3].

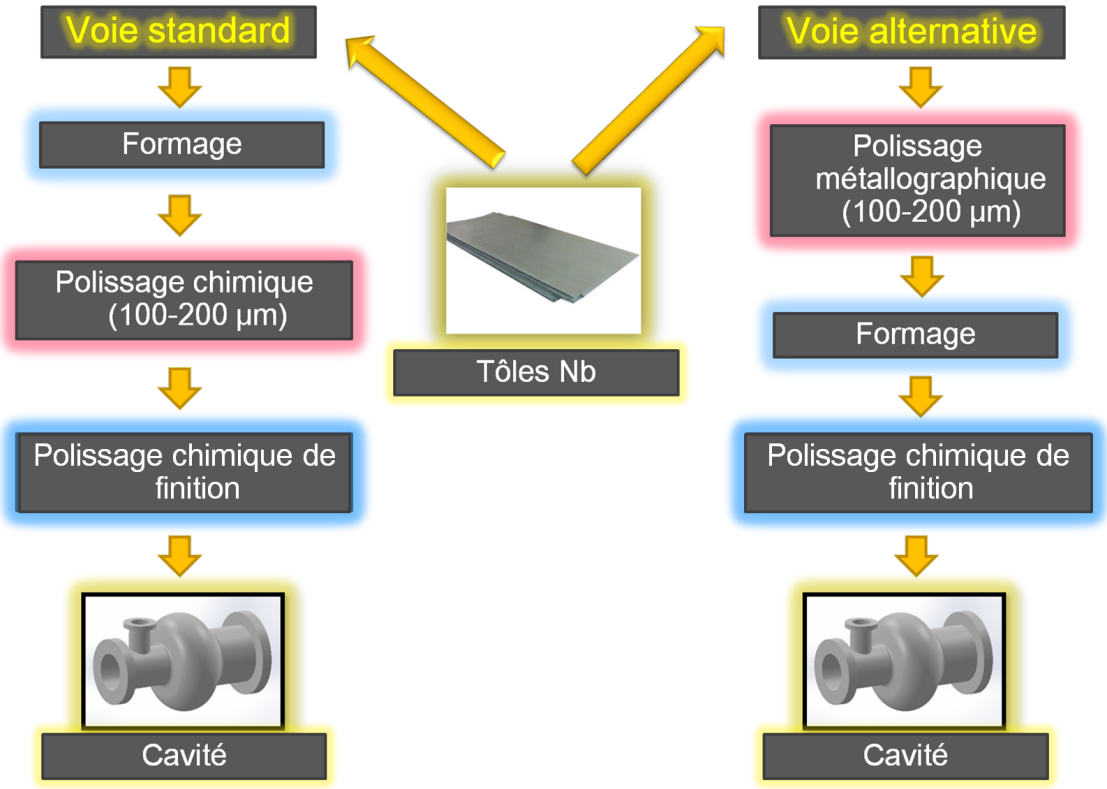

Figure 3: Représentation schématique de la voie conventionnelle et alternative proposée.

La première étape de cette voie alternative a été étudiée dans ces travaux de thèse montrant que le procédé de polissage métallographique développé avec succès et optimisé spécifiquement pour le Niobium polycristallin permet d'obtenir des résultats prometteurs non seulement en termes de rugosité mais aussi en termes de taux d'abrasion, pollution de surface et qualité cristallographique et performances supraconductrices en régime radiofréquence (cf. figure 4 ci-dessous), voir la Section 5.2. Afin de prouver la faisabilité de cette voie alternative, il est nécessaire de transférer le procédé de polissage métallographique à des tôles de grandes dimensions nécessaires pour la fabrication de cavités elliptiques (étude en cours), puis d'appliquer une technique de formage alternative aux tôles polies, voir la Section 5.2.3.4.

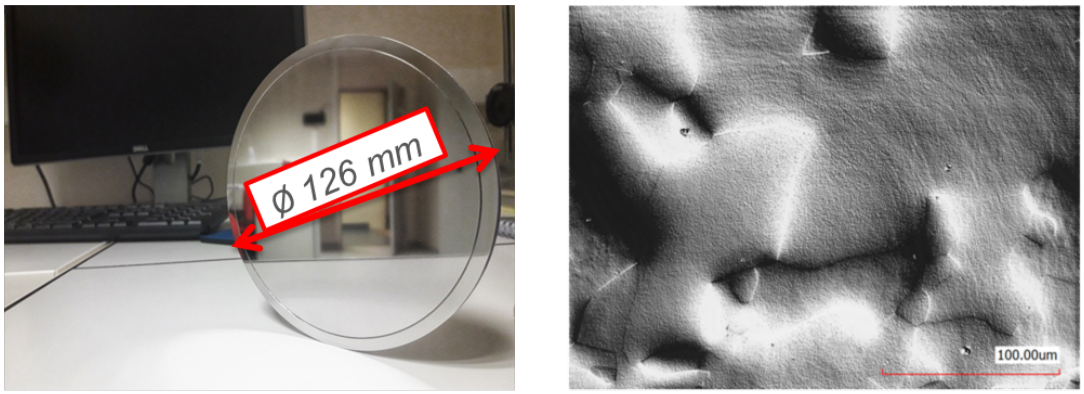

Figure 4: Photographie d'un disque (a) et photographie obtenue par microscopie optique de la surface d'un échantillon de Niobium (b) polis à l'aide du procédé métallographique optimisé.

Chapter 1

Introduction

The PhD work was financed and done in the framework of the TEChnologies for High Intensity Beams and Applications (TecHIBA) workpackage (WP15) of the European Nuclear Science and Applications Research - 2 (ENSAR2) project (grant agreement n°654002) in collaboration with CEA/IRFU, and more particularly with DACM (Département des Accélérateurs, de la Cryogénie et du Magnétisme) [1, 2]. The particular task named ISACA (Improvement of Superconducting Accelerating Cavities) and actually the title of this thesis focuses on improvement of superconducting accelerating cavities by replacing or strongly reducing the use of the chemical polishing techniques (EP, BCP) due to the implementation complexity, safety and recycling issues and some limitations observed in the surface quality regarding superconducting properties in radiofrequency regime. Also according to the substantial increasing demand of superconducting radio-frequency (SRF) cavities, reduction in operation and fabrication costs, and achievement of higher performances are crucial not only for future high-energy particle accelerators but also for other applications (medical, societal and material). Moreover, in order to anticipate the construction of new large scale facilities relying on SRF (ILC, FCC,...), the alternative polishing technique should comply with requirements of industrialization in terms of reproducibility, reliability and processing time (limited number of steps) to allow a large scale production. The future projects are continuously pushing the frontier of the desired energy, beam current and beam power making some technical solutions obsolete or non competitive. It has to be noted that compared to the existing largest linear accelerator based on SRF cavities (XFEL) the planned number of SRF-units for future linear collider is increased at least by a factor 20 (ILC).

The manuscript is organized as follows:

Chapter 2 gives a brief introduction about the different types of particle accelerators, the phenomenon of superconductivity in particular in radiofrequency regime (SRF). In order to understand the main advantages, challenges, and limitations, different effects, models and theories (the Meissner effect, the London theory, the Ginsburg-Landau model, the BCS theory) are presented. Finally, the different type of accelerating structures as well as the future of SRF technology are discussed.

Chapter 3 presents the standard and potential alternative surface treatment techniques and gives the specific requirements for SRF technology. The high surface quality of superconducting material is a key issue to achieve high performances in superconducting accelerating cavities. However, in addition to low surface roughness it is necessary to get rid of material defects, which are described in this chapter.

Within the ISACA task, I have been involved in different types of experimental work on a specific research equipments. Chapter 4 consists of two parts. The first part is dedicated to the description of polishing devices and tools/abrasives which were used for polishing processes. In particular I operated a centrifugal barrel polishing machine and metallographic polishing device to develop an optimized polishing recipes for polycrystalline Niobium. The second part is about tools used for the characterization of sample surface quality (roughness, chemical composition, pollution and crystalline structure) after each polishing step. The surface were characterized with the several techniques or devices: in particular laser confocal microscope, SIMS (Secondary Ion Mass Spectrometer), GIXRD (Grazing Incidence X-Ray Diffractometer), SEM (Scanning Electron Microscope) and EBSD (Electron BackScattered Diffraction).

In this thesis, the work consisted mainly in assessing chemical cleanliness, crystallographic quality of the surface, nanoroughness, abrasion rate, while simplifying the usual CBP and metallographic techniques so that the process is compatible with industrialization and could be used for large scale production. Hence, Chapter 5 presents all experimental results of both CBP and metallographic polishing studies. Optical inspection, pollution characterization, and crystallographic analysis are also presented. Moreover, in order to simplify data characterization (recognition of SIMS patterns and describe statistically de-pollution), several scripts have been written in Python language, see Appendix A.

Although CBP seemed at first sight to be the right alternative technology to allow industrialization as and it could be applied directly to closed geometry, in the case of Niobium superconducting cavities, this technique doesn't comply with large

scale productions due to very strong limitations as it will be shown in Section 5.1. However, mirror-like surfaces have been achieved in three steps.

It has been shown that the damaged layer after cavity fabrication (forming) [4] is much lower than during Niobium sheet production (lamination, rolling, ...). Hence, another pathway for cavity production could be done by reversing the forming and polishing steps by applying metallographic polishing (MP) on flat Niobium sheets before forming cavity parts. The first step of this alternative pathway and the main achievement of this work is the development of a two-steps MP recipe inspired from metallographic techniques (instead of 4-7 steps), which shows promising results not only in terms of roughness but also in abrasion rate, surface pollution, and crystallographic quality, see Section 5.2. The next steps of this study are requiring to apply this recipe on large sheets comparable with the cavity dimensions and then applying an alternative forming technique to polished sheets, see Section 5.2.3.4.

Chapter 2

Fundamentals of Superconducting Particle Accelerators

2.1 Particle Accelerators

The most powerful particle accelerators produce bunched beams of charged particles, such as protons, ions or electrons, accelerated to a velocity as high as the speed of light ($\sim$ c) and to extremely high energies ($\sim$ up to 10 TeV). Nowadays nearly 30000 accelerators with different sizes (from meters to several kilometres), shapes, type of applications (physics, medicine, industry...), mode of operation (CW and pulsed) are in operation all over the world. However depending on the method used for acceleration (electrostatic, radio-frequency, laser plasma...), these all accelerators can be divided into two fundamental types: linear and circular accelerators [5].

LINear ACcelerators (LINACs), accelerate electrons, positrons, protons and ions along a straight line by electrostatic field (DC) or RF (radiofrequency) field. In DC accelerators particles are accelerated between two electrodes due to the voltage difference. Cockcroft-Walton and Van de Graaff generators are two most popular examples of electrostatic acceleration [6]. In Cockcroft-Walton type of accelerators the achieved maximum voltage is equal to 0.8 MV and 25.5 MV for Van de Graaff generator [7]. In order to reach higher energies, RF acceleration is required. A series of RF accelerating structures (DTL, RFQ...) and resonators (cavities), operating at a specific oscillating resonance frequency, are installed all along the beam line to provide a continuous and optimal acceleration. Currently, typical accelerating gradients of 23.6 MV/m (in multi cell structures) have been achieved for such accel-

erators (XFEL) [8]. To reach energies as high as TeV for future projects the length of accelerators would be of 31 km (ILC), see in Section 2.1.2 and up to 50 km (CLIC) [9, 10].

RF cavities are also used for circular accelerators (synchrotron) not only in a straight portion of the ring to increase the beam energy after turn, but also in its injector (typically linear acceleration).

Depending on the beam intensity, 2 types of technologies exist for RF accelerating structures and cavities. The first technology, based on normal conducting (NC) material (usually made of Cu) can only be used for low average power beams (pulsed beam with low duty factor) and with average current of the order of $\sim \mu$A. The second technology based on superconducting material (usually made of Nb), way more complex and expensive to operate, allows to accelerate continuous and high current beams ($\sim$ mA). These 2 technologies are complementary. Copper cavities are cheaper to build and operate so are preferred as far as the RF power dissipated in the RF structure stays reasonable ($\sim$ 10 kW). Superconducting cavities are more difficult to design and operate as these require to be cooled down at -269 °C in complex cryogenic modules. Nevertheless they will dissipate typically one million times less RF power than copper cavities allowing the construction of very efficient accelerators with high current beams (several milliampers) at several GeV, see Figure 2.1. SRF technology is a key technology for future accelerators allowing to reach beam powers above several MW, NC technology wouldn't allow to go above few MW.

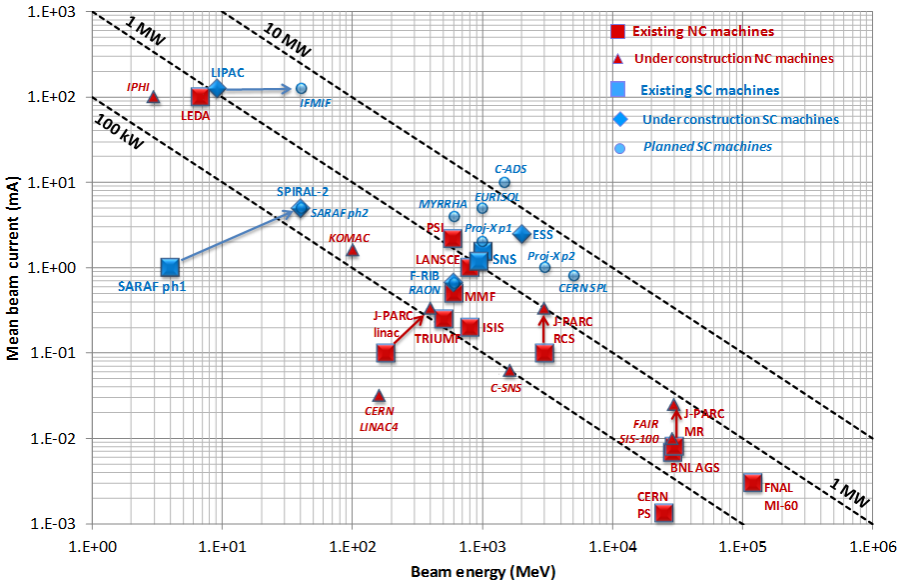

Figure 2.1: Overview of beam parameters (mean current and energy) of existing, under construction and future Normal Conducting and Superconducting [11].

2.1.1 Existing Large Scale Facilities Based on Superconducting Radio Frequency (SRF) Technology: LHC & XFEL

The first acceleration of electrons by SRF technology was performed in lead-plated cavities at SLAC linac in 1965 [12]. Started from 1970s [13], the lead-plated cavities have been replaced by cavities made of Niobium. The first produced Nb cavity had a pill-box shape. However due to strong multipacting phenomenon pill-box shape has been replaced by elliptical one [14]. The first elliptical or TESLA shaped cavity appeared in the 1980s. The first synchrotron based on SRF technology, the Cornell Electron Storage Ring (CESR), was constructed in 1979 [15]. From that time onwards, SRF technology evolved a lot in terms of design, material and surface treatment preparation. Nowadays, the most used cavities are the TESLA-type made of the bulk Niobium, for particles with a high β ratio of $v/c \approx 1$.

Many superconducting accelerators have been constructed and are in operation around the world like S-DALINAC (Darmstadt, Germany, 1991) [16], ALPI (LN Legrano, Italy, 1995) [17], FLASH (DESY, Germany, 1997) [18], ISACII-TRIUMF (Vancouver, Canada, 2006) [19], ISOLDE (CERN, Switzerland, 2015) [20] and many others. Their beam power increased over the years and the most powerful LINEAR SRF accelerator nowadays is SNS (average beam power above 1 MW) [21].

Among all the superconducting accelerators in operation, LHC and XFEL are the two major international large scale facilities based on SRF technology.

LHC

The Large Hadron Collider (LHC) is the largest synchrotron with a circumference of 27 km, which allows colliding 2 proton beams in counter rotation at an energy of 14 TeV (center of mass), or heavy ions at 5 TeV, see Figure 2.2. The aim of these high energy collisions is to explode protons and ions in order to detect subatomic components and characterize different type of elementary particles (quarks, bosons...) [22, 23]. The LHC has four installed detectors (ATLAS, CMS, ALICE and LHCb) to analyse the collisions and to record tracks at beam points interactions.

The first studies for the LHC started in 1982 and project was officially approved

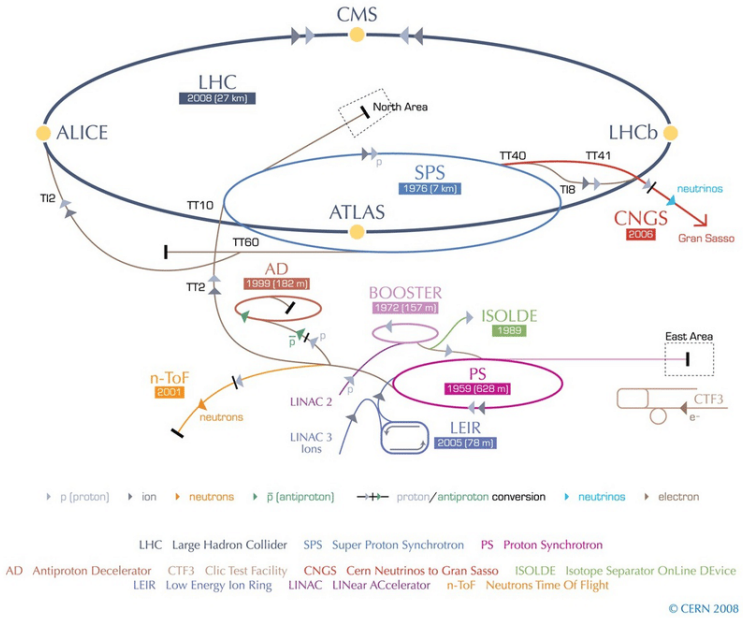

Figure 2.2: CERN accelerator complex [24].

by CERN (European Nuclear Research Council) community just twelve years later in 1994, after the discovery of Z_0 and W bosons and the prediction of High's theory. The construction of the synchrotron started few years later (1996) and finally ended in 2008 [25]. In 2013 the High's boson has been discovered at 125.09 $\pm$ 0.24 GeV by ATLAS and CMS detectors. The achieved luminosity (parameter which characterizes the cross-section of collisions) is 10^{34} [particles/cm$^2 \cdot s$]. To improve measurement accuracy and statistics of High's boson and physics at LHC, an upgrade of LHC (HL-LHC) has been initialized in 2018. Nominal luminosity of $1.7{*}10^{34}$ [particles/cm^2·s] may be achieved approximately in 2021. This upgrade is consisting in replacing dipoles (higher field, shorter length), quadrupoles (at the points of beam interaction) and inserting crab cavities (bunch flipping), see Section 2.2.3 [26].

LHC is composed of several types of superconducting components:

- 1624 magnets (mainly dipoles and quadrupoles made of Nb-Ti)
- 16 elliptical cavities (made of bulk Copper sputtered with Niobium).

Superconducting cavities and magnets operate at a cryogenic temperature of respectively 4.5 K (-268.7 °C) and 1.9 K (-271.3 °C), which is below the superfluid transition temperature of helium. The parameters of the SRF structures used in LHC, are presented in Table 2.1.

Table 2.1: Parameters of the LHC (proton-proton) accelerator

Parameters	Value	Unit
Proton beam energy	7	TeV
Luminosity	$1 * 10^{34}$	$cm^{-2}s^{-1}$
Number of cavities	16	
Accelerating gradient	5.3	MV/m
Radio frequency	400	MHz
Average beam current	530	mA
Circumference	27	km
Beam stored energy	362	MJ
Beam lifetime	10	h
Average beam power	10	kW

A picture of a cavity is presented in Figure 2.3. For the LHC, 4 cavities are grouped in one cryomodule, with 2 cryomodules (8 cavities) per particle beam.

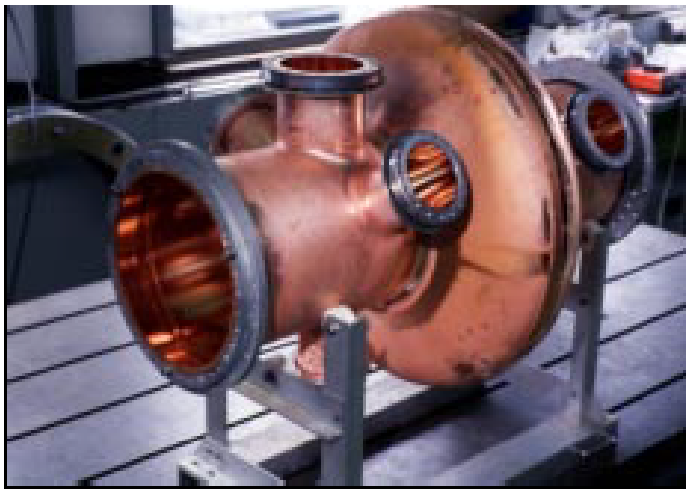

Figure 2.3: The LHC single cell elliptical cavity [27].

As shown in Figure 2.2, achieved beam energy of 7 TeV (at 180 mA beam current) for protons is performed through a chain of accelerators (LINAC 2, Booster, PS, SPS, LHC). Protons, produced by an ion source (duaplasmotron), are first accelerated up to an energy 92 keV (beam current of 300 mA). They are then focused, bunched and accelerated trough the radio frequency quadrupole (RFQ) (up to 750 keV). Afterwards LINAC 2 increases their energy up 50 MeV. Then accelerated particles are injected into a chain of synchrotrons. Bunch of protons are continuously accelerated by a complex system which consists of four synchrotrons. The Booster is the first synchrotron (157 meters in circumference) which ramps the

energy of the beam up to GeV range (1 GeV). Then the beam is extracted and injected in the Proton Synchrotron (PS) and then in the Super Proton Synchrotron (SPS) to increase the beam energy up to 450 GeV. It takes between 5.86 seconds to 17.86 seconds to reach this level of energy. The proton beam then is split into two beams and injected into the LHC. The final energy of 7 TeV for each beam is achieved. Approximately 20 minutes are required in LHC to accelerate the protons from 450 GeV to 7 TeV [28]. Typically duration of beam storage at such high energies is limited by the Touschek effect (loss energy due to scattering of particles in a storage ring) and is equal to 10 hours [29].

Heavy lead ions can be accelerated by a similar chain, however another linac (LINAC 3) is used.

XFEL

The European X-Ray Free-Electron Laser (XFEL) is a 3.4 km long underground facility providing the most intense and time resolved X-rays laser of the world [30]. The project started by the construction of a test facility named Tera-Electronvolt Superconducting Linear Accelerator (TESLA) in 2000 (DESY, Hamburg, Germany), which demonstrated the generation of photon beam with a wavelength of 90 nm. It gave a strong base for the preparation of the future facilities (FLASH, XFEL). The German government accepted the project in 2003 and the construction of XFEL started in 2009. The XFEL accelerator was built at DESY in 2016 and the first beam has been provided in 2017 [31].

As shown in Figure 2.4, the facility consists of an electron injector, bunch compressor, main linac, beam distribution system, undulators and photon beamlines. The injector accelerates the electron beam thanks to a RF gun with an exit energy of 120 MeV.

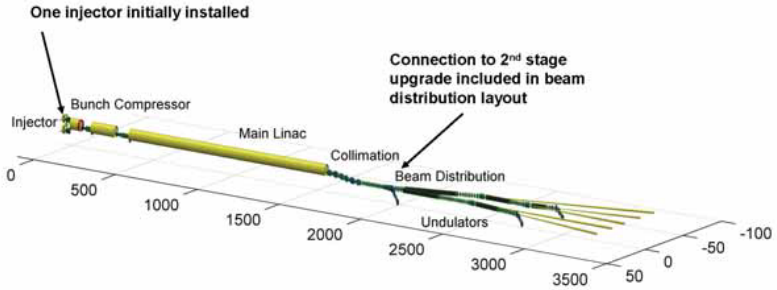

Figure 2.4: Sketch of the XFEL accelerator complex [32].

The superconducting linac (a 1.6 km long) consists of 808 multi-cell cavities made of the bulk Niobium (Figure 2.5). For the XFEL, 8 cavities are inserted per cryomodule. Main characteristics of the SRF linac are presented in Table 2.2.

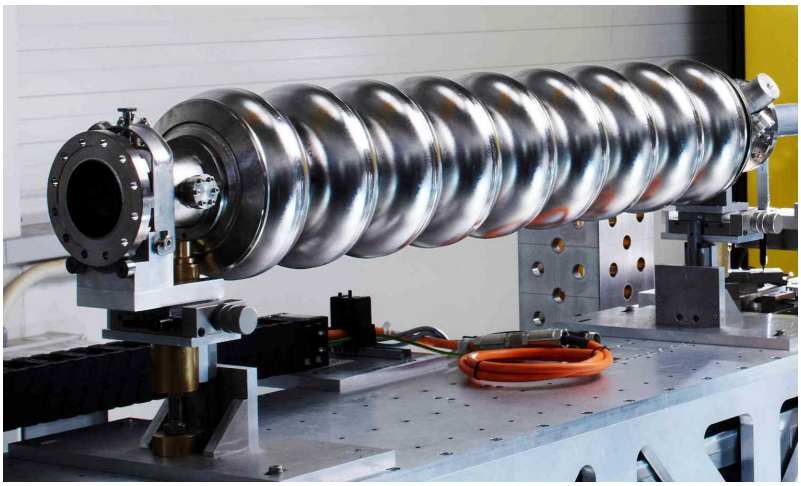

Figure 2.5: The XFEL nine cell elliptical cavity [33].

The SRF accelerator provides a high energy beam of electrons at 17.5 GeV (upgradable up to 20 GeV) which corresponds to a wavelength of 0.1 nm (0.08 nm). In order to produce the short and very dense electron beam, bunch compressors are located along the linac (before enter and after exit) Afterwards, the individual electron bunches are channeled towards electron beamlines by the beam distribution system. Finally, the X-Rays are produced thanks to undulators with energies ranging between 0.25-25 keV.

The production of such huge quantity of cavities (808) has been an industrial challenge and was successful.

Table 2.2: Parameters of the SRF linac for XFEL facility

Parameters	Value	Unit
Beam energy	17.5(20)	GeV
Number of cavities	808	
Accelerating gradient	23.6	MV/m
Radio frequency	1.3	GHz
Average beam current	5	mA
Total length	1.6	km
Average beam power	650	kW

2.1.2 Future of SRF Accelerators: FCC & ILC

Many SRF accelerator projects are appearing because of the capabilities offered by such technology in term of energy, beam current and power. This technology is very attractive not only for particle physics (FCC, ILC, PIP-2, LCLS-2, FRIB) [34, 35, 36, 37, 38], but also for material science (ESS) [39], medical (SIRIUS) [40] and societal applications (MYRRHA).

Lots of efforts are invested to expand our knowledge of the universe, discover new forms of matter (dark matter), and observe a boson with better precision. Such ambitious goals can be achieved using the collision of electrons and positrons at extremely high energies up to 350 GeV in Future Circullar Collider (FCC) [34, 41] and at 250 GeV in International Linear Collider (ILC) [35].

Among all SRF projects under study, FCC and ILC are the most challenging future accelerators not only by their dimension, but also by the technical requirements.

FCC

The Future Circular Collider (FCC) is an ambitious project which will significantly increase the luminosity and energy beams not only for electron-positron collisions, but also for others possible scenarios (proton-proton and proton-electron collisions) [42]. The LHC, described in Section 2.1.1, will be used as an injector for the FCC. The LHC will be connected with the FCC by using a series of superconducting magnets.

First scenario predicts the collision of opposing beams of electrons and positrons at centre energy mass energy at 350 GeV. The point-type collision will give an additional accuracy in the measurements of the bosons and will increase statistics of produced sub-atomic particles. Second scenario will collide the beams of protons/ions under energies of 100 TeV. Such high energies will verify if other sub-atomic particles not predicted by the standard model, exist. Third scenario will study the deep inelastic scattering of proton beam at the energy of 50 TeV and electron beam of 60 GeV.

To achieve such ambitious goals the FCC will show a circumference of 100 km, see Figure 2.6, requires the production of more than 1000 elliptical multi-cell cavities

(Section 2.2.3) operating at frequencies 400/800 MHz, around 300 of single cell and crab resonators operating at 400 MHz. Prototypes of SRF accelerating structures and their characteristics respectively are presented in Figure 2.7 and Table 2.3. For the FCC, 4 cavities will be installed per cryomodule.

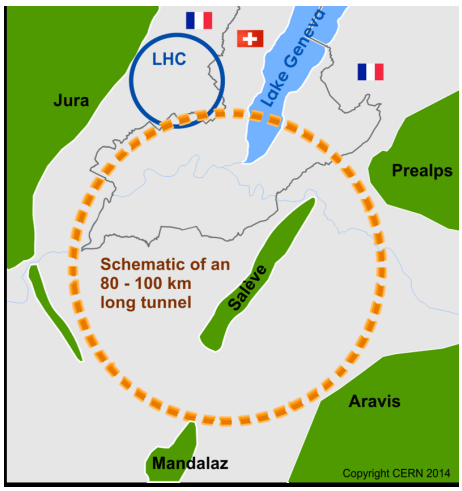

Figure 2.6: Sketch of the FCC accelerator [41].

Table 2.3: Parameters of the FCC (electron-positron) accelerator

Parameters	Value	Unit
Beam energy	350	GeV
Luminosity	$5 * 10^{34}$	$cm^{-2}s^{-1}$
Number of cavities	1286	
Accelerating gradient	10-20	MV/m
Radio frequency	400-800	MHz
Beam current (in pulse)	6.6-1450	mA
Circumference	100	km
Beam stored energy	8.4	GJ
Average beam power	10	MW

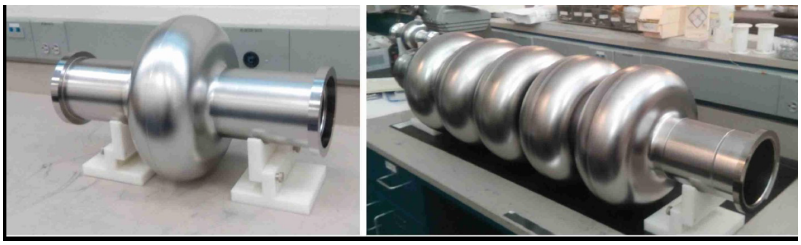

Figure 2.7: Prototype 1-cell and 5-cell cavity for FCC accelerator [43].

ILC

The International Linear Collider (ILC) is the future large scale facility which may be built in Japan. It is planned to collide positrons and electrons at an energy of 250 GeV (upgradable up to 1000 GeV) [44] [45]. To achieve such energies the length of linear collider has to be at least 31 km. A sketch of linear collider is presented in Figure 2.8.

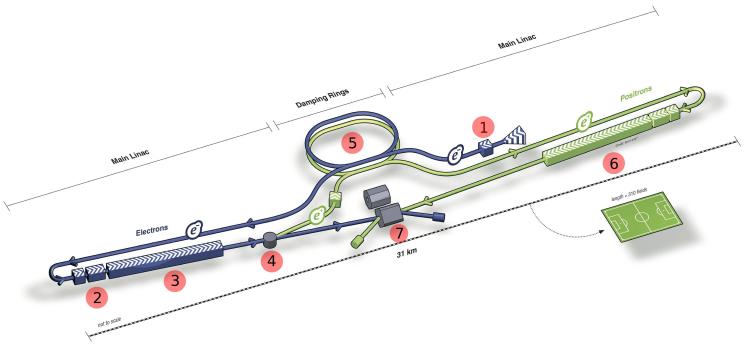

Figure 2.8: Sketch of the ILC accelerator complex [45].

The beam of electrons, similarly to XFEL, produced by a photocathode DC gun (electron source) (1) enters to bunch compressor (2), where beam is compressed and accelerated up to 76 MeV. Afterwards, the electrons beam increases energy up to 5 GeV in a superconducting linac (11 km long) (3) thanks to 1.3GHz multi-cells cavities, see Figure 2.9.

Figure 2.9: Superconducting elliptical nine-cell cavity made of Niobium (1.3 GHz) [45].

Then the accelerated electrons are injected into undulators (4) and the positrons are produced. A dedicated beam delivery system transfers the positrons beam to the second superconducting linac (6), where the positron beam increases his energy up to 5 GeV and similarly to electron beam enters in the damping ring (5). Then electrons enter into the damping ring (3.2 km) in order to reduce the beam emittance which is needed to be minimum and to gain a high luminosity at the interaction

point (7). The 2 superconducting linacs will consist of 16000 (ILC250) cavities. The cryomodules will be composed of either nine cavities or eight cavities and one quadrupole.

After damping rings the beam of electrons and positrons are accelerated again by bunch compressor and energy increased from 5 GeV up to 15 GeV. Afterwards, in the main superconducting linac energy level may be increased up to 125 GeV at a first stage (system upgradable to 250 GeV and then to 500 GeV).

Table 2.4: Parameters of the ILC accelerator

Parameters	Value	Unit
Beam energy	250	GeV
Luminosity	$2 * 10^{34}$	$cm^{-2}s^{-1}$
Accelerating gradient	31.5	MV/m
Number of cavities	16000	
Radio frequency	1.3	GHz
Average beam current (in pulse)	9	mA
Effective acceleration length	22	km
Average beam power	2.63	MW

The project was initiated in 2004. However in order to approach the creation of ILC the R&D programs over the world aimed at improving performance of the SRF cavities and reduce costs of preparation (increase production yield).

Although existing for more than 50 years SRF technology is a very new technology still requiring significant efforts and maturation to make future projects like FCC and ILC possible (financially and technically).

Figures 2.10 and 2.11 provide information about the number of SRF cavities used in the past, in operation and future SRF resonators. It can be stressed that the construction of ILC will multiply by 8 the total number of superconducting cavities fabricated so far. Nowadays about 2000 SRF cavities are in operation and 16000 will be required for ILC. SRF technology is a flourishing business at its beginning and by its capabilities and successful industrialization (XFEL), most of future international accelerator projects will be based on it.

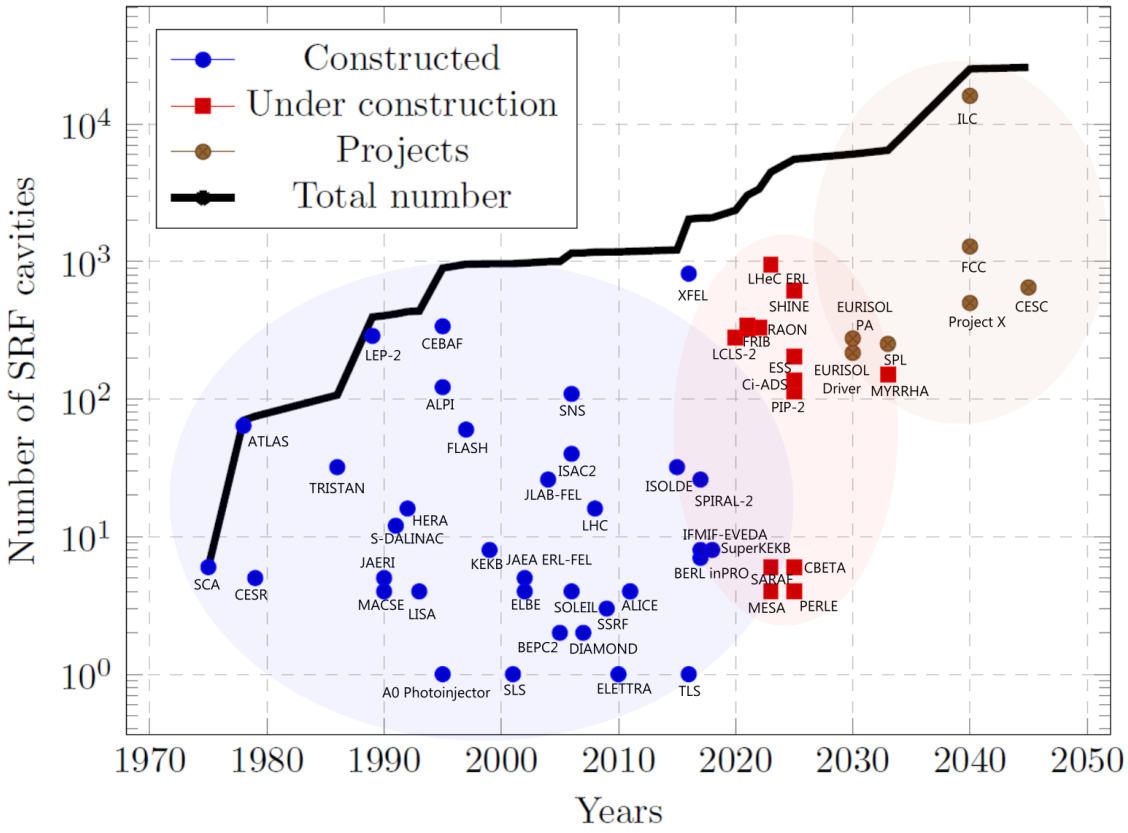

Figure 2.10: Evolution in time of the total number of SRF cavities in the world.

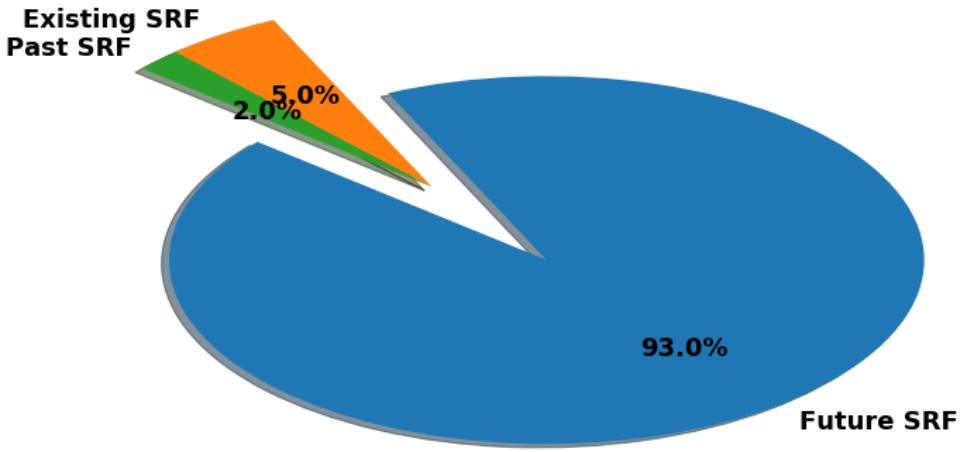

Figure 2.11: Total number of SRF fabricated cavities all over the world (bulk Nb, Nb/Cu): a) past (green), b) in operation (orange), c) to be fabricated (blue). Total number of cavities : 20379 [46].

2.2 Superconducting Radio-Frequency Cavities

Radio-frequency cavity is a key element of linear or circular accelerators where alternating intense electromagnetic fields are used for acceleration of charged particles, see Figure 2.12. RF waves are injected through a power coupler in the cavity. This cavity, could be made of normal conductor (typically copper) or superconductor (typically bulk Nb), and respectively operated at room and cryogenics temperatures. Superconducting RF (SRF) cavities require a cryogenic plant and dedicated auxiliary systems, however the power dissipated in the case of SRF technology is several million times lower than for normal RF cavities (at 1.5 GHz R_s(Cu)= 10 mΩ and R_s(Nb)=20 nΩ at 2 K).

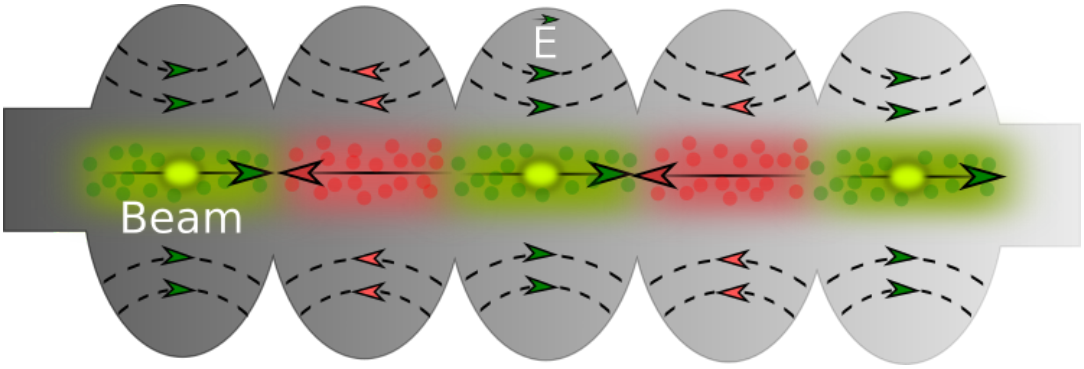

Figure 2.12: Sketch of RF cavity.

RF cavities can operate in two different wave modes: travelling wave (TW) or standing wave (SW) [47], see Figure 2.13.

Travelling wave propagates along the cavity with bunches of particles thus transferring RF energy all along the RF structure. Standing wave (SW) appears due to interaction of incident and reflected waves in the cavity. The principal difference, between these two wave modes is the filling time. TW creates an extremely short RF pulse in the range of microseconds whereas SW requires a longer RF pulse in the range of milliseconds. Travelling wave cavities can reach higher accelerating fields compare to standing wave cavities, as the length of the last is limited by field flatness degradation (typically 1 m). However SW cavities allow a higher duty cycle, low beta operation (non relativistic particles) and a lower energy spread than the travelling wave cavities. This flexibility in operation is giving them wider spectrum of applications (most of projects are based on SW model) [48].

A cavity may be used for low β and high β applications (different particle velocity and pulse length) by adapting the shape of accelerating structure [49, 50]. Because of

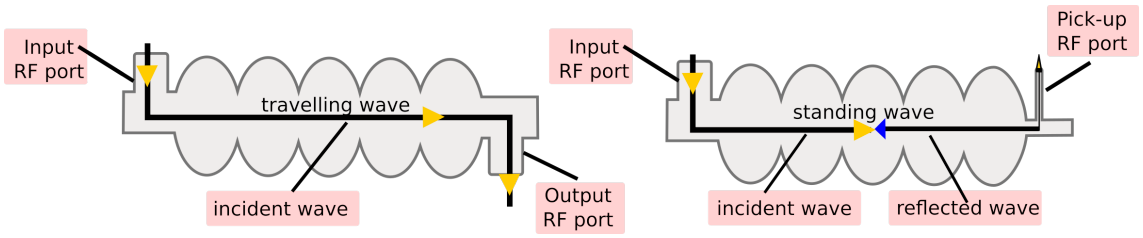

Figure 2.13: Sketch of SRF cavities operated in travelling wave and standing wave modes.

boundary conditions (perfect conductor) these enclosed structures show EM modes, or resonance modes, at given frequencies. When excited at the frequency of a mode, the amplitude of RF is amplified by resonance, and a high field can be achieved.

The EM modes can be calculated by solving wave equations obtained through the Maxwell's equations presented by in the following expressions:

$$\vec{\nabla} \times \vec{E} = -\frac{\partial \vec{B}}{\partial t} \tag{2.1}$$

$$\vec{\nabla} \cdot \vec{E} = 0 \tag{2.2}$$

$$\vec{\nabla} \times \vec{B} = \mu_0 \epsilon_0 \frac{\partial \vec{E}}{\partial t} \tag{2.3}$$

$$\vec{\nabla} \cdot \vec{B} = 0, \tag{2.4}$$

where $\vec{E}$ is the vector of electric field, $\vec{B}$ is the vector of magnetic field, μ_0 is the magnetic permeability and ϵ_0 is the dielectric permittivity (ϵ_0=1 in vacuum) [48].

In order to obtain wave equations for $\vec{E}$ and $\vec{B}$, the following property $\nabla \times (\nabla \times \vec{E}) = -\Delta \vec{E}$ and $\nabla \times (\nabla \times \vec{B}) = -\Delta \vec{B}$ can be applied to equations Equation (2.1) and Equation (2.3). We obtain:

$$\Delta \vec{E} - \mu_0 \cdot \epsilon_0 \frac{\partial^2 \vec{E}}{\partial t^2} = 0 \tag{2.5}$$

$$\Delta \vec{B} - \mu_0 \cdot \epsilon_0 \frac{\partial^2 \vec{B}}{\partial t^2} = 0. \tag{2.6}$$

EM modes formed due to boundary conditions (cavity wall = perfect conductor), implying no tangential electrical field and no normal magnetic field, may be classified as a superposition of plane waves that could exist in several transverse modes: **TE** (transverse electric mode), **TM** (transverse magnetic mode) and **TEM** (transverse electromagnetic) [48]. **TE** modes have no electrical field and only magnetic field along the direction of wave propagation. **TM** modes have no magnetic field and only electrical along the direction of wave propagation. **TEM** mode is characterized by transverse directions of EM fields in the direction of propagation. In order to accelerate particles to high accelerating gradients along cavity length, **TM** or **TEM** mode are used. Three indices m, n and p are used to characterize **TM** modes in order to indicate the number of half-wave patterns.

The simplest solution of the wave equations can be derived analytically in cylindrical coordinates (r,ϕ and z) for a pill-box cavity with a radius R and length l, for the mode TM_{010} along the z-axis in the following way:

$$E_r = 0 \tag{2.7}$$

$$E_z = E_0 J_0(kr) e^{-iwt} \tag{2.8}$$

$$H_\phi = -i\frac{E_0}{c} J_1(kr) e^{-iwt} \tag{2.9}$$

$$w_{010} = \frac{2.405c}{R}, \tag{2.10}$$

where k is the wave number ($k = \frac{2\pi}{\lambda} = \frac{w}{c}$), E_0 is the amplitude of the electric field, J_0 and J_1 are Bessel functions, w is the angular frequency ($w = 2\pi f$, where f is the resonance frequency) and c is a speed of light. The angular frequency does not depend on the cavity length as there is no variation of the fields in the longitudinal direction.

In order to compare performances of SRF cavities the following parameters are used: quality factor (Q_0), shunt impedance r, accelerating gradient (E_{acc}), ratio of peak surface electric field to accelerating field (E_{peak}/E_{acc}) and ratio of peak surface magnetic field to accelerating field (B_{peak}/E_{acc}).

The quality factor represents the ratio of stored energy to energy loss (RF dissipations) per cycle in the cavity structure:

$$Q_0 = \frac{\omega \cdot U}{P_d} = \frac{2\pi \cdot f \cdot U}{P_d}, \tag{2.11}$$

where f is the resonance frequency, U is the stored energy and P_d is the dissipated RF. The cavities operate under vacuum, thus the losses in the electrical volume (V) are negligible, but the RF dissipations take place on the walls of the cavity. The surface currents induced by the tangential magnetic field (B) cause dissipations zones due to the surface resistance (R_s), see Section 2.2.1 (Joule effect is proportional to the R_s of the material). The total dissipated RF can be obtained by integrating magnetic field over the whole cavity surface area:

$$P_d = \frac{R_s}{2 \cdot {\mu_0}^2} \int_S \mid B \mid^2 dS. \tag{2.12}$$

The stored energy in the SRF cavity can be calculated from the cavity volume and the magnetic field:

$$U = \frac{1}{2 \cdot \mu_0} \int_V \mid B \mid^2 dV. \tag{2.13}$$

Thus from Equation (2.12) and Equation (2.13), the quality factor can be written as:

$$Q_0 = \frac{2\pi \cdot f \cdot \mu_0}{R_s} \frac{\int_V \mid B \mid^2 dV}{\int_S \mid B \mid^2 dS} \tag{2.14}$$

or

$$Q_0 = \frac{G}{R_s}, \tag{2.15}$$

where G is the geometrical factor of the SRF cavity, which describes the cavity shape (does not depend on the material properties but only on geometry) and is expressed as:

$$G = 2\pi \cdot f \cdot \mu_0 \frac{\int_V \mid B \mid^2 dV}{\int_S \mid B \mid^2 dS}. \tag{2.16}$$

Accelerating gradient (E_{acc}) of a cavity is defined as the line integral of the longitudinal electric field along length (l) of cavity and given by equation:

$$E_{acc} = 1/l \int_0^l E(z)cos(wt)dz. \tag{2.17}$$

Shunt impedance (r) is the ratio between the square of the accelerating voltage and dissipated power (P_d). So as not to depend on material, the ratio of shunt impedance and quality factor is preferred and is expressed by:

$$\frac{r}{Q} = \frac{1}{2}\frac{E_{acc}^2 \cdot L_{acc}^2}{\omega \cdot U}, \tag{2.18}$$

where L_{acc} is the accelerating length.

Main parameters used for characterization of SRF cavities are presented in Table 2.5 for some low, medium and high beta SRF cavities. Optimization of the geometry aims at maximizing Q_0, r/Q (in order to push the performance) and at minimizing the ratios of E_{peak}/E_{acc} and B_{peak}/E_{acc} (in order to avoid the field emission and to delay quench field).

Table 2.5: Design RF parameters of pill-box , QWR (Spiral2), double spoke (ESS) and elliptical (TESLA) [51], [52], [53], [54].

	Pill-box	QWR (SPIRAL2)	Spoke (ESS)	Elliptical (XFEL)
r/Q , Ω	196	632/520	418	1036
$\frac{E_{peak}}{E_{acc}}$	1.6	5/5.54	4.28	2
$\frac{B_{peak}}{E_{acc}}$, $\frac{mT}{MV/m}$	4.7	8.75/10.1	6.8	4.2

2.2.1 Theory of Superconductivity

Superconductivity was discovered by Heike Kamerlingh Onnes in 1911 [55]. It was observed that the DC resistance of mercury suddenly vanishes below a temperature (called later critical T_c). It is only 22 years later that the Meissner effect has been discovered (1933) [56]. The first empirical model, the London theory (two fluid model) appeared in 1934 [57] and the second, the Ginsburg-Landau Theory (GL model) was later in 1950 [58]. Seven years later (in 1957), was built the first microscopic theory, based on quantum mechanics by Bardeen, Cooper and Schieffler (BCS theory) [59]. In 1962 was finally discovered the so-called Josephson effect [60].

Nowadays superconductivity is a key element not only for particle acceleration (magnets, cavities...), but also for human needs of transportation (Maglev trains) [61]. Among the transport applications, superconductors are used for industrial (SQUID sensors, cables) and medicine (magnetic resonance imaging) applications.

Critical temperature

The critical transition temperature from the normal state to superconducting for each material is different. Table 2.6 shows the critical temperatures characterized by the vanishing of resistance for some superconductors in the absence of the magnetic field. Mercury (Hg) is the first discovered material, which shows its superconducting properties below 4.2 K, see Figure 2.14.

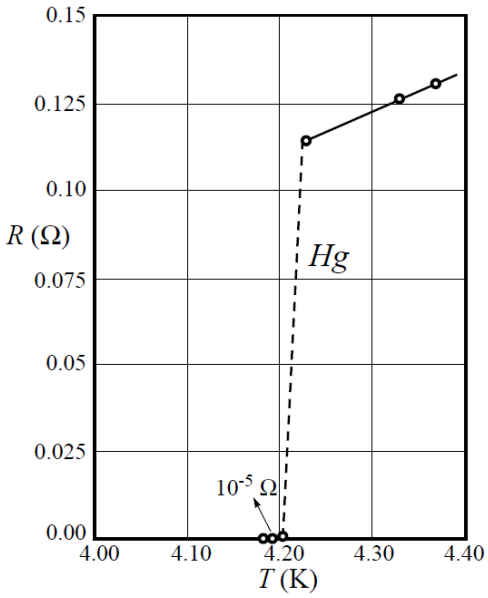

Figure 2.14: The DC resistance vanishing of mercury [62].

Niobium is the pure material showing the highest critical temperature. Several alloys have been then discovered showing higher critical temperature. Niobium-based alloys could reach a T_c of 18.7 K and MgB_2 alloy 40 K. Other types of complex copper-based alloys (cuprates) show T_c up to 93 K.

Table 2.6: The critical transition temperature for some materials.

Material	Ti	Al	Hg	Sn	Pb	Nb	NbTi	NbN	NbTiN	Nb_3Sn	Nb_3Al	MgB_2
T_c [K]	0.4	1.14	4.2	3.72	7.9	9.2	10	16.2	17.3	18.3	18.7	40

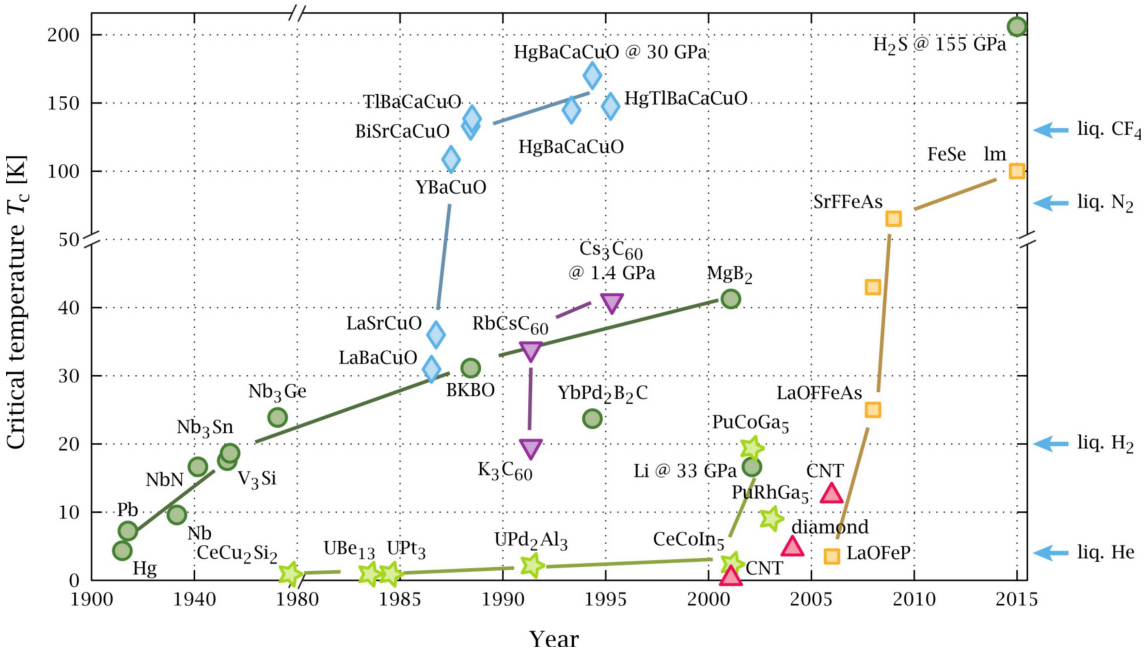

Figure 2.15: Superconductors transition temperature T_c versus their year of discovery [63].

Any superconductor looses its properties (commonly named quench) not only when the temperature goes above T_c but also when the external magnetic field is too high, see Section 2.2.1.

Meissner effect

Once the superconductor is cooled below T_c and in the case of presence of an external magnetic field, magnetic flux is expelled from superconductor. This effect was observed by Meissner and Ochsenfeld (latter named as Meissner effect) and shown in the Figure 2.16. This perfect diamagnetic behaviour appears due to the fact that a superconductor develops surface currents (named later as supercurrents) producing a magnetic counter-field which compensates the external magnetic field. It has to be mentioned that the Meissner effect is not a consequence of a perfect conductivity (ρ=0) but is an independent second characteristic of a superconductor [64].

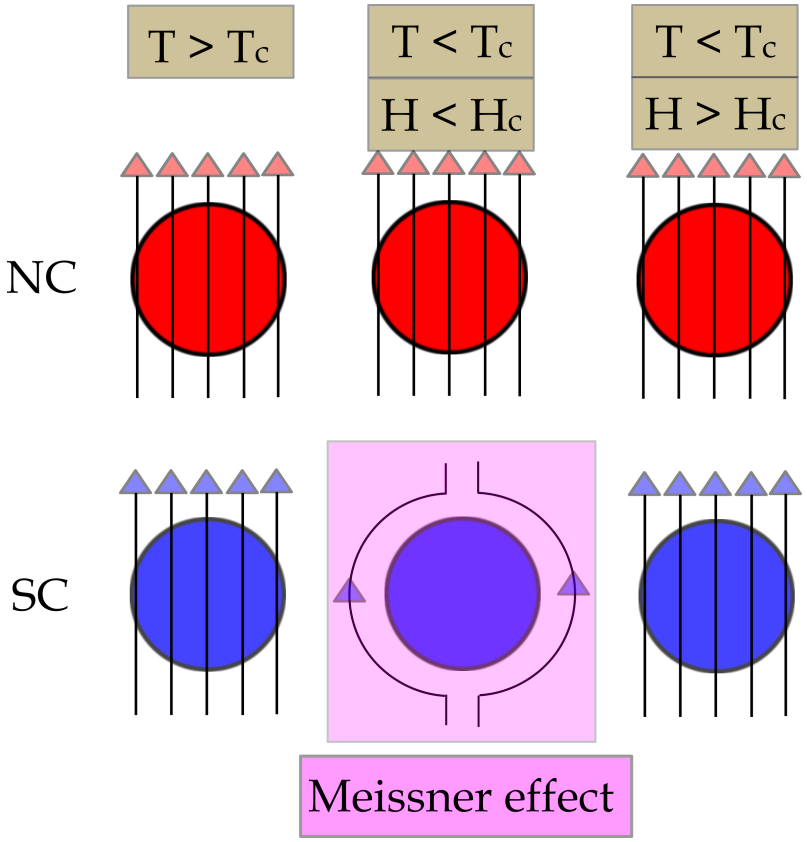

Figure 2.16: Meissner effect: When cooled below the critical temperature, a superconductor expels the residual magnetic field. This Meissner state is destroyed when the external field exceeds the critical magnetic field.

Critical field

The existence of the superconducting state does not depend only on the temperature. Indeed, even below T_c ($T < T_c$), superconductivity could be destroyed if the

external magnetic field is above a threshold called critical magnetic field (H_c), see Figure 2.17. A superconductor can be quenched (loose superconducting properties) either by a too high temperature or/and magnetic field as this H_c depends as well on temperature. The temperature dependence of H_c, can be expressed by the empirical formula which is given below:

$$H_c(T) = H_c(0K)\left(1 - \left(\frac{T}{T_c}\right)^2\right). \tag{2.19}$$

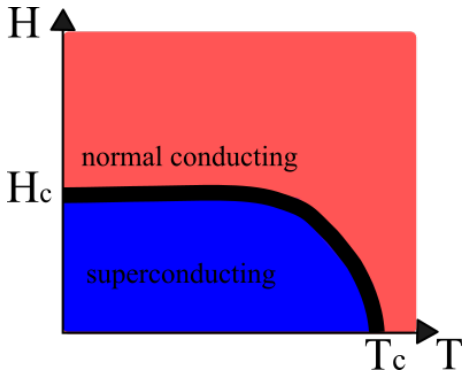

Figure 2.17: The phase diagram of type I superconductor.

Two Types of Superconductors

Two types of superconductors exist: type I and type II. This difference appears due to a different behavior in the presence of an external magnetic field. The first type of superconductor (type I) behaves like a perfect diamagnetic material below critical temperature T_c and critical field H_c. If the external magnetic field goes above the critical ($H > H_c$) the magnetic flux fully penetrates the superconductor and superconductivity breaks down. The phase transition is of first order (abrupt).

As shown in Figure 2.18, the second type (type II) of superconductor has the particularity of having two critical fields, named H_{c1} and H_{c2}. If the external magnetic field goes above H_{c1} (field of first entry), the superconductor doesn't loose completely superconductivity, it enters in a mixed state (phase transition is of second order (progressive)).

In this state, a part of the magnetic flux penetrates the superconductor through vortices. These vortices, named as fluxoids, passing through the material in the same direction as the applied magnetic field. These vortices are normal conducting zones surrounded by supercurrents. These induced currents prevent the propagation

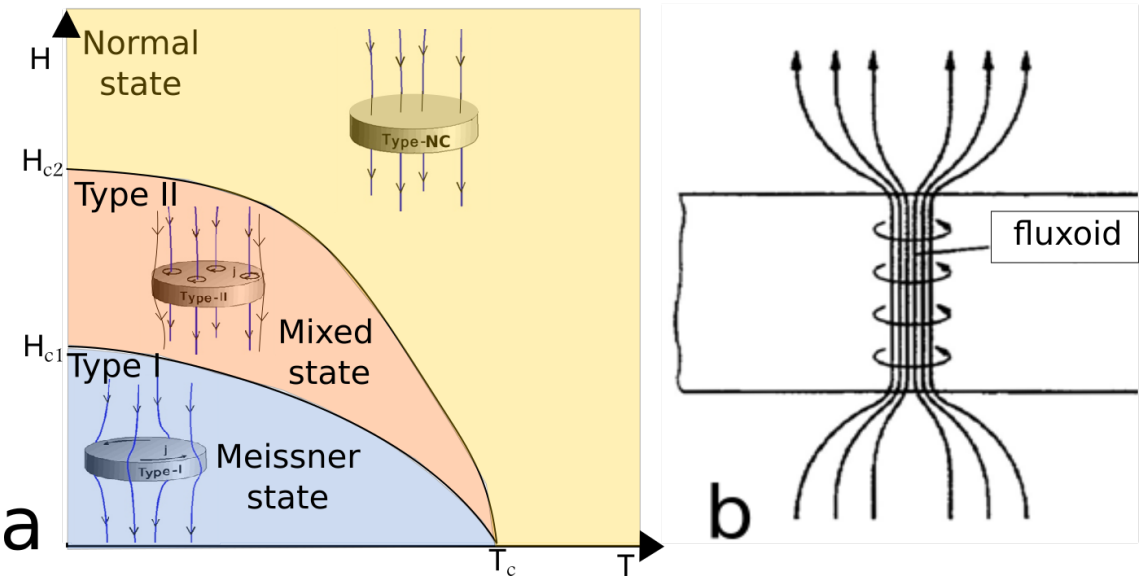

Figure 2.18: The phase diagram of type II superconductor (a) and sketch of the vortex formations for superconductors of type II (b) [65].

of the magnetic field toward the remaining superconducting zones. The magnetic flux in each vortex is quantized. Increasing the field will thus multiply the number of vortices. At some point, the density of vortices is such that the superconducting regions are so narrow that superconductivity is lost. The superconducting state remains in the local regions until the upper critical field H_{c2} is reached. This behavior will be explained later, in Ginsburg-Landau model, see Section 2.2.1.

London Model (two-fluid theory)

The first successful phenomenological model for superconductors was presented by Heinz and Fritz London in 1934 [66]. They assumed that the carriers of charge in the superconductor are divided into two subsystems. The first subsystem describes the density of normal carriers n_n and the second represents the density of superconducting carriers n_s. Consequently the total number of carriers (N) is the sum of normal electrons (n_n) the superconducting (n_s), and is equal to $N = n_n + n_s$. The total number of electrons of the system is constant. Only the balance between n_n and n_s can vary depending on temperature conditions. It is necessary to define the order parameter named ψ, which gives a ratio of the density of superconducting carriers to the total number of carriers and is given by the following equation:

$$\psi = \frac{n_s}{N}. \tag{2.20}$$

From this two-fluid model and from an electrodynamic calculation based on Maxwell's equations (2.1-2.4), the two equations of London were derived in 1935. Scientists assumed that the superconducting electrons are in a frictionless state below the critical temperatures.

The first London equation can be obtained from an equation of motion, which is given by the following equation:

$$m_e \frac{\partial \vec{v}}{\partial t} = -e\overrightarrow{E}, \tag{2.21}$$

where m_e is the mass of electrons, $\overrightarrow{v}$ is the velocity of the electrons, e is the charge of electrons and $\overrightarrow{E}$ is the electric field.

The supercurrent density is expressed as:

$$\overrightarrow{J_s} = -n_s e\vec{v}, \tag{2.22}$$

where n_s is the density of the superconducting electrons.

The replacement of v by the supercurrent in Equation (2.21) gives the first London equation:

$$\frac{\partial \overrightarrow{J_s}}{\partial t} = \frac{n_s e^2}{m_e}\overrightarrow{E} => \overrightarrow{E} = \frac{m_e}{n_s e^2}\frac{\partial \overrightarrow{J_s}}{\partial t}. \tag{2.23}$$

Then using the Equation (2.1), which connects the rotational electric field to the temporal variations of the magnetic field, in the first London equation, the second London equation is obtained:

$$\frac{\partial}{\partial t}(\frac{m_e}{n_s e^2}\overrightarrow{\nabla} \times \overrightarrow{J_s} + \overrightarrow{B}) = 0. \tag{2.24}$$

Then, always considering a static electric field (displacement current is zero), the Maxwell-Ampere equation, Equation (2.3), can be written:

$$\overrightarrow{\nabla} \times \overrightarrow{B} = \mu_0 \overrightarrow{J_s}. \tag{2.25}$$

Combining the Maxwell-Ampere equation and making use of the following relation:

$$\overrightarrow{\nabla} \times (\overrightarrow{\nabla} \times \overrightarrow{B}) = \overrightarrow{\nabla}(\overrightarrow{\nabla} \cdot \overrightarrow{B}) - \Delta \overrightarrow{B} = -\Delta \overrightarrow{B}, \tag{2.26}$$

the statement above works because $\overrightarrow{\nabla} \cdot \overrightarrow{B} = 0$.

Now we express the $\overrightarrow{J_s}$ as $\frac{\overrightarrow{\nabla} \times \overrightarrow{B}}{\mu_0}$ (from Equation (2.25)), insert this expression in the Equation (2.24) and use the Equation (2.26), we obtain the following equation for the magnetic field in a superconductor:

$$\frac{\partial}{\partial t}(\Delta \overrightarrow{B} - \frac{e^2 n_s \mu_0}{m_e} \overrightarrow{B}) = 0. \tag{2.27}$$

Finally, in the case if the magnetic flux is homogeneous in the whole superconductor the second London equation is given by the following expression:

$$\Delta \overrightarrow{B} - \frac{\overrightarrow{B}}{{\lambda_L}^2} = 0 \tag{2.28}$$

with a solution :

$$B_y(x) = B_0 \cdot exp(-x/\lambda_L), \tag{2.29}$$

where λ_L is the penetration depth of the magnetic field into the material, named as the London penetration depth:

$$\lambda_L = \sqrt{\frac{m_e}{\mu_0 n_s e^2}}. \tag{2.30}$$

Contrary to NC, the penetration does not depend on frequency, but only on density of superconducting electrons, or in other word temperature. Indeed, in normal conductor the penetration depth (named as the skin depth δ) into the material is given by:

$$\delta = \sqrt{\frac{2}{\mu_0 \sigma_n \omega}}, \tag{2.31}$$

where σ_n is the electrical conductivity of the normal conductor. For example, the skin depth of Copper at 300 K (σ_n=5.8×10^7 $1/\Omega\ m$) and at frequency 1.5 GHz is equal to 1.7 μm. The penetration depth into bulk Niobium at 2 K is equal to 40 nm independently of frequency.

This explains why a superconductor behaves like a diamagnetic even with a static magnetic field. Contrary to NC for which the skin depth would tend to infinity for a static field, a SC would exhibit a constant penetration depth. The London's penetration depth depends on the number of superconducting electrons, hence on the temperature. The temperature dependence of the penetration depth of the superconductor, can be expressed by the empirical formula which is given below:

$$\lambda_L(T) = \frac{\lambda_L(T=0)}{\sqrt{1-(\frac{T}{T_c})^4}}. \tag{2.32}$$

If we consider that superconductor is subjected to a sinusoidal electric field ($E = E_0 \cdot exp^{i\omega t}$), then the solution of the first London's equation will give the current carried by the superconducting electrons:

$$\overrightarrow{J_s} = -i\sigma_s \overrightarrow{E}(t), \tag{2.33}$$

where σ_s is the conductance of the superconducting electrons:

$$\sigma_s = \frac{n_s e^2}{m_e \omega}. \tag{2.34}$$

Current carried by normal electrons is given by:

$$\overrightarrow{J_n(t)} = \sigma_n \overrightarrow{E(t)} = \frac{n_n e^2 l}{m_e v_F} \overrightarrow{E}(t), \tag{2.35}$$

where l is the average mean free path of electrons and v_F is the velocity of Fermi (v_F=$1.86 \cdot 10^6$[m/s]).

According to the hypothesis of the two-fluid model ($J = J_s + J_n$) and taking into account the Equation (2.33) and Equation (2.35), the total current can be written as:

$$\overrightarrow{J}(t) = \sigma \cdot \overrightarrow{E}(t) = (\sigma_n - i\sigma_s)\overrightarrow{E}(t). \tag{2.36}$$

Hence, we can write the wave equations of an electric and magnetic field for the two-fluid model in the following way:

$$\Delta E - \mu_0 \sigma \frac{\partial E}{\partial t} = 0, \Delta B - \mu_0 \sigma \frac{\partial B}{\partial t} = 0, \tag{2.37}$$

or

$$\Delta E - \mu_0 \cdot \sigma \cdot i \cdot \omega \cdot E = 0, \Delta B - \mu_0 \cdot \sigma \cdot i \cdot \omega \cdot B = 0. \tag{2.38}$$

From Equation (2.38), we can define the factor k:

$$k = \frac{1}{\sqrt{\mu_0 \cdot i \cdot \omega \cdot (\sigma_n - i \cdot \sigma_s)}}. \tag{2.39}$$

The factor k represents somehow the penetration depth of the electric field into polluted material "by non-superconducting electrons" and is defined as:

$$k = \frac{\lambda_{L0}}{\sqrt{\psi + i \cdot \omega \cdot \tau \cdot (1 - \psi)}}, \tag{2.40}$$

where $\lambda_{L0} = \sqrt{\frac{m_e}{Ne^2\mu}}$ is the London penetration depth at T=0 K, and ψ the order parameter as defined in Equation (2.20).

Consequently we can define the real surface resistance of superconductor due to flow of current over the surface in the following way (all details of calculations are presented in this reference [67]):

$$R_s = Re(\frac{j\mu_0\omega\lambda_{L0}}{\sqrt{\psi + i\omega\frac{l}{v_F}(1 + \psi)}}). \tag{2.41}$$

If temperature of the superconductor is much below critical temperature, it is possible to consider that superconducting electrons dominate in the total population N, hence $\psi \sim 1$. Under this condition the Equation (2.41) is simplified and is given by:

$$R_s = \frac{1}{2}{\mu_0}^2\omega^2\lambda_L^3\sigma_n. \tag{2.42}$$

The surface resistance quadratically depends on the frequency of the electromagnetic wave (for normal conducting materials $R_s \sim \sqrt{\omega}$) and depends on the conductivity of the material in its normal state: a higher normal conductivity leads to an increased superconducting surface resistance (Rs).

Actually R_s is the real part of the complex surface impedance (Z_s), which describes the response of a metal to EM fields:

$$Z_s = R_s + i \cdot X_s, \tag{2.43}$$

where X_s is the imaginary part of the surface impedance which describes the surface reactance.

The 2 fluid model gives an explanation to the Meissner effect and the phenomenon of DC resistance disappearance. It does not explain why superconductors exhibit a field limitation (existence of a critical field). A new model is required.

Ginsburg-Landau Theory (thermodynamic model)

In 1950 V. Ginsburg and L. Landau (GL) introduced a new approach in order to explain the behaviour of the superconductor at high magnetic fields [68]. This approach is based on thermodynamic considerations and more specifically on the second principle of thermodynamics. The second principle of thermodynamics defines the free energy F of a system according to its internal energy U and its entropy S:

$$F = U - T \cdot S. \tag{2.44}$$

The free energy of a system in its superconducting state (F_s) is necessary lower compared to its normal state F_n, because the superconducting state is stable. When the superconducting system is exposed to a magnetic field, there exists a value H_c for which the transition to the normal state is possible. The transition of SC state to NC state can be written in the following way:

$$F_n - F_s = \frac{\mu_0 \cdot V_s \cdot {H_c}^2}{2}, \tag{2.45}$$

where V_s is the volume of the superconductor.

GL, based on this statement, conducted a more detailed study, in particular on the evolution of entropy, and they established the relation, which gives the evolution of F_s as a function of T:

$$F_s - F_n = \int dV[\alpha(T)\cdot \mid \psi \mid^2 + \frac{\beta}{2}\cdot \mid \psi \mid^4 + \frac{h}{4\pi m} \mid (\nabla + \frac{2 \cdot i \cdot \pi \cdot \overrightarrow{S}}{\Phi_0}) \cdot \psi \mid^2 + \frac{\mu_0 \cdot H^2}{2}], \tag{2.46}$$

where α ($\alpha = \alpha_0 \frac{T - T_c}{T}$), β and m are the positive phenomenological quantities, ψ is the factor which characterizes the density of the superconducting electrons, h is the Planck constant ($1.05 \cdot 10^{-34}$ $[J \cdot s]$ or $6.58 \cdot 10^{-15}$ $[eV \cdot s]$) and Φ_0 is the fluxoide (magnetic flux of vortices) ($\Phi_0 = \frac{h}{2 \cdot e}$).

In the absence of a magnetic field and at $T \sim T_c$ this expression is simplified:

$$F_s - F_n = \int dV[\alpha(T)\cdot \mid \psi \mid^2 + \frac{\beta}{2}\cdot \mid \psi \mid^4]. \tag{2.47}$$

When $T > T_c$, then the free energy of the superconducting state is higher than for normal conducting state. Indeed, the superconducting phase does not exist under this condition. When $T < T_c$, then exists a value of $\psi \neq 0$ for which free energy is minimal:

$$\psi_0(T) = \sqrt{\frac{\mid \alpha \mid}{\beta}}. \tag{2.48}$$

For this case, the free energy of the transition from SC state to NC state is given by:

$$\frac{F_s - F_n}{V} = \frac{\alpha(T)^2}{2 \cdot \beta}. \tag{2.49}$$

The maximum magnetic energy variation corresponds to superconducting state, there ψ is minimal (ψ_0):

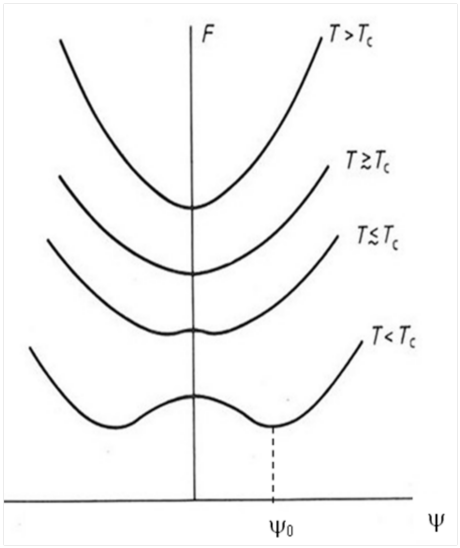

Figure 2.19: Evolution of free energy as a function of parameter ψ for different temperatures [69].

$$\frac{F_s - F_n}{V} = \frac{\alpha(T)^2}{2 \cdot \beta} = \frac{\mu_0 \cdot H_c^2}{2} => H_c(T) = \frac{\alpha_0}{\sqrt{\beta \cdot \mu_0}} \cdot \frac{T_c - T}{T_c}. \tag{2.50}$$

This formula, which is derived from the theory of GL, shows the existence of a critical field that is temperature dependent and above which superconductivity is lost. Moreover, around the critical temperature ($T \sim T_c$) the value of critical magnetic field corresponds to an empirical Equation (2.19) previously mentioned.

Theory of GL introduces several parameters which give the possibility to explain the existence of two types of superconductors. The first parameter is equivalent to the London penetration depth mentioned in Equation (2.30). This parameter λ is the characteristic length of the magnetic field penetration into the superconductor, which depends on temperature and is given by:

$$\lambda(T) = \sqrt{\frac{m_e \cdot \beta}{2 \cdot \mu_0 \cdot e^2 \cdot \alpha_0}} \cdot \sqrt{\frac{T_c}{T_c - T}}. \tag{2.51}$$

The second parameter is the coherence length ξ (T), which characterizes the length of variation of the superconducting electrons population:

$$\xi(T) = \sqrt{\frac{h}{16 \cdot \pi^2 \cdot m_e \cdot \alpha_0}} \cdot \sqrt{\frac{T_c}{T_c - T}}. \tag{2.52}$$

The third parameter, named as the parameter of Ginsburg-Landau (κ), is derived

as a ratio of $\lambda(T)$ to $\xi(T)$. This parameter does not depend on temperature anymore and is only material dependent.

$$\kappa = \frac{\lambda(T)}{\xi(T)} = \sqrt{\frac{m_e^2 \cdot \pi^2 \cdot \beta}{2 \cdot \mu_0 \cdot e^2}}. \tag{2.53}$$

As it was mentioned in Section 2.2.1, two types of superconductors can be defined thanks to this parameter, see Figure 2.20.

Materials with $\kappa \leq \frac{1}{\sqrt{2}}$ are named type I superconductors. In that case, as coherence length is larger than the penetration depth, the superconducting state exists below H_c. Once exceeded, superconductivity is suddenly lost. Both phases (NC and SC) can't coexist (See Figure 2.20).

Materials with $\kappa \geq \frac{1}{\sqrt{2}}$ are named type II superconductors. In that sense, 2 critical fields could be defined (H_{c1} and H_{c2}). Thus, when the first critical magnetic field is achieved, the magnetic flux starts penetrating into the material through vortices (see Section 2.2.1). When the second critical field is reached, the density of vortices is so high that superconductivity is totally lost. These vortices have a radius of the order of ξ, due to decreased density of the superconducting electrons. Vortices extend into the material over a distance λ and the magnetic flux that passes through fluxoides into SC material is quantized and equal to:

$$\Phi_0 = \frac{h}{2 \cdot e} = 2.07 \cdot 10^{-15} [T \cdot m^{-2}]. \tag{2.54}$$

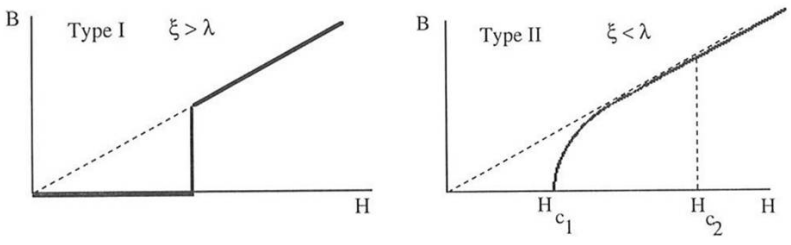

Figure 2.20: Evolution of magnetic induction for 2 types of superconductors as a function of the magnetic field [70].

The values of the critical magnetic fields can be expressed by the following equations:

$$H_{c1} \approx \frac{\Phi_0}{\mu_0 \cdot \pi \cdot \lambda^2}, H_{c2} \approx \frac{\Phi_0}{\mu_0 \cdot \pi \cdot \xi^2}. \tag{2.55}$$

Critical magnetic field for type I SC corresponds to the transition field previously described in Equation (2.50), and for type II SC it is defined as the geometric mean of H_{c1} and H_{c2}:

$$H_c = \sqrt{H_{c1} \cdot H_{c2}}. \tag{2.56}$$

Superheating field is a metastable state at which superconductivity can persist because the nucleation of a vortex costs energy. People have shown experimentally that the real limit of superconductivity under RF would be more likely H_{sh} and not H_{c1} [71], which is given as:

$$\begin{cases} H_{sh} \approx \frac{0.89}{\sqrt{\kappa}} \cdot H_c, & \kappa << 1 \\ H_{sh} \approx 1.2 \cdot H_c, & \kappa \approx 1 \\ H_{sh} \approx 0.75 \cdot H_c, & \kappa >> 1 \end{cases} \tag{2.57}$$

The critical magnetic fields have a direct impact on the choice of material for superconducting accelerating cavities. Except for the critical fields, surface resistance is also a paramount important parameter, which characterizes the losses of superconducting material. The BCS theory gives the best explanation of surface resistance.

BCS Theory

A statement that superconductivity describes the interactions between travelling electrons and an atomic crystal lattice of superconductor was first made by a group of scientists Bardeen, Cooper and Schrieffer (BCS) in 1957 [72]. BCS theory predicts the existence of an energetically favorable bound state between two electrons via an attractive virtual phonon interaction between them. The two electrons which participate in this interaction are called Cooper pairs.

As shown in the Figure 2.21, the first electron travels through the crystalline lattice (made of positive ions) and attracts ions along travelling path. As the result, the crystalline lattice is slightly distorted creating locally a higher positive charge density. The second electron travels along the wake field of the first electron and experiences an indirect attraction due to the creation of a phonon (vibration of the lattice triggered by the first electron). The distance between these two electrons

is relatively large and is of the order of the coherence length (typically 40 nm for Niobium to be compared to the lattice parameter of several angström), which was defined previously.

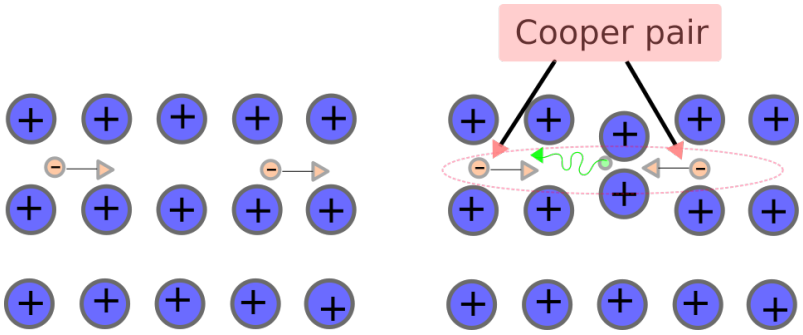

Figure 2.21: Sketch of the formation of the Cooper pair.

The BCS theory shows that only electrons with reduced energy can create the Cooper pairs, at temperatures below T_c, and this energy satisfy the following condition:

$$\epsilon <\mid \epsilon_F - \Delta \mid, \tag{2.58}$$

where ϵ_F is the energy of Fermi and Δ is the energy gap, which basically describes the reduction of energy due to the pairing of electrons. At the temperature $T = 0$, the following equations for the energy of Fermi and the energy gap could be written:

$$\epsilon_F = \frac{\hbar^2 \cdot (3 \cdot \pi^2 \cdot N)^{2/3}}{2 \cdot m_e}, \tag{2.59}$$

and

$$\Delta(0) = 1.76 \cdot k_b \cdot T_c, \tag{2.60}$$

where m_e is the mass of electrons, N is the density of electrons, $\hbar$ is the constant of Plank ($\hbar = \frac{h}{2 \cdot \pi}$) and k_b is the constant of Boltzmann ($1.380649 \cdot 10^{-23}$ $[J \cdot K^{-1}]$). The value of energy gap depends on the material and more specifically on the coupling strength between electrons and phonons.

As shown in Figure 2.22, the energy gap tends to 0 when the temperature reaches critical temperature (T_c). A good approximation of the dependence of the energy gap versus temperature is given by [71]:

$$\Delta(T) = \Delta(0) \cdot \sqrt{cos(\frac{\pi}{2}(T/T_c)^2)}. \tag{2.61}$$

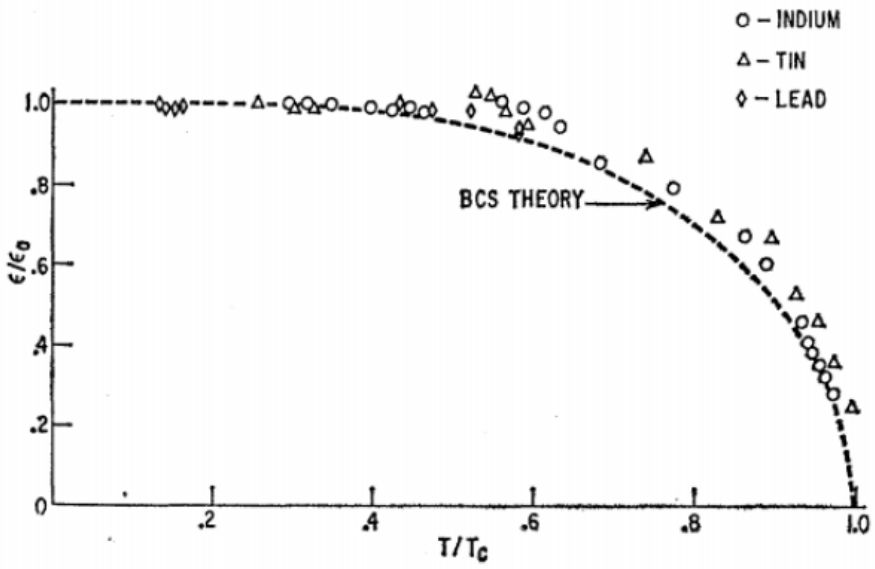

Figure 2.22: The energy gap as a function of T_c/T compared with the BCS theory [73].

As shown in Figure 2.23, in order to destroy the superconducting state (i.e cooper pairs), the thermal energy has to exceed the pairing energy (equal to 2Δ). Above this energy superconductivity breaks down. The Niobium pairing energy (2Δ) is equal to 3.05 meV.

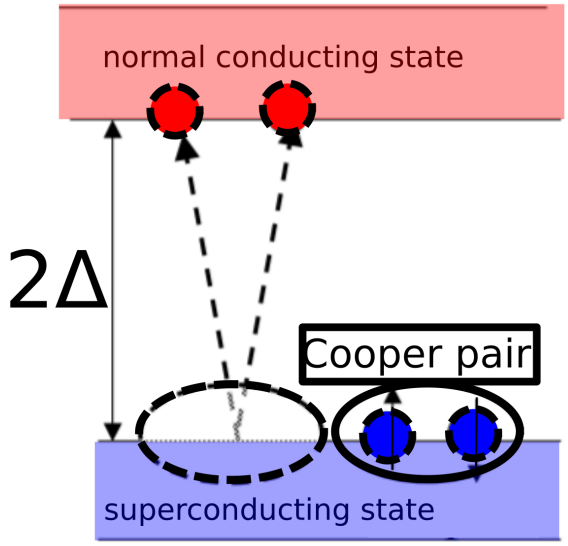

Figure 2.23: Sketch of the transition from superconducting to normal conducting state.

AC Surface Resistance of a Superconductor

Surface resistance based on the two-fluid model has been defined in Equation (2.42). As it was shown in Section 2.2.1, it depends on the frequency of EM fields, λ_L and the σ_n parameters. However, these parameters also depend on the temperature. Hence it is very difficult to estimate the real resistance from this formula. Turneaure and Halbritter [74] derived from BCS theory a semi-empirical approximation of surface resistance for $T < \frac{T_c}{2}$:

$$R_{BCS} = A(\lambda, \xi, l, v_F) \cdot \frac{\omega^2}{T} \cdot exp\left(- \frac{\Delta(0)}{k_B \cdot T} \right), \tag{2.62}$$

where $A(\lambda, \xi, l, v_F)$ is the material parameter.

At absolute zero, we can consider that the total number of electrons belongs to a Cooper pair. When the temperature is not zero, the probability that a pair is broken can be expressed as the ratio between n_n and n_s densities which results from a Maxwell-Boltzmann statistic:

$$\frac{n_n}{n_s} = \frac{1}{1 + exp(\frac{\Delta(T)}{k_B \cdot T})} \approx exp\left(- \frac{\Delta(T)}{k_B \cdot T} \right). \tag{2.63}$$

The BCS theory gives the most successful description of the evolution of the theoretical surface resistance of a superconductor.

More specifically, the BCS resistance of bulk Niobium is given by:

$$R_{BCS} = \frac{9 \cdot 10^{-5}}{T} \cdot f^2 \cdot exp\left(\frac{-1.83 \cdot T_c}{T} \right). \tag{2.64}$$

In the case of a perfect superconductor, BCS theory predicts that the surface resistance vanishes to zero when temperature tends to zero. But in reality, as it can be seen on graph 2.24, the surface resistance tends to stabilize around a non-zero value called the residual resistance. This temperature-independent component of the surface resistance is due to material pollution and imperfections causing the scattering of electrons like in normal conductors.

In that sense, the real surface resistance of a superconductor subject to a RF

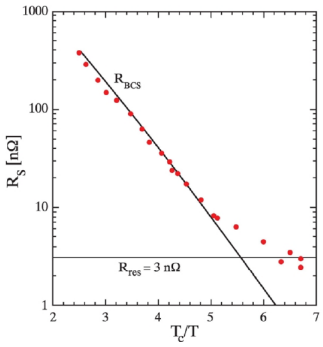

Figure 2.24: The measured niobium surface resistance in a 9-cell superconducting cavity plotted as a function of T_c/T [54].

field can be written as:

$$R_s = R_{BCS} + R_{res}. \tag{2.65}$$

In the same time, the average mean free path of electrons depends on the purity of material and has a huge influence on the BCS resistance, see Figure 2.25. In the dirty limit, the BCS surface resistance is dominated by interstitial impurity scattering. A purification of the material decreases the BCS surface resistance. However, in the clean limit resistance does not improve, on the contrary it increases, due to improvement of normal electric conductivity (surface resistance is proportional to normal conductivity (London model)).

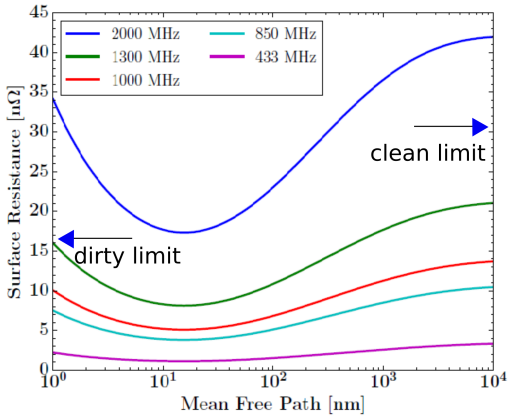

Figure 2.25: BCS surface resistance as a function of the average mean free path [51, 75].

Increased content of contamination reduces the average mean free path of normal conducting electrons, so the electrodynamic response changes from the clean limit ($l >> \xi => R_s \approx l$) to the dirty limit ($l << \xi => R_s \approx \frac{1}{\sqrt{l}}$).

These changes in the characteristic lengths may be approximated as:

$$\frac{1}{\xi} = \frac{1}{\xi_0} + \frac{1}{l}, \tag{2.66}$$

where ξ_0 is the coherence length at $T = 0$ K (ξ_0=39 nm for Nb).

The penetration depth, defined in Equation (2.30), in the dirty limit is given by the following expression:

$$\lambda(l, T) = \lambda_L(T)\sqrt{1 + \frac{\xi_0}{l}}. \tag{2.67}$$

Thus in the dirty limit, the surface resistance decreases with increasing of average mean free path.

2.2.2 Which Material for SRF Applications?

Today superconducting radio-frequency (SRF) cavities are made of Niobium, mostly bulk Niobium (polycrystalline) but also Niobium thin-film on copper substrate. This chemical element is the best material for SRF technology because it has a number of advantages. Firstly, mechanically, it has a highly-workable structure (metal) with good formability to form complex geometries out of sheets. Secondly, physically, its transition temperature and critical magnetic field is the highest of all pure elements. Nb becomes a superconductor at the temperature of 9.2 K and can handle a magnetic field up to typically 200 mT [64].

Nevertheless, in the case of SRF applications, and because most of superconductors are of type II, the real limitation in term of magnetic field is not the critical field H_c but rather the field of first entry called H_{c1}, and more likely H_{sh}, the metastable state. Indeed, above H_{sh}, vortices start nucleating and entering into the material. The motion of vortices, dragged back and forth due to Lorentz forces, induces non-negligible power dissipations causing a very strong Q-slope. In this regime, the cavity operation is not possible.

As a conclusion, and at the sight of existing superconductors (see H_{sh} in Table 2.9), Niobium is by far the best superconductor material for SRF applications. All the mechanical properties of Nb used for SRF applications are presented in

Section 3.1.2.3.

2.2.3 SRF Structures

As it has been shown in Section 2.2, the choice of the right cavity geometry is of paramount importance to ensure an efficient and optimal acceleration. The type of accelerating structure and thus the frequency of operation are, at first order, directly determined by the velocity of accelerated particles.

For low velocities ($0.05<\beta<0.15$), requiring narrow accelerating gaps and low frequency operation (<100 MHz), quarter-wave resonators (QWR) are preferred because of their mechanical stability and compactness, although the accelerating efficiency is not optimal as for elliptical cavities [76].

For medium velocities ($0.15<\beta<0.65$), half-wave resonators (HWR) offer a better acceleration efficiency than QWR (higher gradient and lower transverse kick [77]) and can be operated at higher frequencies (between 150 MHz and 400 MHz) [78].

For particle velocities above 65% of the speed of light, elliptical cavities are optimal. The accelerating gap is now large enough at high frequencies (>600 MHz) for this below-type geometry to show a reasonable stiffness for stable operation [71].

As can be seen in Figure 2.26, three types of SRF structures may be defined depending on the desirable parameter β ($\beta = \frac{v}{c}$, where v is the achieved speed of the particles and c is the speed of the light): quarter-wave resonators (80-150 MHz), half-wave resonators (150-400 MHz) and elliptical cavities (700-3000 MHz).

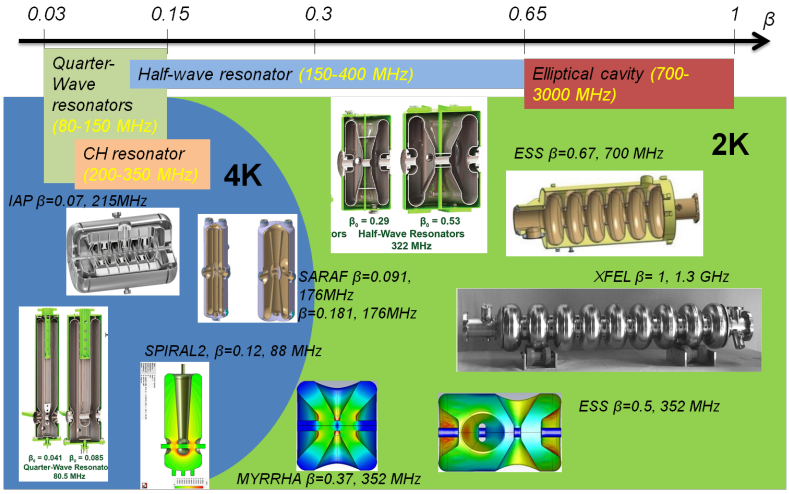

Figure 2.26: Classification of superconducting cavities [79].

An other type of SRF structure exists and serves non-accelerating applications but beam manipulations like deflection (bunch deviation) at high energy or crabbing (bunch rotation) to increase collider luminosity. For example, crab cavities, see Figure 2.27, have been first developed at KEK, in order to rotate the beam of charged particles to increase the interaction between both colliding beams.

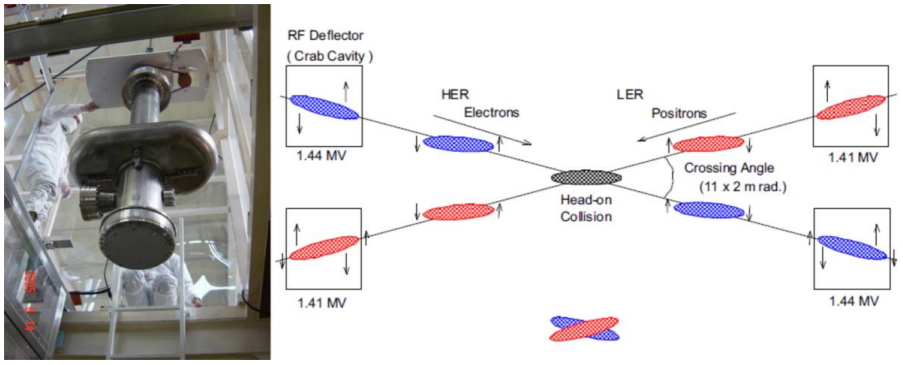

Figure 2.27: Crab cavity (left) and crab crossing scheme for KEKB (right) [80].

2.2.4 Limitations of Superconducting Cavities

The evolution of the quality factor (Q_0) versus the accelerating gradient (E_{acc}) makes possible measuring the evolution of the performances of a cavity and to identify its limits [81]. A typical Q_0 curve of an elliptical cavity is shown in Figure 2.28. During the ramping up of the accelerating gradient, several undesirable effects or processes can occur like multipacting, Q-disease, field emission, thermal instability, Q-slope and quench.

Multipacting

Multipacting (multiple impacting) is a resonant phenomenon that implies a resonant electrons multiplication in a cavity [83]. This phenomenon depends on the geometry and on the ability of a surface to re-emit electrons, which is called the Secondary Electron Yield (SEY) coefficient. When accelerated a primary electron hits the surface of the cavity and it creates one or more secondary electrons, which themselves are re-accelerated by the RF field and hit the surface, creating an exponential growth of electrons.

It is particularly critical in the case of an accelerating cavity because this avalanche of electron can fully absorb the RF energy supplied to the cavity, thus it becomes

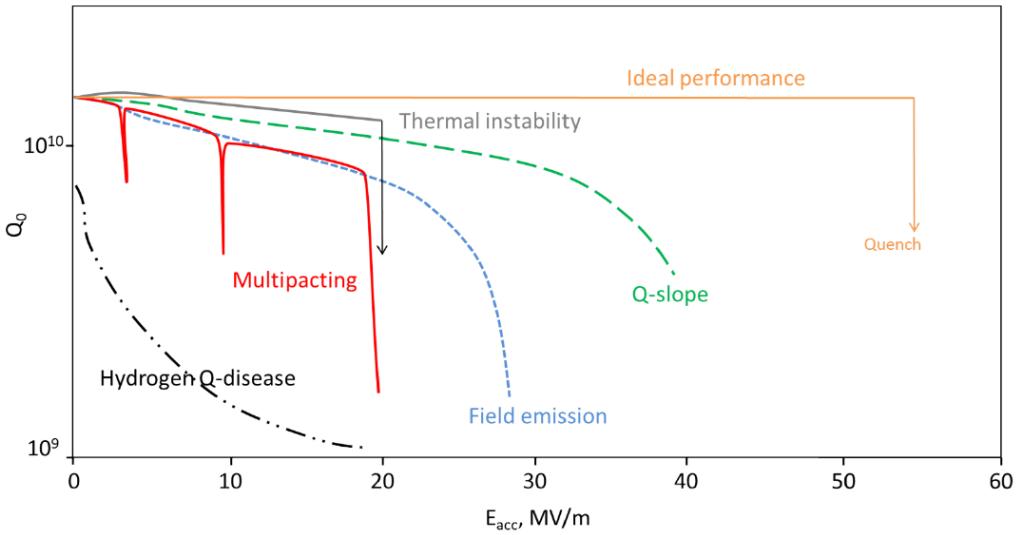

Figure 2.28: Examples of real Q_0-curves measured when the accelerating gradient is ramped up. Theoretically, the Q_0 should stay constant up to the thermodynamical limit of 55 MV/m [82].

impossible to increase the accelerating gradient. Multipacting occurs due to periodic motion of the electron phased with the RF field (closed trajectory) due to resonance condition and when the secondary yield coefficient is more than 1.

To overcome this limitation, the cavity geometry either may be changed or the secondary yield coefficient has to be reduced thanks to surface or thermal processes (baking, cleaning, and RF processing).

Hydrogen Q-disease

Any time there is no natural oxide passivating layer on the surface, bulk niobium can absorb the residual hydrogen at its surface. Such opportunities appear during Niobium sheet production, during cavity fabrication and surface cleaning when precautions are not taken. According to several studies, when the temperature is over 15 C° during the process of extensive chemical and electro-polishing, a significant drop in the cavity quality factor (Q_0) can be noticed [84].

This phenomenon is called Q-disease or 100K effect, because of some historical backgrounds. The quality factor of the cavity is dropping significantly during the cooldown if it remains between 160K and 50K for several hours, see Figure 2.29. The surface resistance is increased because of the formation of non superconducting Niobium hydride precipitates [85]. This degradation is usually reversible and can

be cured by warming up the cavity above 300K to dissolve hydrogen precipitates.

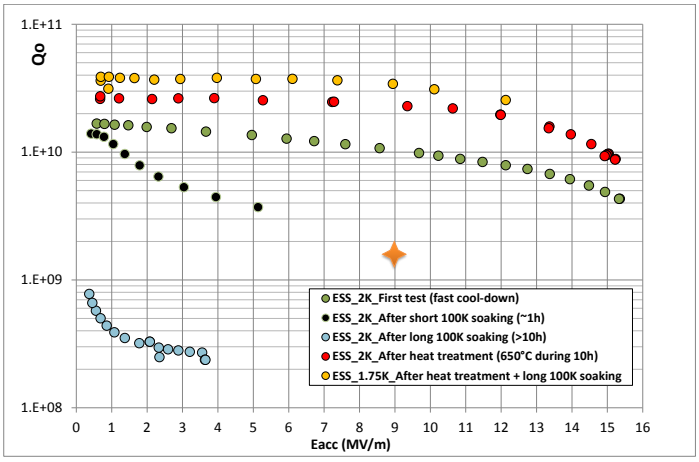

Figure 2.29: The quality factor versus accelerating gradient for ESS prototype (ROMEA) before/after 100K soaking and heat treatment [86].

As can be seen in Figure 2.30, the hydrides may first appear when the cavity is cooled down below 160K. Between 160K and 50K, different phases of hydride precipitates appear on the surface. When hydride precipitation is very significant, surface dislocations (skeletons) can remain on surface leading to unreversible damages and permanent Q_0 degradation. A 300K thermal cycle wouldn't remove such a degradation, an additional chemical etching would be required.

The Q-disease can be mitigated and even avoided by performing a hydrogen degassing heat treatment (typically 800°C during 3h under vacuum) during the surface preparation.

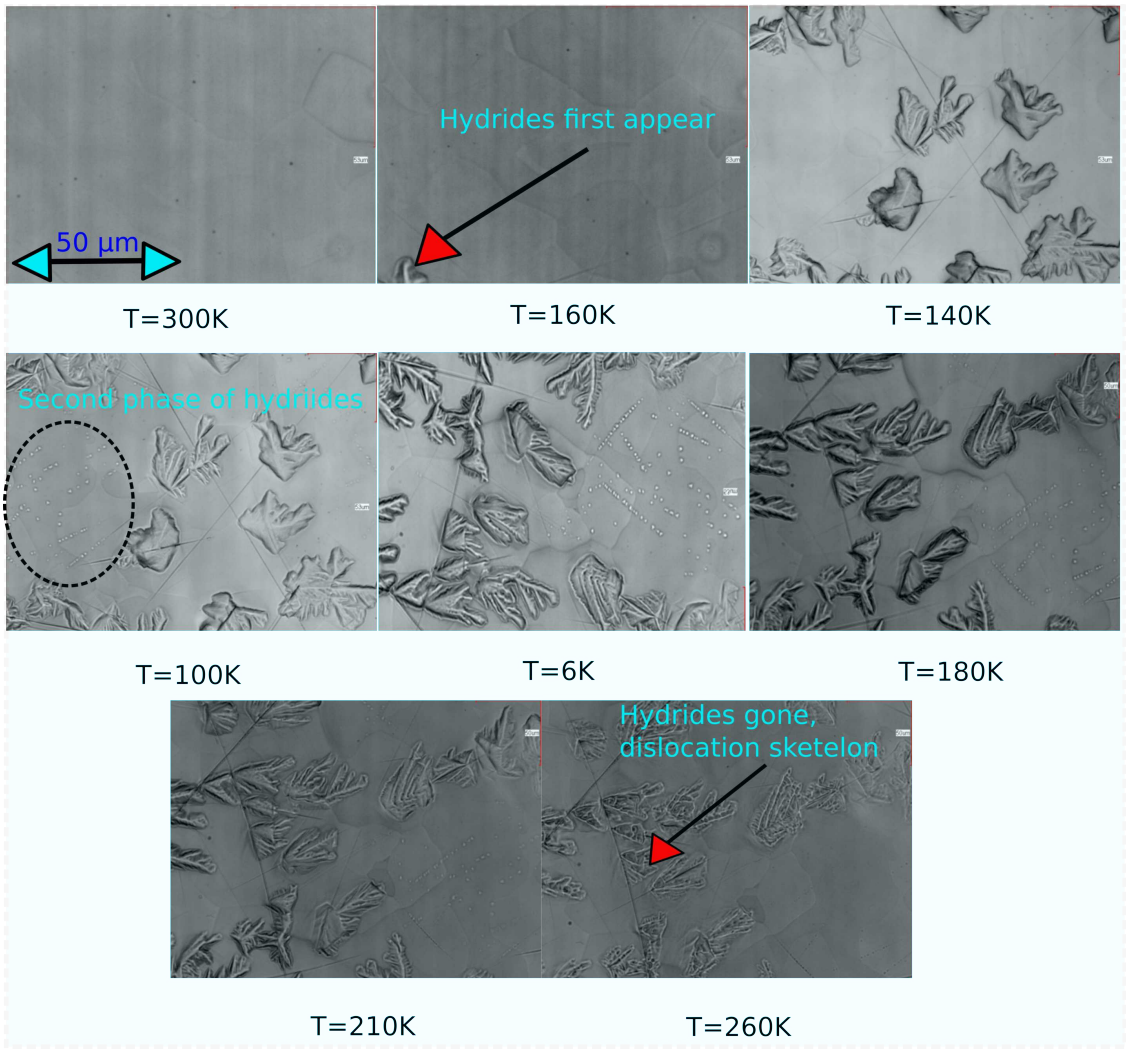

Figure 2.30: Evolution of hydrides forming on Niobium surface. Hydrides grow during the presence of hydrogen contamination of Niobium cooling down to cryogenic temperatures due to hydrogen diffusion and connection with other hydrides [87]. When hydride precipitation is very significant, surface dislocations (skeletons) can remain on surface leading to unreversible damages and permanent Q_0 degradation.

Field Emission

Field emission may occur when a surface is subject to an intense and normal electric field [88], see Figure 2.31. Tunneled electrons may be captured and accelerated by the electric field. This leads to additional RF losses and the collision of those accelerated electrons with the surface may lead to thermal breakdown.

The DC current, in the case of the field emission, is given by:

$$j(E) = C_1 \cdot \frac{E^2}{\Phi} \cdot exp(\frac{-C_2 \cdot \Phi^{\frac{3}{2}}}{E}), \tag{2.68}$$

where C_1 and C_2 are material dependent constants, E is the applied electric field and Φ is the work function of the metal.

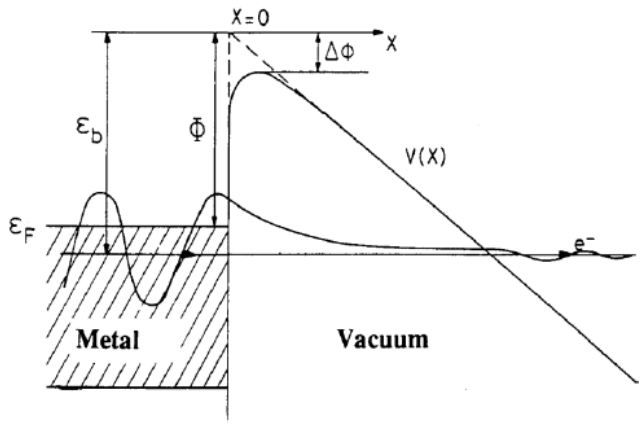

Figure 2.31: Energy diagram of a metal-vacuum interface [88].

Another consequence of the field emission is the production of X-rays due to the Bremsstrahlung effect. X-rays thus produced impose the installation of radiation protection device and limits the accelerating gradient due to the additional power dissipation generated in the helium bath.

To limit field emission, the sources of field emission (usually surface pollution by particulates (local field enhancement)) have to be removed from the cavity surface. Typically to prevent the field emission high-pressure rinsing (HPR) with ultra-pure water and assembly in clean-rooms are used. However, if the sources are still present, surface could be processed either by helium processing or high peak power processing.

Thermal Instability

Thermal instability occurs due to increasing of the RF surface temperature caused by the cooling limitations of the helium bath (global thermal instability) or by the presence of pollution or defects on the RF surface (local thermal instability).

In the case of global thermal instability, the surface resistance is increasing (exponential dependence of BCS resistance with temperature) and critical field is reduced as well (as temperature-dependent) leading to early quench.

In another case, local thermal instabilities will increase the surface resistance because of normal dissipations and could also lead to an early quench. Only a Q_0 degradation is visible as far as the thermal conductivity of Niobium can overcome the propagation of this normal hot spot. Once the thermal load is too important, the normal zone propagates macroscopically resulting in a quench. To mitigate this limitation, a possible pathway would be to improve the thermal conductivity (κ_c) of bulk Niobium by ordering highly purified Niobium (RRR $>$ 300), proceed with high temperature heat treatment above 1000°C with titanification [70]. The RRR is defined as a ratio of the electrical resistivity ρ at room temperature (300 K) to the electrical resistivity at the cryogenic temperature (4.2 K):

$$RRR = \frac{\rho_{300K}}{\rho_{4.2K}}. \tag{2.69}$$

RRR is closely linked to thermal conductivity and an empirical formula exist:

$$RRR \approx 4 \cdot \kappa_c. \tag{2.70}$$

The RRR can be calculated also through the fractional content (f_i) of interstitial impurity i and the resistivity coefficient of this impurity (r_i):

$$RRR = \sum_i \left(\frac{f_i}{r_i}\right)^{-1}. \tag{2.71}$$

The maximum content and resistivity coefficient for different elements present in Niobium is shown in Table 2.7.

Table 2.7: Resistivity coefficient and maximum content of the different elements in Niobium [89].

Element	Resistivity coefficient $r_i, 10^4 \mu g/g$	Content, $\mu g/g$
H	0.36	2
C	0.47	10
N	0.44	10
O	0.58	10
Ta	111	500

Q-slope

Q-slope is a generic denomination characterizing the fact that the quality factor of a cavity is affected negatively or positively by the amplitude of the accelerating gradient. A Q-slope could be caused by any intrinsic processes described previously but not only. Moreover, the Q-slope can be observed only at low field (Low FIeld Q-slope = LFQS), continuously on the full range of field (Medium Field Q-slope = MFQS) or above a threshold (High Field Q-slope = HFQS).

Table below summarises which process could be at the origin of the three different type of Q-slope.

Table 2.8: Summary of Q-slope.

	Processes	How to mitigate/ improve
LFQS	Strong Q-disease, thermal instability due to macroscopic defects	Hydrogen degassing/ surface re-processing
MFQS	Magnetic flux trapping, weak Q-disease, thermal instability due to microscopic defects	Nitrogen doping/ 120°C baking for 4 K operation
HFQS	Field emission, multipacting, vortex penetration, nano hydrides, time barrier	120° baking for 2K operation/ Nitrogen infusion

Quench

As defined in Section 2.2.1, a quench is the loss of superconducting properties due to localized heating on normal-conducting defects (thermal quench) or/and the local magnetic field exceeds the critical field (magnetic quench). A quench can thus be triggered by thermal instabilities as described previously or by surface morphology (local field enhancement).

The way to distinguish a thermal from a magnetic quench would be to measure the field of quench for different RF duty cycles. In the case of a thermal quench, when the average power dissipation is the limiting factor (the magnetic field is a limitation for a magnetic quench), the quench field should be proportional to the inverse of the square root of the duty cycle or in other words, duty cycle multiplied by H^2 is a constant.

To delay the field of quench, the surface would need to be reprocessed to remove large defects like embedded particles or sharp edges (to attenuate field enhancement factor) in the case of magnetic quench or perform heat treatments to attenuate thermal instabilities to delay thermal quench.

2.2.5 Alternative Superconducting Materials

Nowadays bulk Niobium is the main material for SRF cavities, but other superconducting materials have the potential to show higher performance, in particular, lower surface resistance and a higher critical magnetic field could be achieved.

Nevertheless, all alternative superconductors are alloys (NbTiN, Nb_3Sn, MgB_2, ...) or compounds (NbN) showing non-compatible mechanical properties to fabricate complex geometries like cavities. These superconductors can't be used in their bulk version but could rather be deposited as thin films (thickness of few microns) on a workable substrate like Niobium or Copper.

The surface resistance of these materials, given by BCS theory could be relatively smaller as it depends exponentially on the energy gap. It could be thus envisaged to increase the temperature of operation up to 4.2 K instead of 2 K, decreasing considerably the complexity and cost of the cryogenic infrastructure.

As said previously, the real limit in field for SRF applications is H_{sh}. In that

sense, only Nb_3Sn (See Table 2.9) could allow to increase (even double) the accelerating gradient.

Nb_3Sn is today the most promising alternative candidate, as thin-film, capable of improving significantly both the surface resistance and accelerating gradient. Recent experimental results [90] have demonstrated that this technology is mature to build operational cavities with improved performances in term of quality factor. However, the reachable accelerating gradient is still way lower than predicted (22.5 MV/m instead of about 100 MV/m).

The critical temperature (T_c), normal conducting resistivity (ρ_n), the critical (H_{c1}, H_{c2}, H_c) and superheating (H_{sh}) magnetic fields, the London penetration depth (λ_L), the coherence length (ξ) and the energy gap (Δ) are presented in Table 2.9 for main alternative superconducting materials, which may be used in the SRF acceleration.

Table 2.9: Alternative superconducting materials for SRF [91, 92].

Material	Pb	Nb	NbN	NbTi	NbTiN	Nb_3Sn	Mo_3Re	MgB_2	YBCO/Cuprates
T_c [K]	7.1	9.2	16.2	10	17.3	18.3	15	40	93
ρ_n $[\mu\Omega cm]$		2	70		35	20	10-30	0.1-10	
$\mu_0 H_{c1}$ $[mT]$	n.a.	170	20	4-13	30	50	30	30	10
$\mu_0 H_{c2}$ $[mT]$	n.a.	400	15000	11000		30000	3500	7000	100000
$\mu_0 H_c$ $[mT]$	80	200	230	100-200		540	430	430	1400
$\mu_0 H_{sh}$ $[mT]$		219	214	80-160		425	170	170	1050
λ_L $[nm]$	48	40	200-350	210-420	150-200	80-100	140	40	150
ξ_0 $[nm]$		28	5	5.4	5	5		5	0.03/2
Δ $[meV]$		1.76	2.6		2.8	5	2.3/7.2	2.7	

In 2006, a new concept was proposed by A. Gurevich [93] consisting in stacking several very thin layers of high-T_c superconductors separated by isolating layers over bulk Niobium. If the superconducting film is deposited with a thickness d $<<\lambda$, the Meissner state can be kept at a magnetic field much higher than the bulk H_{c1} that appears to be very low for most of superconductors. In that sense, the underlying Niobium would be efficiently shielded by these high-T_c superconductors allowing to reach surface fields way higher. The BCS resistance is also strongly reduced because the superconducting materials used have higher gap Δ (Nb_3Sn, NbTiN ...) than Nb.

This technology is for the moment not mature because of the technical difficulties to grow nanometric-scale layers. The proof of concept and the real efficiency has not been yet fully demonstrated.

One common limitation in all these described technologies (bulk Niobium, Nb_3Sn and multilayers) is the quality of the surface in term of roughness. Indeed, to a lesser extent for bulk Niobium, field limitations are suspected to originate from the surface morphology (local field enhancement caused by roughness). For thin-films the quality of the substrate is a key parameter to achieve high quality films. The roughness of polycrystalline Niobium (used as bulk or as substrate) has to be definitely improved by developing new techniques capable of surpassing current state of the art achievements. The work presented here will try to address this problematic.

Chapter 3

Surface Treatment for SRF Cavities

The fabrication of Niobium SRF cavities, during forming steps (rolling of Nb ingots, half-cell forming), causes the appearance of a damaged layer of the order of 200 μm into the inner surface of the material. This has to be removed to recover optimal superconducting properties and avoid limited performances [4]. EM field penetration inside superconducting material is given by theoretical penetration depth (λ_L), see Section 2.2.1 (and is of the order of 40 nm [94]).

Induced currents penetrate typically into the material and decay exponentially over several hundreds of nanometers. Thus, in order to withstand these extreme conditions, not only the chemical composition, the roughness but also the microstructure are required to meet very high specifications.

In this chapter, all requirements for SRF surface cleaning and description of polishing techniques routinely used for treatment will be presented. In addition, an overview of potential alternative polishing techniques available in industry will be done.

3.1 Properties of a Surface Layer

The surface is the interplay between air and the material [95], see Figure 3.1. The surface of a material is not only a two dimensional property with its topological characteristics, it is a microstructured layer (3D) between outside and inside of material

[96, 97]. The surface layer is strongly impacted by any chemical and mechanical processes formerly applied and thus can show very different topography and microstructure, it is characterized by a deformation layer (dislocations density, stress, strain) and also by a chemical composition with possible inclusions and/or oxidation layer. Bulk material is defined as layer extending between the surface layer and the core of the material where all chemical, physical and mechanical properties are constant, uniform or at least controlled.

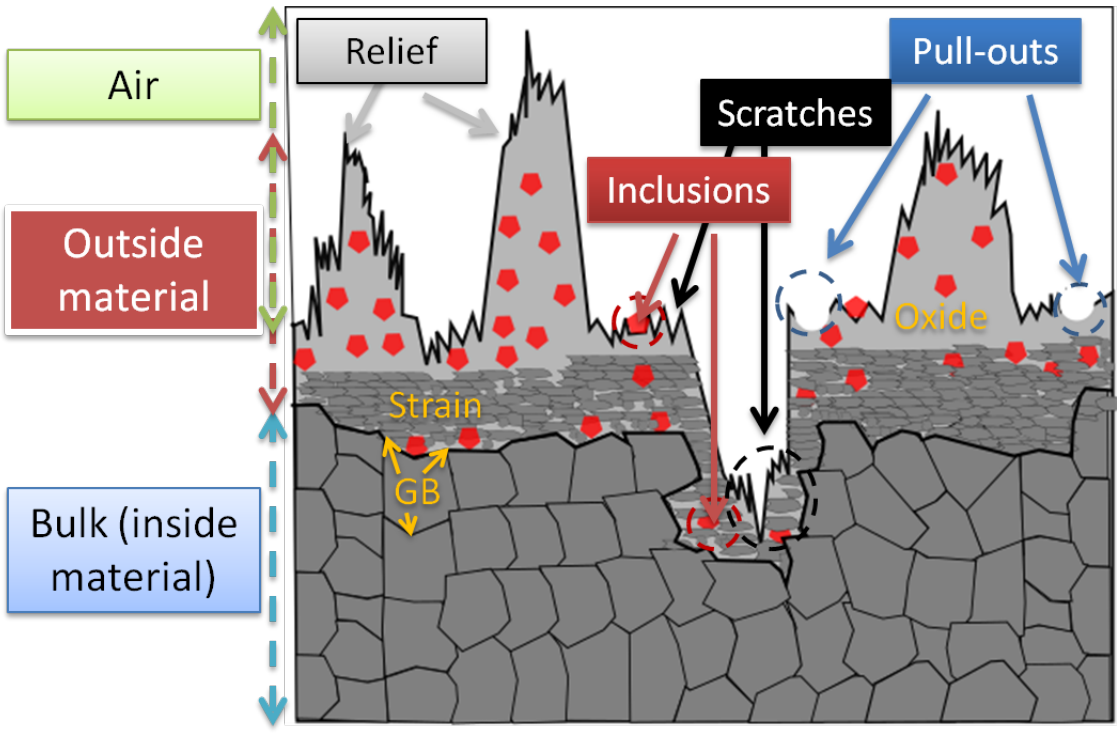

Figure 3.1: Sketch of a surface layer at the interplay between air and bulk material.

3.1.1 Smoothness

The smoothness of the surface has two physical definitions. Firstly, smoothness is the property of material, which describes the value of friction between surfaces due to an applied sliding tangential force [98]. In tribology, the smoothness of the material is measured by the coefficient of friction (COF). COF is proportional to the friction force (F_f) and inversely proportional to the applied normal force (F_N):

$$\mu = \frac{F_f}{F_N} \tag{3.1}$$

Smooth surfaces have lower coefficients of friction than rough surfaces. COF also describes the speed of material wear, as the imperfections at the surface create cracks and corrosion.

Secondly, smoothness describes the real surface topology, as shown in Figure 3.2, which consists of the superimposition of three spatial components (from lowest wavelength to highest): roughness, waviness and form [99], see Figure 3.2. These 3 spatial components could be extracted by applying spatial filters (λ_s, λ_c, λ_f), see Figure 3.3. The filter λ_s gives lower limit of the roughness measurement, λ_c is applied to separate roughness measurement from waviness and λ_f separates form from waviness.

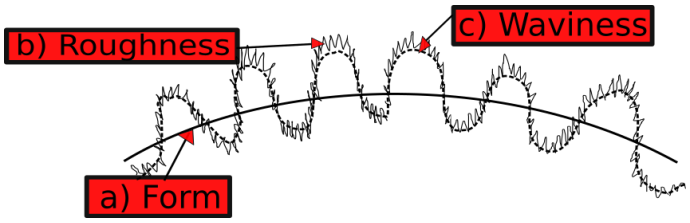

Figure 3.2: Sketch of a real surface, which consists of the superimposition of three spatial components: (a) form, (b) roughness and (c) waviness.

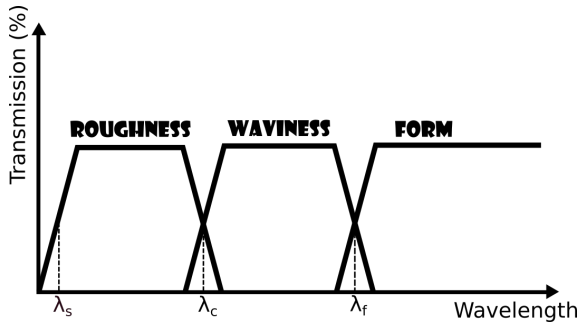

Figure 3.3: Separation of roughness, waviness and form of the measured topography.

These 3 components are not separated by fixed numbers. Their ranges can fluctuate significantly and are usually directly linked to the type of treatment and dimension of the piece. These non-fixed cut-off spatial frequencies make the evaluation of the surface roughness very complex and "operator" dependent (choice of cut-off spatial frequencies). In that sense, several norms have been defined to help specifying not only cut-off numbers but also the minimal distance or surface over which the roughness measurement has to be performed (4287:1997, ISO 25178-2:2012,...).

Form, as shown in Figure 3.2 (a), is the general shape of a surface, which is determined by the accuracy of the fabrication technique (rolling, forming, deep-drawing, spinning, machining, ...) and of the way the piece is hold or adjusted

(piece is moving during the process or is tilted). This parameter describes surface relief at a macrometric scale (typically above millimeter range).

Waviness is the medium range spatial component coming from a periodic or pseudo-periodic pattern. These periodic irregularities are usually attributed to instabilities or defective adjustment of the surface process itself. Waviness could also be triggered when the material is subject to stress and strain [95]. Typically, waviness could vary between several tens of microns and few millimeters. Figure 3.2 (c) shows the extracted waviness from the a real surface.

Finally, roughness (See Figure 3.2 (b)), the high frequency component is determined by the irregularities of height caused by the nature of the interaction between the piece and the surface process (mechanical, chemical or thermal interaction) and by the type of material of the piece (material mechanical and chemical properties, crystallography, ...).

Roughness is an important parameter which is widely used for the quality control of surface processes. Roughness could be measured along a line (linear roughness, noted R) [100, 101, 102] or over a surface (surface roughness, noted S) [101, 103, 104].

Many methods exist for roughness measurement, however it is possible to define two main approaches for the measurement: contact (roughness tester, atomic force microscope) and non-contact (white light interferometer, laser confocal microscope). Contact roughness measurement can damage the surface during the roughness identification due to the mechanical contact with the surface. To overcome this limitation non-contact solutions may be used.

The roughness of Niobium samples, during this work, has been evaluated using a laser confocal microscope. The principle of laser confocal microscope will be presented in the Section 4.2.3. Such microscopes can measure linear and surface roughness parameters. From the 2D data (linear roughness) or 3D data (surface roughness), several surface parameters could be extracted as it will be seen later. The number of parameters depends on the standard/norm used. Several of these exist like JIS B 0601-2001 and ISO 25178-2:2012. In our studies, we used the most recent norm for surface roughness ISO 25178-2:2012.

All 24 parameters defined by this norm may be divided into four categories: height, spatial, hybrid and functional.

Height parameters describe the characteristics of the amplitude deviations of the surface roughness from the mean line. Table 3.1 shows all height parameters, their mathematics formula and their meaning.

Table 3.1: Height parameters of 3D surface roughness.

Parameter, [Unit]	Meaning	Formula
S_a, [μm]	The average deviation of the surface	$\int\int_A \lvert Z(x,y)\rvert dxdy$
S_q, [μm]	The root mean square deviation of the surface	$\int\int_A \sqrt{(Z(x,y))^2 dxdy}$
S_{sk}	Skewness of surface height distribution	$\int\int_A \frac{1}{(S_q)^3}(Z(x,y))^3 dxdy$
S_{ku}	Kurtosis of surface height distribution	$\int\int_A \frac{1}{(S_q)^4}(Z(x,y))^4 dxdy$
S_p, [μm]	The maximum peak height	$\max_A Z(x,y)dxdy$
S_v, [μm]	The minimum valley depth	$\min_A \lvert Z(x,y)\rvert dxdy$
S_z, [μm]	The maximum height of the surface	$S_z = S_p + S_v$

The most common parameters to characterize deviations (Z) of the texture surface (x and y directions) are the average surface roughness (S_a) and the quadratic surface roughness S_q. However depending on application, others parameters may be required, especially in the tribology field.

For example, as shown in Figure 3.4 the S_a of three surfaces are the same [105], but their behaviours are different. Texture A would be in tribology a surface easily eroded compared to B. In the specific field of RF cavities, Texture B would be preferable as would show better RF performances due to a lower field enhancement factor.

Hence to characterize distinguish this kind of surface, additional parameters have been defined. Some of these parameters are local, like S_p, S_v and S_z. These characterize the highest peak, lowest valley and their sum. However these might not be meaningful for the entire scanned surface. Indeed the presence of a dust particle or a scratch incidentally present on the surface would bias these parameters.

To overcome this limitation, the surface may be defined also by more global parameters (integration over the whole surface) like skewness and kurtosis. The parameter of skewness (S_{sk}) characterizes the distributions of peaks or valleys over the surface. If S_{sk} is positive, the surface is showing more peaks than valleys or in other word, there is more material than air above the mean line. If negative, there are more valleys than peaks or said differently, there is more air than material above the mean line. Kurtosis parameter, noted S_{ku}, gives an indication on the "sharpness" of the profile or in other words how points of the surface are distributed around the mean line. If the profile is very sharp, the surface point distribution is very narrow, $S_{ku} > 3$. If the distribution is normal (gaussian), S_{ku}=3 and if the distribution is large, $S_{ku} < 3$ [106].

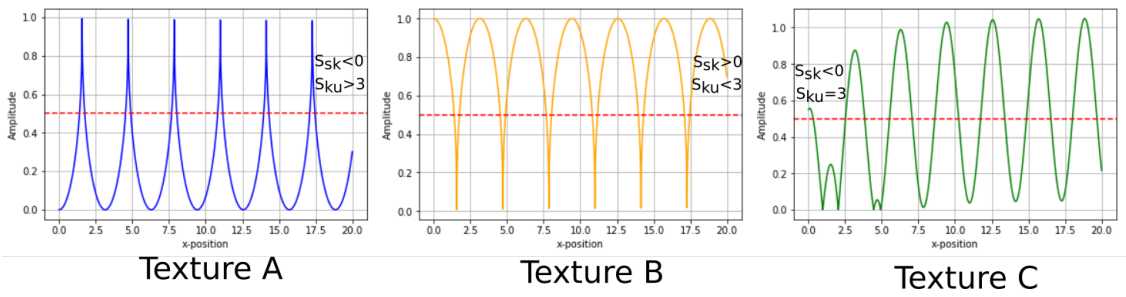

Figure 3.4: Example of different surface profiles showing the same roughness (S_a) but having very different surface properties. Additional parameters like S_{sk} and S_{ku} allow to distinguish such surfaces.

Table 3.2 shows the hybrid parameters (S_{dq}, S_{pc}, S_{dr}, S_{pd}), which describe variation in the height profile and spacing of surface defects of the processed surface [107].

S_{dq} is the root mean square slope. This parameter may be used to characterize the surfaces with similar average roughness. A high S_{dq} indicates a narrow surface profile.

S_{pc} is the mean peak curvature. This parameter indicates the type of contact with another surface. When peaks are very sharp, it will provide a smaller contact of the peak with surface (thus less friction or a surface less resistive to the wear). A smaller value of S_{pc} corresponds to a greater contact with the surface (thus more frictions or a surface more robust to wear).

S_{dr} is the developed area ratio. S_{dr} is defined as the ratio between the measured area (developed area) and the planar area. This property of developed area ratio has been really useful in our study to evaluate surface pollution due to embedded particles.

S_{pd} is the mean peak density. S_{pd} gives the number of points in contact with the surface. This parameter may be used in applications where friction is a dominant process. The smaller the number of peaks the weaker the contact with the surface. S_{pd} could also be used as a tool to estimate the density of embedded particles.

Table 3.2: Hybrid parameters of 3D surface roughness.

Parameter, [Unit]	Meaning	Formula
S_{dq}	Root mean square slope	$\sqrt{\frac{1}{A}\int\int_A (\frac{\partial(Z(x,y))}{\partial x})^2 + (\frac{\partial(Z(x,y))}{\partial y})^2 dxdy}$
S_{pc}, $[mm^{-1}]$	Mean peak curvature	$-\frac{1}{2N}\int\int_N (\frac{\partial^2(Z(x,y))}{\partial x^2})^2 + (\frac{\partial^2(Z(x,y))}{\partial y^2})$
S_{dr}	Developed area ratio	$\frac{1}{A}(\sqrt{\int\int_A [1 + (\frac{\partial(Z(x,y))}{\partial x})^2 + (\frac{\partial(Z(x,y))}{\partial y})^2]} - 1)dxdy$
S_{pd}, $[mm^{-2}]$	Mean peak density	-

Spatial parameters, contrary to hybride parameters, do not give any information about height, however they evaluate the pattern of the surface [107]. A surface can be either isotropic or anisotropic. By definition, an isotropic surface has the same properties in all directions. Anisotropic materials could show different level of anisotropy. After different type of processing (machining, forming, rolling, polishing, ...) the same material could have different level of anisotropy. Different materials have different anisotropic behaviour for the same processing due to different mechanical properties. The three spatial parameters (S_{al}, S_{tr}, S_{td}) are used to evaluate the degree of anisotropy.

S_{al} indicates the horizontal length of the auto-correlation function (ACF) with fastest decay of this function to a specified value, which is equal s=0.2 (specified by ISO 25178-2:2012 standard). ACF is the correlation between two values of a signal shifted in time or space, this difference may represent the periodicity of surface directions [107]. Figure 3.5 B shows the ACF with the maximum in the centre (red colour) and decays along the direction of propagation (green and blue colours). This decay is slower along the direction of propagation and decays rapidly in the perpendicular direction (black colour). High S_{al} represents a long wavelength (low frequency).

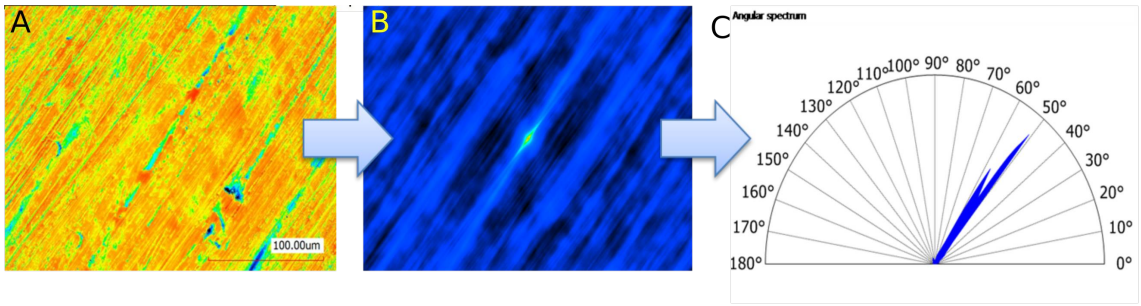

Figure 3.5: Height image of sample after grinding (a), autocorrelation image of the height image (b) and angular distribution of the height image(c).

S_{tr} is the texture aspect ratio parameter, which denotes the level of surface isotropy or the directionality.

Figure 3.5 C shows that parameter S_{td}, which indicates the direction of the surface after processing (grinding).

3.1.2 Hardness

Hardness is the mechanical ability of a material to resist to surface processes (grinding, lapping, polishing) or alternatives like cutting, scratching, wear and penetration into the material surface [108]. This property is linked to the yield strength of material. Two methods are mainly used to measure the hardness of materials.

Firstly, hardness measurements can be carried out by penetration of special tool proposed by: Vickers, Rockwell, Brinell and Knoop [108, 109]. These hardness tests are based on the measurement of penetration depth of a cone, a ball or a pyramid into the material under specific applied pressure or stress (the ratio of applied force to the area) [110, 111, 112].

For example, in the Vickers test, a pyramid made from diamond is pressed with a specific force (F) against the surface. The created valley-area (d^2) is measured under a microscope. Vickers hardness (HV) is defined by:

$$HV = 1.854\frac{F}{d^2} \tag{3.2}$$

Hardness is easily evaluated from the size of the residual deformation left on the surface. As shown in Figure 3.6, softer material has higher depth penetration into the material, the larger the pattern, the deeper the crater and thus the lower the hardness.

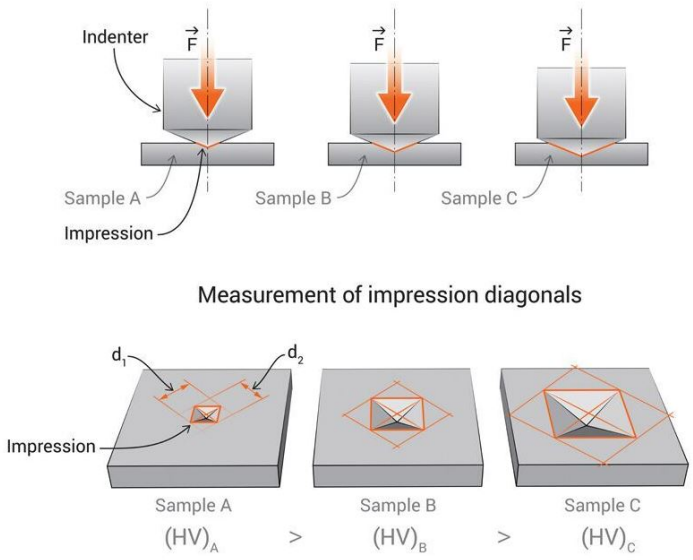

Figure 3.6: Sketch of the Vickers hardness measurement [113].

Secondly, hardness can be measured by scratching method [114] which is presented on the Mohs model. In the Mohs model, ten non-metallic abrasives are used

to define the hardness of the material. Mohs hardness scales from 1 to 10. 1 corresponds to minimum hardness and 10 to the maximum hardness [115]. The abrasive will scratch the surface just in the case if the tested material has a lower hardness, otherwise scratching will not occur.

3.1.2.1 Stress

Stress (σ or τ) is defined as ratio of the applied force (F) by the surface area (A) and can be expressed in Pa or N/m^2).

$$\sigma = F/A \tag{3.3}$$

Stress can induce a change of mechanical property due to the applied pressure and the direction of the pressure leads to different stresses. It is possible to define two types of applied stresses: normal stress (σ) and shear stress (τ) [116].

Normal stress appears due to the action of the normal component of the force (either tension or compression) applied to the surface. Figure 3.7 shows the action of the normal stress on the surface material.

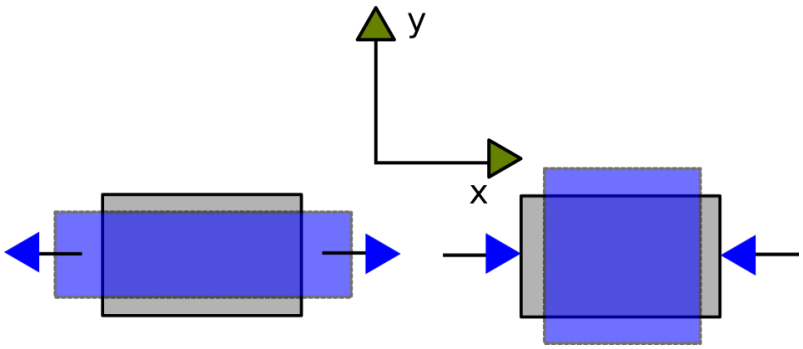

Figure 3.7: Schematic of normal stress. Arrows represent the direction of stress applied on the surface. Gray colour indicates initial state of the surface, blue colour after applied stress.

Shear stress is created by the tangential component of the force. As shown in the Figure 3.8 shear defines the transverse stress.τ_{xy} represents the vertical stress and τ_{yx} the stress in the horizontal direction caused by the tangential force.

A stress can remain in the material even through the external force has been removed (material at rest). This stress is defined as the residual stress. The stress is

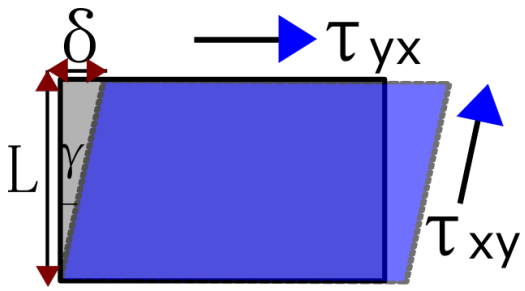

Figure 3.8: Schematic of shear stress. Gray colour indicates initial state of the surface, blue colour after applied stress.

negative when compression of the material is observed or positive due to the tensile action on the material.

At the moment of applying stress, the material starts to experience elastic deformation, but once the stress exceeds a certain value, it will experience plastic deformation. This point, where nonlinear deformation begins is called a yield point, which corresponds to the property of material, which named as yield stress (strength).

3.1.2.2 Strain

Strain of the material (ε) is the deformation of the material caused by a given stress (σ).

When the stress is positive (tension), the strain ε is then positive (elongation) $L > L_0$. When the stress is negative (compression) ε is negative (contraction) $L < L_0$.

$$\begin{cases} \sigma = E\varepsilon \\ \varepsilon = \frac{L-L_0}{L_0} \end{cases} \tag{3.4}$$

where E is the Young modulus, L_0 the initial length and L the stressed length.

Because of elastic behaviour, when the material is stretched (σ_x and $\varepsilon_x > 0$), the transverse dimension (σ_y and ε_y) is reduced and when squeezed (σ_x and $\varepsilon_y < 0$), the transverse dimension is increased. Poisson defined a ratio (Poisson's coefficient) to characterize this behaviour and it is expressed in the following way:

$$\nu = -\frac{\varepsilon_x}{\varepsilon_y} \tag{3.5}$$

Basically this coefficient (ν) represents the ratio between strain in the direction of the applied stress (ε_x) and the strain in the normal direction (ε_y).

The strain of the material under normal stress in the x-direction will be defined as:

$$\varepsilon_x = \frac{\sigma_x}{E} - \frac{\nu\sigma_y}{E} = \frac{1}{E}(\sigma_x - \nu\sigma_y) \tag{3.6}$$

where E is the Young's modulus, σ_x and σ_y are the stresses in the x (longitudinal) and y (transverse) direction respectively.

The strain in the y direction is equal:

$$\varepsilon_y = \frac{\sigma_y}{E} - \frac{\nu\sigma_x}{E} = \frac{1}{E}(\sigma_y - \nu\sigma_x) \tag{3.7}$$

The strain created in z direction is defined as:

$$\varepsilon_z = \frac{\nu}{E}(\sigma_y + \sigma_x) \tag{3.8}$$

In the case of shear stress, the strain is noted γ_{xy}. The displacement due to shear stress is (δ) created along transverse direction to the length (L) under the specific angle (γ):

$$\tau_{xy} = G\gamma_{xy} \tag{3.9}$$

where G is the shear modulus. This material property is expressed as:

$$G = \frac{E}{2(1+\nu)} \tag{3.10}$$

with E the Young modulus and ν the Poisson coefficient.

Exists also the bulk modulus K, which represents the compressibility of the material. The bulk modulus defines the amount of required pressure (p) to decrease a unit of the volume:

$$K = -\frac{p}{\delta V/V} \tag{3.11}$$

The bulk modulus also expressed versus the Young's modulus and Poisson's coefficient by the following equation:

$$K = \frac{E}{3(1-2\nu)} \tag{3.12}$$

3.1.2.3 Ductility

Ductility is the capacity of a material to deform plastically under applied actions (tension or compression) without breaking or cracking. Ductile materials either may be rolled to thin sheets from ingots, or bended, or even drawn into wires. Metals like niobium, copper, silver and magnesium have a high elongation and are called ductile metals. Other material on the contrary with low elongation capability are defined as brittle (ceramic, glass, cast iron...) materials.

Depending on the amount of applied stress the material may be in the elastic or plastic region. In the case of elastic deformation when applied force is removed the strain disappears. The elastic region is characterized by the Hooke's law when the force is applied:

$$\sigma = E\varepsilon \tag{3.13}$$

The plastic region is reached when residual stress and strain remain in the material when the applied force is removed. The frontier between the elastic and plastic regions is defined as the yield strength (σ_Y). Above this value material is plastically deformed until the ultimate tensile strength. The ultimate strength defines the maximum stress which may be applied on the material, before necking (large strain localized disproportionally in small area). The plastic region is thus in between the yield strength and ultimate strength.

Figure 3.9 shows a typical stress-strain curve of a ductile material. The specific stress-strain curve for Niobium is presented in the Figure 3.10.

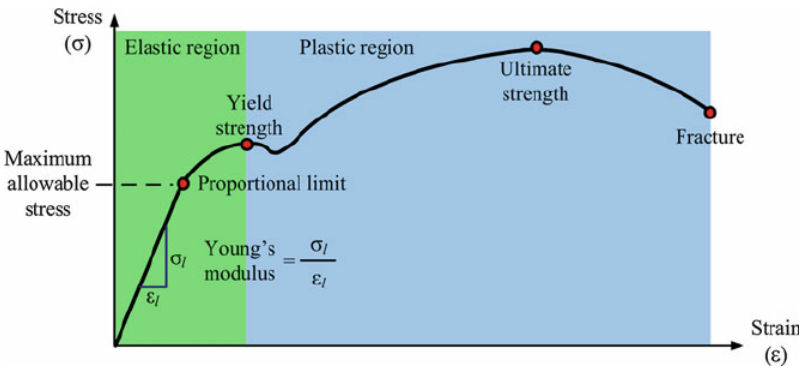

Figure 3.9: Stress-strain curve of ductile materials [117].

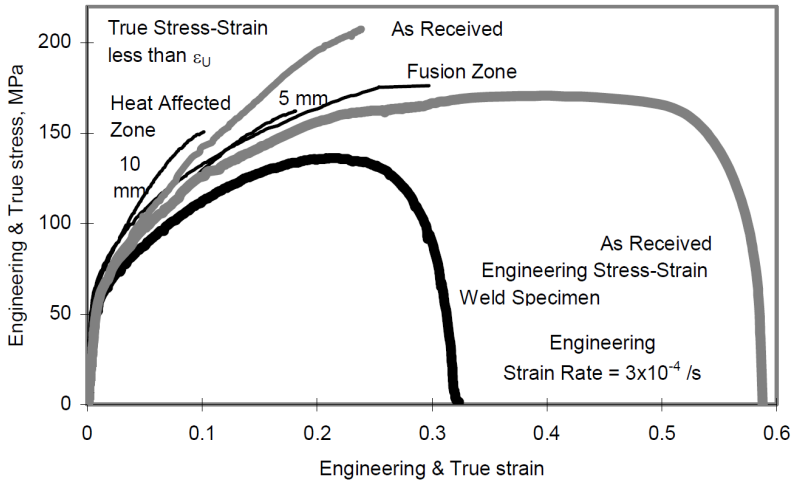

Figure 3.10: Stress-strain curve of Niobium at room temperature [118].

Table 3.3: Mechanical properties of Nb used for SRF applications at room temperatures (high purity polycrystalline) [119].

Mechanical property	Value
Yield strength σ_Y, [MPa]	66
Ultimate tensile strength σ_U, [MPa]	180
Hardness, [HV]	56
Grain size d_g, [μm]	50 (6 in $ASTM$)
Strain hardening coefficient n	0.31
Elongation A_l, [%]	59
Young's modulus E, [MPa]	105000
Bulk modulus K, [MPa]	170000
Shear modulus G, [MPa]	38000
Poisson ratio	0.4

3.1.3 Crystallite

Crystallites are the microscopic grains formed during cool down of a molten material. Crystallite may be single (monocrystalline), polycrystalline or amorphous. In the case of a polycrystalline material grains can have preferable or random orientations. Dimension of grains has a significant impact on the formability and elasticity of materials. The Hall-Petch equation [120] defines the dependence between yield stress (σ_Y) and the grain size (d_g):

$$\sigma_Y = \sigma_0 + \frac{k}{\sqrt{d_g}} \tag{3.14}$$

where k is the constant corresponding to the material and σ_0 is the bulk stress.

Hence the smaller the grains, the more resistant the material is to deformation and the wider the elastic region is.

For SRF applications, a compromise has to be found to have at the same time a high formability (high elongation and ultimate strength coefficients to allow forming), high elasticity (high yield strength to avoid irreversible deformations during the life cycle of the cavity) and high purity (size of crystallites big enough to decrease number of preferential impurity diffusion paths like grain boundaries). The typical size of Nb grains used for SRF cavities is about 50 μm (corresponds to grain size number equal to 6).

Figure 3.11: Example of a polycrystalline Niobium used for SRF cavities (Orientation imaging from EBSD analysis).

Single crystal or large grain materials may be used as well for SRF applications, but it will lead to very soft structures resulting in high sensitivity to mechanical perturbation during operation (vacuum, vibrations, EM forces).

3.1.4 Material Defects

Any material whatever it's quality and purity will have defects. The following defects can be defined: point, dislocations, grain boundaries, inclusions and pull-outs.

3.1.4.1 Point Defects

Point defect is a 0 dimensional irregularity in lattice structure, which may be caused by either a vacancy, substitutional atom, interstitial atom or Frenkel's pair, see in Figure 3.12.

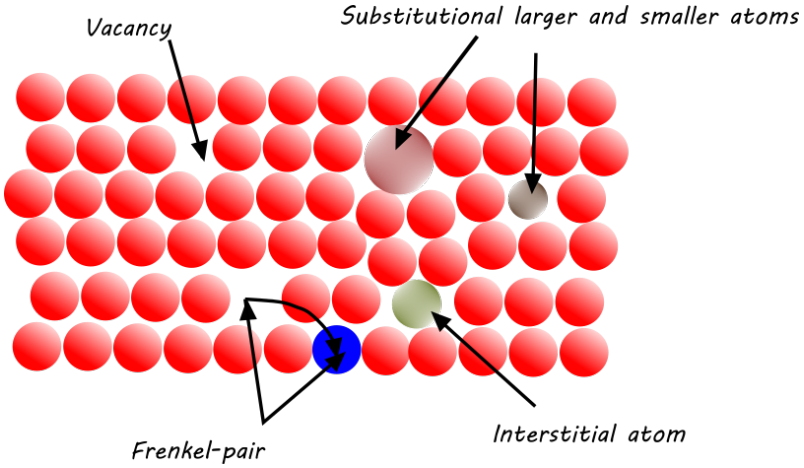

Figure 3.12: Type of point defects (0D) in a crystal lattice.

A vacancy is an empty space in the crystal lattice, which is due to the absence of an atom.

A substitutional atom is a foreign atom in the crystal lattice. This impurity is close in size (larger or smaller) compared to atoms of the lattice (difference is approximately 15 %).

Interstitial atom is additional foreign atom between atoms of the lattice. This impurity is smaller than atoms of the lattice structure.

The Frenkel pair is a pair of a close-located vacancy to an interstitial. This imperfection appears due to the migration of an interstitial leaving a vacancy in the crystal lattice.

The level of substitutional and interstitial atoms defines the purity of the mate-

rial.

3.1.4.2 Dislocations

Dislocations are 1D lattice defects, which can be defined as edge, screw or mixed dislocation (combination of edge and screw dislocations). Dislocations, see Figure 3.13, are places in the crystal lattice where atoms are misaligned due to the termination of atoms of a plane. Dislocations tends to affect significantly and positively the mechanical properties (yield strength, ultimate), but are also a source of lattice disorder causing degradation of superconducting properties (pinning centers for magnetic vortices, diffusion channels for impurities, ...).

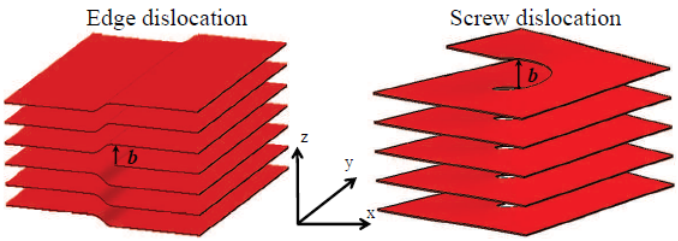

Figure 3.13: Type of 1D defects in a crystal lattice (edge and screw dislocations). The Burgers vector b gives magnitude and direction of dislocations. This vector is perpendicular to the dislocation line along y for an edge dislocation and it is parallel to the dislocation line along z for a screw dislocation [121].

3.1.4.3 Grain Boundaries

Grain boundaries are 2D lattice imperfections, where two crystallites with different grain orientations are in contact. Grain boundaries are locations where impurities can be trapped and are privileged paths for diffusion of impurities (hydrogen, oxygen, carbon...) are exist. As an example, the diffusion coefficient of carbon in a grain boundary is much higher than in a crystallite [122]. Grain boundaries could be of 2 types: twin and tilt boundaries [4].

Figure 3.14a shows twin boundary which indicates the mirror-reflection of atoms across a twin plane (2D equivalent of the 1D screw dislocation). It causes a shear stress in the crystals.

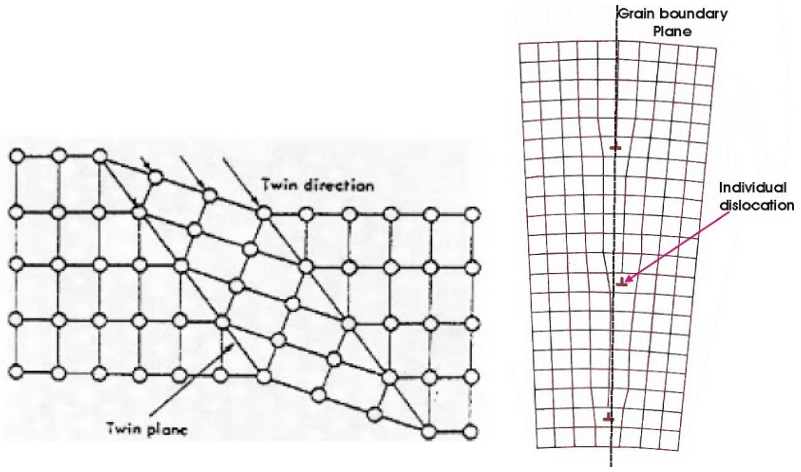

(a) Schematic representation of twin boundary [123].

(b) Sketch of tilt boundary [124].

Figure 3.14: Type of grain boundary.

Tilt boundary, as shown in Figure 3.14b, is the 2D equivalent of the edge dislocation (1D defect). This boundary appears between two slightly misaligned grains.

3.1.4.4 Inclusion

Inclusions are 3D imperfections coming from the insertion of a foreign material (machining, polishing...) into the surface layer. Inclusions can be metallic or non-metallic particles which come from the mechanical contact between 2 pieces. The stress is high enough to exceed the yield stress. The plastic deformation of the piece allows to accommodate the foreign particle into the lattice. The presence of an inclusion on a superconducting surface could be at the origin of premature quench.

3.1.4.5 Pull-out

Pull-out is another 3D imperfection of the surface layer, which has been created by an inclusion. However inclusions could be pulled-out from the surface layer (during cleaning, rinsing...) and as a result, a pit is remaining. Pull-outs are possible sources of thermal breakdown due to sharp edges (field enhancement).

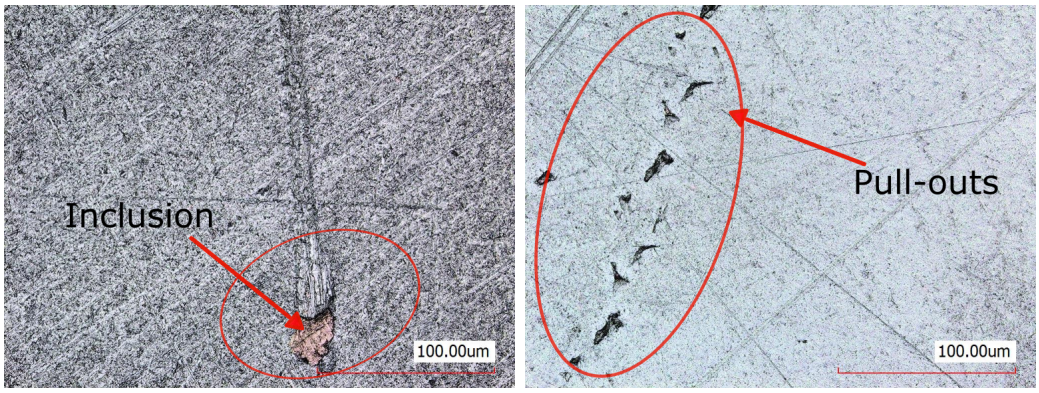

(a) (b)

Figure 3.15: Images of typical surface defects like scratches, inclusions (a) and pull out (b) on Niobium surface due to lapping process. Magnification: 50 times.

3.2 Surface Requirements for Niobium SRF Cavities

The preparation of the cavity walls has been and still be one of the major challenges for SRF accelerator technology. Even microscopic defects (inclusion, scratch, pull-out...), in such large macroscopic structures, could be a cause of local breakdown (quench) and could severely decrease the performance of the cavity. In order to avoid this negative impact on performance, the surface imperfections caused by Niobium sheet and cavity manufacturing have to be removed in order to recover a clean and damage-free surface.The damaged layer thickness varies typically from 100 to 200 μm, however, this value depends a lot from the Niobium supplier.

Niobium sheets are produced by companies capable of purifying Niobium material at a level ensuring optimal superconducting and thermal properties (typically RRR>250, See Section 2.2.4). Several steps are required to produce few-millimeter-thick Niobium sheets with this degree of quality from ultra pure Niobium ingot. These steps are :

- Several steps of forging and rolling of Niobium ingot to obtain uniform thickness;
- Annealing to recrystallize Niobium to ensure optimal superconducting and mechanical properties (yield stress, hardness, ...);
- Surface polishing and chemical etching to remove surface inclusions from previous steps.

Cavities are then built by specialized companies having the capability to form Niobium sheets or pieces by different type of techniques (deep drawing, spinning, machining) and weld formed sheets by Electron Beam Welding. This technique is the only industrial technique adapted to Niobium and capable of limiting sufficiently the diffusion of impurities into the material in the heat affected zone [125].

At the end of this fabrication process, the surface of Niobium has been significantly damaged and polluted. As explained in Chapter 1, the RF wave penetrates into the material only over few hundreds of nanometers. Optimal superconducting properties have to be ensure only over this depth. Deeper into the material, only good thermal properties are required to ensure an efficient heat transport from the RF side to the helium bath side.

It has to be mentioned that a natural oxide layer exists at the surface of Niobium of typically 5 nanometers [126]. This layer acts as a protective layer. The alteration of this passivating layer, caused by a surface treatment (chemical, mechanical or temperature above 250°C) can induce the absorption and diffusion of impurities present at the interface (hydrogen, carbon, oxygen,...).

In that sense, the following requirements for any surface treatment process of Niobium can be listed:

- Remove the damaged layer of hundreds of microns created during Niobium sheet and cavity fabrication;

- Preserve optimal superconducting properties over hundreds of nanometers (surface crystallites free of damages, limit impurities diffusion like Oxygen, Carbon and Hydrogen);

- Preserve optimal thermal conductivity all over the thickness of material (limit impurities diffusion and crystal damages).

In the present time, several surface techniques exist, which match with such requirements and they called as buffered chemical polishing and electropolishing. The detailed characterization of each technique will be presented in Section 3.3.1 and Section 3.3.2.

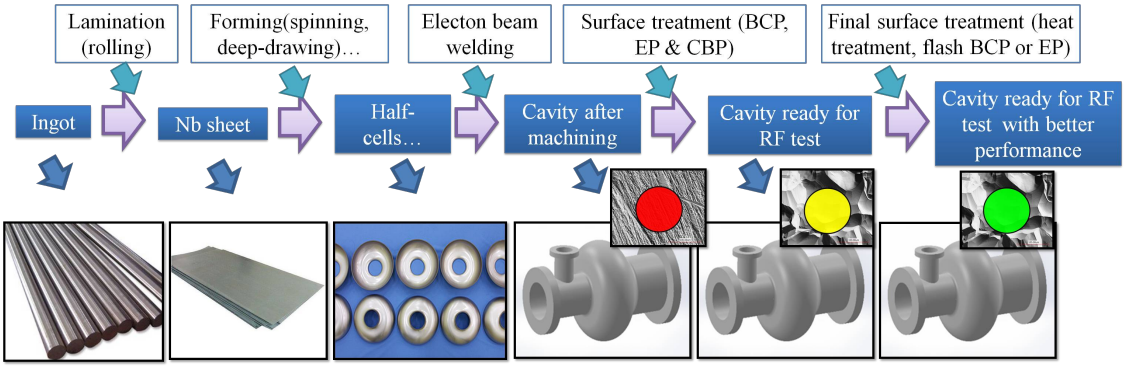

Figure 3.16: Standard path of cavity fabrication: lamination (rolling), forming (spinning, deep-drawing...), electron beam welding, surface treatment (BCP, EP and CBP) and final surface treatment (heat treatment, flash BCP or EP).

3.3 State of the Art for Cavity Treatment: Chemical Treatment

During decades, chemical treatments (buffered chemical polishing and electropolishing) have been used routinely to prepare cavities to accelerate particles to high energies [71]. Buffered chemical polishing (BCP) is not literally a polishing treatment but rather an etching process which etching rate depends strongly on the crystal orientation. As a consequence, for polycrystalline Niobium, the final surface roughness is usually worse than the "as received" roughness. Electropolishing produces smoother surfaces compare to BCP and removes as well the damaged layer, however, the process is more complex.

3.3.1 Electro-Polishing (EP)

Electro-Polishing (EP) is the first technique, which has been used to the clean the surface of SRF cavities. First procedure was developed by Siemens company in 1971 [127] and then adopted for different geometries by KEK, DESY and CEA/Irfu laboratories [128, 129, 130]. During electropolishing the surface of niobium is treated by a solution of hydrofluoric (HF) and sulfuric acids (H_2SO_4) under the flow of an electric current.

The cavity is attached to the positive pole of a power supply (anode). The negative pole (cathode) is usually made of copper or aluminium.

As a result, Niobium is anodized (oxidized) in contact with the electrolytic solu-

tion (sulfuric acid) where currents are flowing toward the cathode. The oxide layer is dissolved by the hydrofluoric acid. Sulphuric acid also plays the role of buffer [131]. Typical ratio of volume acids is 1:1. Anodization:

$$\mathrm{Nb} \longrightarrow \mathrm{Nb}^{5+} + 5\,\mathrm{e}^{-} \longrightarrow \mathrm{Nb_2O_5}$$

Dissolution of Nb oxide:

$$\mathrm{Nb_2O_5} + 10\,\mathrm{HF} \longrightarrow 2\,\mathrm{NbF_5} + 5\,\mathrm{H_2O}$$

The reduction of roughness is obtained (polishing effect) thanks to the applied voltage or more precisely to the surface electric field. The anodization, and thus dissolution are faster where the electric field is higher, meaning on peaks and minimum in valleys. This preferential etching tends to smoothen the surface. The global etching rate is proportional to the applied voltage, the concentration of sulphuric acid and duration of process. This process has to be carefully controlled in term of current and voltage as several regimes can be observed: etching, polishing and strong oxygen evolution in the bulk [132, 133, 134].

Typically achieved surface roughness after EP is bout 100 nm and the etching rate is typically of 0.5 μm/min. Nowadays, EP is is the best surface treatment to achieve very high accelerating gradient in elliptical cavities usually required for electron linac. However, because of the strong dependence of the etching rate versus the distance between electrodes, cavities with complex geometries (no symmetry of revolution) can't be efficiently and homogeneously polished. Another chemical treatment would be more appropriate like BCP.

3.3.2 Buffered Chemical Polishing (BCP)

Buffered Chemical Polishing (BCP), also known as chemical etching, has been investigated since 1980s in order to replace the complex EP treatment, by a simple technique which does not involve electric current [70]. In the past, a mixture of acids consists only of nitric (HNO_3) and hydrofluoric (HF) acids. However the high etching rate (30 μm/min) led to a significant elevation of temperature and to the

degradation of superconducting properties due to the diffusion of impurities like hydrogen [135]. In order to buffer the chemical reaction, phosphoric acid (H_3PO_4) has been added.

The mixture of acids mentioned above: HNO_3, HF and H_3PO_4, respects the following proportions and are between 1:1:1 and 1:1:2.5 depending on local safety regulations [136]. The mixture of acids and the cavity are maintained below 15 °C, in order to reduce the migration of Hydrogen within the bulk material [135, 137]. The role of nitric acid is to oxidize the surface of Niobium. The chemical reaction is described by the following formula [138]:

$$6\,\mathrm{Nb} + 10\,\mathrm{HNO_3} \longrightarrow 3\,\mathrm{Nb_2O_5} + 10\,\mathrm{NO} + 5\,\mathrm{H_2O}$$

The hydrofluoric acid plays the complexing role in chemical treatment. The dissolution of the Niobium oxide is given by the following reaction:

$$\mathrm{Nb_2O_5} + 10\,\mathrm{HF} \longrightarrow 2\,\mathrm{NbF_5} + 5\,\mathrm{H_2O}$$

The etching rate of the BCP mixture depends on the phosphoric acid concentration. For typical mixture proportions, the etching rate ranges between 0.5 and 2 μm per minute [139].

3.4 Studied Alternative Polishing Techniques

3.4.1 Motivations

Chemical polishing (BCP, EP) is the only surface treatment routinely used to clean and polish Niobium surface for SRF applications. However both methods are very hazardous and expensive, as they involve the use of hydrofluoric acid. The operational cost of chemical facilities is high, because of acid aging and recycling. Moreover, another motivation is to replace the chemical polishing by an alternative technique which could not only reduce the cost but also improve even more current accelerating performances of Niobium cavities. The reduction of surface contamination and roughness compared to what is achieved by chemical treatment could

provide higher performances and potentially higher yield.

Finally, thin films deposition of alternative superconductors (Nb_3Sn, MgB_2) is an another way to increase significantly the accelerating gradients. Since quality of thin-film deposition depends on the surface-state (roughness) of the substrate, the development of an alternative treatment technique to reduce substrate roughness at the nanometer level is a key point to produce high quality films and to push the performance of SRF cavities.

3.4.2 Requirements

Alternative techniques require to remove the polluted and damaged layer induced during Nb sheets fabrication and preserve the superconducting properties over few 100s of nm. However the specific requirements for alternative techniques are determined by the drawbacks of chemical polishing. To overcome these disadvantages, which were presented in Section 3.4.1, an alternative treatment technique has to be at least less hazardous than BCP & EP and/or duration of treatment shorter than chemical treatment. In order to make industrialisation possible, the process is required to have limited number of steps, ideally, 2-3 steps and achieved average surface roughness less than 100 nm with a minimum crystalline damages.

3.4.3 Mechanical Polishing

Mechanical polishing (MP) is the material removal process using abrasives as cutting tools which consists typically of agglomerated powder (media) or powder of a hard material (diamond, ceramic, ...). The sizes of these scales from centimeters (media) down to nanometers (colloidal silica) [140]. The cutting effect is obtained thanks to the combination of two forces: a tangential force and normal force. Figure 3.17 shows that an abrasive pressed on the workpiece by a normal force (in the direction perpendicular to workpiece) can remove a chip of material if a tangential force is added [141].

This interaction between abrasive and surface leads to removal of material (chip formation) and/or to the formation of localized increased hardness (also known as the increased dislocation density or shear zone) due to ploughing and sliding of abrasive [142]. As shown in Figure 3.18, the attacking angle of the abrasive

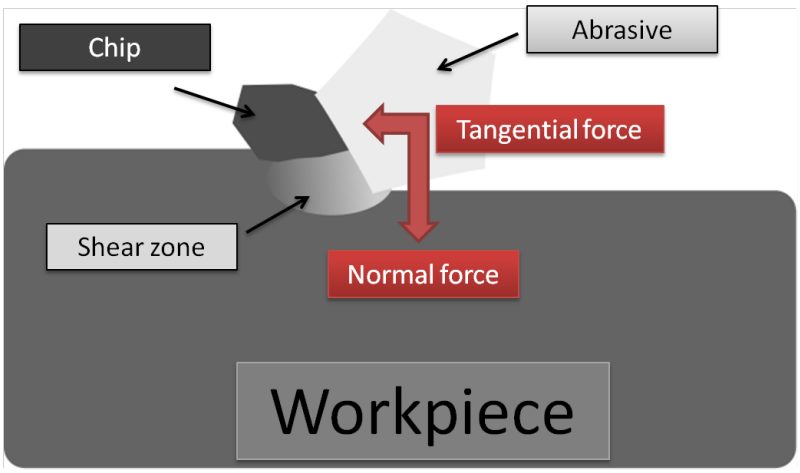

Figure 3.17: Sketch of material removal during mechanical polishing with abrasive.

defines domination either of chip formation or the increasing the layer with increased localized hardness [143].

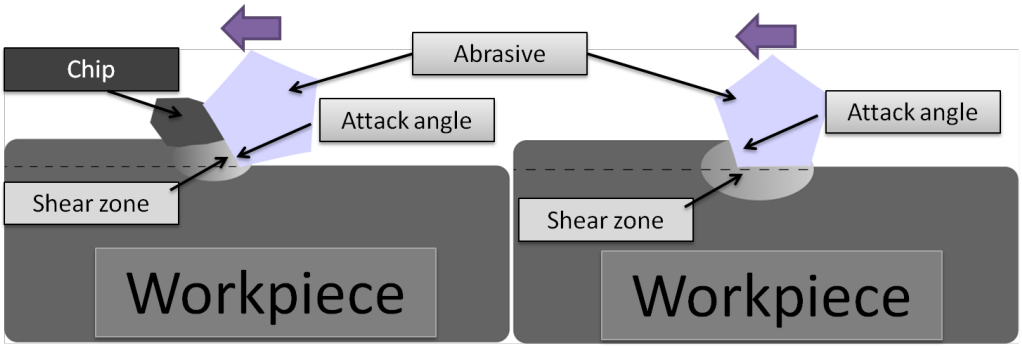

Figure 3.18: Schematic image illustrating the two cutting modes depending on the attack angle of abrasive tool. The violet arrows show the direction of abrasives.

Shear zone is a plastic deformation region (damaged layer), created due to the friction between abrasive and surface of workpiece, which appears in the direction of cutting. The value of shear zone is determined by polished material and abrasive which used for polishing. The size, the shape, the hardness of abrasives and the applied pressure on the abrasive are the main parameters which define the created shear zone and the speed of abrasives wear [144, 145].

The use of successively finer abrasives, one after the other, enables reduce step by step, the sizes of the chips and the shear zones, leading to a gradually improved roughness. MP is a process that produces a smooth mirror surfaces with final roughness in the nanometer scale but leaves a damaged surface from the crystalline point of view[141]. MP is a well established industrial process, but in general, only

the roughness aspect is monitored, and the process is not optimized from the damage point of view.

3.4.3.1 Metallographic Polishing

Metallographic Polishing is a specific mechanical polishing process where the normal and tangential forces are obtained by pressing the workpiece on a rotating disk loaded with abrasives. The typical goal of metallographic preparation is to reveal the microstructure features of material by a specific developed preparation procedure composed of several processes (grinding/lapping/polishing) for further microscopic examination [146, 147]. Figure 3.20 is showing an overview of used abrasives for the 3 processes. Each process will be discussed later.

Depending on the hardness and ductility of materials, metals can be prepared by different type of processes and in many steps. The type of processes and number of steps for each process have to be adapted and optimized empirically for each investigated material. Hence, metallographic preparations have to be developed carefully in order to minimize the damage left by the polishing.

The first step of metallographic preparation, called grinding, aims at reducing the value of surface defects (inclusions, scratches, pull-outs), and at reducing the deformation layer (in particular suppressed crystal lattice, dislocations, inclusions...) and finally at improving the flatness of the surface to ensure the efficiency of the following steps. The size of abrasives ranges typically between 15 and 300 microns depending on the surface layer which has to be rectified.

As an example, the deformation layer created after rolling of Niobium sheets for the fabrication of accelerating cavities is typically of 200 microns [4]. As it will be shown later (See Chapter 5), the grinding step when required was achieved by abrasives as small as 15 microns, as surface damages and shear zone created by bigger abrasives were to significant to be recovered by the following steps.

Next surface processes, see Figure 3.19, aim at removing damages and deformations created during the first aggressive process of grinding. These processes are called lapping and polishing. Lapping is a transitional process between grinding and polishing which removes damages after grinding and produces required flatness and roughness of the sample by a mid-range abrasives (3-51 μm). However after lapping the treated surface is still degraded by the presence of scratches, inclusions,

pull-outs but with a reduced damaged layer which will be removed by action of ultra-fine abrasives during the final polishing step. The polishing step, which is very comparable to lapping process, can produce, if nicely performed, scratch-free surfaces with roughness in order of magnitude of tens nm. Polishing process is less efficient in term of material removal compared to the previous steps, due to the fact that smaller abrasives down to nanometre grain size (25 μm to 0.01 μm) are used on softer disk (cloth). Hence the achieved surface roughness can be reduced and damaged layer is significantly decreased.

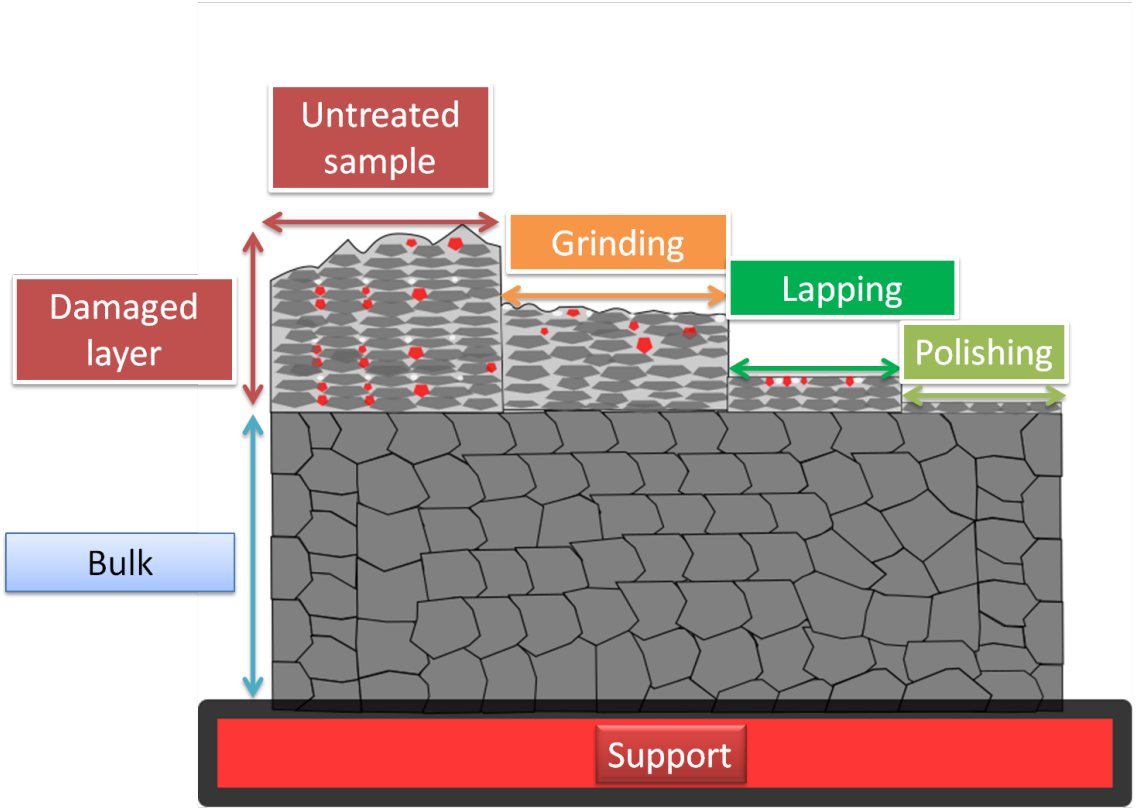

Figure 3.19: Schematic view of surface and sub-surface state after subsequent metallographic polishing steps (untreated, grinding, lapping, polishing). Note: damaged regions is presented with grey bars and inclusions are red dots.

A wide variety of abrasives with different hardness (See Table 3.4), shape (round, polycrystalline or monocrystalline) and sizes exists and are available on the market. The choice of the most adequate abrasive is generally empirically determined because of the number of parameters and the complexity of the interaction between the workpiece and the abrasives that could could be described by three wear modes: creating of chip (material removal, in particular surface described by scratches), sliding (rotating of particles without removing of material, presence of pull-outs) and ploughing (displacement of material, in particular described by the presence of

inclusions).

To control the temperature during these processes and to avoid overheating of the sample and the disk, lubricant has to be used. The lubricant is based on water, alcohol or oil which aims at reducing the friction and cooling down the interface between surface of sample and grinding/lapping/polishing disk.

Cleaning is an essential step before start, between and after each surface process preparation [148]. The size of abrasives varies from 100s of μm down to nanometers during the full polishing process. In that sense, to avoid any pollution and degradation of the surface because of the presence of abrasives used during previous steps, the workpiece and sample holder have to be thoroughly cleaned and polishing disks have to be changed (a disk is dedicated to one type of abrasive). For cleaning three cleaning agent are typically used: deionized water, ethanol and acetone. As recommended in [148], workpiece/holder firstly should be cleaned manually by a flow of deionized water with a cotton ball, secondly degreased by cotton ball dipped in ethanol and thirdly workpiece/holder has to be placed in ultrasonic bath with deionized water/alcohol or acetone.

3.4.3.1.1 Grinding Process

According to K. Geels [149], grinding or "two body abrasion" is a process of material removal using abrasives which are embedded in the disk, as shown in the Figure 3.21. Grinding process is characterized by significant abrasion rate, at the expense of high roughness and significant damaged layer, however smaller then a damaged layer of an untreated surface after forming or cutting processes.

Moreover, an essential goal of grinding process is to rectify the surface (planarize the surface and ensure perfect parallelism between the work piece and the disk) so as to optimize the efficiency of following steps using smaller abrasives. To have the same plane level is of paramount importance to achieve desirable surface quality. The grinding abrasives have different shapes, hardness and sizes. The size of grinding abrasives scales from 269 μm (corresponds to SiC paper P60) down to 5 μm (corresponds to SiC paper P2400[1]).

Many types of abrasives exist depending on the material processed (see Table 3.4) [151, 152]. These abrasives are embedded either in a bond (resin, metal, ceramic)

[1]Grit size of paper according to European system [150]

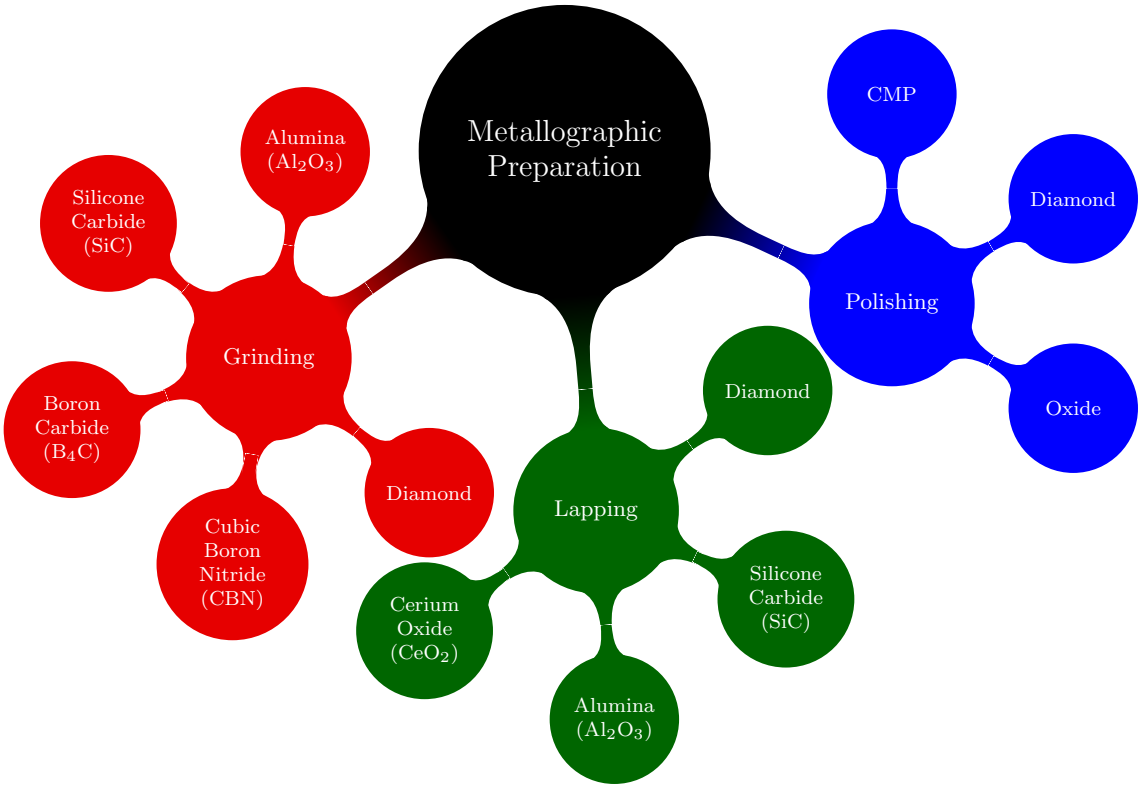

Figure 3.20: Metallographic preparation is divided into three families of surface processing (from left to right): grinding (red), lapping (green) and polishing (blue). Polishing process in his order of particles nature can be divided to three families: diamonds, oxides (silica, alumina, cerium, chromium, ferric) and chemical-mechanical polishing (CMP).

or coated on the flexible backing paper (as SiC paper). However there exists a rule of thumb that hard abrasives should be mounted in a soft bond and soft abrasives with hard disks.

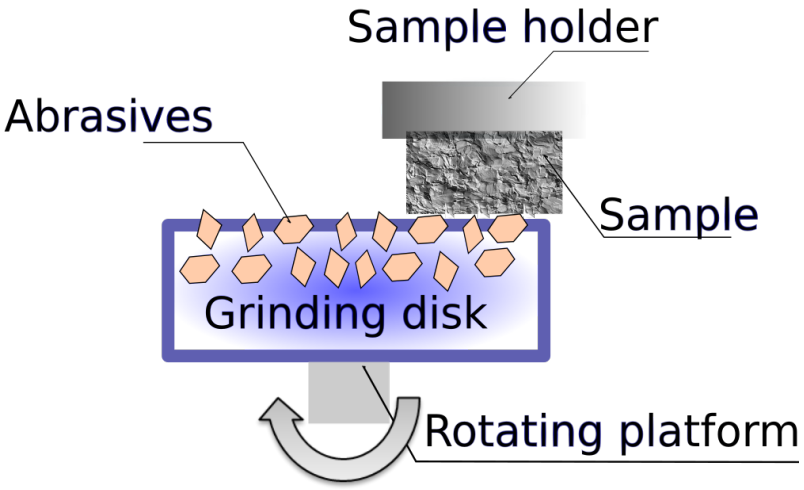

Figure 3.21: Schematic view of the specimen/disk interface during grinding process ("two body abrasion"). Abrasives are bonded in the disk. Bonded material is typically resin, polymer or metal.

Table 3.4: Hardness of commercial abrasives [151, 152].

Abrasive type	Hardness, HV
Diamond	8000-10000
Cubic Boron Nitride (CBN)	4500
Boron Carbide (B_4C)	2800
Silicon Carbide (SiC)	2700
Aluminum Oxide (Al_2O_3)	2500
Silica (SiO_2)	1103-1260
Cerium Oxide (CeO_2)	1688

3.4.3.1.2 Lapping or Polishing Process

L. Samuels [145] defined lapping and polishing as a "three body abrasion". During this process particles aren't embedded in the surface of disk, they are added as a "third body". The loose abrasives are rolling between the two surfaces (disk/sample). In the case of lapping, abrasives are pressed by a rigid disk (metal, composite) against the sample. During polishing, soft disks as pads or cloths are used instead of hard disks surface. The material removal rate of lapping is not as high as during grinding, but higher than for the polishing step.

The purpose of lapping, is to decrease surface damages caused during grinding step at a level sufficiently low to be effectively removed during polishing step. Indeed, inclusions of abrasives used during grinding step (tens of microns) or scratches of several microns deep could not be removed efficiently by polishing abrasives of several tens of nanometers. An intermediate step like lapping process with abrasives of few microns has the ability to remove efficiently surface damages and to limit damaged layer (shear zone).

Finally polishing step, aims at erasing the polluted/affected layer created during lapping step and reaching the desired roughness of typically tens of nanometers.

Polishing process can be divided into 3 categories: diamond polishing, oxide polishing and chemical-mechanical polishing (colloidal silica with pH above 10).

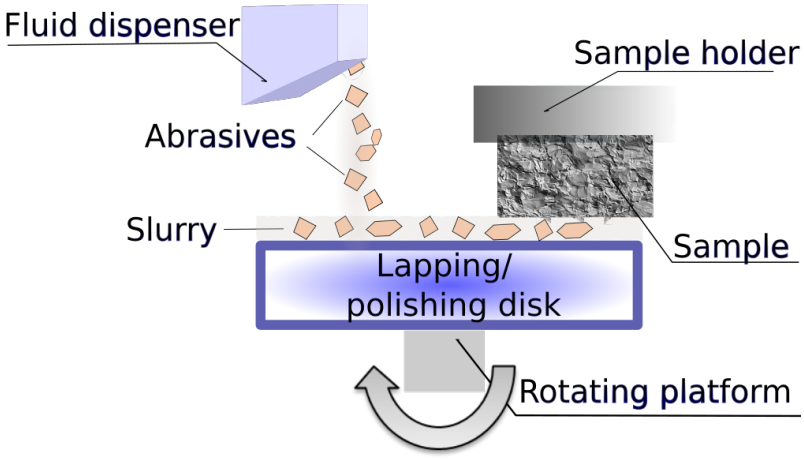

Figure 3.22: Schematic view of the specimen/disk interface during lapping/polishing process ("three body").

Diamond polishing

Diamonds used in metallographic polishing can be polycrystalline or monocrystalline. Polycrystalline structure is more efficient, with higher removal rate, as they have more cutting angles compare to monocrystal. Commercial monocrystalline or polycrystalline diamonds are available in suspensions (based on alcohol, water, oil), sprays or pastes. The grain size varies from 45 μm down to 0.1 μm. Suspensions allow more reproducibility and is easier to handle than others solutions.

Oxide polishing

The choice of the best abrasives is empirical, but is generally linked to the hardness of the sample material (diamond for harder material, Alumina for softer). Alumina, silica, cerium oxide are most used polishing abrasives which used in metallographic preparation, in order to obtain mirror-finished surfaces. The mean diameter of such abrasives could go down to 10 nanometers.

Chemical-mechanical polishing (CMP)

Chemical-mechanical polishing (CMP) was developed mainly for electronics, particularly for wafer and optical fiber preparation [153, 154, 155, 156]. However excellent results are obtained on metals with soft abrasives like colloidal silica (SiO_2). SiO_2 may be bought in suspension of a basic solution ($8.5 \leq pH \leq 11$) composed of oxygen peroxide (H_2O_2) and ammoniac (NH_4OH) [157]. In this case, material removal happens due to a combined mechanical and chemical action. The mechanical action is ensured by colloidal silica. Chemical action is double, oxygen peroxide passivates the surface and ammoniac dissolves the oxide layer. In general oxidized layer of metal is softer than bulk [158], due to the decreased density of this layer, leading to an improved removal rate thanks to the combined actions of dissolution (ammoniac) and friction (colloidal silica).

Moreover, silica suspension tends to break into smaller parts with time, improving even more the surface quality [159]. Finally, proper cleaning after CMP process of the polishing disk and workpiece (by water rinsing) is required, as the solution crystallizes very rapidly and is then very difficult to remove [158].

3.4.3.2 Centrifugal Barrel Polishing (CBP)

CBP is a specific mechanical polishing process where abrasives and the workpiece are contained in a barrel subject to a double rotation. The normal and tangential forces required to achieve material removal are obtained by pressing the abrasives thanks to centrifugal force on the moving workpiece. (CBP), however in a slightly modified configuration as explained later, is one of the mechanical polishing technique extensively used for superconducting elliptical cavities, which has been investigated during decades. First attempts were performed at KEK (Oho, Tsukuba-shi, Japan), by Tamavo Higuchi in 1995 [160]. CBP has been then explored in others laboratories: DESY (Hamburg, Germany) [161, 162, 163], JLAB (Newport News, Virginia, USA) [164, 165, 166], Fermilab (Winfield Township, Illinois, USA) [167, 168, 169, 170, 171], Cornell University (Ithaca, New York, USA) [172], Raja Ramanna Centre for Advanced Technology (Indore, India) [173] and Italian Insitute of Nuclear Physics/Laboratori Nazionali di Legnaro (INFN/LNL) (Padua, Italy) [164].

The cavity, see Figure 3.23, serves as the workpiece and the container. It is partially filled with a mixture of water, abrasives and surfactant [174, 175]. As explained in Chapter 3.4.3, material removal is possible only when a combination of a normal and tangential forces are applied on the surface by the abrasive. In CBP process, the tangential force is obtained by spinning the cavity around its central axis (abrasives are sliding on the surface) and the normal force by a second rotation which axis is away from cavity (abrasives are pressed on the inner surface by centrifugal force).

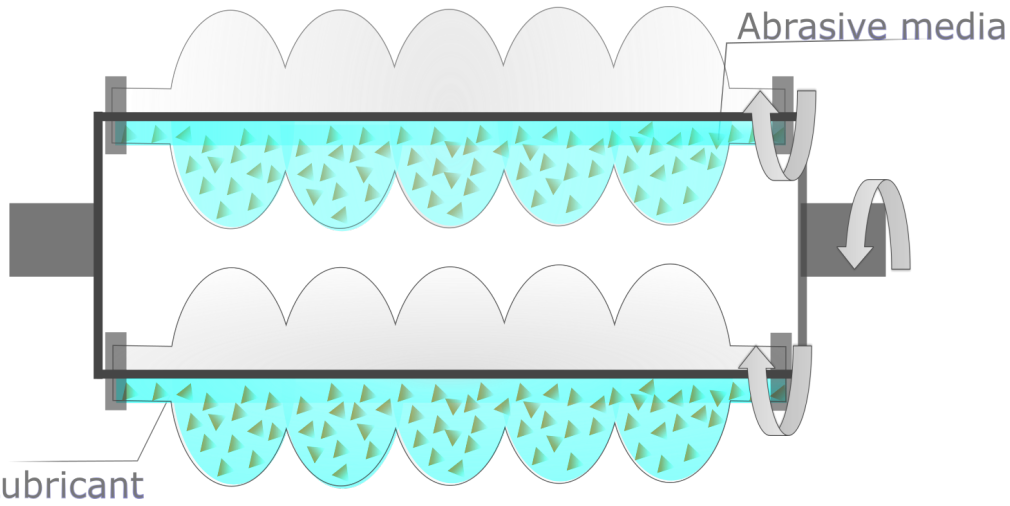

Figure 3.23: Schematic of centrifugal barrel polishing (CBP) applied to elliptical cavities.

In the same manner as metallographic polishing, CBP process consists of several steps, starting with very aggressive abrasion to achieve high removal rate (similar to grinding) and finishing with a polishing step.

For abrasion and intermediate steps, abrasives are bounded together to form media of different mass, compositions and geometries (cubes, balls, cones, pyramids...), as shown in Figure 3.24, [176, 177], in order to improve the process efficiency (centrifugal force is proportional to the mass of the abrasives [178]. For the final steps, abrasives are mixed with some soft carriers (cubes of wood, nut shells, corns...). Depending on the abrasive material, media bounding material, geometry and size of media, a very aggressive or a very soft abrasion could be performed.

Figure 3.24: Typical shapes of the abrasive media used for centrifugal barrel polishing.

CBP can achieve mirror finish surfaces and has been used as a complementary technique to chemical polishing so as to repair some of the surface defects done during manufacturing [167, 170]. The CBP process could be an alternative technique to the standard chemical polishing but would require 4 to 5 polishing steps as described in [161, 162, 163, 164, 165, 171]. The level of pollution, the thickness of damaged layer and surface roughness decrease gradually step by step [169, 170].

According to the experiments [160, 165] the best conditions to optimize the abrasion rate and the surface pollution were investigated.

CBP is very efficient at removing the main damages after manufacturing but induces a strong pollution due to embedded abrasives over several tens of μm [171]. This contamination can be reduced in depth by using soft abrasive media and slower rotating speed. Several experiments [170, 171] as well as the work which results will be presented in Chapter 5, concluded that after a full cycle of mechanical polishing (96-150 hours), it is required to remove 10-20 μm of the polluted layer by electropolishing [167]. BCP could also be used, however it degrades very quickly the

roughness (See Chapter 5).

The decreased surface roughness achieved after CBP in combination with light electro-polishing potentially leads to higher accelerating gradient and higher achievable quality factor in superconducting cavities compare to bulk EP [168]. However the extremely long time of treatment (96-150 hours), the numerous polishing steps (usually 4-5) and elongation of cavities iris after whole cycle pushes investigations of alternative polishing technique for SRF cavities like metallographic polishing.

3.4.4 Other Polishing Techniques

3.4.4.1 Laser Polishing

Laser polishing is a surface treatment technique, which has been used for polishing of metals, glasses, fibers, quartz and etc. [179, 180, 181, 182, 183, 184]. A lot of work has been done to adapt and optimize this method for different type of surface (different material, shape and area) [185, 186, 187, 188, 189, 190, 191].

Laser polishing melts the surface without removing the material. Laser works either in continuous wave (CW) mode or in pulse mode. CW is used for really rough surfaces as the melted depth varies from 10 to 80 μms. And in pulsed regime the melted surface is less than 5 μm [192]. Schematics of laser polishing procedure in both mode are presented in Figure 3.25.

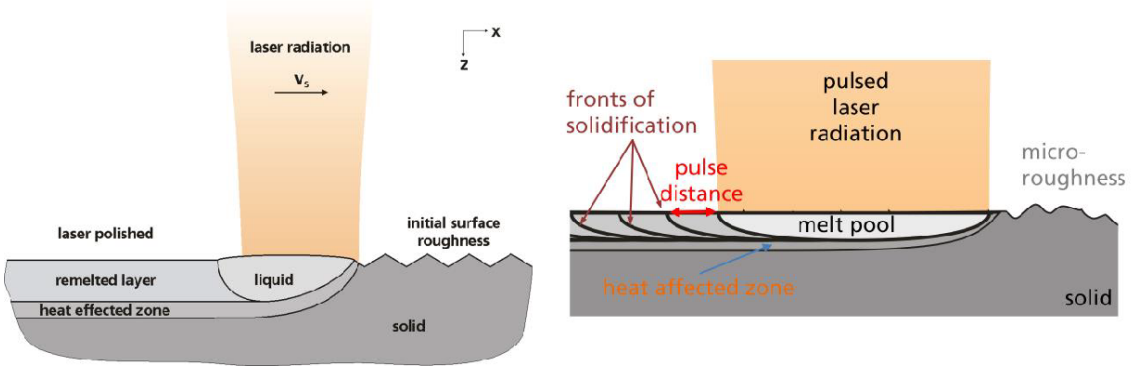

Figure 3.25: Sketch of laser polishing in CW-mode (left image), sketch of laser polishing in pulsed mode (right image) [192].

First results of Nb laser polishing were obtained by Zhao in 2013 on flat samples [193]. Several studies have been performed to optimize parameters of laser radiation [194, 195].

This technique shows many advantages for SRF cavities due to fact that laser polishing can be applied on complex geometries and does not induce significant deformations or stress. However the achieved roughness is higher (of the order of microns) compare to metallographic flat polishing technique due to the fact that roughness of the laser polished surface strongly depends on the initial state of the surface [195].

Additional work has to be carried out on complex geometries and superconducting properties of polished surface has to be verified under RF and at cryogenic temperatures down to 2K.

3.4.4.2 Plasma Polishing

Plasma etching (PE) or polishing have been first developed for fabrication of the integrated circuits [196] and surface preparation of the Josephson junctions [197, 198, 199]. The plasma, composed of reactive gas, generates high energy ions which bombard the surface. Surface atoms are sputtered out of the surface and evacuated by active pumping.

Figure 3.26 shows the steps of plasma etching. First step consists in the creation of ions from reactive gas during electrical discharge. Then, the diffusion process, where reactive elements are attracted toward the sample thanks to an applied voltage. Finally, surface atoms are ejected due to etching reactions.

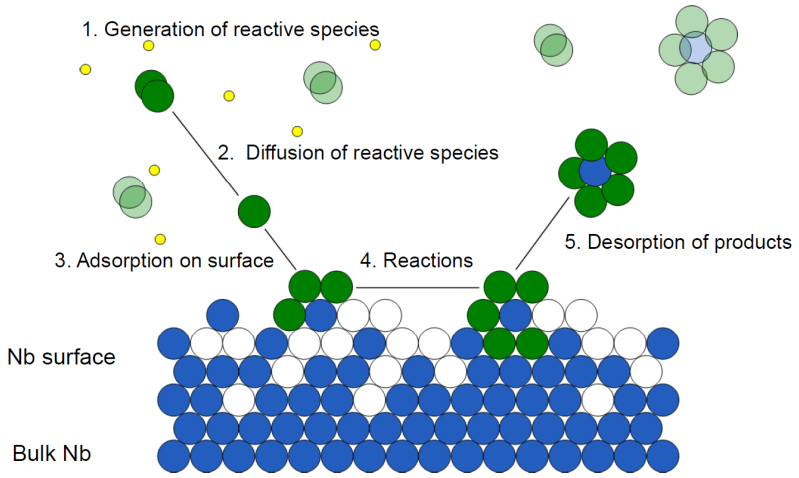

Figure 3.26: Sketch of plasma etching process. Courtesy of M. Rašković

This contactless technique has the advantage to generate no deformation layer as mechanical polishing techniques. Significant etching rate of the order of few

micrometer per minute could be achieved [200, 201]. Plasma treatment is a dry process, which involves no water, electrolyte or acid. Contrary to wet processes the plasma polishing eliminates hydrogen impurities from material, but at the expense of contaminating the surface from cathode material.

Plasma polishing of Nb for SRF purposes has been investigated by Upadhyay and Vušković [202]. A lot of effort has been spent to adapt this technique specifically for Niobium by defining the gas composition, pressure, voltage, power density and geometrical characteristics of the cathode (due to anisotropy) in order to obtain the best characteristics of the polished surface [203, 204, 205, 206, 207, 208].

The first cryogenic RF test of a plasma treated single cell cavity were presented in 2017 [209].

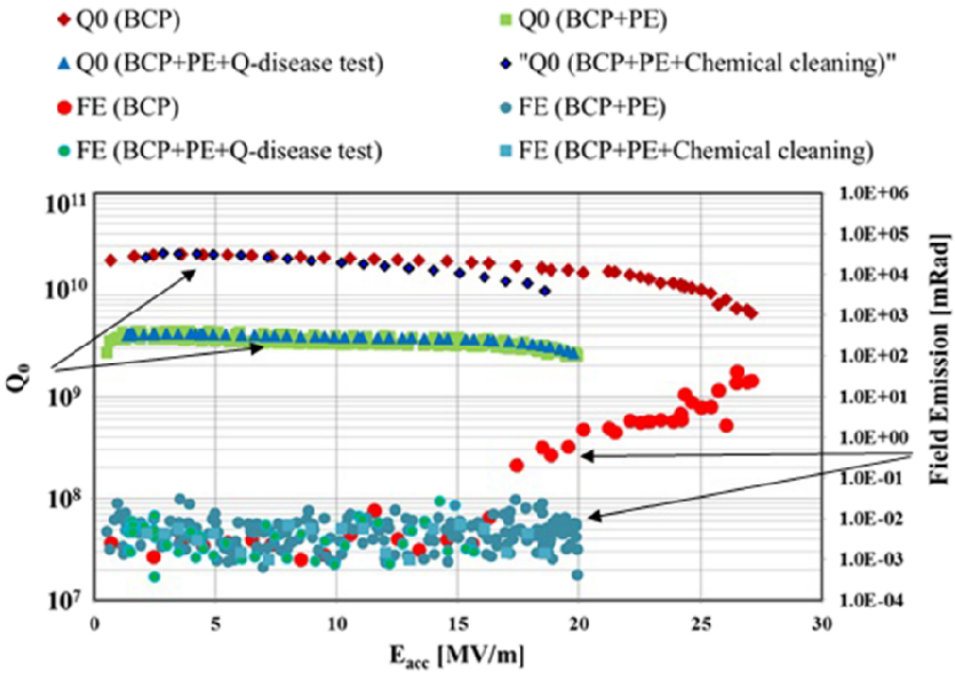

Figure 3.27: The RF performance measurement of the plasma treated single cell cavity (made from bulk Nb) [209]. Quality factor Q_0 and field emission (FE) are plotted versus accelerating gradient E_a.

Figure 3.27 shows that plasma etching leads to the degradation of quality factor of almost an order of magnitude (blue triangles and green rectangles curves) to be compared to BCP (red rhombus curve), due to the pollution of the surface by the cathode material (stainless steel particles).

Chemical cleaning without HF acid has been used in order to remove the impu-

rities and avoid the roughening of the surface. As a result the RF performance has been recovered at the same level as BCP treatment.

This technique improves roughness compare to BCP treatment, but if initial roughness is in the tens of nanometers, plasma etching leads to increase the roughness up to hundreds of nanometers [210].

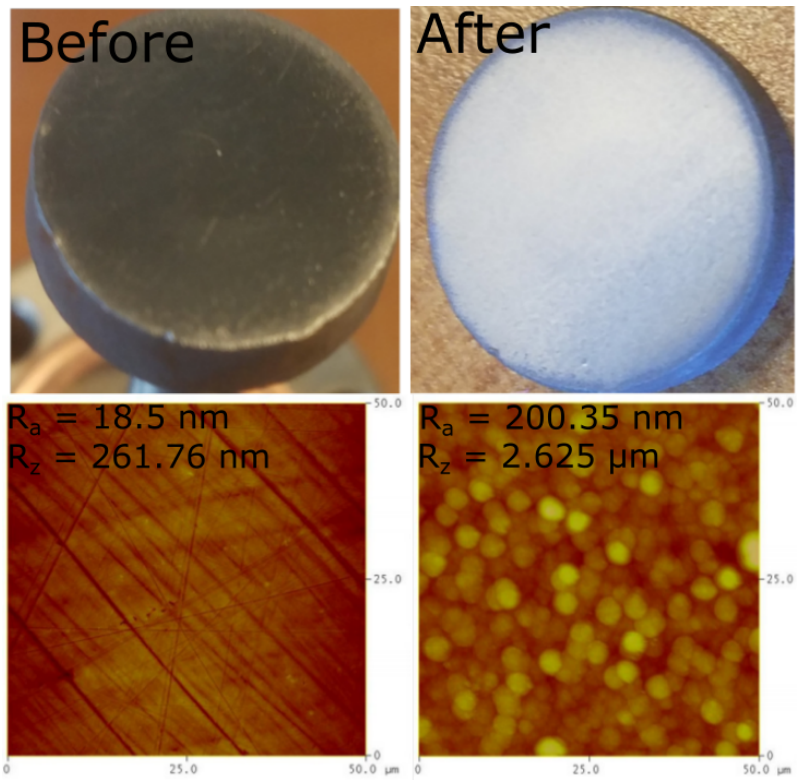

Figure 3.28: Photographs of a Niobium sample before (left) and after (right) plasma etching. The sample has been polished mechanically before plasma etching. [210].

Upadhyay concluded that the future investigations may be done with cathode made from Nb in order to remove surface pollution and reduce the number of steps during surface processing.

3.4.4.3 Electrolytic Plasma Polishing

Electrolytic plasma polishing (EPP) was invented in 1979 [211]. EPP is an environment-friendly technique for surface treatment of metals. Indeed, the workpiece is immersed in a salty solution rather than in an acidic solution [212, 213]. EPP requires significantly higher applied voltage (180V-320V) compared to electrolytic polishing or electropolishing (5V-20V) [214], in order to ignite the plasma

discharge around the anode and start preferential dissolution of peaks of the sample as depicted in Figure A2.2.

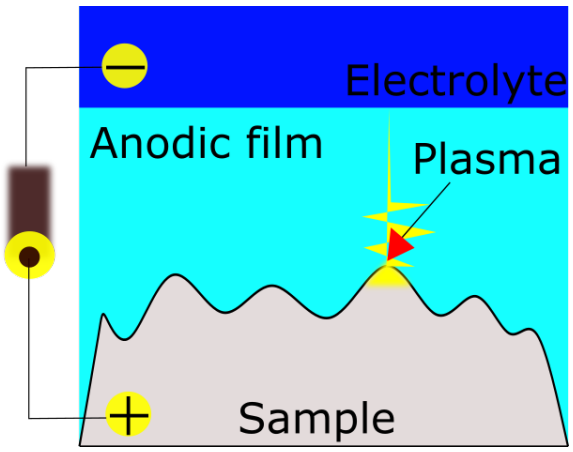

Figure 3.29: Electrolytic Plasma Polishing.

The electrolyte (type of salt) and parameters (current-voltage on the electrodes) of plasma discharge have to be adapted and optimized empirically for each investigated material [215]. Nowadays very few materials are polished by this technique [216, 217, 218, 219] in particular Niobium for which no studies have been found in the literature. However, we had the opportunity to send Niobium samples to German company Plasotec and V. N. Karazin National University who performed electrolyte and parameters optimization specifically for Niobium. The first results (surface roughness measurement and pollution investigations) can be found in Appendix B.

3.4.4.4 Magnetorheological Polishing

Historically magnetorheological polishing (MRP) has been developed and optimized for glass [220]. However others materials [221] may be polished as well. MRP involves magnetorheological suspension, which viscosity can be switch from liquid to quasi-solid when subject to magnetic field [222]. Suspension consists of ferromagnetic particles (carbonyl iron, nickel, cobalt ...), which size varies from 10 down to 0,1 μm, of abrasives (silica carbide, aluminium oxide, cerium oxide ...) and of a lubricant (oil or water).

MRP process can be assimilated to the two body abrasion process (as grinding), as abrasives are fixed over carbon iron particles in a magnetic field region.

Thanks to the levitation of the iron particles, the polishing abrasives are pushed

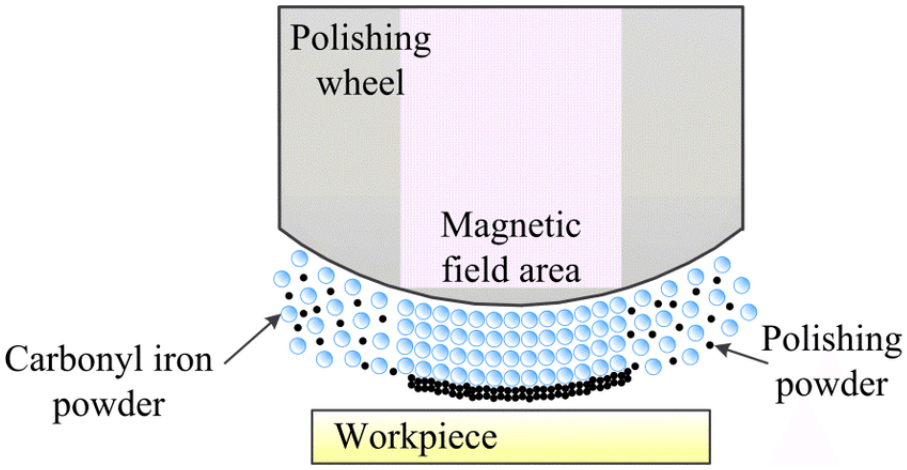

Figure 3.30: Magnetorheological polishing [223].

to the top of the slurries, applying a pressure force on the workpiece [223]. The magnetic field arranges the abrasives along the magnetic lines. Abrasives are put into motion by making the magnetic wheel rotate.

Depending on the wheel rotation speed (tangential force), material removal could be considered either as two body (grinding) or three body abrasion (lapping, polishing) processes [224]. Two body abrasion corresponds to the case when tangential force is higher than the resistance of the material. In this case the abrasives are fixed in the ferromagnetic particles. Otherwise, when tangential force is lower than resistance of the material, the bonding connection between carbon iron and abrasives particles lost, leading to the rotation of particles, which corresponds to three body abrasion.

Polishing efficiency of MRP is proportional to the value of the magnetic field (the penetration of abrasives in material defined by the value of the magnetic force) and composition of suspension [225].

As far as we know, Niobium has not been polished by this technique due the complexity of the process and low efficiency of the material removal (MRP may be used just for final step of polishing) [226].

Chapter 4

Experimental Tools for Mechanical Polishing and Characterization

4.1 Studied Polishing Devices

This chapter will first describe the machines used for the R&D studies on mechanical polishing (MP). Two experimental studies have been carried out during the PhD work:

- Metallographic polishing (MP) has been carefully investigated as this technique allows to reach efficiently very promising surface quality. This technique is not only offering an attractive alternative solution to the standard chemical polishing but is of first interest for all studies on alternative superconducting materials. Indeed, these alternative materials have to be applied as thin films on high quality substrates (other than sapphire) that are nowadays very difficult to obtain (Niobium).

- Centrifugal Barrel Polishing (CBP) has been studied as well to understand carefully limitations of the current state of the art of alternative polishing techniques. Moreover, this study was not only to reproduce the state of the art, but to investigate a slightly modified process which could allow the treatment of complex 3D geometries and not only 2D geometries with rotational symmetry like elliptical cavities.

The different consumables studied for each technique consisting in polishing disks and abrasives for metallographic polishing and media for CBP technique will be as

well described.

Secondly, the different tools used for the quality control of each step of the process and characterization of surface quality will be described.

4.1.1 Metallographic Polishing Machine

Mechanical polishing has been performed on a metallographic machine MasterLAM 1.0, see in Figure 4.1, manufactured by a French company LAM PLAN [227] which is based in Gaillard, France. This device is an automatic machine with a rotating and oscillating sample holder and a rotating polishing disk. The rotational speed of header changes from 20-150 RPM and speed of disk varies from 20 to 650 RPM.

This model has a very interesting feature compared to other devices on the market allowing to ensure an optimal homogeneity of surface quality when the treated surfaces are above several tens of centimeter square. This feature in the oscillation capability of the polishing arm. This slow oscillation with a typical period of 5 seconds helps spreading homogeneously the lubricating fluid as well as abrasives during lapping and polishing processes.

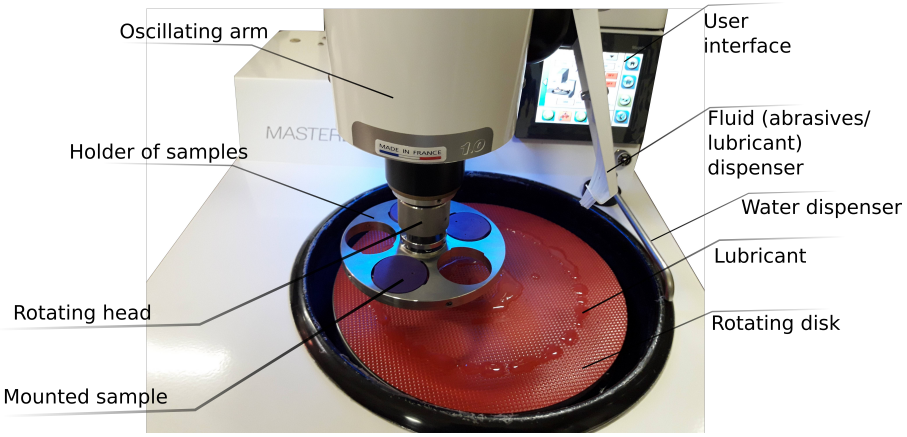

Figure 4.1: Photograph of a polishing machine MASTERLAM 1.0. Grinding disk CAMEO Platinum 4 (resin - 15 μm diamonds) is installed at rotating plate with distributed lubricant "Booster" on surface of the disk.

The sample holder is pressed against the abrasive disk to get a polishing action. Direction of rotation header/disk either can be complementary or contra. Complementary means that the header and disk are rotating in the same direction, contra in the opposite direction. Pressure is applied on the centrer of sample holder. Pressure can be controlled by an applied force, variable between 5-400 N, on the unit of

polished area.

As shown in Figure 4.2a, for easier handling purposes polishing plate consists from aluminium plate on which is placed an adhesive disk, which helps to easily remove the grinding or polishing disk. As a part of advanced preparation the samples are mounted on a sample support (3D printed plastic part) clumped by screws in the support holder, Figure 4.2b and Figure 4.3. It gives the possibility to exchange easily polished samples.

This model only allows to apply a uniform force on the sample holder ("central force") and not on each sample ("individual force"). As the sample holder is mounted in a ball joint, at least 3 samples have to be installed for the pressure to be uniform.

Moreover samples installed in the holder usually show positioning error of several hundreds of microns have a tilted face compared to the disk and show significant surface waviness (sample cut from laminated sheets). A grinding step of about 100 μm is required to start each polishing study in optimal conditions.

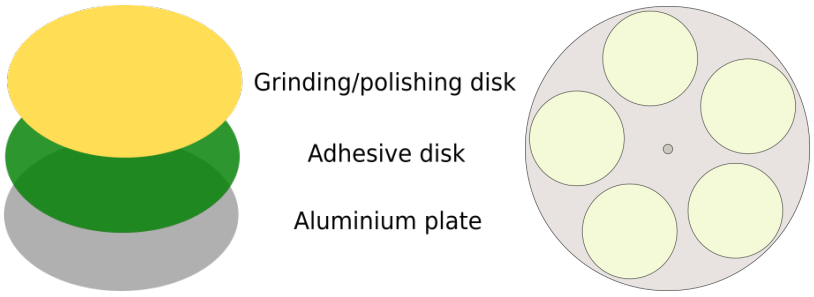

(a) (b)

Figure 4.2: Schematic structure of polishing disk(a) & 5-cell holder for specimens (b).

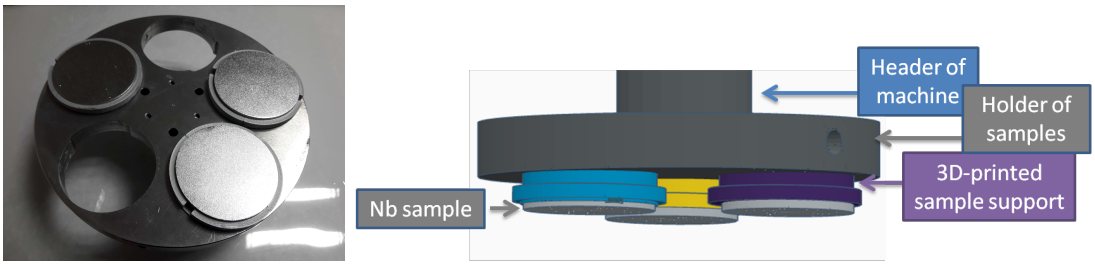

(a) (b)

Figure 4.3: Photograph (a) and schematic view (b) of the 5-cell holder with installed samples.

Table 4.1: Technical parameters of polishing device.

Parameters	Min value	Max value
Rotational speed of header, [RPM]	10	150
Rotational speed of disk, [RPM]	20	650
Applied central force, [N]	5	400

4.1.1.1 Grinding disks

The SiC or Al_2O_3 paper disk are the most used abrasives for grinding process. However sharp edges of abrasive grains have a tendency to loose the cutting efficiency from aggressive removal of material, especially in first tens of seconds, down to ploughing. The short lifetime of the paper is due to broken grains which caused by the blunt of abrasives and requires to change the grinding disk.

In order to increase the lifetime of disk and to keep efficiency of removal rate, diamonds embedded in a bond are recommended for long grinding steps. The diamond leaves the bond when the grain is worn, in order to keep the cutting efficiency of other diamonds burried a little deeper in the bond.

Company LAM PLAN produces grinding disks with honey-cell structure charged with diamonds in resin. Meshed structure, contrary to solid SiC paper or solid bond, reduces the contact area between sample and polishing disk and optimizes the uniform distribution of lubricant on the whole surface of the disk. Moreover, the presence of cavities plays the role of debris evacuation during abrasion step, see Fig. 4.4. A typical grinding disk of Cameo Platinum series, Platinum 2 is shown in Figure 4.5a. For example, Platinum 2 has fixed diamonds with grain size of 59 μm which corresponds to SiC paper P240. Table 4.2 presents all grinding disks used in this research. In the beginning of disk utilization, a layer protection (made from resin) has to be removed by grinding stone which supplier add to each disk.

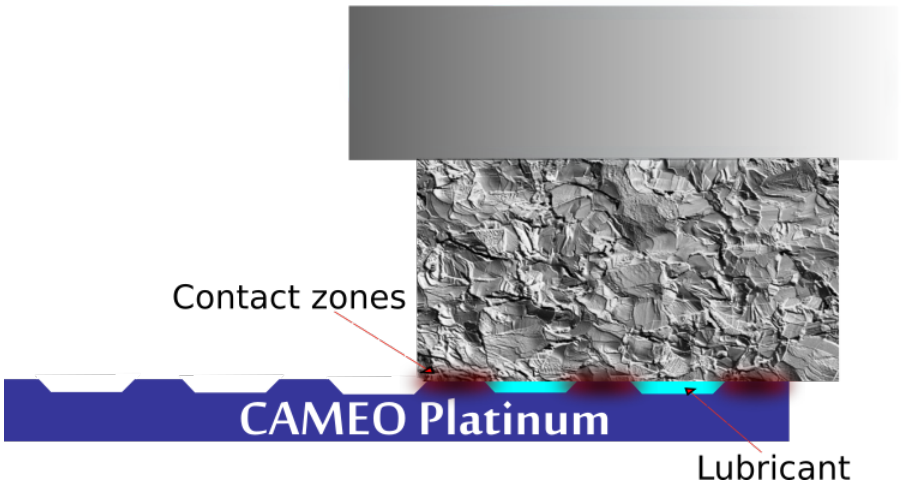

Figure 4.4: Schematic principle of grinding disks Cameo Platinum with meshed structure. Note: the red locations correspond to increased temperature and wear of contact area.

Table 4.2: Classification of the CAMEO grinding disks.

Grinding disk	Color code	Equivalent to paper SiC	Grit size, μm
Platinum 1	Blue	P120	125
Platinum 2	Green	P240	59
Platinum 3	Yellow	P600	26
Platinum 4	Red	P1200	15

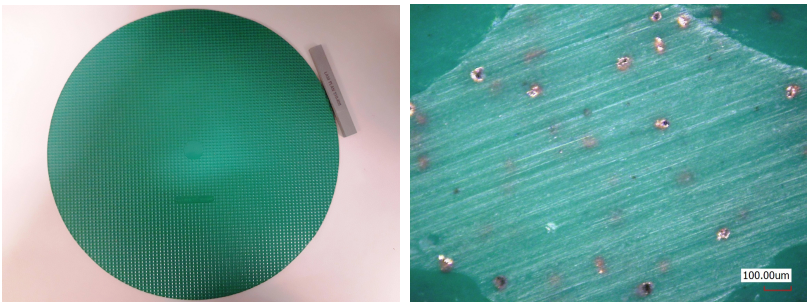

(a) (b)

Figure 4.5: Photograph of grinding disk Cameo Platinum 2: a) optical image, b) laser confocal image. Embedded diamonds with a grain size of 59 μm are visible.

4.1.1.2 Lapping disks

Lapping disk is a disk for processing of surface, which gives possibility to achieve perfect flatness of the workpieces with a uniform abrasion rate due to the continuous supply of abrasives on rigid disk. However for soft non-ferrous materials, as for Niobium, very rigid lapping disks (iron based disks) could create a huge deformation layer. In order to obtain a relatively little damaged layer, rigid composite disk (RCD) may be used for processing. RCD is based on mixture of resin with metallic powder (Fe, Cu...) [158]. RCD combines the benefits of lapping disks (constant and relatively high material removal rate, high reproducibility) and polishing disks (reduced damaged layer compare to grinding).

For these purposes, to avoid deformation of soft materials and to have a resonable Material Removal Rate (MRR) (μm/min). LAM PLAN company, developed special RCD with patented honey-meshed structure (described in Section 4.1.1.1). The worn abrasives and debris are eliminated in the cavities of RCD disks.

In Figure 4.6a is shown a hard RCD based on the mixture of resin and powder of stainless steel. For softer materials like Niobium, another solution is indicated which is based on softer powder of copper (See soft RCD on Figure 4.6b).

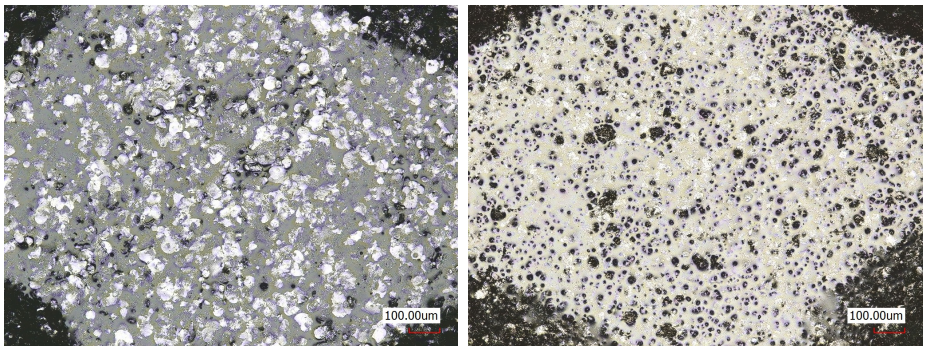

(a) (b)

Figure 4.6: Optical image of hard composite disk (a). Recommended to use with hard abrasives as diamonds from 6 to 15 μm. Optical image of soft composite disk (b). Recommended to use with hard abrasives as diamonds from 3 to 6 μm.

These lapping disks have to be charged with abrasives, as they just play the role of carriers. The best choice for RCDs are diamonds because of their hardness. For hard composite disk, LAM PLAN recommends to use diamonds with diameters between 6-15 μm (softer abrasives could also be used). For soft RCD, only diamonds (softer abrasives reduce the lifetime of disk), in the range 3-6 μm, are recommended.

LAM PLAN can provide a large variety of abrasives solutions (mixture of abrasive and lubricating fluid) composed of soft abrasives like cerium oxide, harder abrasives like silicon carbide and aluminium oxide up to the hardest abrasives: diamonds (See Table 3.4 in Chapter 2).

For our application, solutions of polycrystalline diamonds are preferred as said in previous chapter (See Chapter 2).

4.1.1.3 Polishing disks

Polishing disks from different materials have been tested. Actually it is possible to define many types of material used for disks preparation: non-woven, woven (synthetic, natural, satin, silk, wool), flocked and polyurethane. Polishing cloths have to be combined with polishing abrasives (diamonds, alumina, silica, cerium...).

Elasticity or compression defines the resilience of the disks, the disk may be a hard or soft [158]. Hard disk contrary to soft disk has a lower compression and provides a higher removal rate, however the surface is rougher. A softer disk has a lower abrasion rate, but the final roughness is better.

The choice of the best disk is done depending of the type of material, abrasives and the required balance between removal rate and final roughness (also important to control the number of polishing steps).

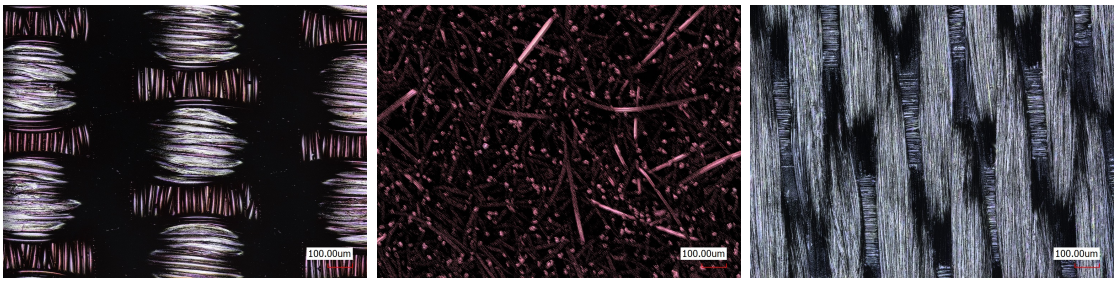

(a) (b) (c)

Figure 4.7: Optical images of tafetta woven syntetic fiber pad(a), flocked soft long viscose fiber pad(b) and satin woven natural fiber pad(c) sold by LAM PLAN company.

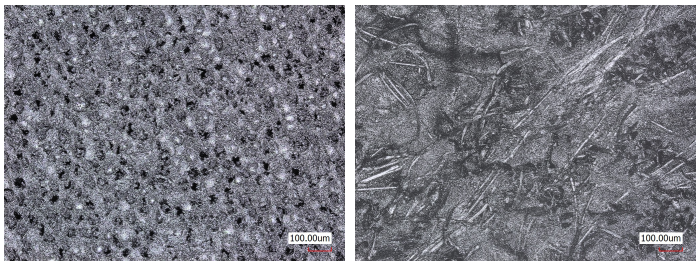

(a) (b)

Figure 4.8: Optical images of microporous polyurethane pad(a) and compressed polyurethane pad(b) sold by LAM PLAN company.

4.1.2 Centrifugal Barrel Polishing Machine

Mechanical polishing of superconducting cavities has been investigated for decades on such machines (See Chapter 2). So as to understand plainfully limitations of this technique, a CBP device has been rented for several months. Mechanical polishing was investigated on centrifugal barrel polishing (CBP) machine from ABC SwissTech company [228], see Figure 4.9.

Figure 4.9: Photograph of CBP machine with 4 barrels (ABC SwissTech production).

This device has 4 barrels distributed on a main shaft around its center of rotation. So as to keep balance, opposite barrels compared to rotating axis have to be loaded with the same weight. Barrels are filled with abrasive media (bonded abrasives), deionized water, surfactant and parts to be polished. These can be left free to move inside the barrel or fixed. So as to simulate the polishing efficiency of this technique for cavities (as said in Chapter 2, the cavity is the barrel itself), the sample was mounted on a holder to keep the sample at a several fixed positions (See Figure 4.10b). Deionized water is used for cooling during polishing process and

surfactant is added in order to reduce the tension between interface media/material and to prevent the hardening of the polishing slurry.

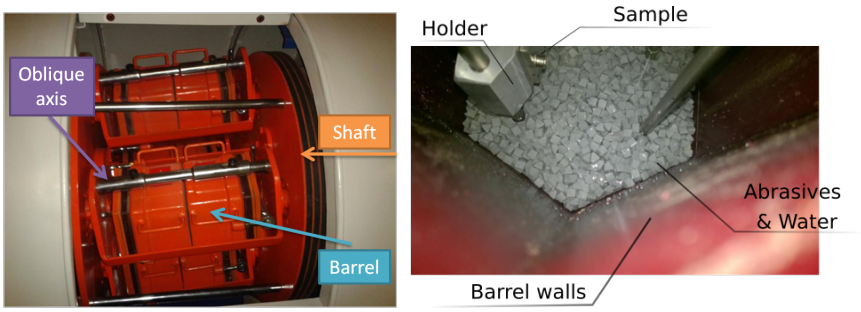

(a) (b)

Figure 4.10: Photographs of CBP machine: a) main elements, b) inside of barrel.

ABC Swisstech proposes several type of these machines. Besides various dimensions, they fabricate CBP machines in which barrels are tilted or not compared to the axis of rotation of the main shaft. All previous studies on superconducting cavities have been performed on non-tilted barrels as these were limited to elliptical cavities showing a symmetry of revolution. So as to investigate the possibility to process more complex 3D geometries like Spoke resonators or QWR (See Chapter 1), a tilted version has been rented. Indeed, the tilted barrels give abrasives a 3D motion known to provide a more homogeneous surface of 3D parts, see Figure 4.11.

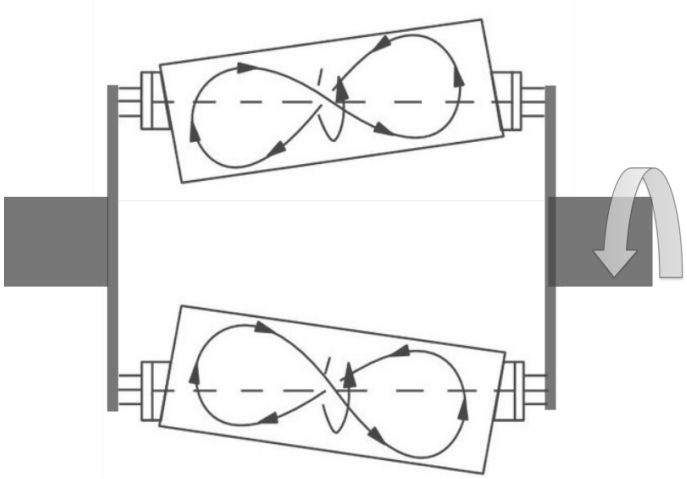

Figure 4.11: Abrasives motion (”8” pattern) in a CBP machine with oblique axis.

During polishing process the barrels are spinning around their own oblique axis in the same direction to a horizontal shaft. The rotation of shaft creates a centrifugal force (F_c), which presses the media onto walls of barrel and the tilted-barrel rotation ensure the tangential force to provide surface friction.

The value of centrifugal force depends on value of rotational speed of the shaft (v), load of the barrel and distance between the horizontal shaft and the barrel (R). As the distance between shaft and the barrel is fixed, rotational speed and weight of barrels (media, sample...) are the only variable parameters.

The type of abrasive media, time and rotation speed have to be optimized in order to achieve the best polishing recipe.

As for metallographic polishing, the barrels have to be emptied and cleaned and samples thoroughly cleaned in between each step to limit pollution of the polishing mixture from previous step (debris).

Different types of abrasive media can be loaded in the barrels during CBP polishing [229]. These media are available in different shapes (pyramid, cones, triangle...), sizes and compositions. However three main types of abrasives, based on bonding material composition exist: ceramic, plastic and organic. In the case of soft materials like Niobium, the media has to be chosen extremely carefully in order not to damage too deeply the surface that will be exposed to intense RF fields. During investigations of CBP at DESY, E. Tamachevich concluded that ceramic media creates a huge damaged layer for Nb [230]. Hence, plastic media has been chosen as the abrasives for the first polishing step.

(a) (b) (c)

Figure 4.12: Photographs of plastic media from ABC SwissTech production: a) pyramides TET-TKS, b) pyramides TET-TKP and c) cones TKV.

Plastic media consists of combinations of polymer and abrasives as SiC, Al_2O_3 or silica, in different proportions. As mentioned in Chapter 2, the fact that abrasives are agglomerated as media provides a more intense normal force (centrifugal force in proportional to weight) and the embedded abrasives in polymer play role of the cutting tools.

Final polishing steps have been performed with organic media, which are composed of natural hardwood material. This media has to be used in combination with

Table 4.3: Used media for CBP experiments.

Type of the abrasives	Size or Mesh size	Grain size of the cutters	Hardness
Pyramids TET-TKS	12 mm	Not defined	Not defined
Pyramids TET-TKP	12 mm	Not defined	Not defined
Cones TKV	12 mm	Not defined	Not defined
Hardwoods + powder SiC	12 mm + #400	16.5 ± 1 μm	2700 HV
Hardwoods + powder Al_2O_3	12 mm + #800	6.3 ± 1 μm	2500 HV
Hardwoods + powder Al_2O_3	12 mm + #3000	0.38 ± 0.1 μm	2500 HV
Hardwoods + powder SiC	12 mm + #6000	0.06 ± 0.01 μm	2700 HV

(a) (b) (c)

Figure 4.13: Photographs of organic media and abrasive powders from ABC SwissTech production: a) hardwood blocks, b) powder Al_2O_3 and c) powder SiC.

abrasive powders, which varies from #400 to #6000 in mesh size (higher number corresponds to smaller size of the abrasives).

4.2 Tools for Process and Quality Controls

This section describes the techniques used to characterize the surface after mechanical treatment: laser confocal microscope (mainly for roughness measurement, in particular material removal rate characterization and preliminary pollution study), secondary ion mass spectrometry (chemical composition and depth profiling), X-Ray diffraction in the conventional and grazing modes (strain measurements at different depths), electron backscattered diffraction (dislocation density measurement), micrometer and weight meter (material removal rate studies). A careful characterization of the material, after each step of treatment (grinding, lapping, polishing), is of paramount importance in order to achieve the best quality of the treated material in the minimum number of steps. After each polishing step, each sample was investigated by average measurement of thickness, weight, roughness and pollution. During MP procedure temperature measurement and level of lubricant/polishing suspension was systematically performed.

4.2.1 Temperature Control

The increase of temperature during the grinding, lapping and polishing processes leads to additional stresses, strains, inclusions, pull-outs within the material and specifically for Niobium and superconducting properties, leads to a higher contamination and diffusion of hydrogen into the surface of the sample [231].

Control of temperature is an essential key to avoid overheating and right dossing of lubricant. Infrared thermometer FLIR TG165 [232] has been used to measure the changes of temperature during polishing procedure. FLIR is a spot thermal camera, which can differentiate cold and hot regions by detection of infrared light emitted by elements.

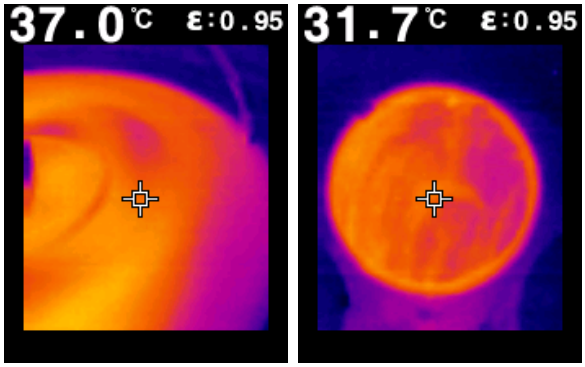

(a) (b)

Figure 4.14: Infrared images of disk/cloth (a) and sample (b) under normal conditions.

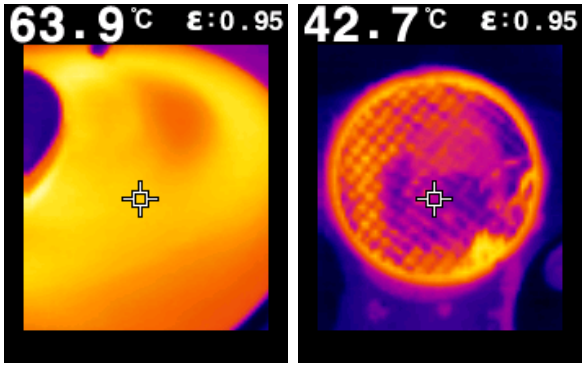

(a) (b)

Figure 4.15: Infrared images of disk/cloth (a) and sample (b) under non-normal conditions. Note: overheating.

However, during grinding/lapping/polishing steps, the amount of lubricant should be continuously monitored and rightly dosed to avoid overheating (lack of lubricant) or aquaplaning (overdosed lubricant). Aquaplaning is a situation where the sample is floating (hydraulic pressure) on lubricant preventing abrasives from being in contact with both disk and sample.

Figure 4.14a and Figure 4.14b show the infrared images during abrasion under normal conditions, such as a level of lubricant is proper (not too dry, not too wet) and level of debris (mixture created by used abrasives and removed material) is

limited. Under others conditions, overheating is possible as shown respectively in Figure 4.15a and in Figure 4.15b.

In particular, during long runs, debris can accumulate significantly and induce overheating. It is recommended in these case to interrupt the supply of solution while keeping rotation of disk and sample holder and to flush out abrasives and debris with water. This will help decontaminating the surface and cool down parts.

4.2.2 Abrasion Rate Control

The abrasion rate or material removal rate MRR characterizes the thickness of removed layer (μm) per minute and it actually determines the duration of treatment processes. This parameter is an important polishing parameters (as roughness and deformation) which aims actually at predicting the costs of processing (in general abrasion rate has to be as high as possible, but higher rate leaves bigger deformation and rougher surface).

The abrasion rate depends on preparation step/method (grinding, lapping or polishing) and varies from abrasives used, lubricant and parameters of machine (applied pressure, rotation speed, counter-rotation...). Mathematically abrasion can be described by Archad's model for grinding (abrasive wear) and by Preston's model (abrasive lose) for lapping/polishing.

Archad's model considers that grinding by fixed abrasives can be modelled by a knife sliding on/cutting the surface. The removed volume is expressed by following equation:

$$V = \frac{kFL}{H} \tag{4.1}$$

where k is the removal rate constant, L is the sliding distance, F is the normal force, H is the hardness of sample, V is the removed volume.

Preston's model, as it was mentioned above, describes the lapping and polishing processes due to loose abrasives rolling on the surface in the follow way:

$$\frac{dz}{dt} = kPV \tag{4.2}$$

where dz/dt is the abrasion rate, k is the removal rate constant, p is the applied pressure on the interface between sample and disk, V is the removed volume.

Both models give the theoretical prediction of the abrasion rate, however these tend to overestimate the real abrasion rate as the wear of abrasives (roundening of cutting edges, loss of abrasives) is not taken into account. Abrasion rate has to be experimentally characterized several times during each process as this is decreasing drastically with time depending on the type and quality of abrasives, grinding and polishing cloths, ...

In this study, several methods were used to characterize the abrasion rate:

1. Weight difference of the sample before and after a process

2. Thickness difference of the sample before and after a process

3. Depth difference of a grove/scratch before and after a process.

4.2.2.1 Weight Measurement

The weight of the sample has been measured before and after each processing step. In order to determine the weight loss, a precision scale has been used (accuracy of measurement is 1 mg).

In order to reduce the measurement error, the averaged value over 5 measurements is calculated. The thickness of the removed layer can be estimated in the following way:

$$dx = \frac{m_b - m_a}{\rho_{Nb} S} \tag{4.3}$$

where m_b and m_a are the weights before and after processing respectively, ρ_{Nb} is the density of Niobium, which is equal to 8570 kg/m^3 and S is actual processed surface area.

The advantages of this method are its simplicity, the absence of contact with polished face and is an averaged estimation of the removed layer all over the sample. This technique is insensitive to potential non uniform removed layer caused by problems of sample alignment or sample flatness. However, so as to limit errors, the samples have to be removed from support holder and properly cleaned in order to remove the contamination stuck on the sample.

4.2.2.2 Direct Thickness Measurement (Micrometer)

Micrometer is a common tool to control directly and precisely (accuracy $\sim$ 1 micron) the thickness of a piece and is thus very convenient to estimate removal rate. However due to the contact with the polished surface, this measurement can be performed only after roughness measurement. Micrometer leaves series of scratches on the contact area.

This method allows, if the sample holder has been nicely designed, to perform a very quick, local and precise thickness estimation during the process without the hassle of disassembling the sample from its holder. Moreover, by sampling all over the sample area, problems of sample flatness or alignment can be detected. To reduce uncertainties, at the end of the process, an averaged thickness is estimated from 10 measurements all over the sample, see Figure 4.16.

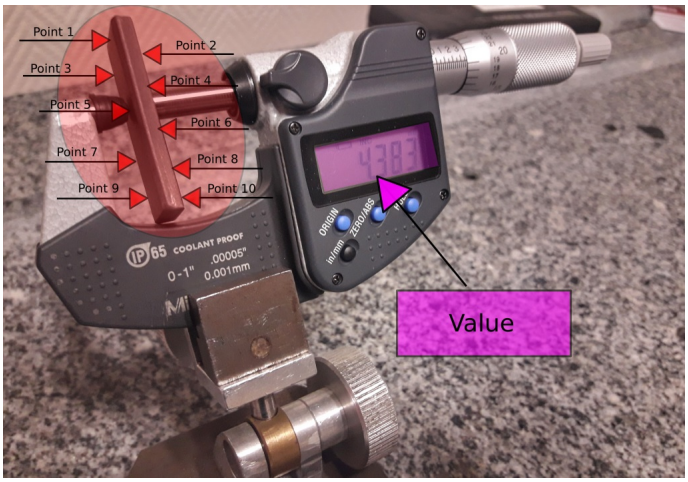

Figure 4.16: Micrometer for the thickness measurement with the accuracy 0.001 mm.

4.2.2.3 Depth Measurement of Surface Defect with Microscope

In order to increase the precision of the thickness of the removed layer (nanometre scale), an another approach has been used. The samples were stamped and the initial depth of groove/scratch is measured by laser confocal microscope. The principle of the laser confocal microscope will be described in the next Section 4.2.3. After processing the scanning procedure is repeated. The advantage of this method is its precision (hundreds of nanometers) and allow a very local estimation. As the micrometer, problems of sample flatness or alignment can be detected. However this technique is more time consuming and requires to damage the polishing face. Figure 4.17a shows the initial state of the surface and Figure 4.17b presents the final state of the processed surface.

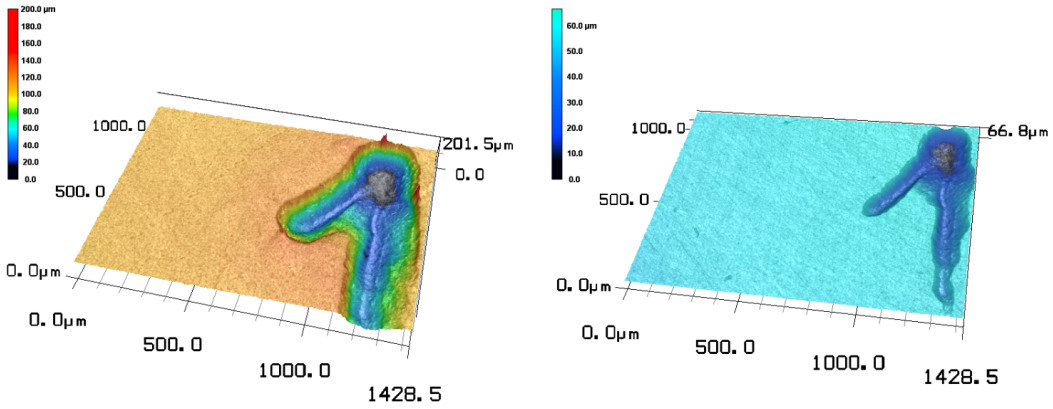

(a) unpolished surface (b) polished surface

Figure 4.17: 3D-profile of "mark" have been taken with laser confocal microscope.

Table 4.4: Summarizing advantages and figure of merit of each technique. Note: color code represents the advantages (green), drawbacks (pink) and neutrals (orange) properties for each used technique.

Technique	Tool	Type of Measurement	Sensitivity to flatness/misalignment	Investment	Compatibility with Process	Error (relative/absolute)
Weight	weighing machine	average over whole sample	No	minor	no damage	relative 20%
Thickness	micrometer	average over several mm^2	Yes if sample large enough	minor	minor damages (scratch)	absolute 5 microns
Depth	confocal microscope	local	Yes	expensive	major damage (groove/scratch	absolute 100 nm

4.2.3 Surface Optical Control with Laser Scanning Confocal Microscope

The first principle of the confocal microscope has been introduced by Marvin Minsky in 1957 [233] and the invention of the first laser was in 1960 [234]. Finally after several decades Wilson presented the first confocal microscope based on laser emission in 1990 [235].

Laser light is reflected by the dichroic mirror into the objective (Figure 4.18). The reflected light from analysed sample is transmitted through the dichroic mirror into the detector.

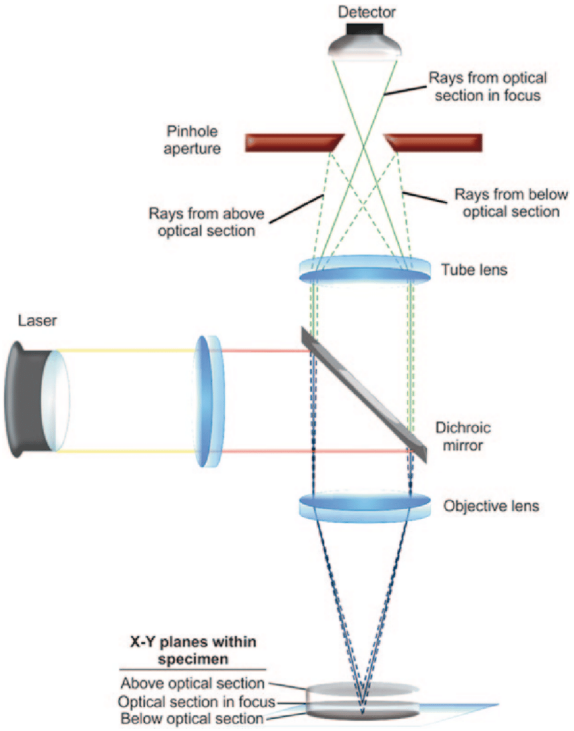

Figure 4.18: Principle of the laser confocal microscope [236]

While an optical microscope produces a blurred image of the sample (a sample is never perfectly flat), a confocal microscope has the ability to reconstruct a sharp one. It is achieved thanks to the insertion of a pinhole between the mirror and the detector on the focal plane of the tube lens. As a result, only light coming from the focal image plane of the objective can pass through the pinhole. Light coming from points out of the focal plane is stopped. So as to reconstruct the full image, the objective focal plane is moved vertically. The exact position of each point (X,Y,Z) is then known.

The laser scanning microscope, shown in Figure 4.19 is a useful measurement

technique in which the sample is scanned point by point, layer by layer. The surface is reconstructed in 3D (optical profilometer) with a lateral resolution better than 150 nm and a vertical resolution better than 5 nm allowing the measurement of 2D (roughness parameters, profile) and 3D (roughness parameters) surface properties without any contact (no damages are generated on the surface as a conventional mechanical profilometer).

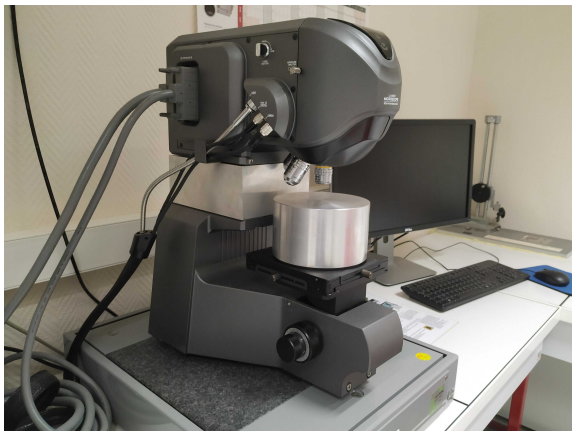

Figure 4.19: Photograph of IPNO laser confocal microscope.

The quality of polished surface have been measured by the confocal microscope VK-X 200 SERIES distributed by Keyence. The microscope can provide 5 types of surface images thanks to the 2 integrated light sources (white light and 408-nm violet laser light) and 2 light detectors (CCD camera and Photomultiplier Tube):

1. Optical image (source: white light, detector: CCD) gives color informations allowing material and phase identification.

2. Laser image (source: laser, detector PMT) gives a highly resolved image in light intensity (black & white).

3. The combination of the two images allow to obtain a highly resolved colored image.

4. The "height" image provides information on the topology of the surface by attributing to each point of the image a fake color related to its vertical position.

5. The DIC image (Digital Interference Contrast) is a method to enhance significantly the contrast of the image topology (sharp edges, steps,...). This feature has been used extensively so as to detect sub-grain damages in the BCP study presented in Section 4.2.5.1.

For example, the height difference information is presented in Figure 4.20.

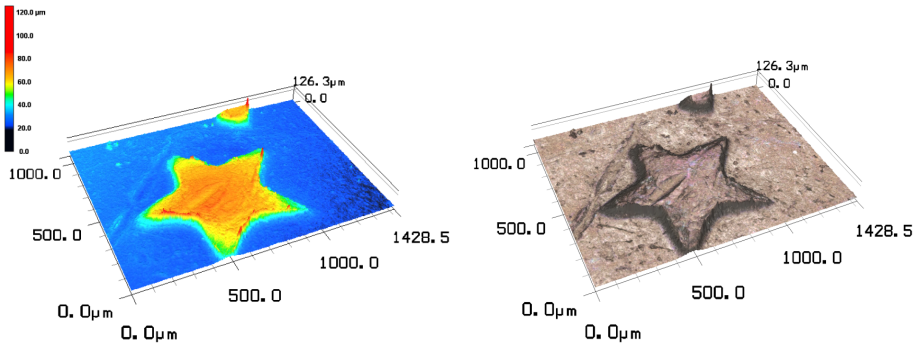

(a) (b)

Figure 4.20: Example of the height (a) and the texture (b) image taken by laser confocal microscope of 5 euro cents.

Surface roughness parameters can be evaluated thanks to an associated software(VK analyser). This software can output either the 2D roughness, or the 3D roughness. All parameters were defined in Chapter 2.

4.2.4 Surface and Sub-surface Pollution Analysis with SIMS (Secondary Ion Mass Spectroscopy)

During any surface treatments, the surface may be polluted by the embedded impurities on the surface or the near-surface. Moreover, during chemical treatments or cleaning, foreign elements could diffuse into the near-surface or alter the protective oxide layer. Secondary ion mass spectrometry is a powerful and destructive technique used for characterization of the surface elemental composition at a nanometer scale [237].

A primary ion beam with a typical energy between 1 and 20 keV is focused on the sample, see Figure 4.21. Surface atoms are sputtered and a small portion of them are ionized, accelerated and then analyzed thanks to a mass spectrometer. Because the sputtering yield and ionization are very different for all elements, the evaluation of elements concentration (quantitative measurement) is very complicated and would require the use of expensive calibrated samples. However, qualitative or relative measurements (comparison with a reference sample) are straightforward. SIMS analysis is a very sensitive technique (concentrations of few ppb can be detected). Depending on the type of primary ion beam, electro-positive (Argon, Oxygen) or

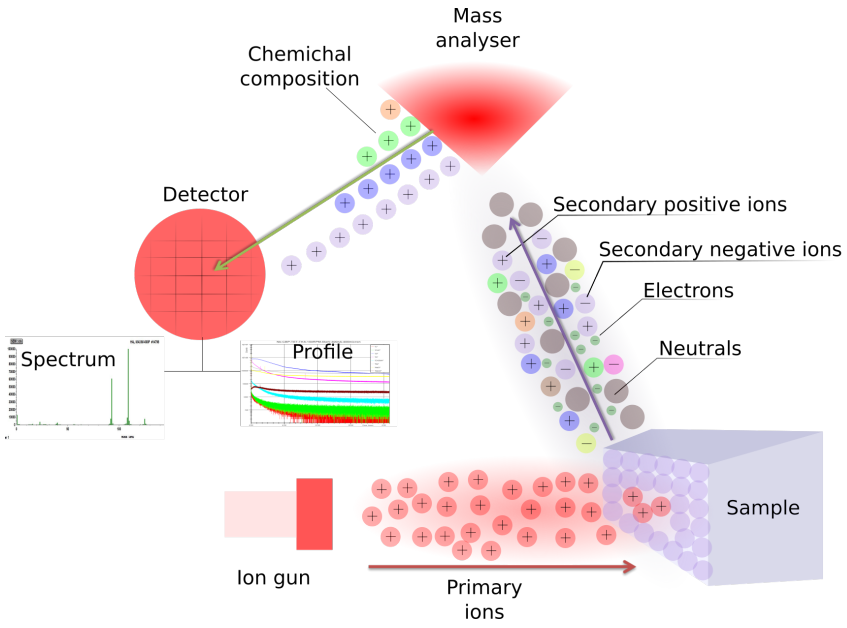

Figure 4.21: Principle of SIMS.

electronegative (Cesium) species or compounds are detected. Depending on the intensity of the primary beam, the analysis can be static or dynamic. Static analysis (very low current) consists in analyzing the surface elemental composition of the sample by plotting the mass spectrum. Dynamic analysis (high current) takes advantage of the sputtering process and consist of measuring the evolution of some elements as a function of depth (depth profiling).

The etching rate can be tuned by adjusting several parameters like beam current and scanned surface area and strongly depends on the type of predominant element (matrix material). The following formula gives a rough estimation of the etching rate (V_{sp}):

$$V_{sp} = \frac{1}{10^{-9}} \cdot \frac{Y \cdot I \cdot m_a}{e \cdot S \cdot \rho} = \frac{1}{10^{-9}} \cdot \frac{Y \cdot I \cdot V_m}{e \cdot S \cdot N_A}, \tag{4.4}$$

where Y is the sputtering yield [238] (strongly dependent of the sputtered element, energy and type of primary beam), I is the current of the incident beam, e is the charge of electron, S is the sputtered surface, m_a is the atomic mass of the sputtered element, ρ is the density of material, V_m is the molar volume of a given material and N_A is the number of Avogadro.

At IPNO, the compact SIMS workstation has been used supplied by Hiden Analytical [239], see Figure 4.22. Ar and O beams have been used at energies range from 1 to 5 keV to sputter Nb (for example at I=30 nA and S=400 μm^2 the etching

rate is ranging from 0.6 up to 2.5 nm/min for Ar gas). The current on the filament was controlled between 30 nA up to 300 nA (for example at 5 keV and S=400 μm^2 the sputtering speed changes from 0.6 nm/min to 25 nm/min for Ar).

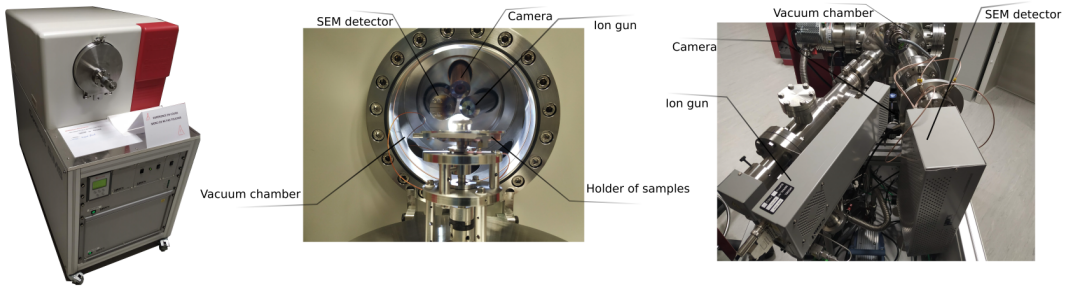

Figure 4.22: Photographs of the compact SIMS workstation (left), the analysis chamber (center) and ion source and detector (right).

4.2.5 Damaged Layer Characterization

In order to characterize the damaged layer created by mechanical preparation procedures, investigations of the polished samples have been done with three methods: multi-step BCP etching followed by optical analysis, grazing angle X-rays diffraction and electron backscattered diffraction (EBSD) on SEM microscope.

4.2.5.1 Multi-step BCP Etching

Buffered chemical polishing could reveal the damages on a processed surface. Indeed, this chemical treatment isn't actually polishing but etching. The etching rate is strongly affected by the crystalline structure (cristal orientation, dislocation density, ...). As a result, BCP etching is revealing any crystallographic defects as these tend to be more resistant. In order to estimate the depth of the damaged layer and investigate the residual stresses after mechanical preparation (rolling, lapping, grinding, polishing), the processed surface has been observed by optical imaging after multiple BCP etching of 5 μm. The image contrast is enhanced by in digital interference contrast (DIC) mode by the laser confocal microscope. DIC mode gives detailed information about the morphology of the analyzed surface. As shown in Figure 4.1.9, surface damages (scratches, ...) due to rolling are clearly identified. After 10 micron BCP removal, the surface scratches disappeared but the crystalline damages caused by the stress of the process are still visible. It is only after 150 micron removal that sub-grain patterns disappeared to leave the place to a nice polycrystalline structure known as damage-free.

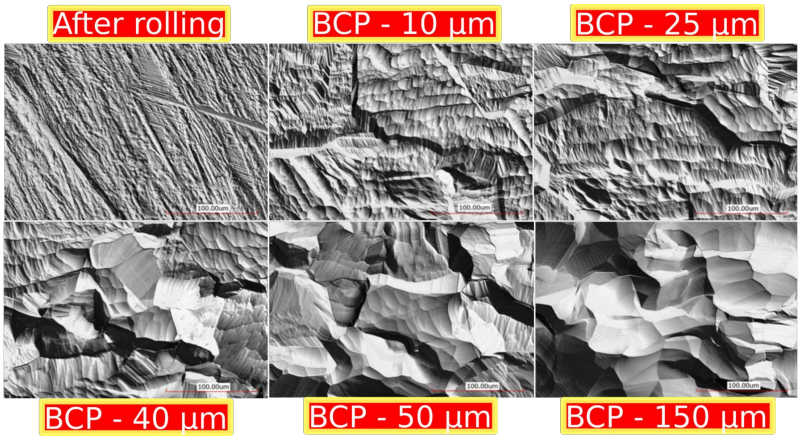

Figure 4.23: Etching figures of Nb surface after rolling.

4.2.5.2 X-Ray Diffraction

Crystal Microstructure

Crystal can be presented in the 3-D symmetry as the repetitive unit of volume (cell). As can be seen in Figure 4.24, the unit cell represents a parallelepiped with the X, Y and Z-axes and lengths respectively a, b, c, and angles between the cell edges (α, β and γ). There are 14 different lattice types (Bravais lattices), which grouped in seven lattice families: triclinic, monoclinic, tetragonal, orthorhombic, trigonal, hexagonal and cubic.

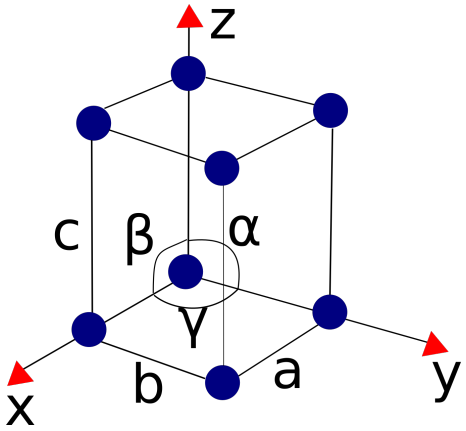

Figure 4.24: Unit cell of a crystal.

In particular, cubic lattice may be divided into primitive cubic, body-centered cubic and face-centered, see Figure 4.25. The crystalline material studied in this thesis (Nb) has a body-centered cubic lattice ($a = b = c$ and $\alpha = \beta = \gamma = 90°$).

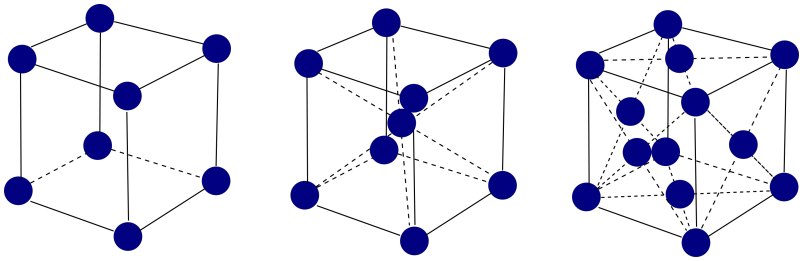

Figure 4.25: The types of cubic family (from left to right): primitive cubic, body-centered cubic and face-centered cubic.

In order to describe certain planes in the crystallographic material, the Miller indices are used. Crystallographic planes are defined by the values h, k and l, which correspond respectively to crossing with X, Y and Z-axes, see Figure 4.26. When

the Miller index is zero it means that the plane is parallel to the corresponding axis (the axis is intercepted by plane at infinity).

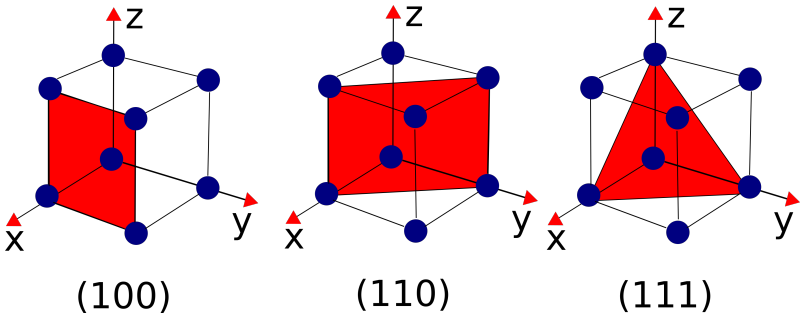

Figure 4.26: Examples of the crystal planes in the cubic lattice for different directions (from left to right): (100), (110) and (111).

The crystal planes may be defined by the following expressions:

- (hkl): indicates the crystal plane,
- $\{hkl\}$: indicates the set of symmetry equivalent planes to (hkl).

X-Ray Diffraction (XRD)

In 1912 Max von Laue discovered that X-Rays due to their electromagnetic nature can be diffracted by crystalline materials. The condition at which X-Ray diffraction (XRD) occurs has been defined by Bragg.

During diffraction, see Figure 4.27, X-rays are elastically scattered by the atoms of the crystal, which consists of periodic crystal planes, thereby creating secondary waves scattered by each plane. The scattered waves from the crystal planes can have constructive or destructive interference. A constructive interference satisfies the Bragg law, which is given by the following condition:

$$2 \cdot d_{hkl} \cdot sin\theta = n \cdot \lambda, \tag{4.5}$$

where d_{hkl} is the distance between crystal planes, λ is the wavelength of X-Rays and 2θ is the angle of the diffraction.

The distance between the crystal planes can be expressed also by using the Miller indices and the length of cell. In the case of the cubic lattice, the distance is defined

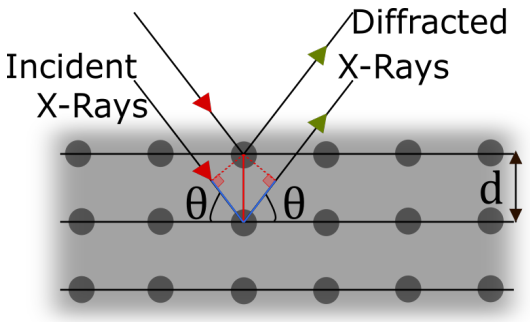

Figure 4.27: Principle of X-ray diffraction. In specific conditions (Bragg conditions), the diffracted X-rays have a constructive interference.

by the following expression:

$$d_{hkl} = \frac{a}{h^2 + k^2 + l^2}, \tag{4.6}$$

where a is the lattice parameter, which for niobium in unstrained state is equal to $a = 3.033$ [$\mathring{A}$]. For example, Miller indices, Bragg's angle, distance between planes and intensity of Niobium diffracted peaks are shown in Table 4.5.

Table 4.5: Miller Indices (hkl), distance between planes (d), Bragg's angle (2θ), and intensity of diffracted peaks for Niobium.

Miller Indices	d, [$\mathring{A}$]	Angle 2θ	Intensity, %
110	2.336	38.492	100
200	1.652	55.567	18
211	1.348	69.647	28
220	1.168	82.502	8
310	1.045	94.974	11
222	0.954	107.715	3
321	0.883	121.39	13
400	0.826	137.633	2

A monochromatic spectrum of X-rays is diffracted on the surface when a family of planes is favorably oriented according to Bragg's law. This diffractogram plots the diffracted X-ray intensity versus the angle 2θ. The diffractogram may be disturbed

by background noise (I_{noise}) originating from the X-ray fluorescence emitted by the sample, by the incoherent diffusion or by the diffusion of the optical systems, the supports of the sample, the air, etc.). The real height of the intensity peak (I_{real}) is then based on the difference between I_{max} and I_{noise}, for the 2θ position, which is corresponding to I_{max}, see Figure 4.28.

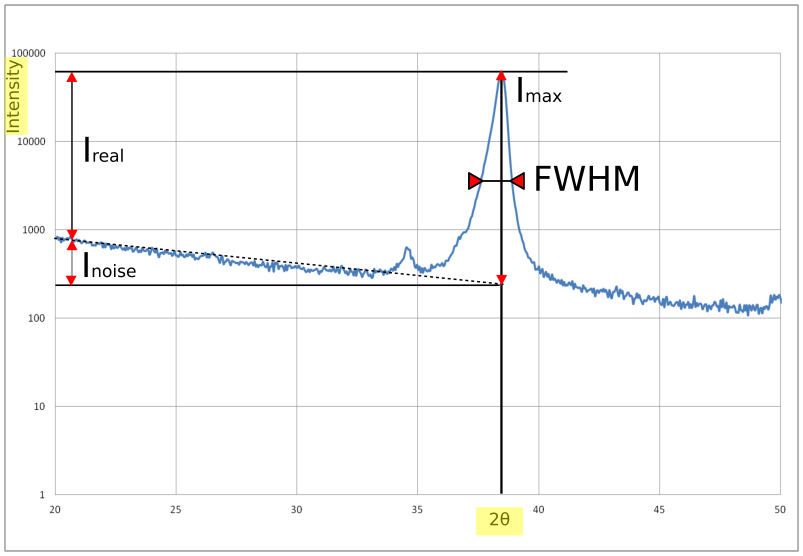

Figure 4.28: Representation of the diffracted intensity as a function of the angle position 2θ. Note: diffraction pattern measured for Nb 110.

Not only the amplitude but also the position, and width (FWHM = Full Width Half Maximum) contain microstructural information. Thus a change in distance between planes, due to strain or an inclusion, will be reflected by a change in the peak position and its width. The lattice size (a) of the crystal may be correlated with FWHM by the Scherrer equation:

$$a = \frac{K \cdot \lambda}{FWHM \cdot cos\theta}, \tag{4.7}$$

K is the Scherrer constant (in cubic lattice K varies from 0.83 to 0.91).

Strain Measurement by XRD

The measurement of strain by X-Ray diffraction is based on the variation of the interplanar distance between crystalline planes. When a material is strained, either elongated or compressed, this distance respectively increases or decreases compare to stress-free material. The normal strain to the surface can be measured with the following empirical formula:

$$\epsilon_z = \frac{d_n - d_0}{d_0}, \tag{4.8}$$

where ϵ_z is the strain in the normal direction (z), d_n is the distance between planes of the strained material and d_0 is the distance between planes of the unstrained material.

The strain of the planes at an angle ψ can be calculated using the following expression:

$$\epsilon_\psi = \frac{d_{\phi\psi} - d_0}{d_0} \tag{4.9}$$

Diffracted peaks either can be broadened due to plastic deformation or shifted due to elastic deformation. The broadening of peaks might be caused by inhomogeneous distribution of strain (inclusion,...). The shift of peaks corresponds to an homogeneously distributed strain in the material. If the distance d_{hkl} decreases then the material is compressed and increased if stretched, see Figure 4.29.

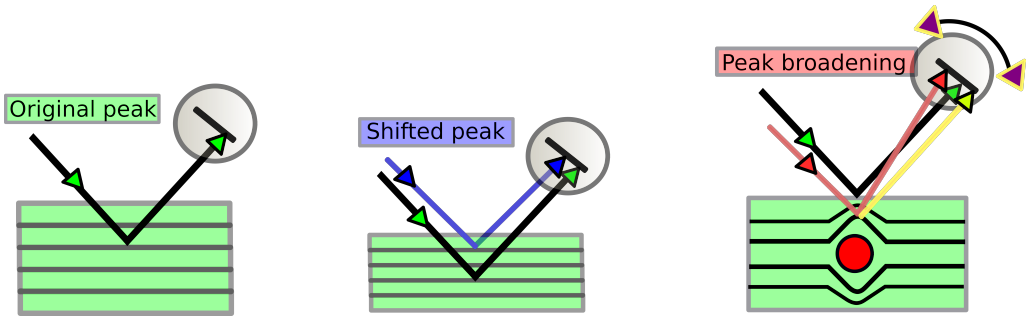

Figure 4.29: Sketch of the crystalline planes of the crystalline material (from left to right): non-strained crystal, homogeneously strained crystal (compressed) and non-homogeneously strained crystal (inclusion).

In the case of an elastic deformation, when strain is isotropic and homogeneous, the strain at the angle $\phi\psi$ can be calculated using:

$$\epsilon_{\phi\psi} = \frac{1+\nu}{E}(\sigma_1 \cdot cos^2\phi + \sigma_2 \cdot sin^2\phi) \cdot sin^2\psi - \frac{\nu}{E}(\sigma_1 + \sigma_2), \tag{4.10}$$

where parameters ν is the Poisson's coefficient, E is the Young's coefficient, σ_1 (σ_x) and σ_2 (σ_y) are planar stresses in the X and Y direction. All parameters were defined in Section 3.1.2.2 and some of these parameters were given for Nb in Section 3.1.2.3.

Stress Measurement by XRD

As was mentioned in Section 3.1.2.2, the stress can be evaluated through the Young's modulus and strain of the material.

To calculate the stress in any chosen direction, see Figure 4.30, in the case of an elastic, isotropic and homogeneously distributed deformation, we can assume that the stress in the XY-plane is non-zero and the normal stress is equal to zero (as for strain). Thus, the residual stress can be calculated using the interplanar distances obtained from measurements made in the normal plane and plane defined by its normal vector (n) at specific angle $\phi\psi$:

$$\sigma_\phi = \frac{E}{(1+\nu)\cdot sin^2\psi}\frac{d_{\phi\psi}-d_n}{d_n}, \tag{4.11}$$

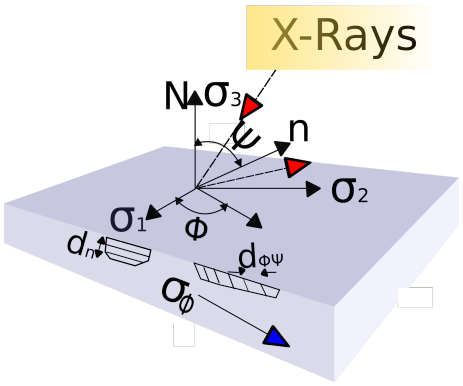

Figure 4.30: Sketch of the angles used to calculate the surface strain and stress of planes parallel to the surface and at angle $\phi\psi$. Note: σ_1, σ_2, σ_3 correspond to σ_x, σ_y, σ_z respectively.

The traditional method for stress evaluation is called the $sin^2\psi$ ("ψ") method [123]. In this method, the interplanar distances for the same plane are measured versus different ψ-tilts and plotted. The stress may be calculated using the gradient (m) of the plotted curve. Hence, Equation (4.11) can be written:

$$\sigma = \left(\frac{E}{1+\nu}\right)\cdot m \tag{4.12}$$

To measure the residual stress by the $\sin^2\psi$ method, the samples can be rotated by two different techniques:

- the Omega method,

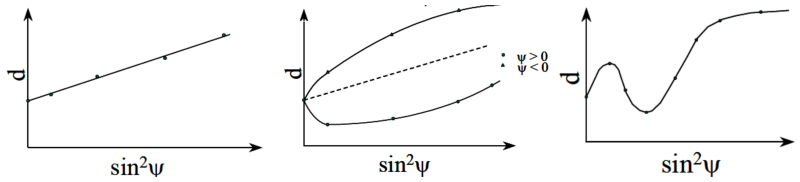

Figure 4.31: The evolution of the inter-planar distances versus $sin^2\psi$. Left image shows that stress/strain is homogeneous due to elastic deformation. Center image shows that the state of stress is triaxial, which is the case of rectification, the shear brings a more particular form of the curves and splitting at different angles. Right image shows that stress/strain is inhomogeneous due to the preferred orientations.

- the Chi method.

Figure 4.32 shows diffraction geometry used in residual stress analysis.

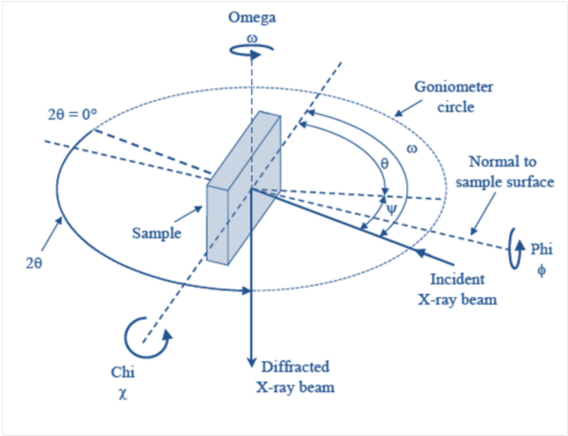

Figure 4.32: Sketch shows the diffraction geometry used for residual stress measurement [240].

In the Omega method, samples are rotated about the omega axis, which is in the same plane with the 2θ-axis. In the Chi method, the samples are rotated in normal direction towards incident X-Rays, see Figure 4.33.

In this PhD work, we have used both the Omega (at Phi=0°) and Chi methods to evaluate the stress in the material by varying Psi angle (either in positive or negative directions). The most precise measurements have been obtained by Omega method in positive range due to lower defocussing effects. The Omega method (with negative angles) and offsets for Chi method exhibit lower intensities of the diffracted peaks.

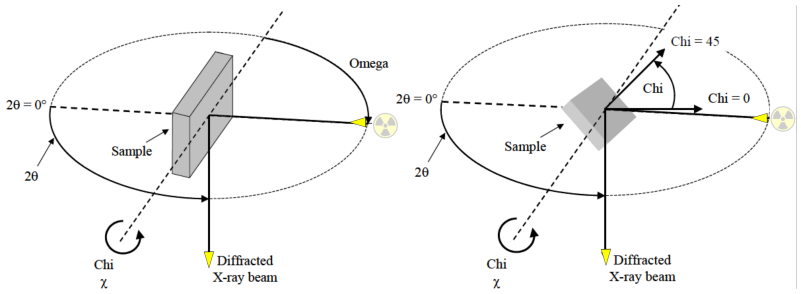

Figure 4.33: Rotation of the sample towards incident X-rays during the Omega (left) and the Chi (right) methods for residual stress measurement [240].

Penetration depth of X-Rays

Residual stress could be measured by X-Rays at different depths. Penetration depth of X-Rays (z) into the metallic material depends on the physical properties of material, incidence angle (ω) and the Bragg angle (θ). To estimate the penetration depth the following expression is used:

$$z = -ln\frac{I}{I_0} \cdot \frac{1}{\mu(\frac{1}{sin\omega} + \frac{1}{sin(2\theta-\omega)})}, \tag{4.13}$$

where $\frac{I}{I_0}$ is the attenuation of the intensity, μ is the material property.

In the symmetric case, when the incidence angle is equal to Bragg angle, Equation (4.13) could be simplified by the following expression:

$$z = -\frac{sin\theta}{2\mu} ln\frac{I}{I_0} \tag{4.14}$$

Figure 4.34 shows the penetration depths versus incidence angle at different Bragg angles for Nb material (μ=1187.3 $\frac{1}{cm}$). Note: attenuation is equal to 90% ($I/I_0 = 0.1$).

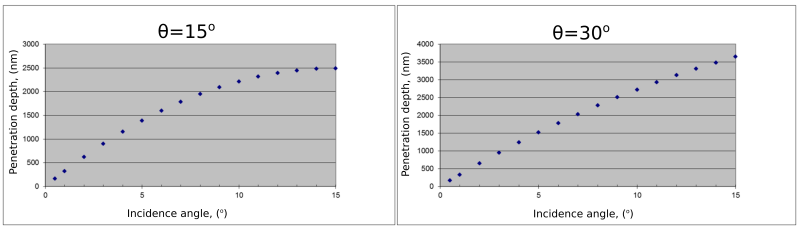

Figure 4.34: Penetration depths of X-Rays versus incidence angle at different Bragg angle for Nb material.

Diffractometer

Figure 4.35 shows the X'Pert PRO diffractometer from PANalytical, which uses a Cu X-Ray tube operated at 45 kV and 40 mA. Copper tube produces bremsstrahlung emission and X-rays at three different wave-lengths: 1.5406 Å ($K_{\alpha 1}$ emission), 1.5440 Å ($K_{\alpha 2}$ emission) and 1.39 Å (K_{β} emission). In order to have the monochromatic beam and to remove $K_{\alpha 2}$, K_{β} and bremsstrahlung radiations, graphite monochromator behind tube has been used. Hence, finally only the $K_{\alpha 1}$ emission is used for the diffraction measurements. In order to control the divergence of the beam, the slit can be inserted in the Cu-tube. Data has been collected by pixel detector made by CERN. The pixel detector collects the scans of 2θ-angle.

Figure 4.35: Picture of X-Ray diffractometer from PANalytical.

Peak intensities versus $\theta - 2\theta$ gives the possibility to measure the elastic strain in the normal direction towards surface.

The main elements of the diffractometer described above are shown in Figure 4.36. The samples are installed on a goniometer that allows to change four angles (θ, 2θ, ω, χ) and to perform translations in X, Y, Z-axes.

The diffractometer may work in 2 modes (gonio mode = conventional XRD for bulk analysis and Grazing mode = low incident angle to probe near surface of material). Gonio mode gives information about crystal structure at depth of several tens of micrometers due to the high value of incidence angle, typically more than 10 degrees. For example for Nb this depth varies between 2 to 3 μm, depending on the Bragg angle, see Figure 4.34. For measurement of thinner layer, grazing mode can be used, typically the incident angle is between 2 and 10 degrees. In the case of Nb, the penetration depth of X-Rays at 2 degrees is approximately 600 nm.

Figure 4.36: Interior of X-Ray diffractometer from PANalytical.

4.2.5.3 Scanning Electron Microscope with Electron Backscatter Diffraction Tube

Introduction

First electron backscatter diffraction (EBSD) pattern was measured by Nishikawa and Kikuchi in 1928 [241]. However, the obtained pattern had poor quality due to a low transmission of set-up and contamination of sample (low vacuum) and required an optimization of experimental conditions. Nowadays the high quality of images is obtained due to the integration of the EBSD technique on a commercial scanning electron microscope (SEM) operated under high vacuum. First modern EBSD pattern was introduced by J. A. Venables and C. J. Harland in 1973 [242].

The interaction between electron beam and sample generates several types of signal like secondary electrons (SE), backscattered electrons (BSE) and X-rays, which could be detected to provide complementary informations on the morphology, structure and nature of the surface, see Figure 4.37 [243].

Secondary electrons (SE) are emitted by surface atoms excited by the incident electron beam. SE, because very low in energy, can only cross a very thin layer of material of several tens of nanometers. The detection of SE electrons allows then to get a very resolved image (laterally and in depth) ideal to study the morphology and topography of the surface. Back-scattered electrons (BSE) are the portion of incident electrons bouncing back out of the material. They interact elastically

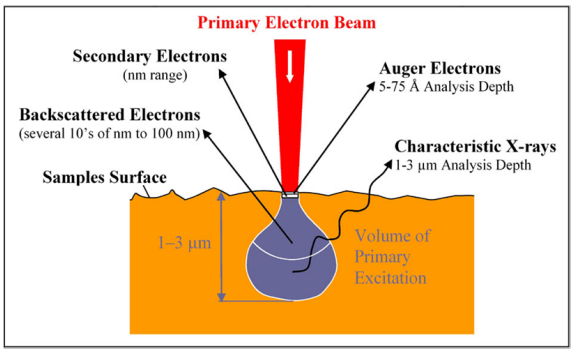

Figure 4.37: Sketch shows the interaction volume of SE, BSE and X-rays [244].

with surface atoms within the first micrometers. The detection of these electrons, because of the strong interaction with atoms, make this technique sensitive to the chemical composition and crystalline structure (phase) at the expense of a worse lateral and depth resolution. Excited atoms by the incident electrons emit X-rays when undergoing de-excitation. The energy spectrum of these X-rays is determined by the type of atoms. The detection of these X-rays by EDS (Energy-Dispersive X-ray Spectroscopy) allows to identify the chemical composition of the surface with a resolution of few microns. Finally, more than the chemical composition, crystalline structure, cristal orientation, phase and strain can be analyzed thanks to the EBSD technique (Electron Back Scattered Diffraction). When BSE exit the surface near to the Bragg angles, they diffract accordingly to crystal planes (Kikuchi bands). Many cristalline information, as mentioned previously could be then extracted by the analysis of diffraction patterns (EBSP).

Outputs from EBSP

Based on the EBSP information, it possible to extract the following images: Image Quality (IQ), the Inverse Pole Figure (IPF), the Kernel Average Misorientation (KAM), the Grain Average Misorientation (GAM) and the grain orientation spread (GOS).

IQ is probably one of the paramount important images of EBSP, which represents information about orientation and local crystalline state caused by sample preparation (surface contamination, phase). IQ also reveals features that are invisible in the secondary electron images, such as grains, grain boundaries, and surface artifacts.

The IPF pattern shows the basic microstructure and reveals the crystallographic

orientation of the grains with respect to the sample normal direction. These changes in orientation are displayed using an RGB color map.

Other images (KAM, GAM and GOS) may describe the dislocation density in the crystallographic material trough the calculation of a grain misorientation by different methods. The grain misorientation is the difference in orientation of crystal lattice of one grain into coincidence with another grain.

KAM image may be used to measure grain misorientation locally. This pattern calculates the average dislocation angle of a given pixel concerning surrounding neighbor pixels. The local misorientation is measured assigned to the center pixel of a particular grain with respect to all points in the perimeter of the kernel. Generally, high dislocation density corresponds to higher KAM. KAM pattern gives information about local lattice distortions, localized deformation, and high dislocation density, hence it reveals information about strain, which is given in the grain.

Another output that measures grain misorientation locally is named GAM. Here the average dislocation angle is calculated over all points in a given grain. The misorientation is calculated between each neighboring pair of points within the grain. The average misorientation value is then determined and assigned to each point within the grain. Generally GAM is high in deformed grains due to higher dislocation density.

The GOS describes the global distribution of the misorientation for all grains in the microstructure and shows the degree of this misorientation by comparing every pixel in the grain with the grain's average orientation. Similarly to KAM and GAM, GOS is higher in deformed grains due to higher dislocation density.

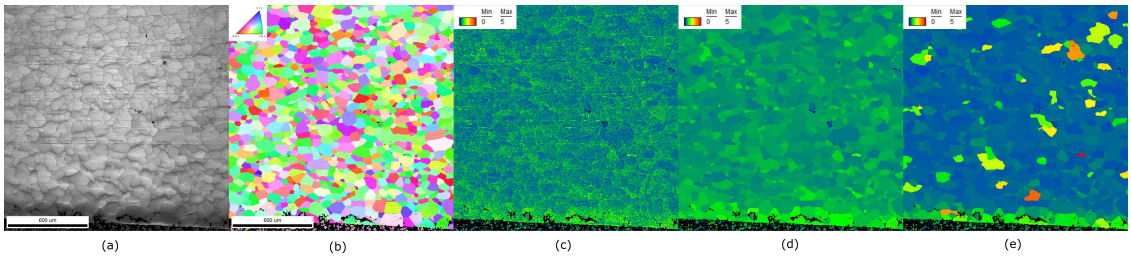

Figure 4.38: Outputs of EBSD patterns: a) image quality, b) inverse pole figure, c) Kernel average misorientation, d) grain average misorientation, e) grain orientation spread.

In order to verify the plastic deformation created during processing cross-sections may be prepared by the following procedure, see Appendix C.

Experimental Setup

The EBSD analysis was performed using a SEM of Sigma Family (Figure 4.39) from ZEISS [245] located at the Institut de Chimie Moléculaire et des Matériaux d'Orsay (ICCMO) lab (Université Paris Sud, Orsay, France). Measurements were done using the following parameters: the tilt of samples under an angle of 70°, accelerating voltage of 20 kV, current of 10 nA and working distance has been selected between 17 and 19 mm. The measurement step size was 0.5 microns.

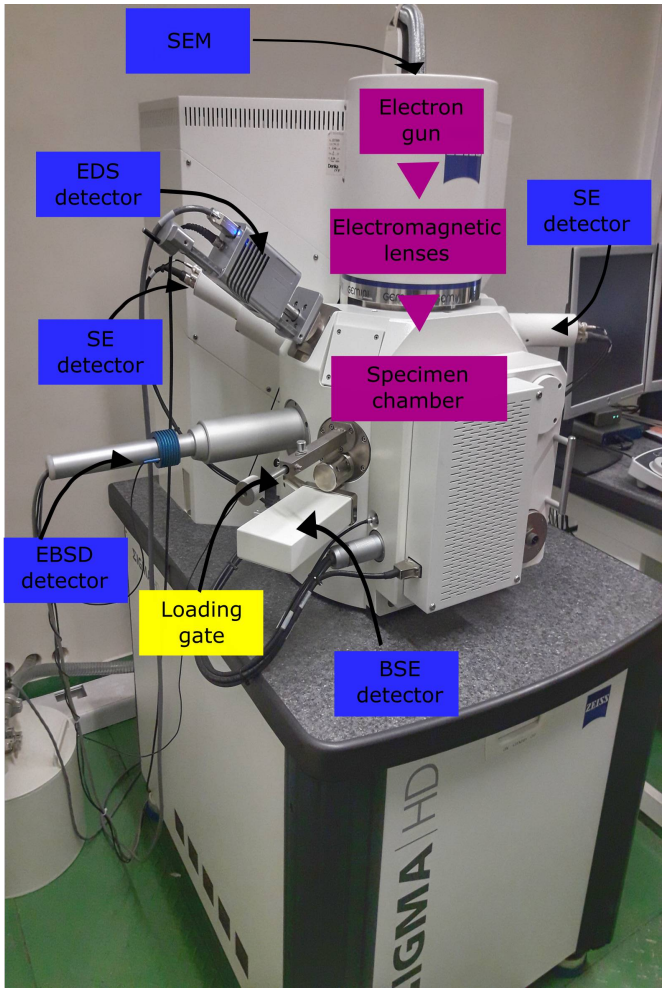

Figure 4.39: SEM with EBSD and EDX tubes (electronic microscope is located at ICCMO).

There are two detectors to measure secondary electrons and a detector based on 4 diodes to measure BSE. The analysis system consists of an EBSD (NORDIF) detector and an *EDS* (SAMx) detector. Special dimensions of the samples for analysis have been achieved (2x2X15 mm) and metallographic preparation of the surface for EBSD has been done. All step of specimen preparation starting from cutting and finished by polishing is presented in Appendix C.

Chapter 5

Experimental Results

5.1 Centrifugal Barrel Polishing of Niobium

Introduction

There are many different type of abrasive media available on the market which may be used for CBP. At JLab, Fermilab and DESY laboratories CBP treatment were performed on elliptical SRF cavities in 4-5 steps. As a result, after about 100h of processing time (excluding handling time of the operator to change abrasive media and to perform surface cleaning of the cavity between each step), the final surface roughness obtained is of typically 10s of nanometers [168]. However, because of the hammering of the surface by abrasive media, the surface pollution is such that at least 20 μm has to be removed by chemical polishing. The standard recipe is presented in Table 5.1 [230].

Table 5.1: Fermilab CBP recipe [230].

Step	Media	Characteristic Size	Duration
1	Ceramic media - $Duramedia^{TM}$	10 mm	8 hours
2	Plastic media - $VF - RG^{TM}22$ cones	14 mm	15 hours
3	Hardwoods + aluminium oxide #600	21 μm	30 hours
4	Hardwoods + colloidal silica	40 nm	40 hours

The existing CBP recipes developed by Fermilab or DESY for Niobium are thus not in line to allow large scale production (too many steps, too long processing time). However, this technique appeared to be complementary to standard chemical treatments as some defects resistant to chemical process could be removed by this mechanical process. Our activities have been focused on optimizing the recipe by the reduction of surface pollution (embedded abrasives), thickness of damaged layer and processing time (in particular, the reduction of intermediate steps) on a CBP machine allowing the polishing of 3D geometries as described previously in Chapter 3.

In order to avoid the plastic deformation and limit surface pollution of Nb during polishing, the ceramic media should be excluded from the polishing procedure [230]. Some prelimary runs done with media composed of different bonding material (ceramic, porcelain and plastic) showed that beside plastic, all other media would pollute and damage too significantly the Niobium surface to allow the reduction of the number of steps (See Figure 5.1). Hence, further investigations have been focused on the plastic media (type/shape) as this media is used for a combined step (abrasion + pre-polishing).

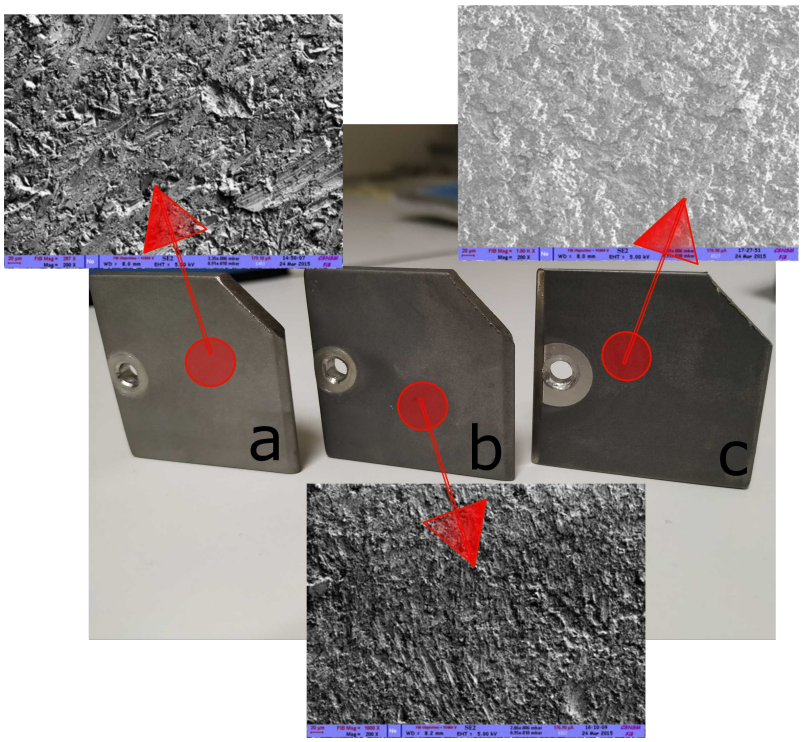

Figure 5.1: Surface state after polishing with different bonding material: a) plastic, b) ceramic and c)porcelain. In the case of ceramic and porcelain, the surface is significantly blackened.

The CBP treatment in this thesis was carried out in 3 steps on a polishing machine described in Chapter 3 with several type of abrasive media supplied by ABC SwissTech [228]. The polishing was done on flat polycrystalline niobium samples. These samples were cut from rolled niobium sheets of 4.5 mm thickness, which were provided by the company Tokyo Denkai. The initial state of the samples used to study material removal rate and surface roughness studies was as "received". The samples used to study the damaged layer and pollution left after CBP process have been previously treated by BCP before polishing (≈200 μm) to ensure that damages/pollution are only due to the CBP process and not from previous processes during Niobium sheet fabrication. The development and optimization of procedure has been done on the samples of 40 mm by 40 mm.

In order to have a global view of the impact of input polishing parameters (rotation speed, time, shape and type of media) on the surface state, the set of output parameters (MRR, surface roughness, and pollution) was analyzed, see Figure 5.2. To measure the MRRs, samples were characterized before and after polishing by the three different techniques, which were described in Chapter 4. To measure the resulting surface roughness and pollution, the surfaces were characterized by laser confocal microscope. Afterwards, to identify the nature of embedded particles and study the depth of pollution, destructive SIMS-analysis was done in static and dynamic modes. All these outputs gave the optimized parameters, to achieve the best surface quality for SRF standards in a minimum of steps. Finally, the finished surface obtained thanks to the optimized recipe has been characterized by XRD and multi-step BCP in order to characterize the value of damages after polishing.

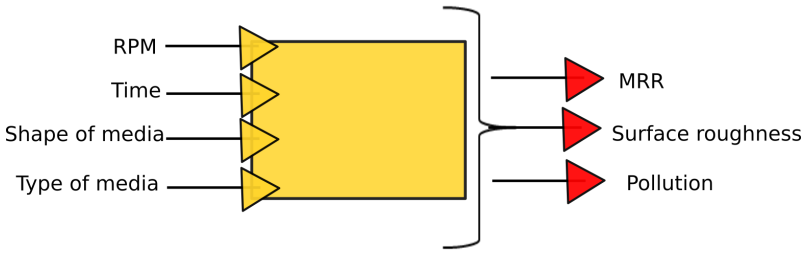

Figure 5.2: Set of input/output parameters during optimization of CBP process.

5.1.1 Optimization of Process Parameters

In order to choose the abrasive media for first potential step three type of the abrasive media made of plastic were tested, see Figure 5.3. The media have the

shape of the pyramid and cone with different composition giving them different abrasive power (see Table 5.2).

(a) plastic pyramids TET-TKS (HF)

(b) plastic pyramids TET-TKP (UF)

(c) plastic cones Cone-TKV (GF)

Figure 5.3: The tested plastic media which could be used as first potential step for CBP polishing.

Table 5.2: Properties of abrasive media [228].

Grade	Description	Abrasive power	Dimensions
HF	Very abrasive plastic	9	10x10 mm
GF	Medium abrasive plastic	5	12x12 mm
UF	Polishing plastic	0	10x10 mm

For the second and last polishing steps abrasive powder in combination with organic media (hardwood blocks) were used. Hardwoods are complementary elements during these steps of CBP, which have to be used to create the weight-impact and produce pressure to increase the polishing efficiency. We carried out the tests with abrasive powder of different nature and sizes: #400, #800, #3000 and #6000. Table 5.3 shows the specifications of those powders.

For all runs, whatever the type of media or powder was used, the water and surfactant quantities were kept constant. The barrel was typically half-filled (some minor volume adjustment were done to balance the 2 opposite barrels). From company experience a half-filled barrel provide optimal performances.

Table 5.3: Specifiaction of the used abrasive's powders for CBP experiments.

Type of the powder	Size or Mesh size	Grain size of the cutters	Hardness
SiC	#400	16.5 ± 1 μm	2700 HV
Al_2O_3	#800	6.3 ± 1 μm	2500 HV
Al_2O_3	#3000	0.38 ± 0.1 μm	2500 HV
SiC	#6000	0.06 ± 0.01 μm	2700 HV

5.1.1.1 Material Removal Rate Measurement

The material removal rate of each used abrasive media was verified by changing the following parameters: rotation speed of a CBP machine (rotations per minute RPM) and duration of run.

Material removal rate has been measured at 100, 125 and 150 RPM. The results are presented in Figure 5.4. The experimental data shows that higher speed leads to higher MRRs. The plastic cones Cone-TKV media looks more efficient in sense of abrasion compared to the plastic pyramids TET-TKS and TET-TKP media even-though its abrasive power is considered as medium. Its slight bigger dimensions (12x12 mm instead of of 10x10 mm) might explain this better efficiency.

Moreover, and surprisingly at first sight, with similar dimensions, the MRR of TET-TKP media (low abrasive power) is better than for TET-TKS (high abrasive power). This lower efficiency of "aggessive" media could be caused by the very rapid wear of media. Indeed, media is not only interacting with the sample but also between them.

As a consequence, the process duration is an another parameter to investigate, as these type of media has a tendency to wear over time, which also leads to different final quality (in terms of the surface roughness and pollution) of the polished surface.

In order to verify the efficiency of abrasion over time (wear of abrasives), the duration of polishing runs have been changed between 5 and 20 hours, at fixed rotation speed - 150 RPM. As can be seen in Figure 5.5, the abrasive media wears during the CBP process.

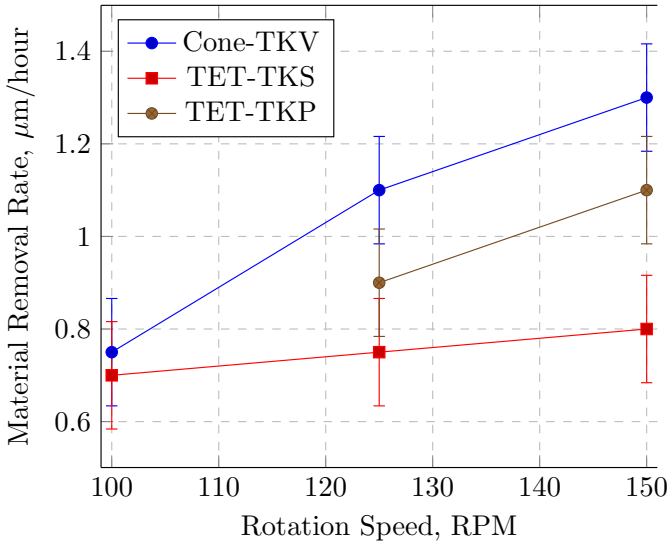

Figure 5.4: The material removal rate of different plastic media (Cone-TKV, TET-TKS, TET-TKP) versus rotation speed (100, 125 and 150 RPM). Processing time 10 hours.

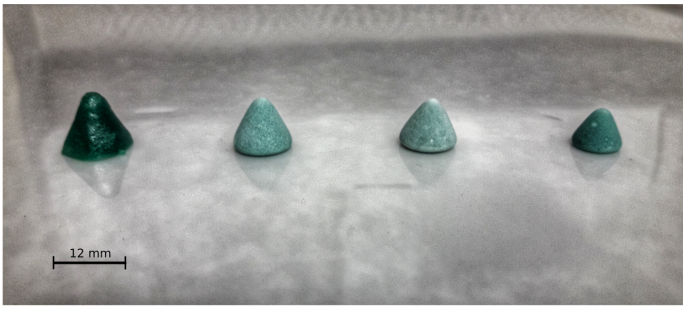

Figure 5.5: Wear of abrasives versus time of polishing (from left to right): initial, 5 hours, 10 hours and 20 hours.

The study of the removed layer versus time aims at evaluating the MRR of the different abrasive media for several process duration. The results are reported in Figure 5.6a and Figure 5.6b. The first graph shows that plastic media looses significantly (more than a factor of 2) its cutting efficiency between 5 and 20 hours.

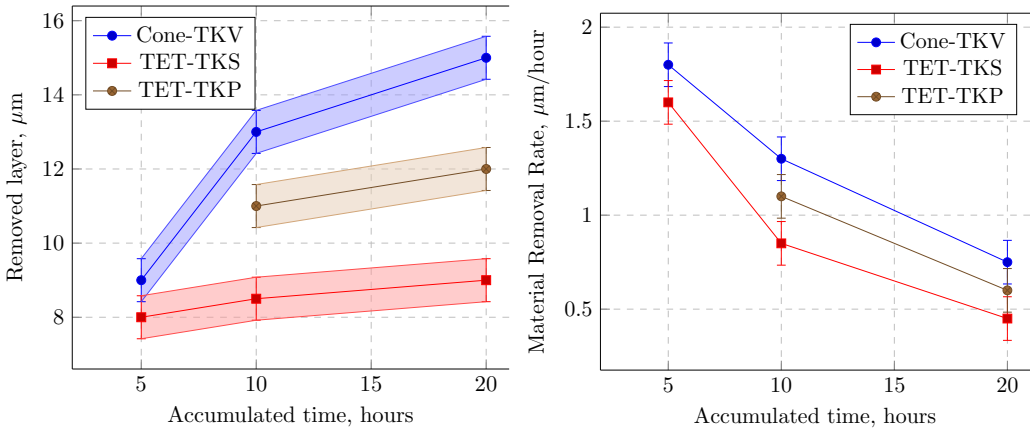

(a) (b)

Figure 5.6: Accumulated removed layer (a) and material removal rate (b) versus time of treatment. Rotation speed - 150 RPM.

As mentioned earlier, we can observe the very rapid wear of TET-TKS media between 5 and 10h. This explains why the total removed layer is only of 9 μm for TET-TKS after 20h instead of 15 μm for CONE-TKV. After 20h, the MRR is so low that the total removed layer tends to saturate. It is thus recommended to perform runs of 10h and not longer than 20h. Hence, in order to remove at least 150 μm of material as required, the first step of CBP process would require to divide it into 12 runs of 10h with CONE-TKV to optimize processing time.

As it will be discussed in the next sections about roughness study and pollution, the intermediate step, involving hardwood blocks and abrasive powder, has to not only remove embedded particles but also erase surface defects (scratches, ...) generated during previous step. Thus, this step has to remove about 20 μm, requiring a processing time of about 100 hours. Table 5.4 shows material removal rate for whole spectrum of tested abrasives.

5.1.1.2 Surface Roughness Analysis

The evaluation of the surface parameters were monitored during the three polishing steps.

Table 5.4: Polishing rates for the studied polishing abrasives and estimated run duration. Rotation speed - 150 RPM.

Step	Type of the abrasive	Size or Mesh size	MRR, $[\mu m/hour]$	Initial S_z	Estimated run duration
Abrasion step	plastic cones CONE-TKV	12 mm	1.3 ±0.12	9.23 ±1.41	12 steps of 10 hours
Pre-polishing step	Hardwoods + SiC	#400	0.19 ± 0.04	7.28 ± 1.35	5 steps of 20 hours
Pre-polishing step	Hardwoods + Al_2O_3	#800	0.13 ± 0.02	4.94 ± 1.37	8 steps of 20 hours
Polishing step	Hardwoods + Al_2O_3	#3000	0.013 ± 0.003	3.48 ± 0.21	6 runs of 20 hours

Figure 5.7 shows evolution of the average surface roughness during CBP process with plastic media measured for several run durations (5h, 10h and 20h). As can be seen, the duration of run influences not only the MRR, but also the final surface roughness.

Indeed, the surface roughness tends to slowly decrease versus time during the first 10h. The abrasive power is high. After 10, the wear of abrasives is such that the abrasive power decreases significantly allowing the reduction of surface roughness. In that sense, so as to prepare the surface for pre-polishing, the last run of the 12 runs recommended for the first abrasion step would need to be extended in time of at least 10h.

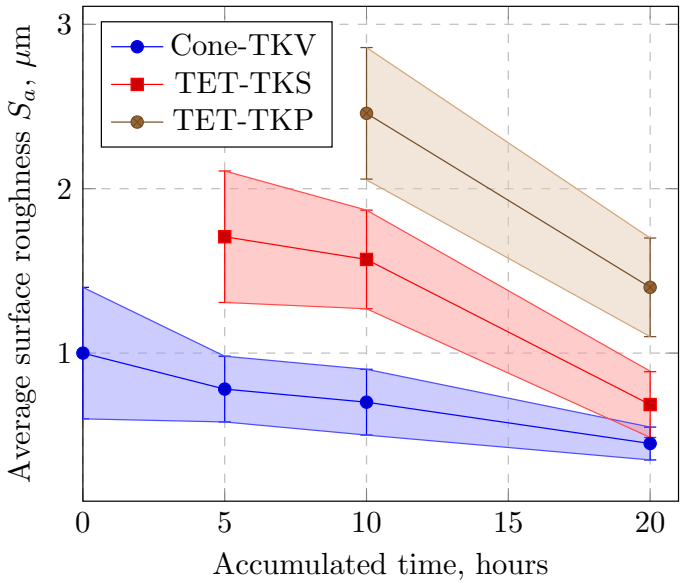

Figure 5.7: Evolution of surface roughness versus time for the three type of media.

Table 5.5 is summarizing the initial and final achieved surface parameters (S_a, S_z, S_{sk} and S_{dr}) after 20h of processing for all processing steps. It appears, for the first abrasion step, that CONE TKV is providing the best surface quality allowing to limit the duration of the following steps. Indeed, the surface roughness and S_z parameters are the lowest. Moreover, The other surface parameters S_{sk} and S_{dr} (representative of the density of embedded particles as described in chapter 2) are showing that Cone TKV media is inducing a lower surface pollution (S_{dr} is low and S_{sk} is negative).

Table 5.5: Surface roughness parameters before and after the three polishing steps. Note: rotation speed - 150 RPM, time of polishing run - 20 hours.

3D Surface Roughness								
Parameters	As received	BCP	Cone-TKV	TET-TKS	TET-TKP	SiC#400	Al_2O_3#800	Al_2O_3#3000
S_a, μm	0.57 ± 0.10	1.8 ± 0.7	0.48 ± 0.08	0.69 ± 0.09	1.4 ± 0.3	0.69 ± 0.20	0.13 ± 0.05	0.071 ± 0.003
S_z, μm	5.65 ± 1.81	15.65 ± 2.58	9.23 ± 1.41	10.32 ± 1.55	14.52 ± 1.33	7.28 ± 1.35 ±	4.94 ± 1.37	3.48 ± 0.20
S_{sk}	-0.38 ± 0.14	0.06 ± 0.02	-0.64 ± 0.17	-0.60 ± 0.35	-0.51 ± 0.15	-1.05 ± 0.09	-1.41 ± 0.19	-1.78 ± 0.45
S_{dr}	0.10 ± 0.03	0.02 ± 0.01	1.30± 0.16	1.72 ± 0.15	2.60 ± 0.27	0.49 ± 0.04	0.10 ± 0.04	0.02 ± 0.03

The surface is optically of better quality when processed with CONE-TKV, in line with the previous conclusions on surface quality.

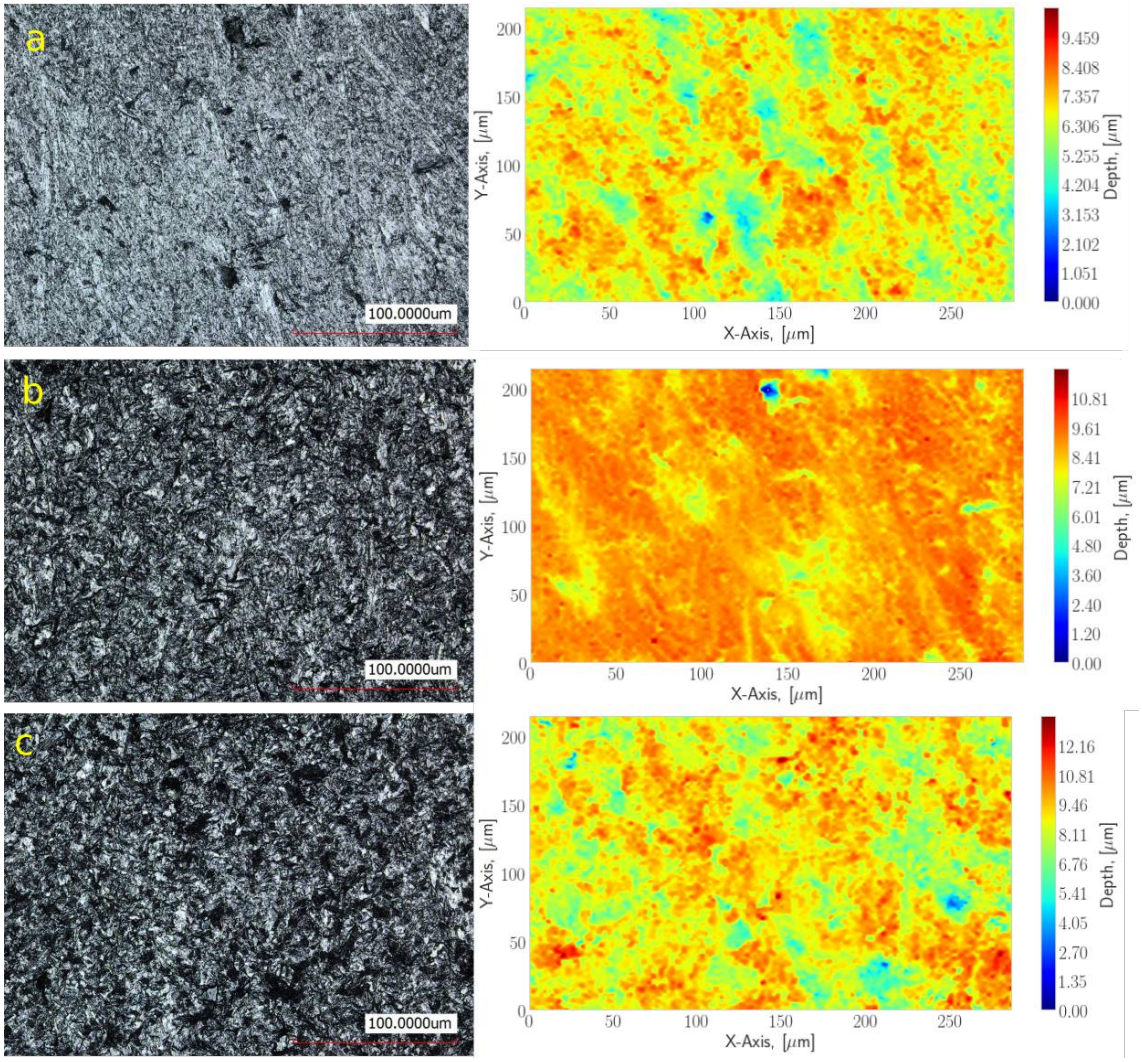

Figure 5.8: Laser scanning microscopy (left) and height (right) images of Nb surface after the CBP process with the plastic media Cone-TKV (a), TET-TKP (b) and TET-TKS (c). Note: 20 hours run at 150 RPM.

5.1.1.3 Surface Pollution Analysis

The surface pollution is not limited to the analysis of surface parameters (S_{dr} and S_{sk}).

The pollution evaluation has been performed by SIMS analysis, as described in Chapter 4, with 5 keV argon ion beam. Investigations of the chemical composition of surface have been performed in static mode and recognition of elements has been done by using script define in Appendix B. Depth profiling was carried out on

a window of 400 × 400 μm. In order to estimate the depth of sputtered region so as to correlate precisely analyzed depth and sputtering time, the crater depth measurement was done using a laser confocal microscope (cf. Chapter 4).

Figure 5.9a is showing how aluminium pollution (abrasive embedded in media) is extending inside the surface over approximately 25 μm depending on the type of media used. In agreement with previous conclusions, the SIMS analysis is confirming that the pollution is more limited when CONE-TKV media is used and is independent of rotation speed contrary to TET-TKS media.

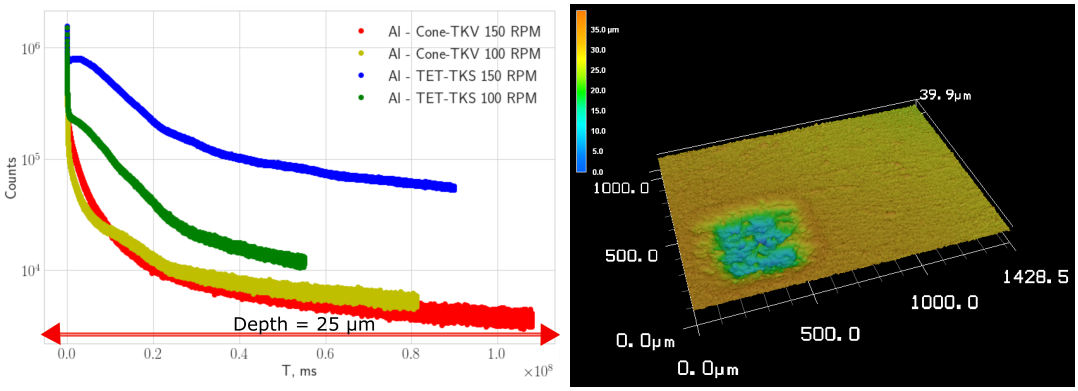

(a) (b)

Figure 5.9: Comparison of SIMS depth profiles after the polishing (20 hours) by different plastic media (Cone-TKV and TET-TKS) at different rotation speeds (100 and 150 RPM) - (a), laser confocal 3D image of 25 μm crater induced by SIMS (b).

For the following polishing steps with polishing powders, no direct surface pollution has been performed. However, the surface depollution (removal of embedded particles from previous step) has been studied versus time. An optical inspection after steps of 20 hours was carried out over more than 200 hours (See Figure 5.10). One can appreciate how surface pollution is decreasing with time. After more than 280h, some surface pollution is still visible eventhough the less polluting media was used in the first step. The fact that the depollution process fails has been also observed by other labs (FNAL, DESY). Moreover, a simplified procedure has been proposed at DESY for cavity fabrication: a single CBP step with plastic media followed with depollution by chemical etching [246].

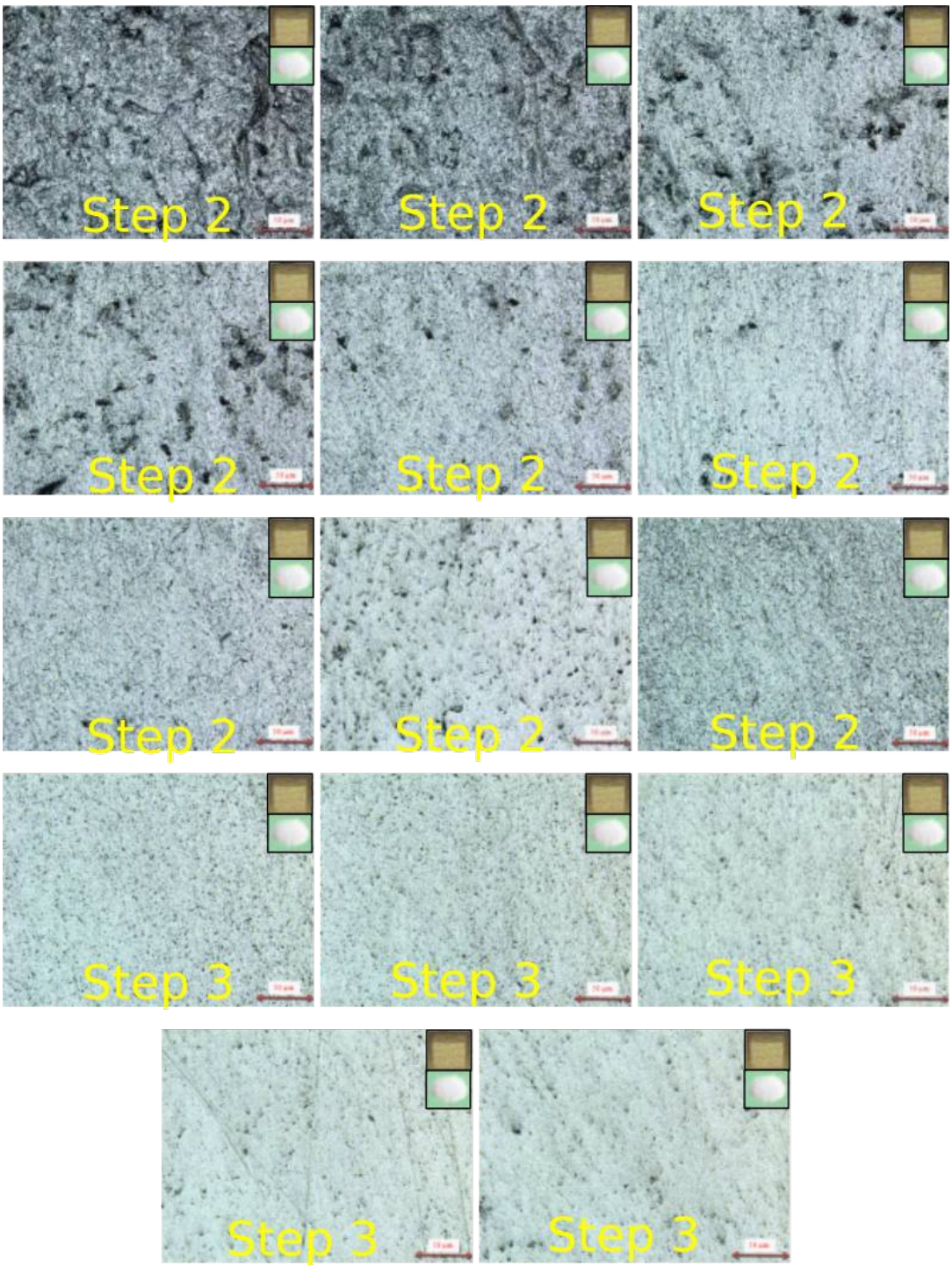

Figure 5.10: Laser scanning microscopy images after steps of 20 hours duration.

5.1.2 Optimized CBP recipe for Polycrystalline Niobium

Thanks to all the analyzes performed, an optimized recipe could be suggested to ensure the best surface quality achievable with this technique and the optimal superconducting properties (cf. Chapter 2 requirements of alternative polishing technique). The proposed recipe takes also into account industrialization constraints by limiting as much as possible the duration of the full process as well as number of steps. However, the conclusions of this study are not very positive at first sight :

- Although optimized, the duration of the CBP process is longer than 300h
- The MRR during the first abrasion step is very low compared to chemical etching rates
- The depollution efficiencies of the second and last steps are not sufficient to remove totally the surface pollution in a reasonable time.

So as to conclude definitely on this technique and its ability to maintain good superconducting properties, a specific sample has been treated thanks to the optimized recipe. This sample, a niobium disk of 126 mm of diameter can be mounted on a resonant cavity to be tested down to 2K. The surface resistance can be evaluated thanks to the measurement of the cryogenic load generated by a radiofrequency wave at 2.8 and 5.6 GHz [247].

So as to demonstrate the quality of this treatment, the sample has been previously chemically etched to remove any surface defect. In this way, the first polishing step could have been limited to only 65 hours. The recipe is the following :

Step 1: Plastic cones (12x12 mm), de-ionized water, surfactant (Pulib 72), 150 RPM, 65 hours, 4 runs;

Step 2: Hardwood blocks, Al_2O_3 powder # 800, surfactant (Pulib 200), de-ionized water, 150 RPM, 40 hours, 2 runs;

Step 3: Hardwood blocks, Al_2O_3 powder # 3000, surfactant (Pulib 200), de-ionized water, 150 RPM, 40 hours, 2 runs.

The evolution of the niobium topography after sequential polishing steps is compared. The final surface roughness of CBP-polished disk is 30 nm.

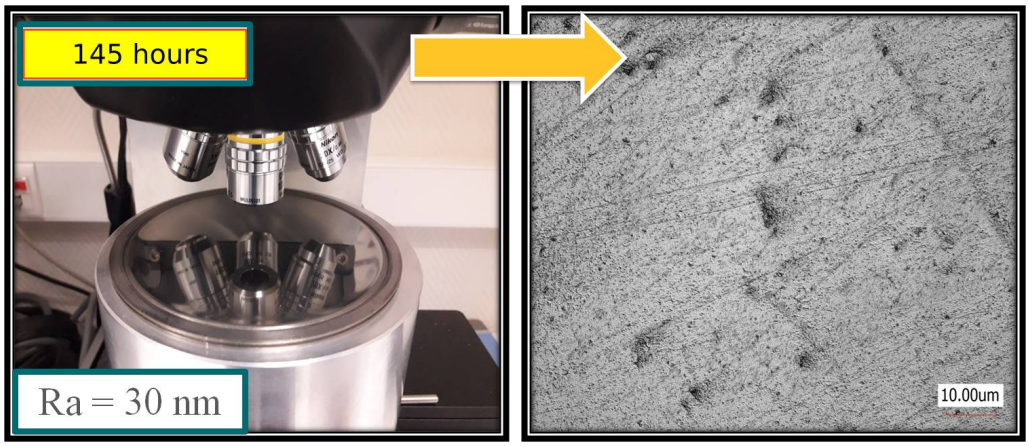

Figure 5.11: Photography (left) and laser confocal image (right) of mirror-finished surface after 3-step CBP. Note: residual pollution is still visible even after 145 hours of polishing.

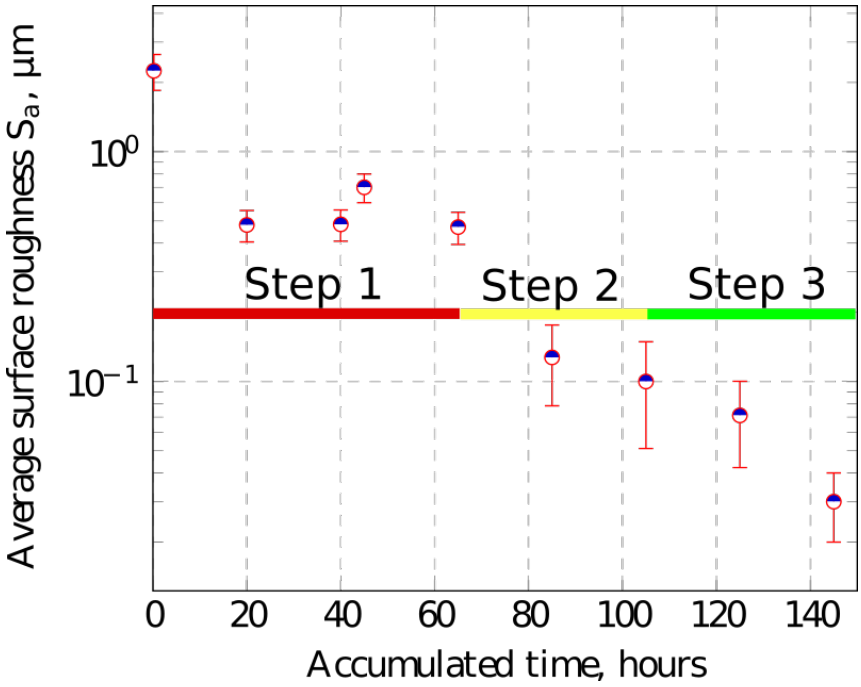

Figure 5.12: Evolution of average surface roughness of RF disk with optimized 3-step CBP recipe.

Table 5.6: Surface roughness parameters of RF disk after 3-step CBP.

Step	S_a, μm	S_z, μm	S_{sk}	S_{dr}
3-step CBP	0.035 ± 0.005	2.5 ± 0.3	-2.9 ± 0.4	0.014 ± 0.004

5.1.2.1 Multi-step BCP Analysis for Damaged Layer Evaluation

This study characterizes deformations of Nb after CBP polishing by two methods described in Chapter 4: Optical image of the surface after multiple BCP etching steps and X-Ray diffraction measurements.

The crystal damages are determined by the presence of subgrain patterns magnified by digital interference contrast (DIC) images. Pattern analysis is qualitatively carried out by visual inspection. Results are presented in Figure 5.13. After 11 μm removal, the density of subgrain patterns is very high and visible on all grains. After 65 μm removal, very few grains show subgrain damages but still remain up to 143 μm. The hammering of the surface by media during the first step is obviously too significant causing very deep shear and compression strains.

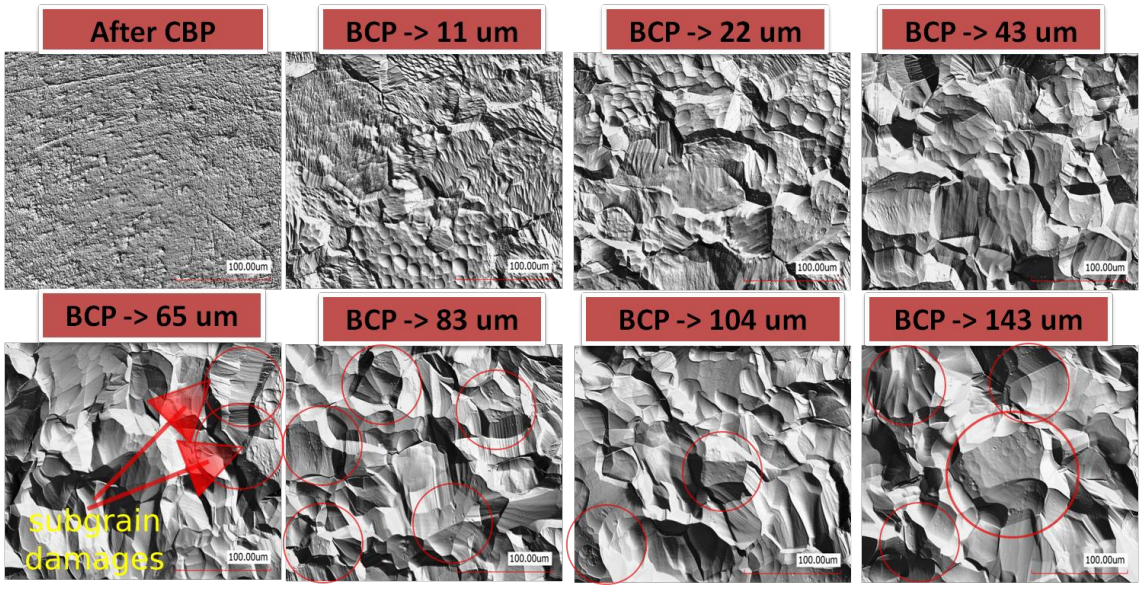

Figure 5.13: DIC images of Nb surface state after CBP polishing for different removed layer by BCP.

5.1.2.2 XRD Diffraction Analysis

As discussed in Chapter 4, X-ray diffraction analysis in grazing angle allows to probe different crystallographic properties like interplanar distances and evaluate useful information like residual strain (shift of peak) and inclusions (broadening of peak). In this study, we analyzed samples treated by two type of media (CONE-TKV and TET-TKS) in Gonio and grazing mode. In Gonio mode, the X-rays penetrate 2.5 μm and at a grazzing angle of 2 ° only 600 nm.

Figure 5.14a shows typical XRD diffractogram after first step of CBP polishing with plastic media Cone-TKV. XRD analysis confirms the appearance of strain in the material. The expected diffraction peaks positions and their relative intensities are presented in green circles for non-deformed state of niobium.

As can be seen in Figure 5.14b and Figure 5.14c, the 2 diffraction peaks in gonio mode and grazing angle after abrasion step (respectively Cone-TKV and TET-TKS) are plotted. In Gonio mode, the diffraction peak is exactly centered on the theoretical position. Whereas in grazing mode, the peak is clearly shifted toward a lower angle sign of compression strain. The peak is also broadened sign of the presence of non linear strain caused by inclusions.

Figure 5.15 shows XRD diffractogram after optimized three step CBP polishing. Peaks are broadened and shifted to values comparable to after a simple abrasion step. Hence, a preliminary conclusion can be done: damages after the first step couldn't be removed by a three-step procedure with this polishing technique.

The fact that no strain is apparently detected as deep as 3 μm is in contradiction with the previous multi-step BCP analysis showing a very deep propagation of damages. Unfortunately, no diffractogram of a BCPd sample could have been performed because of the very rough surface (presence of multiple peaks). This reference would have been required to really confirm this shift as well as the broadening of the peak.

Some further investigations have to be done to understand the link between subgrain patterns, residual strain and in particular their impact on superconducting properties.

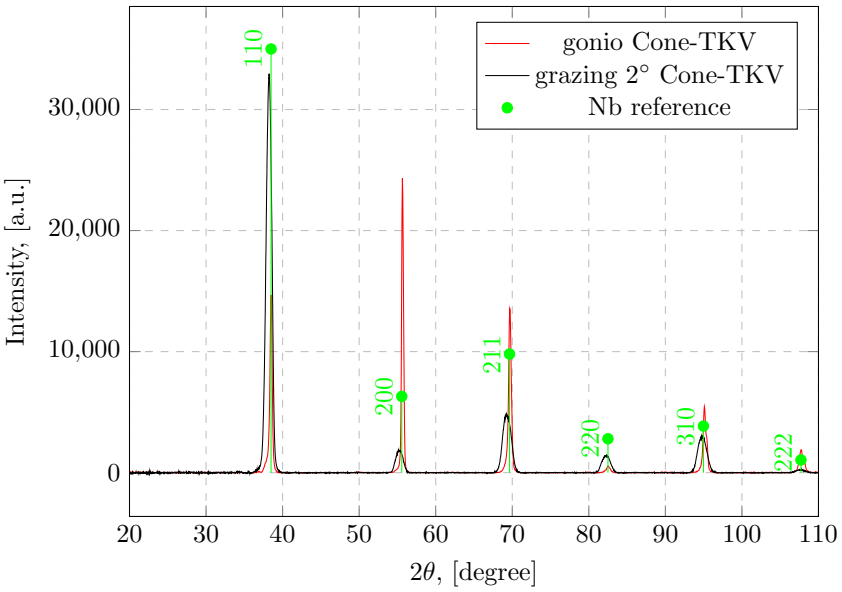

(a) XRD pattern of Nb after the first step CBP.

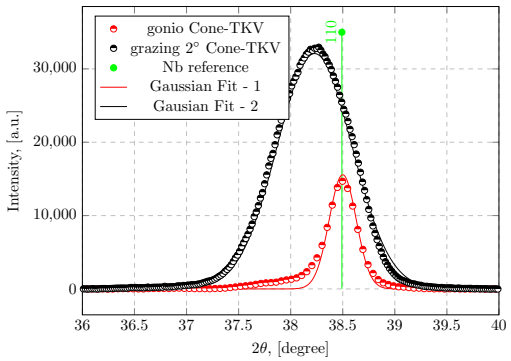

(b) After polishing with Cone-TKV

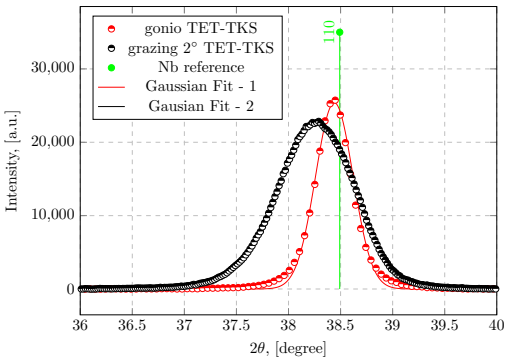

(c) After polishing with TET-TKS

Figure 5.14: XRD patterns in Gonio and Grazing modes.

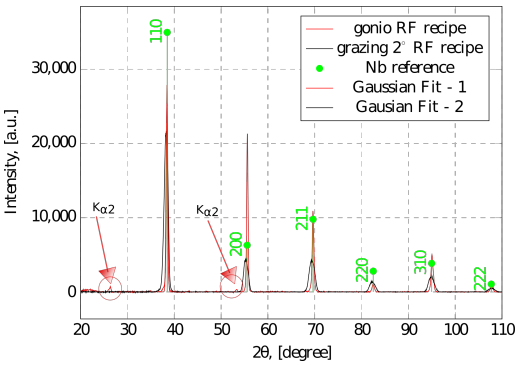

(a) XRD pattern after the three step CBP.

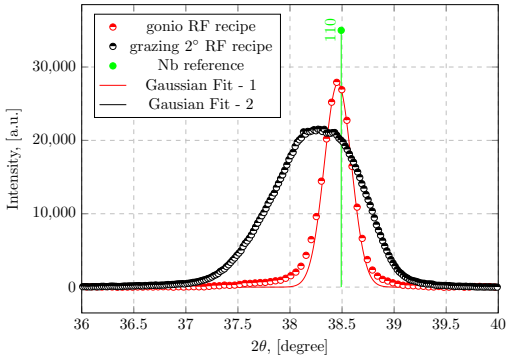

(b) Magnified first peak of XRD pattern after the 3 step CBP.

Figure 5.15: XRD pattern of Nb after 3-step CBP.

Table 5.7: Peak position and width of peak after first and three step CBP.

Step	Type of the abrasive	Mode of XRD	Deviation from theoretical position, degree	Peak position, degree	Width of peak, degree
Abrasion step	TET-TKS	grazing 2 degree	-0.102	38.390	0.792
Abrasion step	TET-TKS	gonio	-0.107	38.385	0.208
Abrasion step	CONE-TKV	grazing 2 degree	-0.214	38.278	1.152
Abrasion step	CONE-TKV	gonio	-0.015	38.477	0.338
3 step CBP	CONE-TKV/Al_2O_3	grazing 2 degree	-0.187	38.305	0.944
3 step CBP	CONE-TKV/Al_2O_3	gonio	-0.043	38.449	0.328

5.2 Metallographic Preparation of Niobium

As was mentioned in Chapter 3, the standard pathway of cavity production has a specific order in which the forming of cavity from Niobium sheets is before the surface polishing step. However, metallographic polishing can not be applied directly on enclosed geometries, in that sense, an alternative path has to be created (See Figure 5.16) where Niobium sheets are polished before the forming of the cavity [3]. It has been shown that the observed damaged layer after forming is significantly thinner (10 microns) than after fabrication (150 microns) of Nb sheets and would only require a "flash" (5-10 μm) BCP or EP to prepare the surface for RF [248].

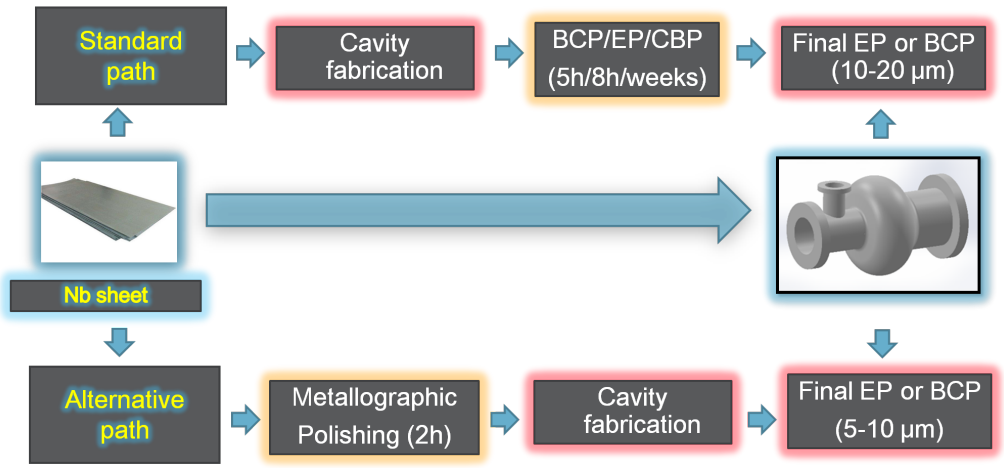

Figure 5.16: Alternative path of cavity fabrication: lamination (rolling), mechanical polishing (150 μm), forming, electron beam welding, final surface treatment (heat treatment, flash BCP or EP).

Remarks:

- A careful study will have to be carried out to upgrade forming procedures/techniques so as to maintain as much as possible the surface quality of Niobium sheets. This study is not part of this PhD study but contactless techniques like hydroforming [249] or electro-hydroforming [250] appear at first sight to be very promising candidates.

- Some metallographic polishing procedure for Niobium have already been developed and are available in the literature (See Appendix E). However, these procedures focused on achieving the best surface quality but where not taking into consideration any requirements in term of industrialization, cost or sub-surface crystal quality.

The aim of this study is to optimize the metallographic polishing procedure for Niobium so as it meets the specifications required for SRF applications and alternative polishing technique as described in Chapter 3. In particular:

- removal of 150 μm
- limitation of number of steps (2-3)
- Limitation of surface pollution and residual strains over several hundreds of nanometers.

5.2.1 Selection Strategy of Consumables (Disks, Abrasives) for First Abrasion Step

At first stage, the experiments were carried out with a wide spectrum of grinding/lapping/polishing disks provided by company LAM PLAN [227]. MRR and surface parameters (S_a, S_{dr}, S_{sk}) were measured by protocols as described in Chapter 4.

The grinding and lapping disks and associated abrasives achieving a MRR and a final surface quality away from the specific requirements were set aside. Secondly, sample treated with the most promising disks/abrasives selected were analyzed with more powerful techniques like SIMS, XRD, EDS and EBSD (cf. Chapter 4) to address the induced surface contamination and crystallographic damages.

5.2.1.1 Preliminary Results for Grinding/Lapping

The tables 5.8, 5.9, 5.10 and 5.11 summarise MRR and final surface parameters for each type of grinding/lapping and polishing disk tested. 14 different type of disk and several combination of disk/abrasives have been tested. Duration of each polishing step - 5 min. Rotation speed of disk - 300 RPM and rotation of header - 150 RPM. Pressure applied on the set of three samples is equal to 120 kPa (40 kPa per sample).

A color code has been added on these tables to validate whether the value is acceptable at the sight of specifications (green) or at the limit (orange) or out of specifications (red).

For the abrasion step, so as to be competitive with standard chemical polishing, MRR should be above 1 $\mu m/min$.

As MRR of polishing step is of the order of 0.01 $\mu m/min$ (cf. Table 5.11) and aims at "erasing" surface damages and pollution of abrasion step, the typical S_a below 0.1 μm.

For final polishing step, the surface roughness has to be at least of the order or better than typical roughness obtained after EP, meaning below 0.1 μm. Depollution of the surface has also to be observed.

Table 5.8: MRR and final surface parameters for each type of grinding disk tested for abrasion step. Disk rotation speed: 300 RPM, header rotation speed: 150 RPM. Pressure: 40 kPa. Direction of disk/header rotation: counter-rotation.

Material, Type and Size of Abrasive	MRR, μm/min	S_a, μm	S_z, μm	S_{sk}	S_{dr}	Observations
Resin - diamonds 125 μm	145.83 ± 3.88	1.65 ± 0.33	19.32 ± 2.63	-0.74 ± 0.06	1.20 ± 0.13	Rapid wear (with Niobium - 10 min)
Resin - diamonds 59 μm	52.66 ± 1.55	0.37 ± 0.03	8.83 ± 0.96	-2.10 ± 0.03	0.40 ± 0.04	Rapid wear (with Niobium - 15 min)
Resin - diamonds 26 μm	23.33 ± 0.88	0.17± 0.04	8.43 ± 1.72	-3.74 ±1.36	0.23 ± 0.09	Rapid wear (with Niobium - 20 min)
Resin - diamonds 15 μm	20.66 ± 0.55	0.15± 0.02	5.09 ± 1.39	-1.59 ± 1.08	0.23 ± 0.05	Rapid wear (with Niobium - 25 min)

Table 5.9: MRR and final surface parameters for rigid lapping disk tested for abrasion step. Disk rotation speed: 300 RPM, header rotation speed: 150 RPM. Pressure: 40 kPa. Direction of disk/header rotation: counter-rotation.

Material, Type and Size of Abrasive	MRR, μm/min	S_a, μm	S_z, μm	S_{sk}	S_{dr}	Observations
Hard composite disk + diamonds 9 μm	18.46 ± 3.02	0.14 ± 0.05	5.29 ± 1.20	-0.41 ± 0.09	0.29 ± 0.06	Extremely slow wear (more than 10 hours)
Hard composite disk + Al_2O_3 3 μm	4.70 ± 0.51	0.22 ± 0.04	6.88 ± 0.65	-0.07 ± 1.15	0.65 ± 0.06	Extremely slow wear (more than 10 hours)

Table 5.10: MRR and final surface parameters for soft lapping disk tested for abrasion step. Disk rotation speed: 300 RPM, header rotation speed: 150 RPM. Pressure: 40 kPa. Direction of disk/header rotation: counter-rotation.

Material, Type and Size of Abrasive	MRR, μm/min	S_a, μm	S_z, μm	S_{sk}	S_{dr}	Observations
Soft composite disk + diamonds 3 μm	3.3 ± 0.66	0.05 ± 0.01	3.61± 0.3	-0.78 ± 0.4	0.04 ± 0.02	Slow wear (5-6 hours)
Soft composite disk + diamonds 1 μm	0.51 ± 0.04	0.07 ± 0.01	3.4 ± 0.75	-1.39 ± 0.24	0.03± 0.01	Slow wear (more than 5 hours)
Soft composite disk + Al_2O_3 3 μm	9.72 ± 1.41	0.11 ± 0.01	4.72 ± 0.41	-0.46 ± 0.07	0.27 ± 0.03	Very rapid wear of disk
Synthetic fiber cloth + diamonds 9 μm	2.2 ± 0.45	0.1 ± 0.04	4.15 ± 0.13	-0.89 ± 0.24	0.21 ± 0.14	Slow wear (several hours)
Synthetic fiber cloth + diamonds 3 μm	0.95 ± 0.25	0.09 ± 0.02	3.55 ± 0.13	-1.05 ± 0.24	0.11 ± 0.04	Slow wear (several hours)

Table 5.11: MRR and final surface parameters for each type of polishing disk tested. Disk rotation speed: 300 RPM, header rotation speed: 150 RPM. Pressure: 40 kPa. Direction of disk/header rotation: complementary-rotation.

Material, Type and Size of Abrasive	MRR, μm/min	S_a, μm	S_z, μm	S_{sk}	S_{dr}	Observations
Viscous fiber cloth + diamonds 1 μm	-	0.045 ± 0.005	1.49 ± 0.29	-1.92 ± 0.48	0.0007 ± 0.0002	No-depollution
Microporous polyurethane cloth + SiO_2 50 nm	0.01 ± 0.01	0.03 ± 0.2	2.0± 0.2	-2.05 ± 0.56	0.008 ± 0.003	Depollution observed, re-appearance of grains
Compressed polyurethane cloth + SiO_2 50 nm	0.025 ± 0.003	0.05 ± 0.3	2.2± 0.4	-1.95 ± 0.95	0.018 ± 0.023	Depollution observed, re-appearance of grains

As a preliminary conclusion, grinding disks (cf. Table 5.8) are inducing very significant surface damages which would extend drastically the duration of the polishing step. Such disks are not recommended for the abrasion step if the target is a 2-step recipe. However, the finest grinding disk (resin - 15 μm diamonds) could be envisaged in case the workpiece is showing a bad flatness or is tilted relatively to the disk . The recovery of form errors and waviness could be very inefficient with abrasives dimensions below 10 μm. During sample studies, resin - 15 μm diamonds disk has been used several times to correct tilt (for small samples) or flatness (large samples) issues.

Rigid lapping disks (cf. Table 5.9) have been tested but observations comparable to grinding disks have been done. Moreover, abrasives dimensions below 9 μm is not recommended [251] with such disks. For smaller abrasives, soft lapping disks (cf. Table 5.10) have to be used. The surface roughness is significantly improved at the expense of a reduced, but still reasonable MRR. Scratches are visible on the surface with a typical depth of few μm (See first picture of Figure 5.22) but these could be "erased" by the polishing step within few hour.

Finally, efficient depollution is observed only with colloidal silica which allows a combined mechanical-chemical polishing (See Chapter 3).

This preliminary study highlighted that the following disks/abrasives are suitable for further analyzes :

- Grinding disk with 15 μm embedded abrasives or hard rigid lapping disk with 9 μm diamonds as an optional corrective step;
- Soft composite and textile (synthetic fiber) lapping disks with respectively abrasives of 3 μm and 9 μm;
- Colloidal silica with soft textile polishing disks (microporous and compressed polyurethane).

Remarks:

The influence of polishing parameters has been characterized in term of MRR but are not detailed in this manuscript and can be summarized as follow:

- The rotation speed is not impacting significantly the MRR.

- MRR is proportional to the pressure applied on samples for grinding disks (fixed abrasives) only. For lapping, the effect is way lower (12 times increased pressure is increasing MRR by approximately 65 %).
- The counter-rotation is increasing MRR by approximatively 10 %.

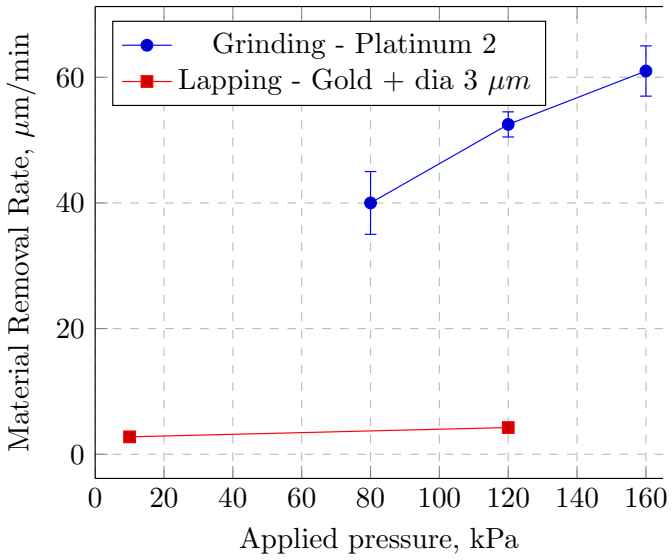

Figure 5.17: MRR versus applied pressure for grinding and lapping processes.

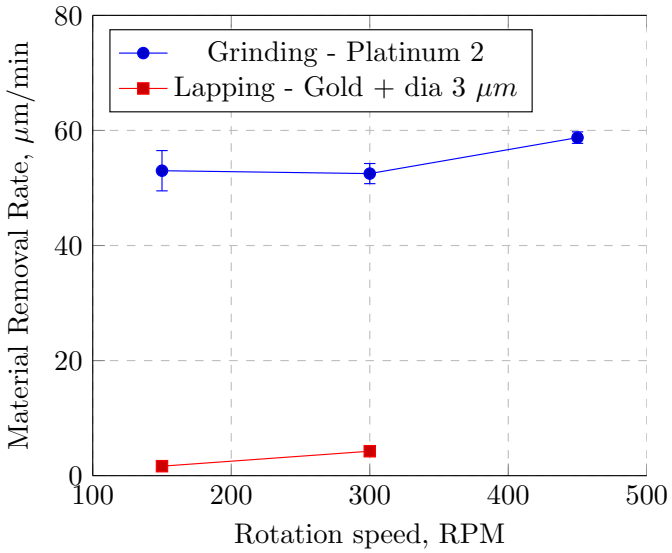

Figure 5.18: MRR versus rotation speed for grinding and lapping processes.

5.2.1.2 Refined Analysis of Best Performing Disks/Abrasives

Further investigations have been focused on a set of the following disks: resin - 15 μm diamonds (fixed abrasives), hard composite disk + 9 μm diamond suspension

(non-fixed abrasives), synthetic fiber + 9 μm diamond suspension (non-fixed abrasives) and soft composite disk + 3 μm diamond suspension (non-fixed abrasives).

5.2.1.2.1 Multi-step BCP

We performed multi-step BCP characterisation of niobium samples processed with the disks defined in the previous section. Results are presented in Figure 5.19 for resin - 15 μm diamonds, Figure 5.20 for hard composite disk + diamond 9 μm, Figure 5.21 for synthetic fiber + diamonds 9 μm and Figure 5.22 for soft composite disk + 3 μm. The grains appeared just after 24 microns of BCP. The density of subgrain patterns is generally very high and remains on all grains up to 69 microns of removed layer.

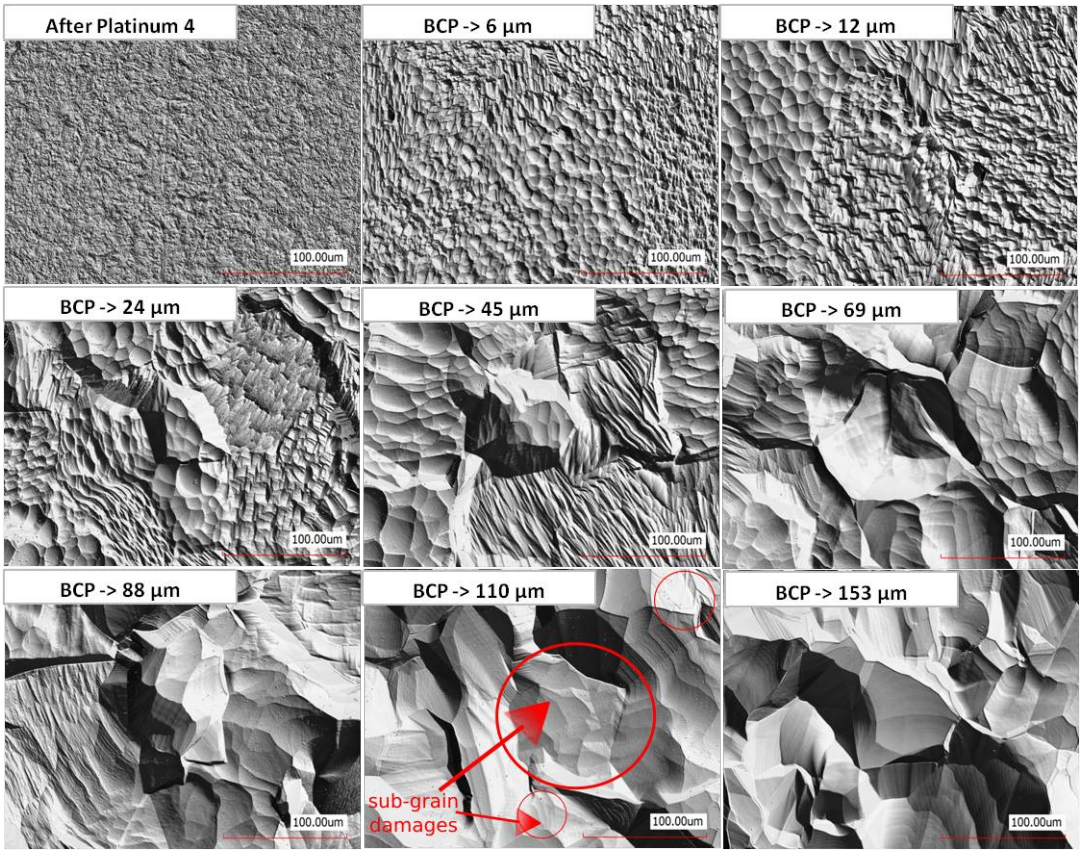

Figure 5.19: DIC images of Nb surface state after grinding with resin - 15 μm diamonds for different removed layer by BCP.

This very qualitative technique is showing that all these solutions tend to affect the crystal down to a depth of the order of 100 μm. Nevertheless it can be emphazised that the polycrystalline structure tends to re-appear deeper when rigid disks are used. Indeed, the surface looks amorphous up to approximatively 24 μm for resin - 15 μm diamonds and hard composite disk whereas for soft disks, the crystalline structure is already visible after a removal of 6 μm. So as to quantify more precisely stresses induced by these, XRD analyzes have been performed and results will be discussed in the following section.

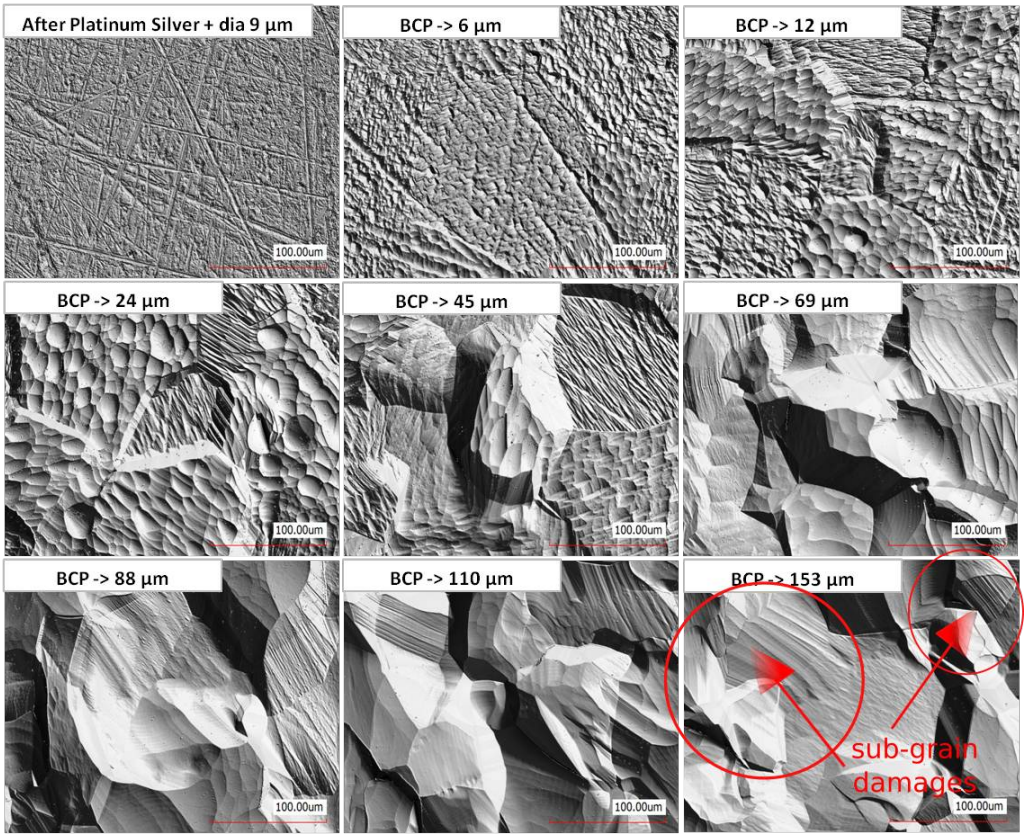

Figure 5.20: DIC images of Nb surface state after lapping with hard composite disk + diamonds (dia) 9 μm for different removed layer by BCP.

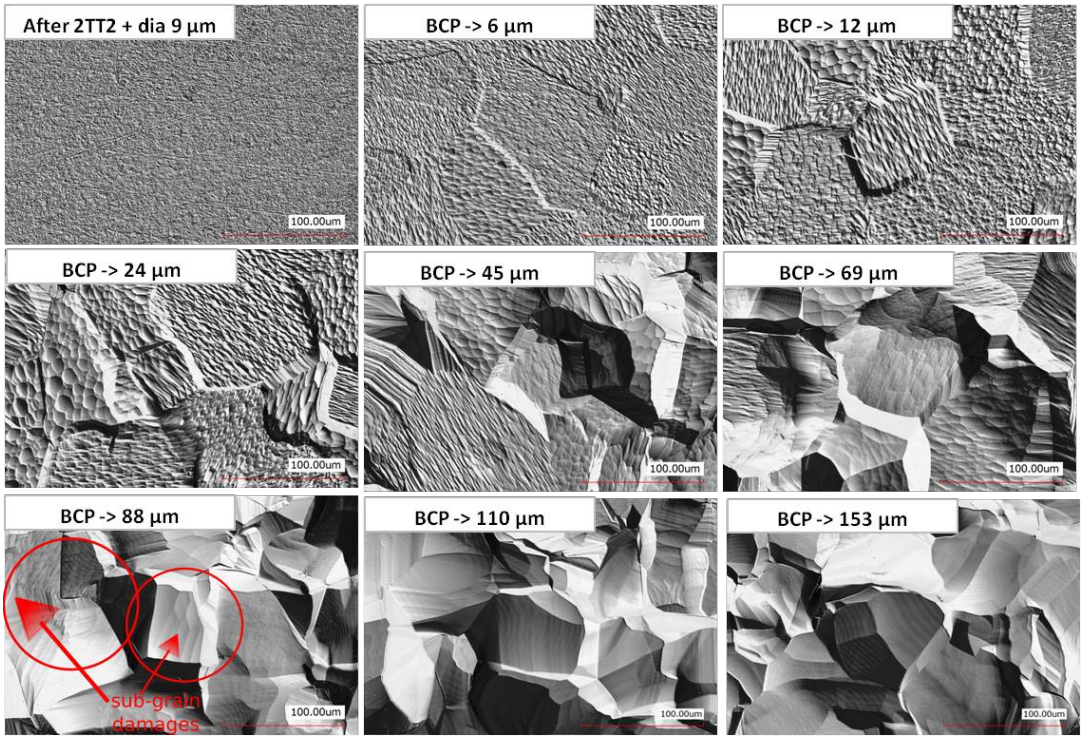

Figure 5.21: DIC images of Nb surface state after lapping with synthetic fiber + diamonds (dia) 9 μm for different removed layer by BCP.

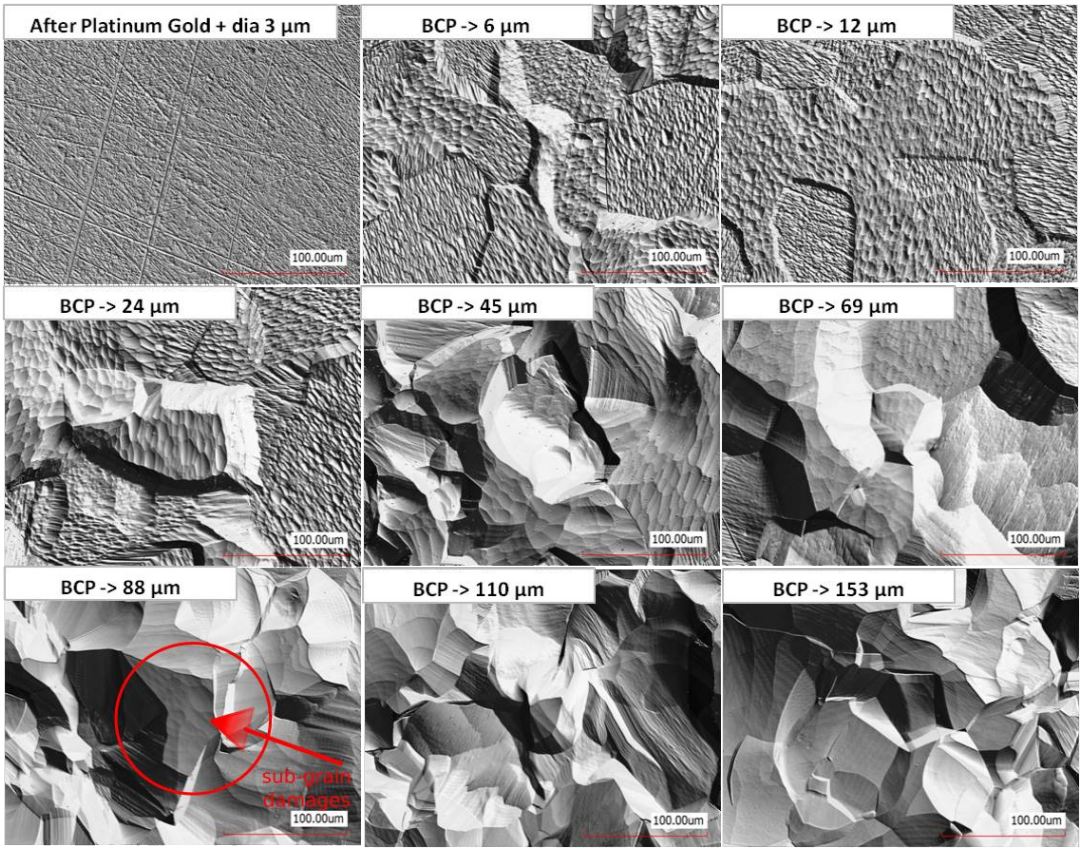

Figure 5.22: DIC images of Nb surface state after lapping with soft composite disk + diamonds (dia) 3 μm for different removed layer by BCP.

5.2.1.2.2 XRD Analysis

XRD analyzes have been carried out on the four type of polishing disks mentioned previously. The four following plots (Figures 5.23a, 5.23b, 5.23c and 5.23d) show how the lattice parameters are changed depending on the analyzing angle Psi. The residual stress can be evaluated from the curve (See description of method in Chapter 4). In the case of a non-textured crystal, the curve should be linear. Non-linearities or oscillations indicate the presence of an inhomogeneous distributed strain due to the preferred orientation of Niobium.

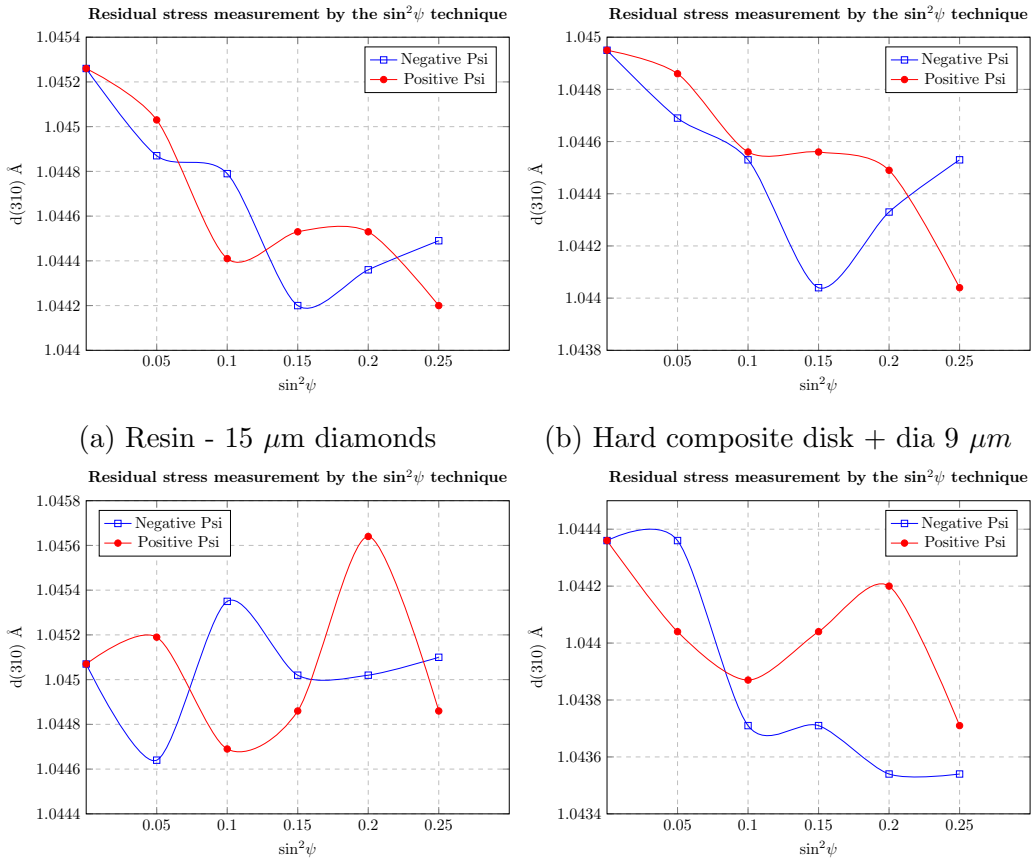

(a) Resin - 15 μm diamonds

(b) Hard composite disk + dia 9 μm

(c) Synthetic fiber + dia 9 μm

(d) Soft composite disk + dia 3 μm

Figure 5.23: Inter planar distance (d) versus $sin^2\psi$ in the case of applying different disks on Niobium.

Table 5.12 shows the evaluated residual stress for Niobium samples with omega rotation method based on $sin^2\psi$ technique.

At the sight of Table 5.12 we can conclude that, in agreement with multi-step BCP analysis, that rigid disks like resin - 15 μm diamonds (grinding) and hard composite disk (lapping) are inducing more residual stress on the sample surface than softer disks like synthetic fiber and soft composite disk.

Table 5.12: Residual stress (Positive + negative tilt range) measurements in Omega mode.

Step	Stress, MPa	Error, MPa
Synthetic fiber + 9 μm dia	-76	21.34
Hard composite disk + 9 μm dia	-182.5	55.4
Soft composite disk + 3 μm dia	-142.1	25.1
Resin - 15 μm diamonds	-238.6	56

Eventhough it is difficult to know at which extent the residual stress can affect superconducting properties, the simple rule "the lower the better" can be adopted in this case [4]. It is known from some experiments done on elliptical cavities that a stressed surface would entail an increase of the surface resistance [4].

To conclude on that point, the combination of several techniques like multi-step BCP analysis, XRD analysis and RF test would be required. Indeed, in between each etching step, the measurement of surface resistance under RF and the residual stress by XRD could give a complete picture on how superconducting properties and surface stress are correlated and evolving versus depth.

5.2.1.2.3 EBSD Analysis

EBSD analysis on the cross-sections have been accomplished for four recipes mentioned above. A special procedure has been required to prepare the samples for measurements (see Appendix C). Figure 5.24 shows general patterns which show the level of dislocations in material. GAM and GOS patterns show that first row of grains, at edge, has higher level of dislocations compare to other grains, in the bulk. In order to describe these dislocations more statistically misorientation of grains could be calculated locally in each pixel. Results are presented in Figure 5.25.

Samples treated with softer lapping disks and in particular with soft composite disk is showing lower KAM at higher degree of misorientation sign of a less damaged, less strained crystal. This observation is in agreement with other analyzes presented previously.

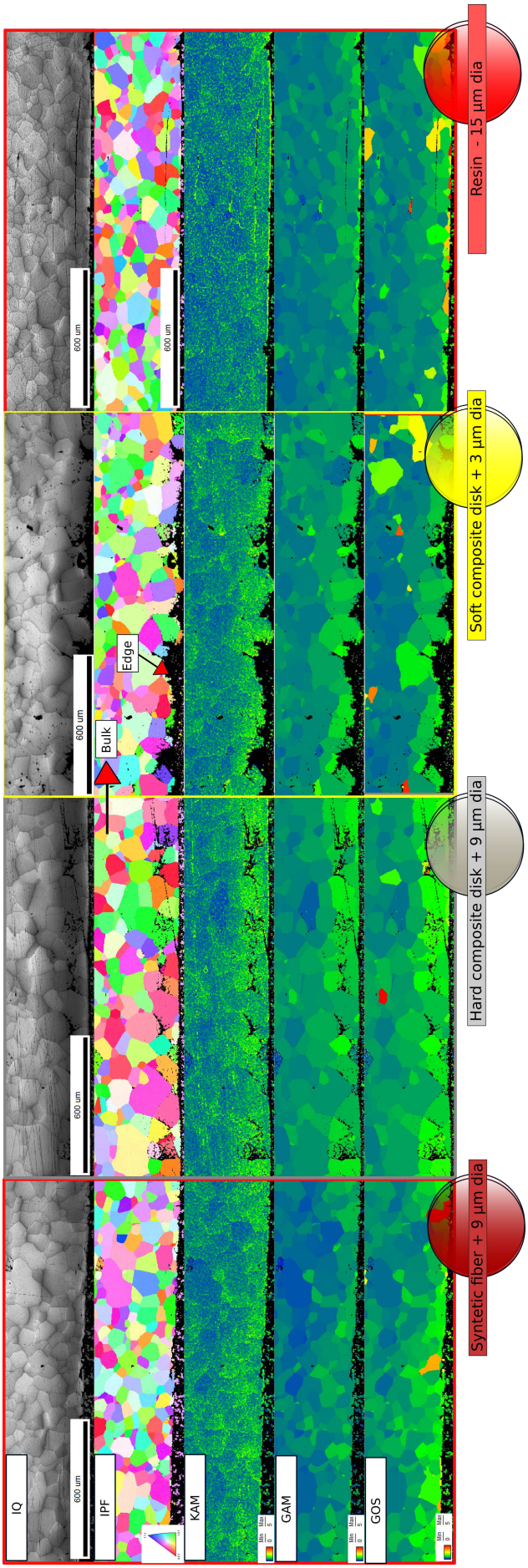

Figure 5.24: Image Quality (IQ), Inverse Pole Figure (IPF), Kernel Average Misorientation (KAM), Grain Average Misorientation (GAM) and Grain Orientation Spread (GOS) patterns of cross-section after abrasion step.

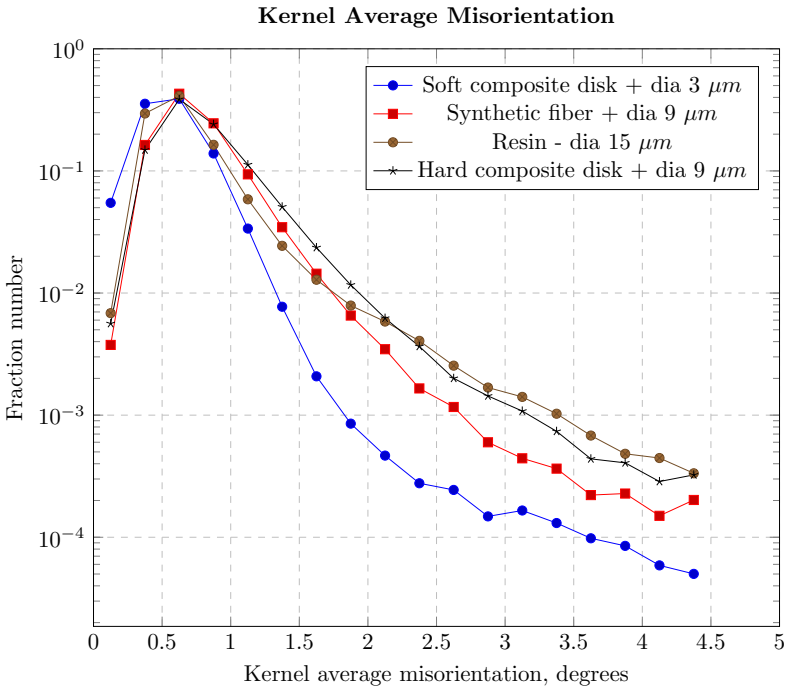

Figure 5.25: EBSD analysis (KAM measurements) of surface after abrasion step.

5.2.2 Polishing Step Study

The second step is aiming at not only reducing the surface roughness but also at removing enough material damaged during the previous abrasion step.

5.2.2.1 Final Roughness

For this final polishing step, only 3 configurations have been tested and were sufficient to converge toward very satisfying results, see Table 5.13. As visible in Figure 5.26, the use of regular diamond abrasives couldn't achieve a surface cleanup although the final surface roughness achieved is very good. It appears very quickly that a combined chemical-mechanical action was necessary to observe an efficient removal of embedded abrasives. Colloidal silica used in a basic solution (pH=9) has been tested with 2 different type of disk showing very similar results.

The optimal roughness is achieved very rapidly after approximately 15 minutes (See Table 5.13). As it will be seen in next section, this second polishing step has to be extended to ensure a complete de-pollution of the surface. Because of the chemical action, grains re-appear inducing a degradation of the surface roughness

Table 5.13: Surface parameters for polishing step.

Material, Type and Size of Abrasive	S_z, [μm]	S_a, [μm]	Processed time, [min]
Viscous fiber + dia 1 μm	1.49 ±0.29	0.04 ±0.01	15
Microporous polyurethane + SiO_2 50 nm	3.44 ±0.38	0.02 ±0.01	15
Microporous polyurethane + SiO_2 50 nm	2.58 ±0.43	0.1 ±0.05	200
Compressed polyurethane + SiO_2 50 nm	2.5 ±0.45	0.10 ±0.03	200

but could be lower then after electro-polishing ($S_a \sim 50$ nm) if time of treatment is adapted (less than 225 min).

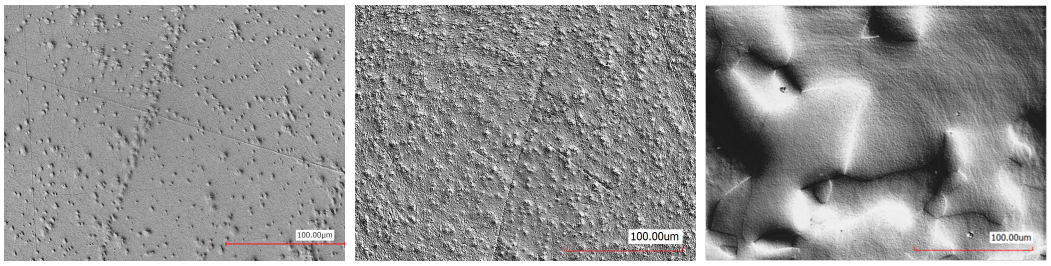

(a) after viscous fiber cloth + diamond 1 μm (15 min)

(b) after microporous polyurethane cloth + SiO_2 50 nm (15 min)

(c) after microporous polyurethane cloth + SiO_2 50 nm (200 min)

Figure 5.26: Laser confocal images after polishing step.

5.2.2.2 Depollution efficiency

De-pollution efficiency has been studied only with colloidal silica by observing the surface every 15 minutes. Figure 5.27 is showing how the polluted surface after first abrasion step (Soft composite disk + 3 μm diamonds) is evolving versus time. After 15 minutes, the "amorphous" scratched surface is turned into a scratch-less surface with a very obvious pollution with embedded diamonds. After 100

minutes corresponding to a removed layer of about 1 μm, no surface inclusion is observed anymore. The polishing process could be stopped at that point but as it is emphasized with red circles on Figure 5.27, some grains exhibit a very rough surface (or sub-grain patterns) up to 200 minutes. This corresponds to a removed layer of about 2 μm.

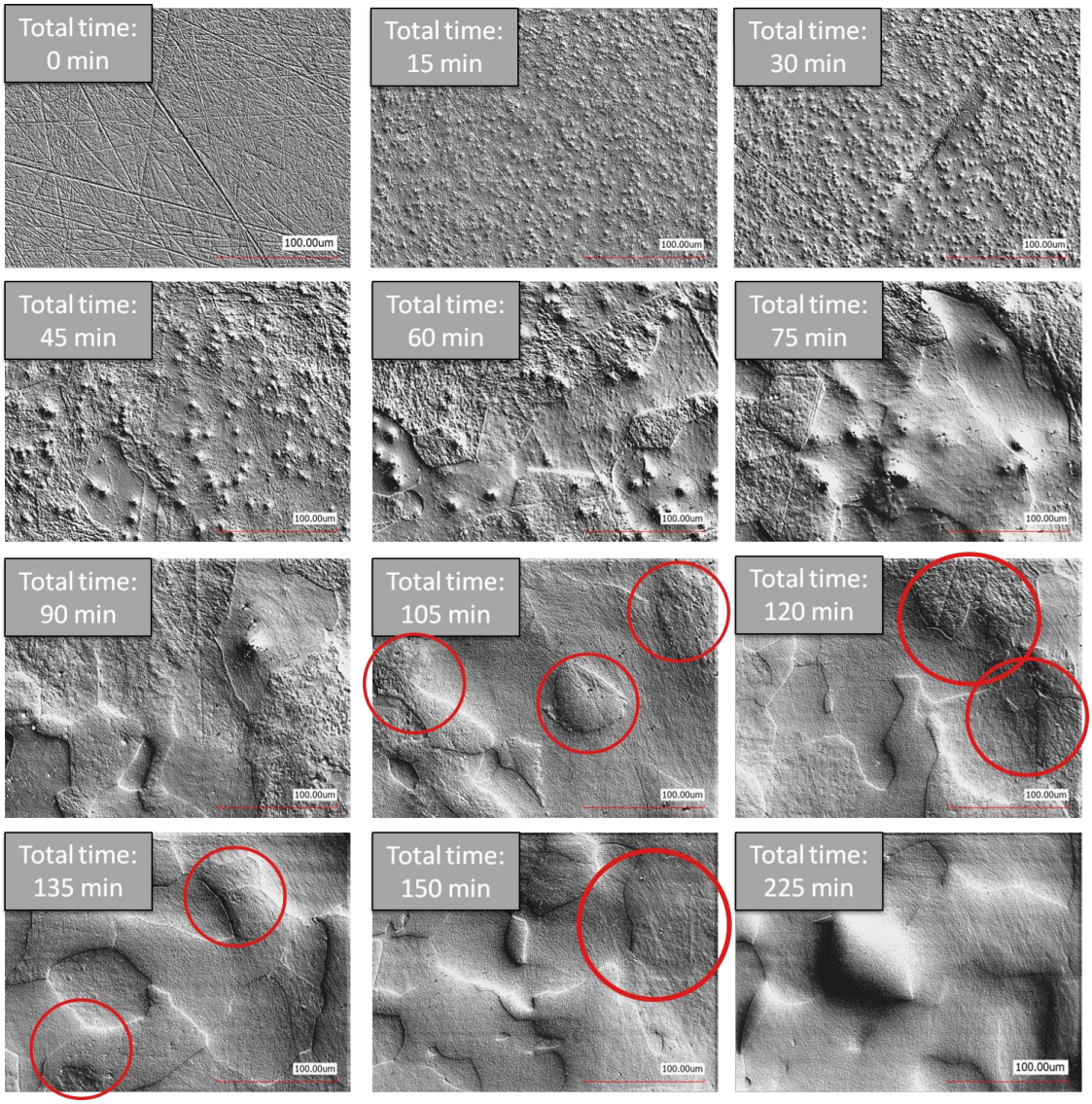

Figure 5.27: DIC images: surface de-contamination during 2 step (CMP polishing). Total thickness removed after 225 minutes is equal to 2.4 μm.

An alternative de-pollution method has been investigated consisting in performing a BCP treatment of few minutes. Figure 5.28 depicts the evolution of the surface roughness versus the duration of BCP. The surface roughness increases very rapidly and wouldn't satisfy the requirements already after 3 μm. A similar solution has been adopted by DESY. The abrasion step carried out by CBP would be followed by a "flash" EP [246].

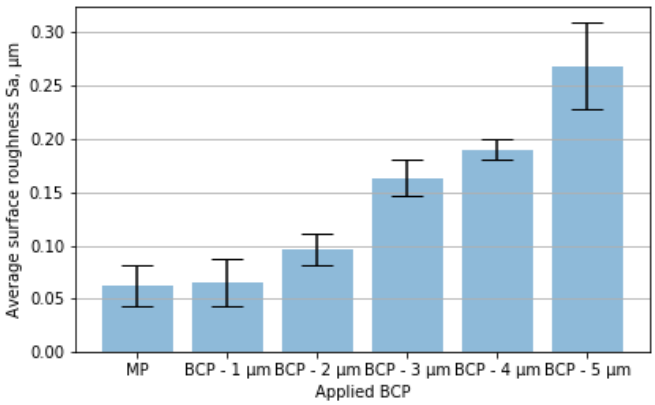

Figure 5.28: Surface roughness degradation versus accumulated BCP.

5.2.3 Optimized metallographic recipe

At the sight of all results presented for abrasion and polishing step, the optimal recipe that would allow to meet all requirements for SRF standards is the following:

- A suspension of polycrystalline diamonds with a grain size of 3 microns in combination with soft composite disk have been chosen for the abrasion step. The MRR of about 3 μm/min, constant versus time, could allow to remove 150 μm in a reasonable time (50 minutes);
- Polishing step has been performed by a special solution composed of 50 nm grain sized particles of colloidal silica (SiO_2, pH = 9) diluted in deionized water (20 %), carried on microporous polyurethane cloth. The depollution of the surface is obtained after about 200 minutes.

Important remark: So as to keep an efficient process, every 30 minutes during abrasion step and 15 minutes during polishing step, the supply of abrasive solutions is stopped while the polishing device running and water is flushed on the disk during several seconds to rinse out polishing residues.

Mirror-like surfaces are obtained as showed in Figure 5.29.

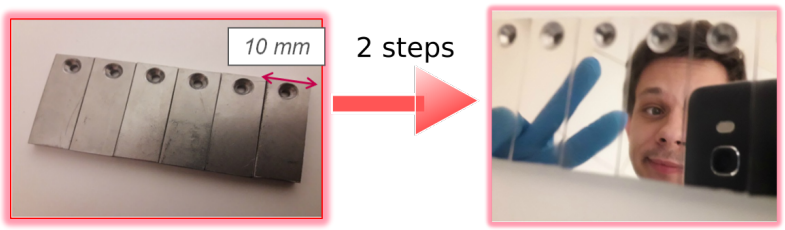

Figure 5.29: Raw Nb specimens before (left) and after (right) 2 step metallographic polishing recipe.

5.2.3.1 On Small Sample

Working pressure has been reduced to a pressure of 30 kPa instead of 120 kPa for 3 samples (10x40 mm) in order to simulate the polishing conditions of larger surfaces (limitation of device due to increased area and limited force up to 400 N). Mirror finished surfaces have been obtained for all Nb samples by using 2 steps polishing recipe.

Figure 5.30 is showing how the surface roughness is changing versus time during the full process.

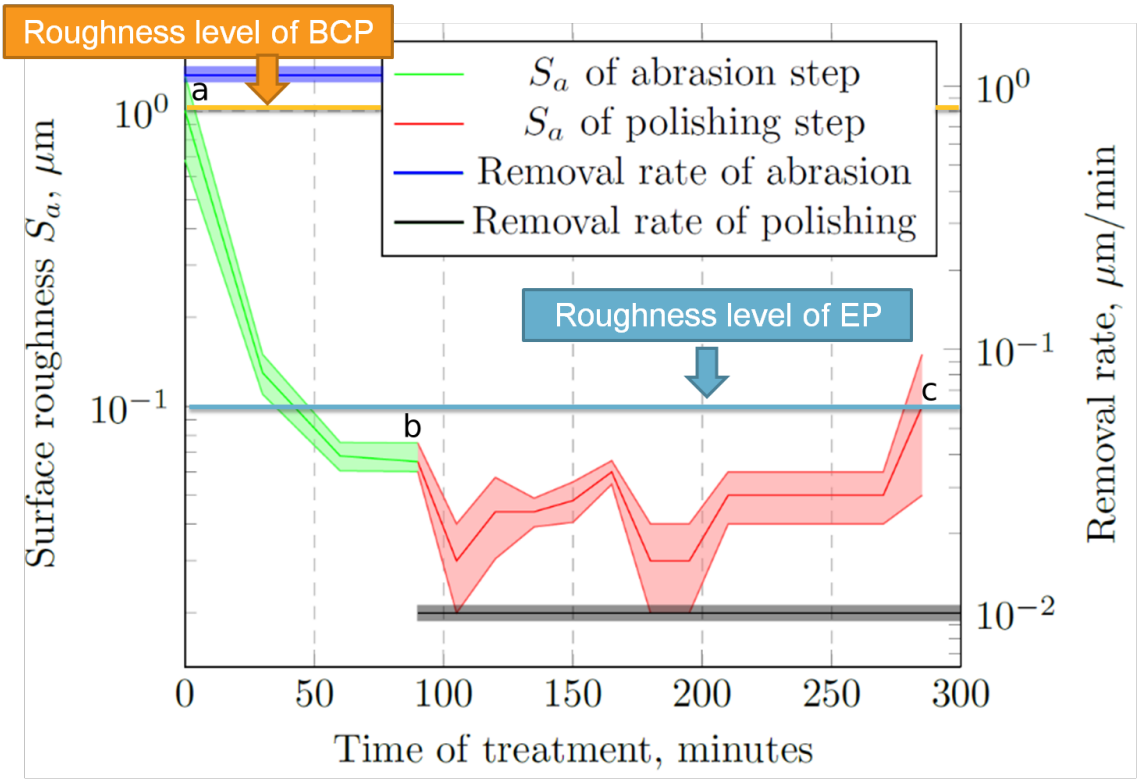

Figure 5.30: Evolution of the average surface roughness as a function of time [252].

In this example, we started from a surface that has been previously chemically etched by BCP (Picture a in Figure 5.31). The abrasion step (Soft composite disk + 3 μm-diamonds) was performed during about 90 minutes to compensate some misalignments between the sample and the disk. Picture b of Figure 5.31b is showing the surface state at the end of this step. The polishing step was then performed during 200 minutes to remove about 2 μm and obtain a very clean surface (Picture c in Figure 5.31c). The surface roughness is however slightly increased caused by the appearance of grains. This observation is in one sense very positive confirming that this process is inducing very little residual strain on the surface.

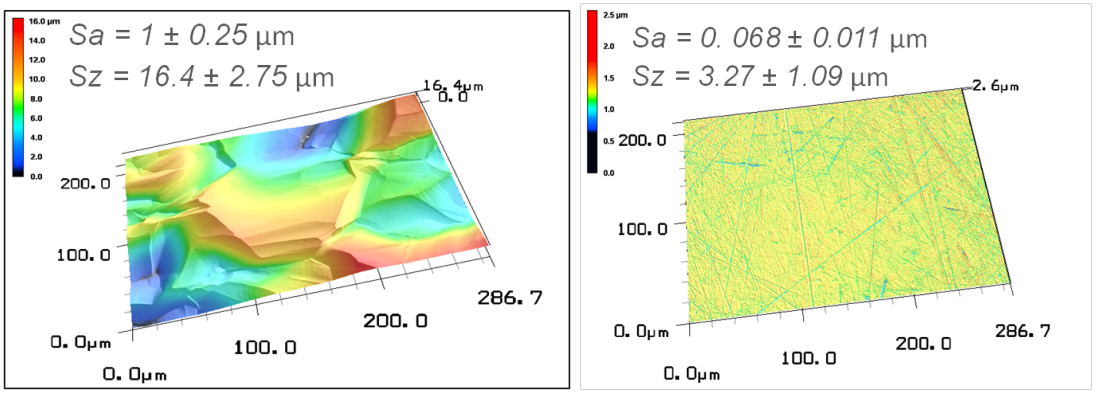

(a) (b)

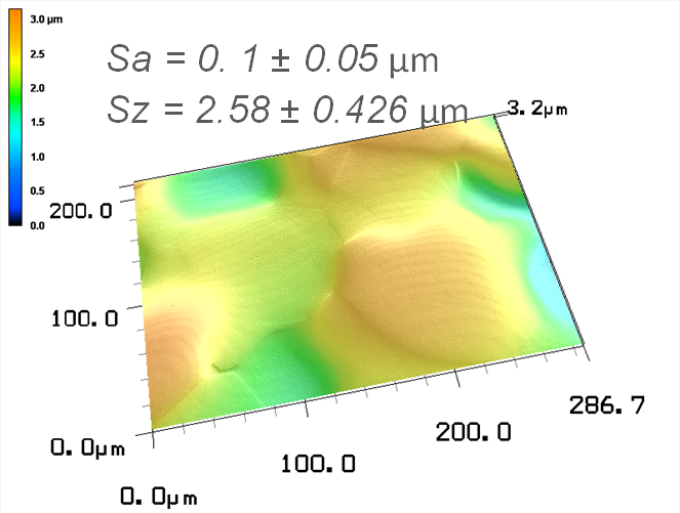

(c)

Figure 5.31: 3D reconstruction of Nb surface state after BCP (a), first step MP (b) and second step MP (c) [252].

5.2.3.1.1 Final surface parameter

Typically polishing step reduces roughness parameters, but due to the CMP action, roughness tends to reappear. After 15 min of a polishing run, the minimum surface roughness has been achieved (20 nm). However, this step could not be stopped directly and requires the prolongation of polishing run to remove all embedded particles and grain damages.

Table 5.14: Surface roughness parameters after abrasion and polishing steps. Disk rotation speed : 150 rpm, header rotation speed : 150 rpm, Pressure : 10 kPa, no counter-rotation.

Step	Ref disk	Type and Size of Abrasives	MRR, $[\mu m/min]$	S_z, μm	S_a, μm	Estimated duration time
Abrasion step	Soft composite disk	diamonds 3 μm	1.20 ± 0.1	3.27 ± 1.09	0.07 ± 0.01	125 min [1]
Polishing step	Microporous polyurethane	SiO_2 50 nm	0.01 ± 0.01	2.58 ± 0.43	0.1 ± 0.05	200 min [2]

Remark: The abrasion rate is divided by 2.5 in this case as the pressure was divided by 4.

5.2.3.1.2 XRD Analysis

The XRD analysis performed after this optimal recipe is showing that the residual stress after the first abrasion step has been significantly reduced, see Figure 5.32 and Table 5.15.

One can appreciate how residual stress is removed by this technique compared to CBP process, for which the residual stress (peak shift) remained constant after

[1] Every 30 minutes the supply of diamond suspension is stopped while the polishing device running and water is flushed on the disk during 30 seconds

[2] Every 15 minutes the supply of SiO_2 is stopped while the polishing device running and water is flushed on the disk during 30 seconds and cleaned with brush

polishing step (See Table 5.7).

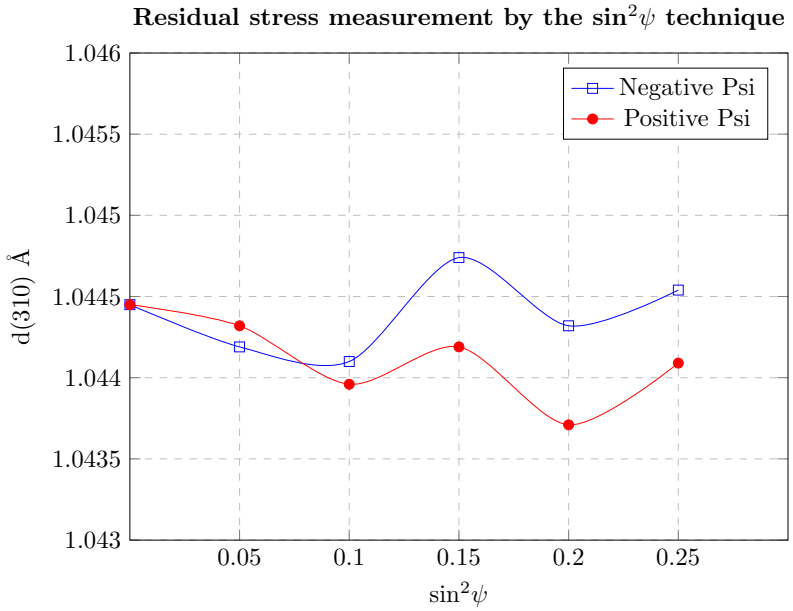

Figure 5.32: Inter planar distance (d) versus $sin^2\psi$ after 2 step MP recipe.

Table 5.15: Residual stress (Positive + negative tilt range) measurements in Omega mode.

Step	Stress, MPa	Error, MPa
1 Step	-142.1	25.1
2 Step	-20.7	60.4

5.2.3.1.3 EDS Analysis

The chemical composition evaluation of surface has been done with a resolution a few microns by using EDS at 20 kV. The energy spectrum of the polished surface after the 2 step recipe is showing a clean surface, comparable chemical etching (BCP), see Figures 5.33a and 5.33b. Examples of polluted surfaces with alumina and silicon are presented in the case of non-optimized polishing recipe, see Figures 5.33c and 5.33d respectively.

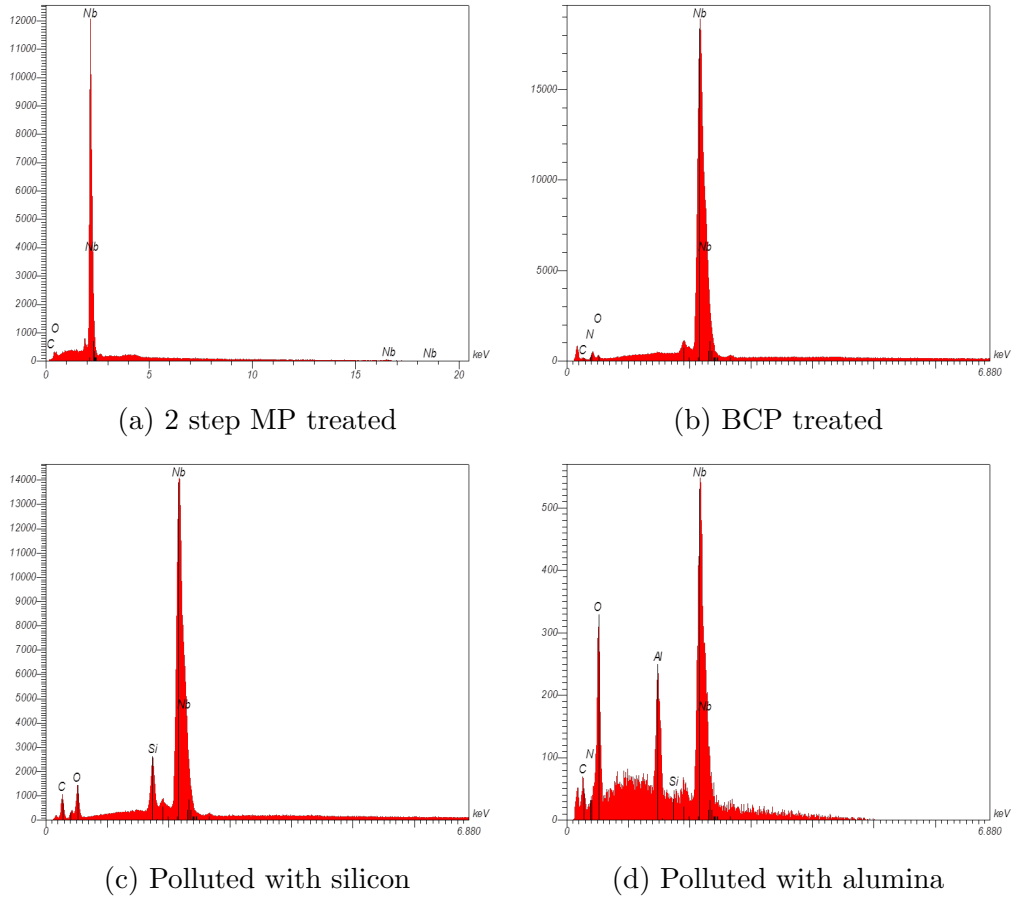

(a) 2 step MP treated

(b) BCP treated

(c) Polluted with silicon

(d) Polluted with alumina

Figure 5.33: EDS results of niobium surface after different type of polishing at a voltage of 20 kV.

5.2.3.1.4 EBSD Analysis

An EBSD analysis has been performed directly on the polished face contrary to previous EBSD analyzes that were done on the side after slicing and polishing. Figure 5.34 is depicting a very homogeneously crystallized surface with a deformed layer obviously very limited (IPF image). Indeed, the "information depth" of EBSD is of the order of several tens of nanometers. The KAM is highlighting a non-

homogeneous polishing quality. The center of the sample is showing a higher density of surface defects than the sides. This problem of polishing homogeneity is limited in this case of small samples but will be, as presented in next section, a real limitation for larger samples.

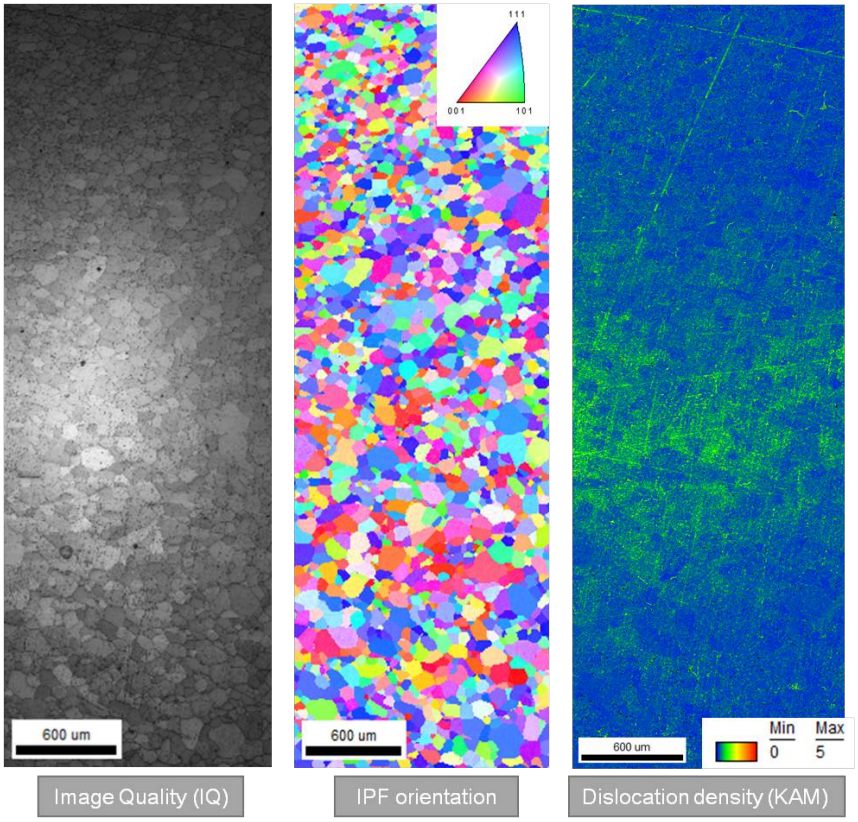

Figure 5.34: EBSD analysis of polished face. Chemical-mechanical action of SiO_2 during 90 mintues.

5.2.3.2 Recipe Transfer to Large Sample (126 mm)

In an effort to perform a final test to address the superconducting properties a Niobium surface polished by the optimal recipe, a Niobium disk of 126 mm in diameter has been prepared. This disk, similarly to the disk polished by CBP as presented previously, can be mounted on a resonant superconducting cavity to measure directly the surface resistance down to 2K [253]. Such a disk could be polished on the polishing device installed at IPNO but several problems have been encountered.

The polishing parameters should have been reduced as the polishing device was not powerful enough to apply the same pressure and speed parameters on such a large surface. The device was stuck due to a "suction cup" effect. The applied pressure was then reduced from 30 kPa down to 10 kPa. Moreover, the formation of "bright" and "dark" spots on the disk as been observed (See Figure 5.35b). After careful optical analysis, it appears that "bright" spots correspond to significant higher polluted regions compared to "dark" spots. Such a non-uniform surface quality is explained by a very bad distribution of the solution between the polishing cloth and the Nb disk. So as to ensure the uniformity of the polishing step, the polishing cloth (plain cloth) used on small samples was replaced by a meshed cloth (See Figure 5.36). As a result, the applied pressure on the disk could have been increased back to a normal value (30 kPa) and a very homogeneous surface quality has been achieved (See Figure 5.35c).

So as to carefully assess the depollution of such a large sample in different zones, a specific script as been written in Python, see Appendix A.1. This routine is able to localize and thus count the number of embedded particles from the optical image acquired with the confocal microscope.

Figure 5.37 is showing outputs of the script of a bright zone and dark zone for several duration of runs. The depollution efficiency versus time could be then monitored in various zones. Eventhough the starting number of embedded abrasives is approximately the same as well as their distribution in term of diameter (See Figures 5.37 and 5.38), their number in bright and dark zones don't seem to reduce at the same speed. This difference could be explained by a problem of flatness, leading to a non-homogeneous distribution of the polishing fluid. Such type of effect has not been observed with meshed disk as meshed structure helps at distributing the polishing fluid uniformly all over the surface.

(a) Initial state

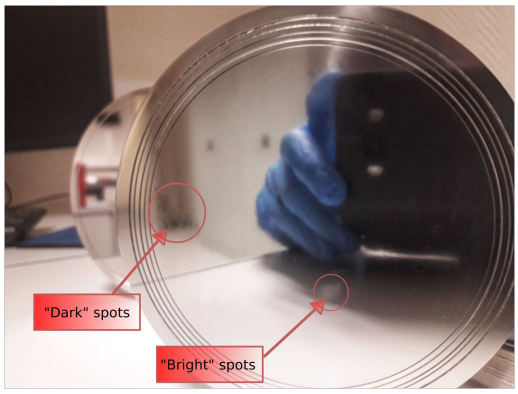

(b) After 2 step polishing (plain cloth)

(c) After 2 step polishing (meshed cloth)

Figure 5.35: Photographies of Nb disk before (a) and after 2 step metallographic polishing with plain (b) and meshed (c) microporous polyurethane cloths.

(a) Microporous polyurethane cloth is plain.

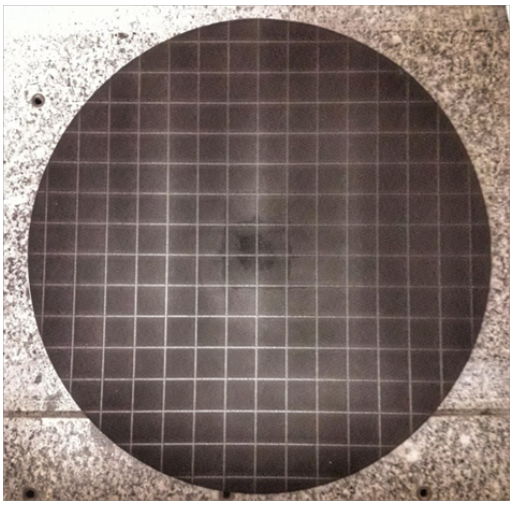

(b) Microporous polyurethane cloth is meshed

Figure 5.36: 300 mm-diameter polishing cloth used for polishing step.

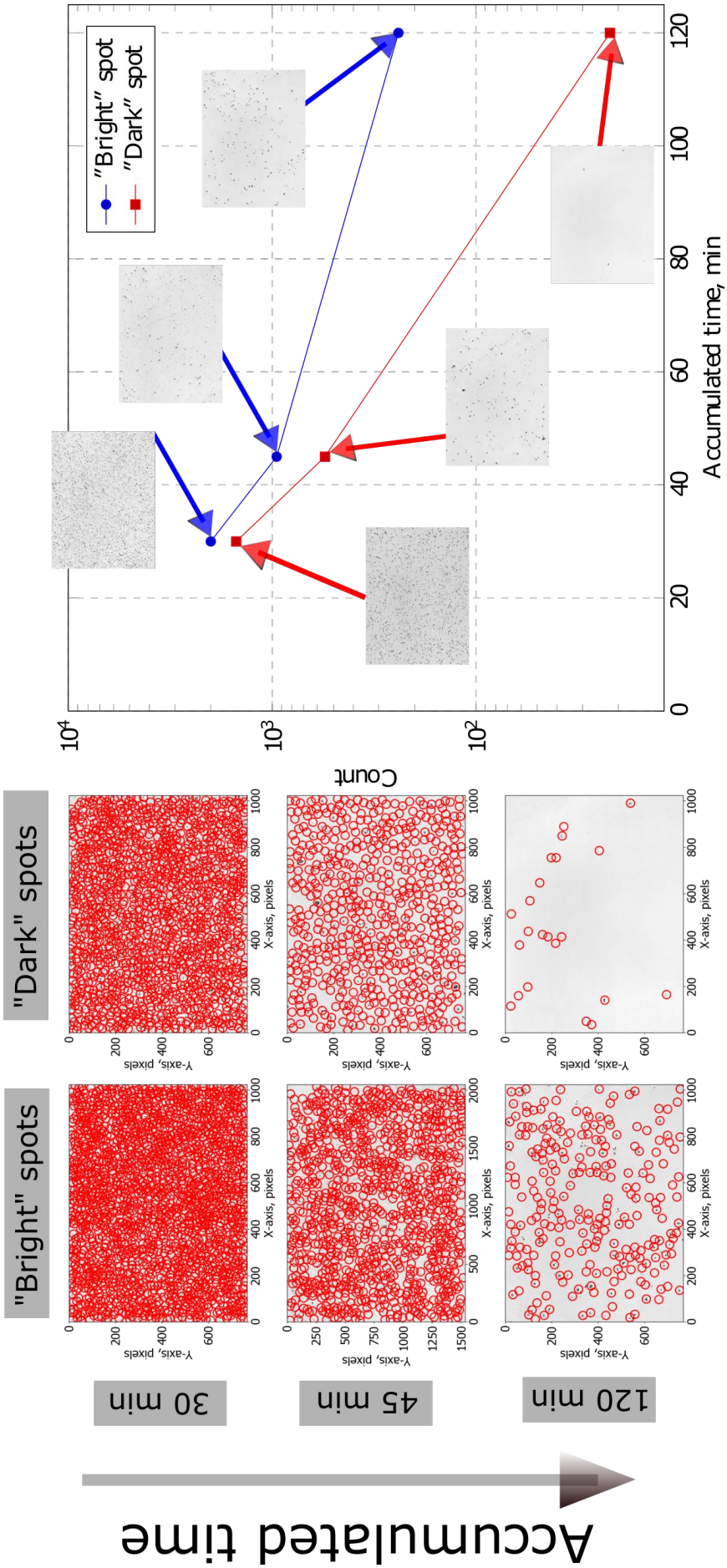

Figure 5.37: The calculated number of embedded particles from the optical image acquired with the confocal microscope.

Figure 5.38 represents sizes of embedded abrasives in "bright" and "dark" spots versus accumulated time of polishing run.

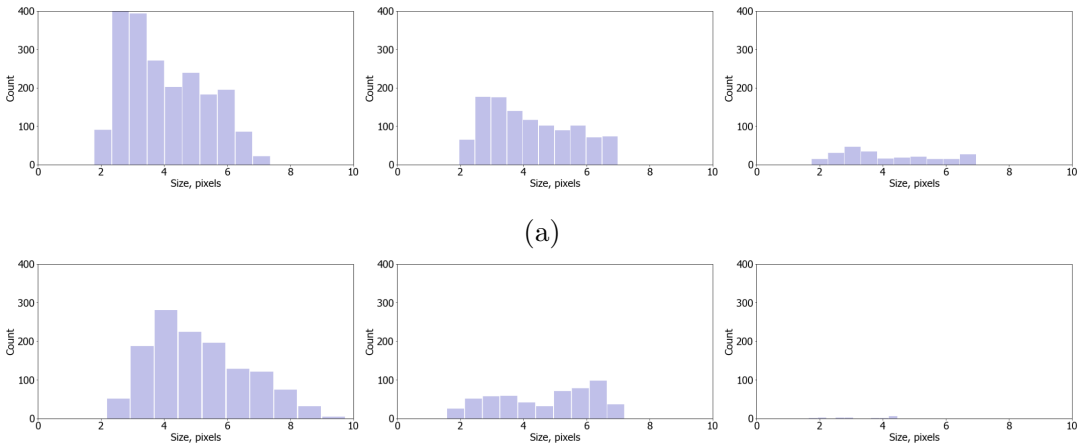

(a)

(b)

Figure 5.38: Evolution of particle size in "bright" (a) and "dark" (b) spots versus time (left image - 30 min, center image - 45 min and right image - 120 min).

5.2.3.3 RF analysis in sample test cavity at SLAC

RF measurements of flat disks have been done at SLAC in a hemispherical cavity which operates in TE_{032} mode (only magnetic field, no electrical field) at high frequency (11.4 GHz) and at cryogenic temperatures between 12 K and 3.8 K [254]. This test-bench does not require to be cooled down in liquid helium, the cryogenic temperatures are achieved thanks to a used cryocooler (whole cycle of cooling takes less than 24 hours). The walls of cavity are made of bulk copper sputtered with Niobium thin film on the RF side (the cavity is thus superconducting below 9.2K). Host-cavity, see Figure 5.39, gives the possibility to mount flat disks made of superconducting material with a diameter of 50.8 ± 0.3 mm and with the follow thicknesses: 0.43, 1.07, 1.78, 2.44, 3.00, 5.00 and 6.35 mm. The sample which has been polished by CBP could not be tested in such host-cavity, as disk with a diameter of 126 mm.

Two samples with final thicknesses of 3.00 ± 0.1 mm were prepared and treated at IPNO with the optimized 2-step chemical mechanical polishing recipe (CMP) as presented previously and with the standard chemical polishing (BCP) used as a reference, see Figure 5.40b.

The magnetic field on the disk is 2.5 times higher than on the walls of the

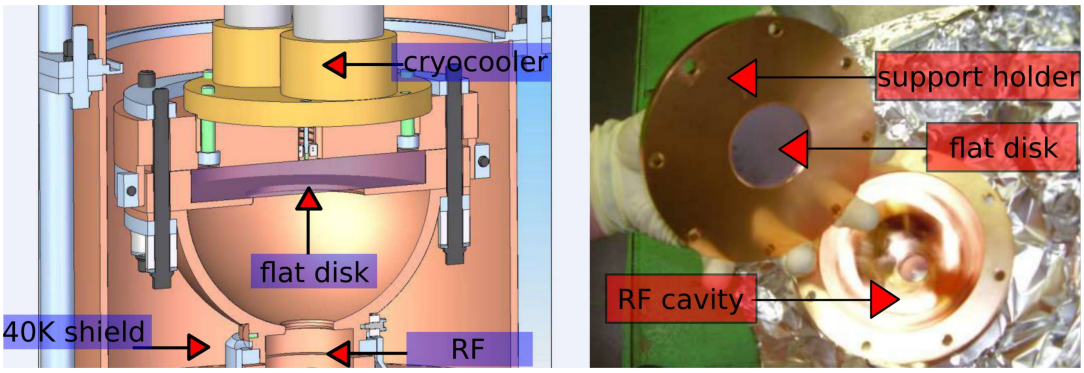

Figure 5.39: Left: Design of the hemispherical cavity at SLAC. The RF power is fed into the cavity from the bottom, the flat disk (purple) is held in place by clamping in the support holder. Right: Real image [254].

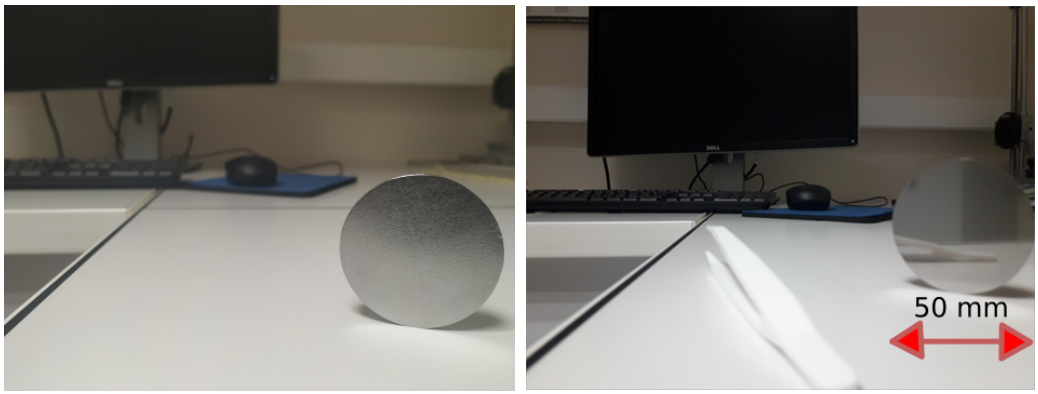

(a) (b)

Figure 5.40: Photographies of Nb disk after BCP (a) and after 2 step MP for RF test at SLAC.

hemispherical cavity. The RF losses on the tested disk, in the case if the surface resistance does not depend on the RF amplitude and is assumed homogeneous on the disk and the cavity, is equal to 33 % of all losses (67 % of losses on the hemispherical cavity) . The simulation of the magnetic field distributed on the disk shows the zeros of the magnetic field in the center and on the edges of the disk, see Figure 5.41. All surface H-fields are radial on the sample, so surface currents are azimuthal.

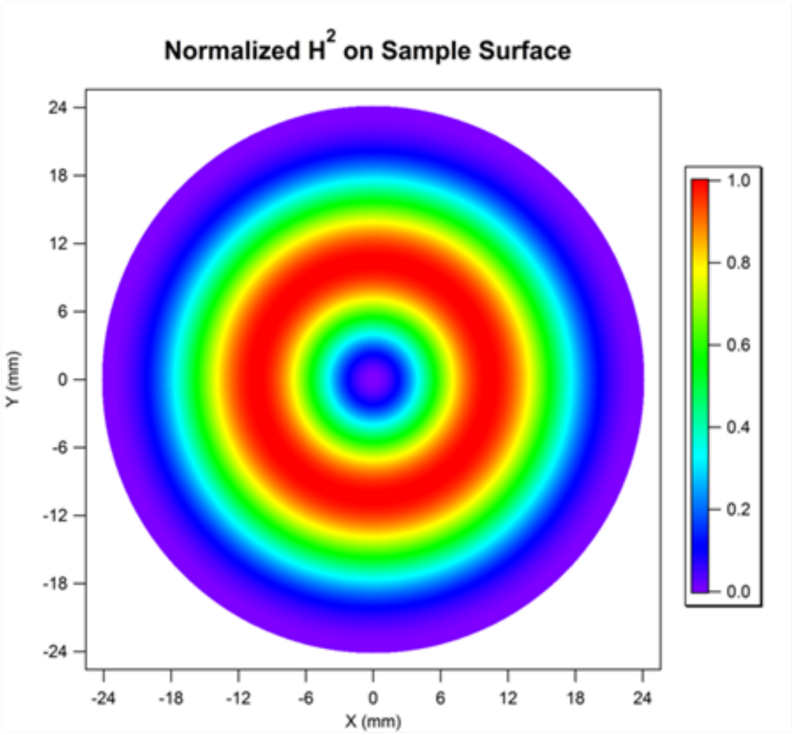

Figure 5.41: Distribution of magnetic fields on the disk. Courtesy of P. Welander.

For the resonating cavity with a disk plate, the quality factor is given by [255]:

$$Q_0 = \frac{G_{total}}{R_{total}} = \frac{G_{disk} + G_{cavity}}{\alpha_{disk} R_{disk} + \alpha_{cavity} R_{cavity}}, \tag{5.1}$$

where G_{total} is the total geometrical factor of the resonating cavity, which consists of G_{disk} (geometrical factor of the disk) and G_{cavity} (geometrical factor of the hemispherical cavity) and equal to 1403 Ω, $\alpha_{disk} = 0.33$, $\alpha_{cavity} = 0.67$, R_{disk} and R_{cavity} respectively the surface resistance of the disk and the surface resistance of the hemispherical cavity.

The quality factor of the resonance cavity is measured continuously while cooling down to 3.8 K. The measured quality factors of the tested disks are presented in Figure 5.42. The blue curve corresponds to IPNO reference sample (BCP) and the red curve to the CMP polished sample. At critical temperature T_c (9.2 K)

the Niobium material has its transition from normal state to the superconducting state, which is characterized by the significant increase of the quality factor. This transition temperature could be reduced in the case of a heavily polluted surface with non-superconducting materials. At 9.2 K both samples show a sharp increase of quality factor as a consequence of the transition of Nb material from normal to the superconducting state. However, a lower quality factor is observed below 4 K after CMP process, indicating the presence of surface pollution or damages.

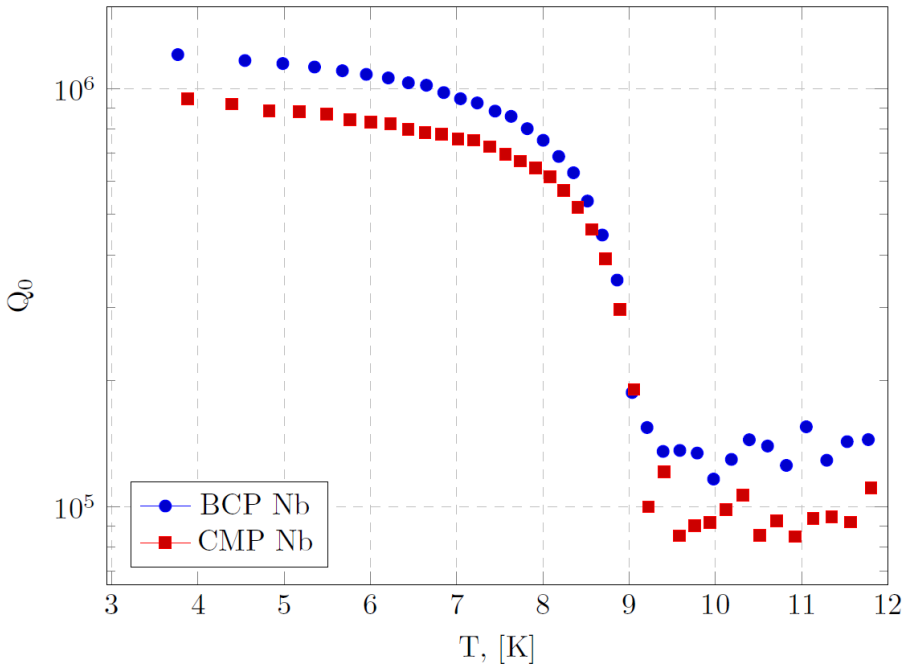

Figure 5.42: The quality factors of the BCP (blue curve) and the CMP (red curve) polished disks as a function of temperature [252].

The surface resistance of the disk, either after BCP or CMP, may be extracted from quality factor in the case of a strong assumption that the surface resistance of the reference disk is the same as for the hemispherical cavity [255]:

$$R_{cavity} = \frac{1}{(\frac{1}{G_{cavity}} + \frac{1}{G_{disk}})Q_{0,BCP}} \tag{5.2}$$

and

$$R_{disk} = G_{disk}(\frac{1}{Q_{0,CMP}} - \frac{R_{cavity}}{G_{cavity}}), \tag{5.3}$$

where G_{disk}=$\frac{G_{total}}{\alpha_{disk}}$ = 4251 Ω and G_{cavity}=$\frac{G_{total}}{\alpha_{cavity}}$ = 2094 Ω.

The behaviour of extracted surface resistance versus T_c/T ratio is presented in Figure 5.43. Measured surface resistance consists of the sum of the BCS surface

resistance (ideal Nb) and the residual resistance (presence of the impurities in Nb). As shown in Figure 5.43, according the BCS model, see Equation (2.64), the surface resistance should be well below measured values (at 4 K and at frequency 11.4 GHz the BCS resistance would be typically of the order of 80 $\mu\Omega$). However the tested disks, even the BCP treated Nb shows a very early saturation of the surface resistance caused by a very high residual resistance (2 mΩ). These early stabilizations of the surface resistance for both disks could be the sign of the Q-disease (See Chapter 2) as samples were not degassed in a furnace before RF test or the existence of anomalous dissipations (bad RF contacts, magnetic field trapping or pollution of the sputtered cavity itself).

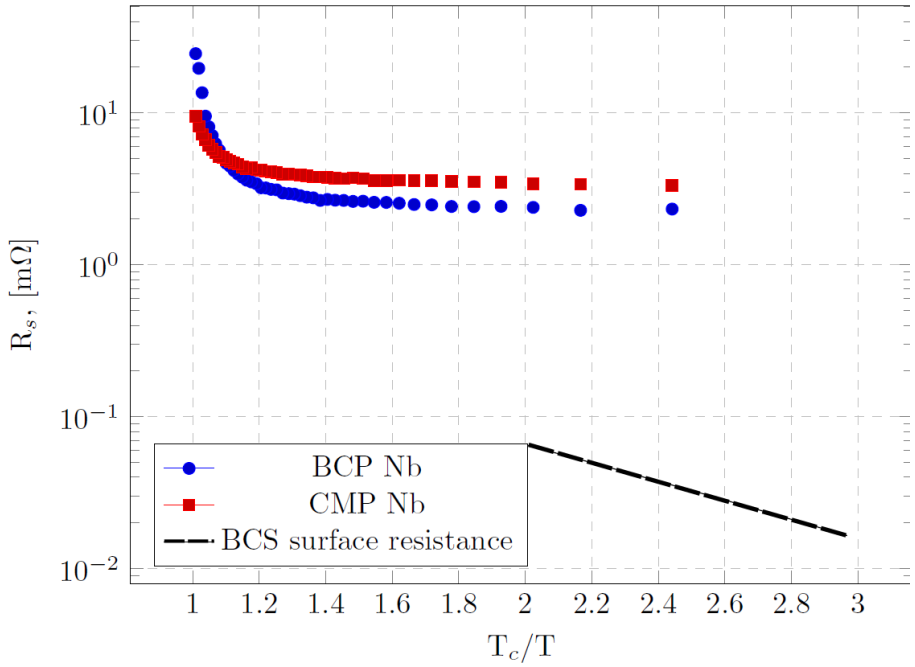

Figure 5.43: The surface resistance of the BCP and CMP samples versus T_c/T [252].

The test results were extremely encouraging, since CMP polished disk reached lightly lower quality factor than BCP polished disk. At this frequency, very strong limitations are encountered as even the reference sample is exhibiting an anomalous and very early saturation of the surface resistance versus temperature. It is thus in our case not possible to address the surface resistance degradation due to CMP. A way to mitigate these "high frequency" limitations would be to test a disk at a lower frequency (3.88 GHz), as on IPNO test bench (TE_{011}, the disk diameter is 12.6 cm) as soon as this one would be available (the disk is ready to be tested). Also both disks were not heat treated in order to remove the Hydrogen from surface, which increased the R_{res}.

5.2.3.4 Recipe Transfer to Very Large Disks (330mm)

Final goal of this thesis is to prepare one-cell cavity based on 2-step MP recipe, but this goal is postponed due to lack of time. This thesis has been mainly focused on the development of polishing recipe, which required to investigate plenty of parameters (rotation speed, abrasives, disks...) and how they affect on Nb surface, leaving the preparation of cavity outside the scope of this manuscript. However, there are some future steps for prolongation of this study:

- extend the polishing process to larger sheets (at least 300 mm);
- apply alternative cavity forming technique, as electro-hydroforming, to polished sheets (no-direct contact with dies in order to protect the polished surface).

Concerning on the dimensions of required disks for cavity fabrication, see Figure 5.44a, such disk could not be polished by metallographic polishing machine at IPNO (diameter of workpiece has to be below half the diameter of the disk), so alternative solution will be carried out at LAM PLAN company on a lapping machine (diameter of plate is 1000 mm). However, a transfer of 2 step recipe from metallographic to lapping machine requires adaptation of the first polishing step by replacing soft composite disk. A preliminary plan has been discussed with our collaborator LAM PLAN and results will be presented in the near future.

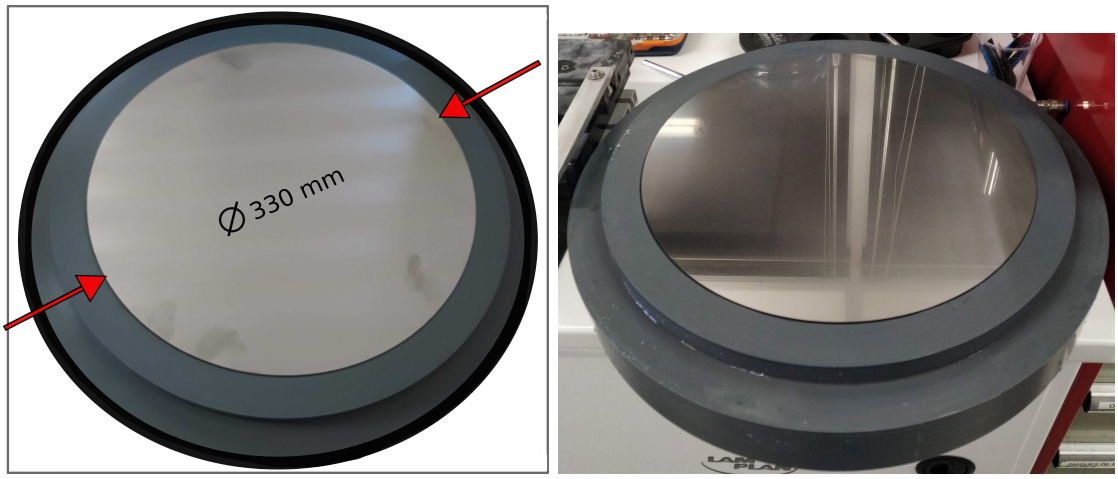

(a) (b)

(c)

Figure 5.44: Photography of disk with a diameter of 330 mm before polishing (a), after 2 steps polishing (b) and a lapping machine (b) [227].

Chapter 6

Conclusion & Perspectives

Conclusions

The aim of this PhD was to study an alternative path to reduce the cost of fabrication and surface preparation of SRF cavities to make the construction of future projects like ILC or FCC possible. Moreover, these cavities are nowadays mainly made of high-purity polycrystalline bulk Niobium, but other superconductors called alternative (compounds or alloys) could offer significant improvements in term of accelerating gradient and cryogenic losses, but require to be deposited as thin films on a workable substrate like Niobium or Copper. Hence, defect-free (no-damage, no-pollution), flat and smooth substrates are required as the quality of the deposited film strongly depends on the initial surface quality of the substrate. The roughness of polycrystalline Niobium (used as bulk or as substrate) has to be definitely improved by developing new techniques capable of surpassing current state of the art achievements obtained by standard chemical treatment (BCP, EP). The study of alternative polishing techniques could help addressing these 2 problematics. Considering requirements to recover Nb surface after fabrication step (remove damaged layer), preserve superconducting performances (high specifications of the chemical composition and the microstructure) and industrialization constraints (cost, environment, ...), this thesis was articulated in three steps. The first step was devoted to the study of potential alternative polishing techniques and selection of the most promising one. An overview of the following techniques has been done: laser polishing, plasma polishing, electrolytic-plasma polishing, magnetorheological polishing, metallographic polishing (MP) and centrifugal barrel polishing (CBP). However, not all of them could satisfy the aforementioned requirements. Based on the paper

review of the literature and our personal research, the following conclusions were drawn:

- Laser polishing shows many advantages for SRF cavities because laser polishing can be applied on complex geometries and does not induce significant deformations or stress. However the achieved roughness is higher compare to metallographic polishing due to the fact that roughness of the laser polished surface strongly depends on the initial state of the surface. Conclusion: this technique, could only be used as a final polishing step (material removal is not possible) to recover crystallographic damages from a previous abrasion step.

- Plasma Polishing (PP) and Electrolytic Plasma Polishing (EPP) both improve roughness compared to BCP treatment with an equivalent material removal rate. However chemical cleaning is required due to significant contamination of the surface from cathode. Conclusion: too many steps for industrialization, but could be used as complementary technique to EP. Needs optimization.

- Electrolytic plasma polishing (EPP) as plasma polishing (improves roughness, has pollution from cathode and electrolyte), basically has the same results. Conclusion: these techniques could be used as complementary for the abrasion step as no stress is applied on the material and the material removal rate is reasonable. However the induced chemical pollution of the surface requires to perform the final polishing by another technique.

- Magnetorheological polishing shows low efficiency in term of material removal, but extremely low roughness gives a possibility to use this technique as final polishing step. Conclusion: cannot be used for large scale production.

- CBP (already applied in SRF-community) provides a better surface roughness and could be more efficient at removing some surface defects compared to EP and BCP. However, this process does not satisfy requirements for large scale production due to strong surface pollution and an extremely long processing time. Conclusion: could be used as complementary technique to EP. Needs optimization: reduce number of steps and pollution.

- Metallographic polishing provides an improved roughness and material removal rate compared to conventional chemical treatments. However, MP cannot be directly applied on enclosed geometries, but only on flat geometries. This technique could be potentially used for abrasion and polishing steps for large scale production. However, more advanced studies have to be performed

to check if any forming methods could maintain or not degrade significantly surface properties of Niobium.

Hence, the second step of thesis has been devoted to understand the state of the art of mechanical polishing by operating a CBP and MP devices.

At JLab, Fermilab and DESY laboratories CBP treatment were performed on elliptical SRF cavities in 4-5 steps. Contrary to CBP, metallographic polishing has been not performed yet for SRF cavities, but recipe for Nb already exists (5-6 steps). However, these recipes are not optimized in term of industrialization or crystallographic quality for SRF needs.

The final step of this work has been focused on the optimization of recipe for both polishing techniques.

Firstly, we tried to reproduce the state of the art of CBP with a slightly different device (oblique axis to allow polishing of 3D geometries), trying to understand limitations and to optimize the recipe by the reduction of the processing time (reduction of intermediate steps) and surface pollution.

For both techniques, abrasion capabilities have been thoroughly investigated to address not only material removal rate and final surface parameters, but also the extension of induced crystallographic damages and pollution. For both techniques, it appeared that a real trade-off has to be done between achieving a reasonable removal rate (to optimize duration of this first step) and limiting surface defects and pollution (to optimize duration of polishing step). For CBP, plastic media with a medium abrasive power is recommended. For MP, pre-polishing lapping disks with relatively small diamond abrasives (between 3-9 μm) appear to be the best compromise.

The final polishing step for both techniques has been studied also extensively in order to check residual strains and pollution. the following conclusions are drawn:

- For CBP
  - Ultra-smooth mirror finished surface ($S_a \approx 30$ nm).
  - The depollution efficiencies are not sufficient to remove totally the surface pollution in a reasonable time.
  - The minimum polishing processing time would be 400 hours in 3 steps recipe.

  - The mechanically damaged layer produced after CBP was investigated by multi-step BCP with the following optical analysis and XRD technique in gonio and grazing modes. Exploring such a layer by so different physical techniques are shown that the results in the agreement and damages after the first step couldn't be removed by the following steps, just slightly reduced.

- For MP technique:

  - After 15 min of a polishing run, the minimum surface roughness has been achieved (S_a - 20 nm). However, this step could not be stopped directly and has to be extended to ensure a complete de-pollution of the surface. Because of the chemical action, grains re-appear inducing a degradation of the surface roughness but could be lower then after electro-polishing ($S_a \approx 50$ nm) if time of treatment is adapted (less than 225 min).
  - An alternative de-pollution method has been investigated consisting in per- forming a BCP treatment of few minutes. However, the surface roughness increases very rapidly and wouldn't satisfy the requirements already after 3 μm.
  - Optimized recipe on small samples has been successfully transferred to larger samples of 126 mm in diameter (disk).
  - Crystallographic quality (strain, dislocation density,...) after 2 steps polishing recipe has been verified by XRD and EBSD techniques. The crystal quality has been preserved underneath the surface.
  - Chemical composition of surface after 2 steps recipe has been checked by EDS technique. Pollution by abrasives has not been observed.
  - Finally, RF cryogenic test has been performed at 11.4 GHz. The results were extremely encouraging, since CMP polished disk reached lightly lower quality factor than BCP polished disk. At this frequency, very strong limitations are encountered as even the reference sample is exhibiting an anomalous and very early saturation of the surface resistance versus temperature. It is thus in our case not possible to address the surface resistance degradation due to CMP. A way to mitigate these "high frequency" limitations would be to test a disk at a lower frequency (3.88 GHz), as on IPNO test bench (TE_{011}, the disk diameter is 12.6 cm) as soon as this one would be available (the disk is ready to be tested).

Perspectives

This thesis has been mainly focused on the development and optimization of polishing recipes, which required to investigate plenty of parameters (rotation speed, abrasives, disks...) and how they affect on Nb surface, leaving the fabrication of cavity outside the scope of this manuscript. However, based on the work presented in this thesis we give some recommendations for future on mechanical polishing.

Metallographic polishing (MP) is a candidate not only for bulk Nb treatment, but could also provide the mirror-finished substrate for alternative SRF thin films deposition. Roughness of polished surface by a 2 steps recipe has been proven better than standard EP/BCP treatment and less polluted than CBP. MP provides on flat surfaces a high removal rate (above 1 μm/min) and high reproducibility. So as to remove the damaged layer and recover superconducting properties it requires less than 6 hours of treatment (one day treatment). There are some future steps required to fully qualify metallographic polishing as an alternative to chemical treatment:

- characterize the polishing disk at lower frequencies (few Ghz) at IPNO in order to mitigate technical limitations (RF contacts)encountered at frequencies higher than 5 GHz.
- extend the polishing process to larger sheets (at least 300 mm), corresponding to dimensions of disks needed to form half-cells for 1.3 GHz elliptical cavities.
- apply alternative cavity forming technique, as electro-hydroforming, to polished sheets (no-direct contact with dies in order to protect the polished surface). Preliminary studies carried out by CERN with $BMAX$ company are very encouraging [256].
- study more carefully the real impact of sub-grain/stress in surface on superconducting properties after MP procedure.

Appendix A

Python Algorithms

A.1 Script for Identification of the Chemical Elements in SIMS Spectrum

To identify the chemical elements presented in the spectrum, the Python algorithm has been developed.

Listing A.1: Python code

```
import csv
import peakutils
from plotly.offline import plot
from plotly.graph_objs import Scatter, Layout, Figure


def read_file(file_path):
with open(file_path, "r") as file:
lines = file.read().split("\n")
for i in range(len(lines)):
lines[i] = lines[i].replace(";", ",")

stream = csv.reader(lines, delimiter=',', quotechar='|')

arr = []
for row in stream:
arr.append(row)
return arr

def get_data_file1(file):
```

```
21 file = read_file("D:/SIMS/file1.csv")
22 file.pop(0)
23 file.pop(0)
24
25 mass = []
26 sem = []
27 for i in file:
28 if len(i) == 5:
29 mass.append(float(i[3]))
30 sem.append(float(i[4]))
31 return mass, sem
32
33 def get_data_file2(file):
34 file.pop(0)
35 dataDic = {}
36 for i in file:
37 if len(i) > 0:
38 key = int(i[0])
39 dataDic[key] = []
40 for j in i[1:len(i)]:
41 if len(j) > 1:
42 dataDic[key].append(j)
43 return dataDic
44
45
46 def get_peaks(mass, sem, thres):
47 indexes = peakutils.indexes(sem, thres, min_dist=0.1)
48 maxY = [sem[i] for i in indexes]
49 maxX = [mass[i] for i in indexes]
50 return maxX, maxY
51
52
53 file1 = read_file("D:/SIMS/file1.csv")
54 file2 = read_file("D:/SIMS/file2.csv")
55
56 mass, sem = get_data_file1(file1)
57 dataDic = get_data_file2(file2)
58
59 # threshold of measured elements
    ----------------------------------------
60 thres = 1000 / max(sem)
61 # ----------------------------------------
62
63 maxX, maxY = get_peaks(mass, sem, thres)
64 labels = []
```

```
65
66 for i in maxX:
67 if int(i) in dataDic.keys():
68 labels.append(",".join(dataDic[int(i)]))
69 else:
70 labels.append("#")
71
72 scat1 = Scatter(
73 x=mass, y=sem, name ="Measured Spectrum", mode='lines+markers'4
74 )
75 scat2 = Scatter(
76 x=maxX, y=maxY, name="Identified Peak", mode='markers',
77 marker=dict(color='red',symbol="star", size=12), text=labels
78 )
79
80 data = [scat1, scat2]
81 layout = Layout(
82 xaxis=dict(title="Mass of elements, [amu]",visible=True,
83 rangeslider=dict(visible=True, range=[min(maxX), max(maxX)])
84 ),
85 yaxis=dict(title="Counts per second",
86 type='log',autorange=True
87 ),
88 title="Identification of chemical elements"
89 )
90 figur = Figure(data=data, layout=layout)
91 plot(figur)
```

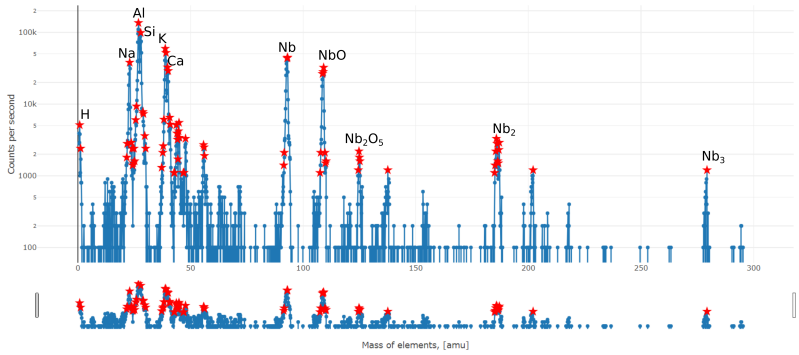

Figure A1.1: SIMS spectrum of Nb sample after mechanical polishing with identified elements.

A.2 Script for the Data Analysis of Roughness Parameters

This script displays a solution (graph) of measured roughness parameters by showing a chosen parameter in a quick way (among 24 parameters).

Listing A.2: Python code

```
# -*- coding: utf-8 -*-
"""
@author: $hryhorenko
"""
#import all libraries-------------------------------
import sys
import csv
import glob
import pandas as pd
import matplotlib as mpl
import matplotlib.pyplot as plt
import numpy as np
mpl.rc('figure',  figsize=(15, 10))
plt.style.use('classic')

# get raw data from file names, directory 1-----------------------------------------------------
path =r'D:\Laser confocal microscope\BCP_damage_layer study\After Platinum 4 fixed 15 um diamons\30 kPa\csv x50'
filenames = glob.glob(path + "/*.csv")
files_csv = [f for f in filenames if f[-3:] == 'csv']
files_csv
# get raw data from file names, directory 2-----------------------------------------------------
path =r'D:\Laser confocal microscope\BCP_damage_layer study\After Silver + 9 um diamonds\csv x50'
filenames_1 = glob.glob(path + "/*.csv")
files_csv_1 = [i for i in filenames_1 if i[-3:] == 'csv']
files_csv_1
# get raw data from file names, directory 3-----------------------------------------------------
path =r'D:\Laser confocal microscope\BCP_damage_layer study\After Platinum Gold + 3 um diamonds\30 kPa\csv x50'
filenames_2 = glob.glob(path + "/*.csv")
files_csv_2 = [k for k in filenames_2 if k[-3:] == 'csv']
files_csv_2
```

```
# get raw data from file names, directory 4----------------------------------------------------
path =r'D:\Laser confocal microscope\BCP_damage_layer study\After 2TT2 +9 um diamonds\csv x50'
filenames_3 = glob.glob(path + "/*.csv")
files_csv_3 = [l for l in filenames_3 if l[-3:] == 'csv']
files_csv_3
# get raw data from file names, directory 4----------------------------------------------------
path =r'D:\Laser confocal microscope\BCP_damage_layer study\After lamination\csv x50'
filenames_4 = glob.glob(path + "/*.csv")
files_csv_4 = [s for s in filenames_4 if s[-3:] == 'csv']
files_csv_4
#DataFrames ------------------------------------------------------------------------------------


df = pd.DataFrame()
df_1 = pd.DataFrame()
df_2 = pd.DataFrame()
df_3 = pd.DataFrame()
df_4 = pd.DataFrame()
#cycle1 ----------------------------------------------------------------------------------------


for f in files_csv:
data = pd.read_csv(f,sep=';',skiprows=50)

df = df.append(data)
#cycle2 ----------------------------------------------------------------------------------------


for i in files_csv_1:
data_1 = pd.read_csv(i,sep=';',skiprows=50)
df_1= df_1.append(data_1)
#cycle2 ----------------------------------------------------------------------------------------


for k in files_csv_2:
data_2 = pd.read_csv(k, sep=';', skiprows=50)
df_2 = df_2.append(data_2)
#cycle3 ----------------------------------------------------------------------------------------


for l in files_csv_3:
```

```
data_3 = pd.read_csv(l, sep=';', skiprows=50)
df_3 = df_3.append(data_3)
#cycle4
```

```
for s in files_csv_4:
data_4 = pd.read_csv(s, sep=';', skiprows=50)
df_4 = df_4.append(data_4)
#
```

```
#files_csv=files_csv.reset_index()
#files_csv.reset_index(inplace=True)


# Choose the surface roughness (24 parameters) parameter from 6
    categories
#Height parameters       : Sq, Ssk, Sku, Sp, Sv, Sz, Sa
#Spatial parameters      : Sal, Str, Std
#Hybrid parameters       : Sdq, Sdr
#Functional parameters   : Sk, Spk, Svk, Smr1, Smr2, Sxp
#Functional volume par   : Vvv, Vvc, Vmp, Vmc
#Features                : Spd, Spc
parameters_list = ['Sa']
Sur_Par = df[df.iloc[:, 0].isin(parameters_list)]
Sur_Par_1 = df_1[df_1.iloc[:, 0].isin(parameters_list)]
Sur_Par_2 = df_2[df_2.iloc[:, 0].isin(parameters_list)]
Sur_Par_3 = df_3[df_3.iloc[:, 0].isin(parameters_list)]
Sur_Par_4 = df_4[df_4.iloc[:, 0].isin(parameters_list)]
#size of plot
fig, ax = plt.subplots(figsize=(14,7))
#arrays with points of removed layer with the BCP
```

```
T_Gold=[0,6,12,24,45,69,88,110,153]
T_Silver=[0,6,12,24,45,69,88,110,153]
T_Fiber=[0,6,11,21,43,65,86,113,157]
T_P4_30=[0,6,12,24,45,69,88,110,153]
T_Lam=[0,13,25,37,49,60,83,106,129,152,174,240,310]
T_Lam_20=[0,37,49,60,83,106,129,152,174,240,310]
T=[0,300]
Ref=[60,60]

#ax.annotate('local max', xy=(70, 2), xytext=(55, 2.5),
#             arrowprops=dict(facecolor='black', shrink=0.05),
#       )
```

```
101 plt.plot(T_Lam, Sur_Par_4['None'],marker='>', linestyle='--', color='y'
    , linewidth=2, markersize=12, label='Lamination')
102 plt.plot(T_Fiber,Sur_Par_3['None'],marker='d', linestyle='--', color='m
    ', linewidth=2, markersize=12, label='After 2TT2 + dia 9 $\mu$m')
103 plt.plot(T_P4_30,Sur_Par['None'],  marker='x', linestyle='--', color='g
    ', linewidth=2, markersize=12, label='After Platinum 4')
104 plt.plot(T_Silver,Sur_Par_1['None'],marker='*', linestyle='--', color='
    b', linewidth=2, markersize=12,  label='After CAMEO Silver + dia 9
    $\mu$m')
105 plt.plot(T_Gold,Sur_Par_2['None'],marker='o', linestyle='--', color='r'
    , linewidth=2, markersize=12, label='After CAMEO Gold + dia 3 $\
    mu$m ')
106 #plt.xticks(np.arange(0, 320, 10))
107 #plt.xticks(np.arrange)
108 #print(plt.style.available)
109 #Auto-correlation length as a function of BCP removed layer - Sal
110 #Arithmetical mean height as a function of BCP removed layer - Sa
111 #Texture aspect ratio - Str
112 #Root mean square gradient - Sdq
113 #Developed interfacial area ratio - Sdr
114 #Density of the peaks - Spd
115 #Arithmetic mean peak curvature - Spc
116 mpl.style.use('fivethirtyeight')
117 ax.set_title("Average surface roughness as a function of BCP removed
    layer", size = 20)
118 ax.set_xlabel(r"Removed layer, $\mu$m", size = 16)
119 ax.set_ylabel(r"Sa, $\mu$m", size = 16)
120 ax.legend(loc='best')
121 ax.set_yscale('log')
122 ax.grid()
123 ax.set_ylim([0.01,100])
124 ax.set_xlim([0,160])
125 #ax.set_yscale("log", nonposy='clip')
126
127 # Save the previous figure
128 fig = ax.get_figure()
129 fig.savefig("parameters_raw.png", bbox_inches="tight")
```

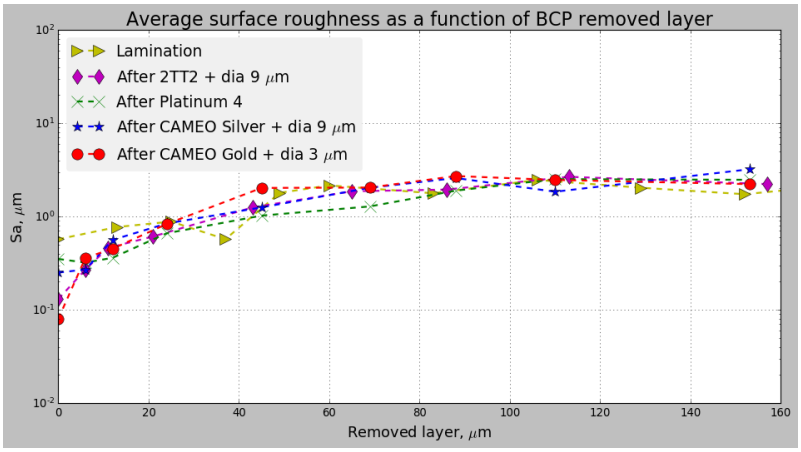

Figure A1.2: Degradation of average surface roughness versus accumulated BCP treatment.

A.3 Script to Count Embedded Particles

This script statistically describes the de-pollution by counting number and size of embedded particles trough recognition of bright/dark locations from laser confocal images [257]. Dark locations correspond to embedded particles.

Listing A.3: Python code

```
# -*- coding: utf-8 -*-
#libraries for arrays and data analysis
import numpy as np
import pandas as pd
from pandas import DataFrame, Series
#download special packages (pims and tp), detailed procedure of
    installation is described on:
#https://soft-matter.github.io/trackpy
import pims
import trackpy as tp
# library to plot graphs
import matplotlib as mpl
import matplotlib.pyplot as plt
import matplotlib.ticker as ticker
%matplotlib inline

#optional styles for fonts and graph
plt.rcParams.update({'font.size' : 22})
plt.rcParams.update({'font.family' : 'Tahoma'})
mpl.rc('figure',  figsize=(12, 6))
mpl.rc('image', cmap='gray')
#image converted to array
```

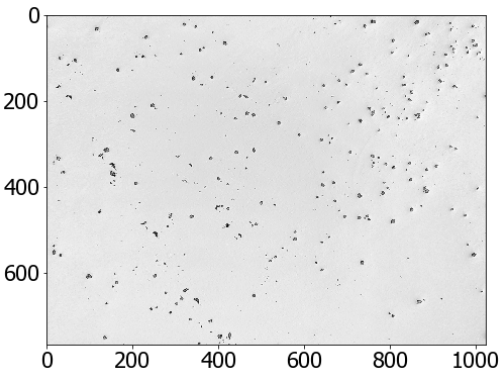

(a) non-identified embedded particles

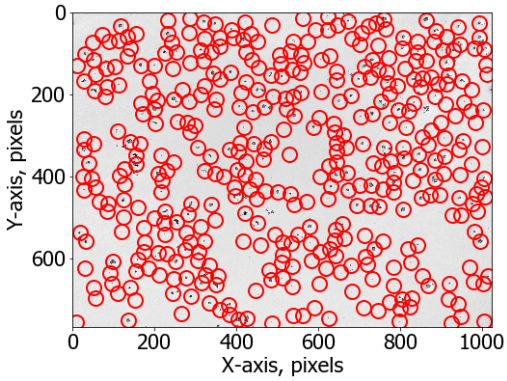

(b) identified embedded particles

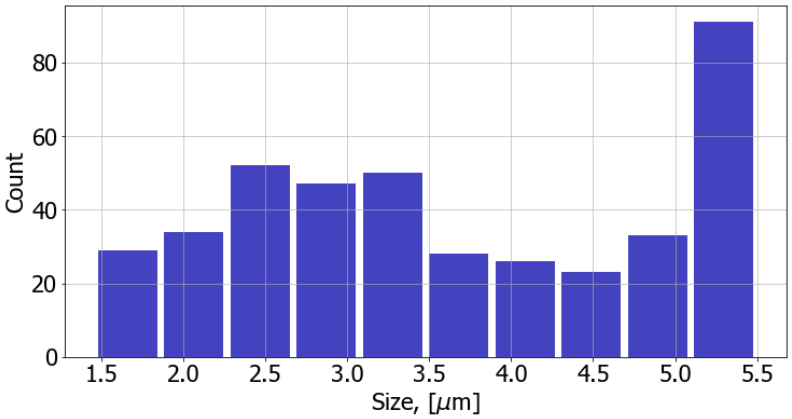

(c) Statistical description of embedded particles versus their size.

Figure A1.3: Statistical characterization of de-pollution.

```
22 arr = pims.ImageSequence("C:/Users/Hryhorenko/Documents/Particles/nb-
       bright-spot-x-50-3.bmp", as_grey=True)
23 #Package tp for identification of embedded abrasives
24 loc=tp.locate(arr[0],19,maxsize=5, invert=True)
25 ax.set(xlabel='Size', ylabel='Count')
26 ax.grid()
27 plt.figure()
28 plt.xlabel('X-axis, pixels')
29 plt.ylabel('Y-axis, pixels')
30 tp.annotate(loc, arr[0])
31 #histogram shows size-variation of embedded abrasives over all surface
32 fig, ax = plt.subplots()
33 commutes = pd.Series(loc['size'])
34
35 n, bins, patches = plt.hist(x=commutes, bins=10, color='#0504aa',
36 alpha=0.75, rwidth=0.9)
37 plt.grid(axis='y', alpha=0.75)
38 plt.grid(axis='x', alpha=0.75)
39 ax.set(xlabel='Size', ylabel='Count')
```

Appendix B

Electrolytic-Plasma Polishing (EPP)

Figure A2.1 shows the view of an initial surface, a polished by BCP and a polished by EPP (initial state of surface corresponds to BCP treated). The samples after BCP have been EPP-treated during 10 minutes in a special electrolyte. It can clearly be seen, see Figure A2.2, that a reduction in the surface roughness S_z has occurred. The BCP polished surface has a surface roughness S_z of approximately 21 μm. However, in the EPP-polished surface, S_z-values approximately of 8 μm were obtained. Furthermore all plasma polished workpieces are glossy in contrast to unpolished and BCP-treated samples.

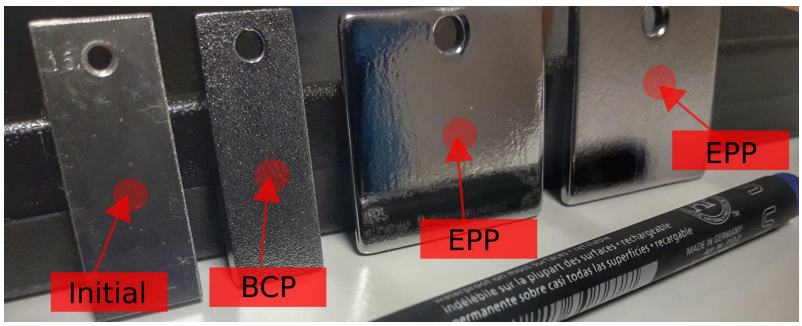

Figure A2.1: Photographies of samples at different states: initial, after BCP and after EPP.

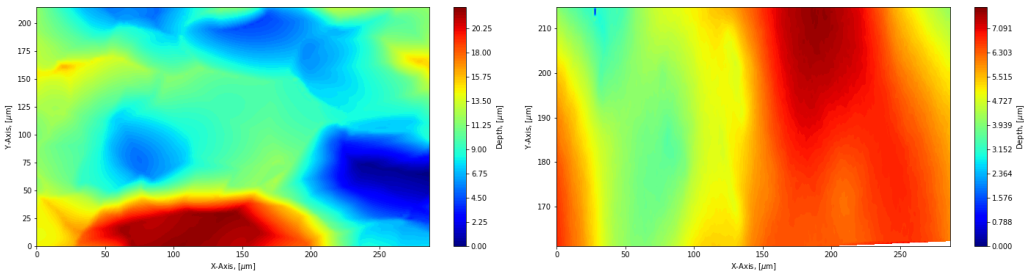

(a) (b)

Figure A2.2: Height image before EPP (after BCP) - (a) and after EPP - (b). Note: initially samples have been BCP-treated.

Additional analysis has been performed by SIMS in order to verify the chemical composition of the surface after EPP. Figure A2.3 shows the appearance of significant pollution (H, Fe,...), which corresponds to elements used in the electrolyte. Hence, further investigations could be performed in order to find the best conditions for Nb (replace Fe cathode by Nb,...).

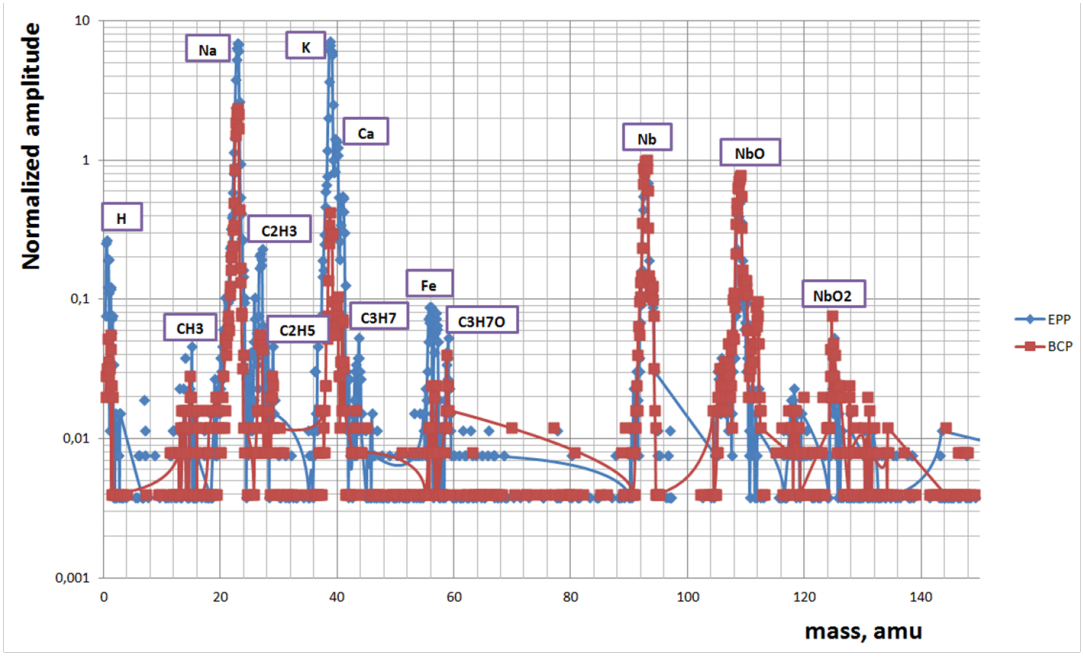

Figure A2.3: Chemical composition of the surface after BCP and EPP.

Appendix C

Cross-Section Preparation for EBSD Analysis

Special procedure of the surface preparation for EBSD measurements has been inspired from metallographic science and were adopted for our needs. EBSD analysis requires the mirror polished surface, proper cleaned surface and the compact sizes.

Typically the general preparation of the EBSD samples starts from sectioning in order to obtain the required dimensions for SEM chamber. After sectioning is mounting, several grinding steps and several polishing steps. Before and after each step the samples were rinsed by deionized water, degreased by ethanol and cleaned in the ultrasonic bath. Blow-drier have been used in order to remove the water from the analyzed surface to the edges of the sample, otherwise evaporated hydrides from surface will disturb the images of the grains.

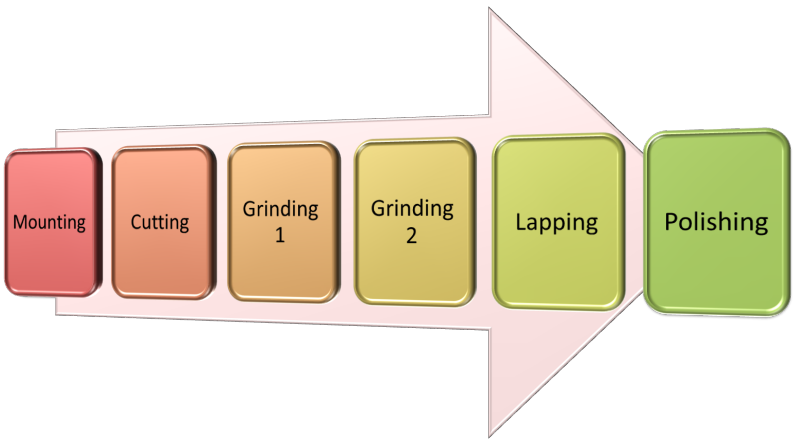

Figure A3.1: Cross-section preparation of polished material for EBSD analysis

However for our samples the operations of sectioning and mounting were reversed (1-mounting, 2-sectioning), as shown in Figure A3.1 in order to protect already polished surface interface. Investigations of the cross-section required the extremely careful procedure damaged layer created by the abrasives used for polishing.

Mounting

After metallographic polishing the samples were mounted in the epoxy by the cold method technique. This technique represents the mixing of the resin-solution with hardener, the volumes 2 to 1 respectively. During mixing it is necessary to avoid the air bubbles. Epoxy is polymerized during 10 hours under normal conditions (ambient pressure and room temperature). As during curing the temperature of the epoxy is increased, the system with cool air blow was installed.

The ceramic balls were used in order to increase the hardness of the resin and decrease their shrinkage due to reduced fallen edge effects. They are available in various colours (red, blue, yellow) to identify the mounted samples.

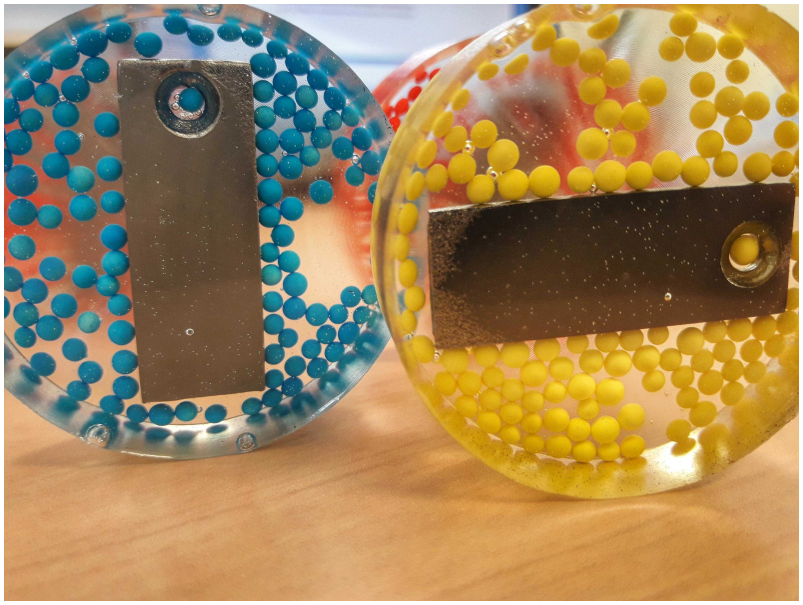

Figure A3.2: Mounted samples in the epoxy with the different ceramic balls (yellow, blue and red).

Cutting

After metallographic polishing the samples were cut by the high-speed cut-off machine Mecatome T210 manufactured by a French company, PRESI. The view of machines exterior is shown in Figure A3.3a and interior in Figure A3.3b.

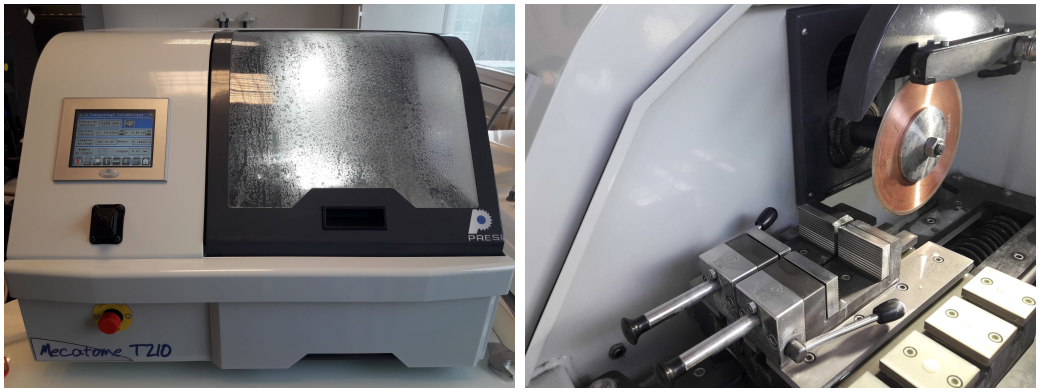

(a) (b)

Figure A3.3: Images of high-speed cutting machine from PRESI: a - view outside, b - view inside.

Different types of cutting wheels were studied and the produced cross-sections were investigated by confocal imaging (laser mode). There are two types of abrasives used in cut-off wheels: SiC and diamonds. Diamonds in their order are bounded in resin (LR disk) or metal (LM and LM+ disks). As can be seen in Figure A3.4, diamonds bounded in resin give better surface quality after cutting process compare to others disks.

Hence LR disk has been chosen for EBSD cross-section preparation. Cutting parameters which were used for cutting procedure:

- Cutting wheel: diamond (LR from PRESI production),
- Rotational speed of wheel: 1500 RPM,
- Diameter of the wheel: 150 mm,
- Speed of the platform: 0.1 mm/s
- Used Lubricant: deionized water

Figure A3.5 shows how the prepared samples are looks for treatment procedure (the region of EBSD interest is in contact with the epoxy).

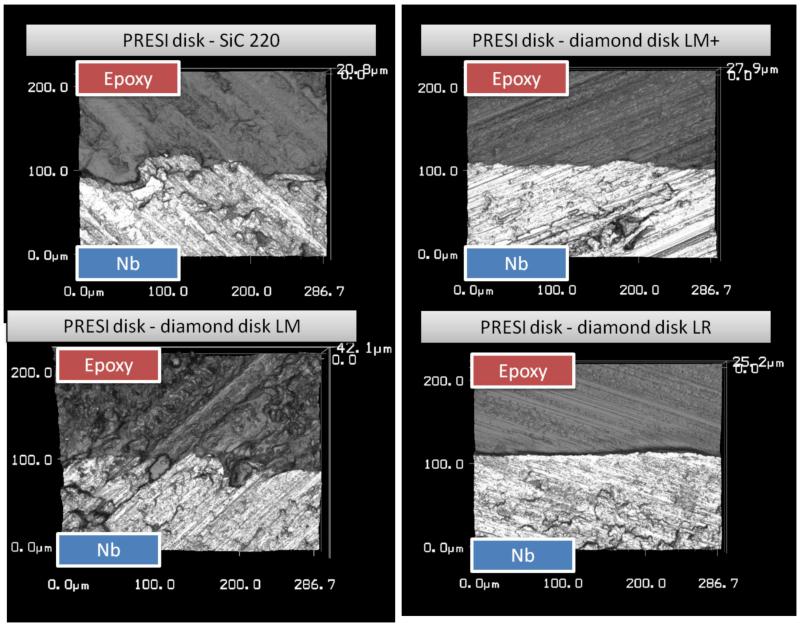

Figure A3.4: Laser confocal images of Nb surface produced by different cut-off wheels.

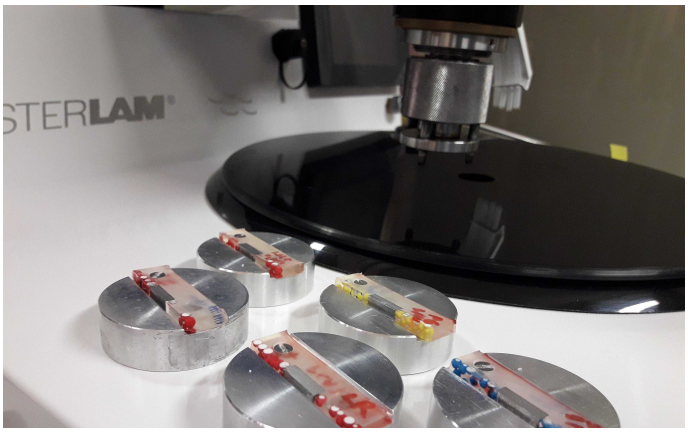

Figure A3.5: Prepared samples for the treatment procedure.

Polishing

Polishing of cross-sections have been done on the metallographic polishing machine described in Section 4.1.1. A set of samples was first polished by the RCD lapping disk (Platinum Gold) charged with diamonds (3 μm) during 45 minutes. The polishing was then continued with 1 μm diamond suspension on the soft viscose fibre cloth (4FV3) during 15 minutes, followed by the final chemical mechanical polishing step (90 minutes). CMP is a good method for removing the damaged layer of the sample which has been affected by abrasives during the abrasion and polishing steps. The CMP was carried out with special silica colloidal solution (liquid final from Lamplan). At several intermediate steps of the each process individual samples were taken in order to study the effect of the polishing procedure up to that point. The samples were analysed with a laser confocal microscope in laser and DIC-modes Section 4.2.3. The polished cross-section is presented in Figure A3.6.

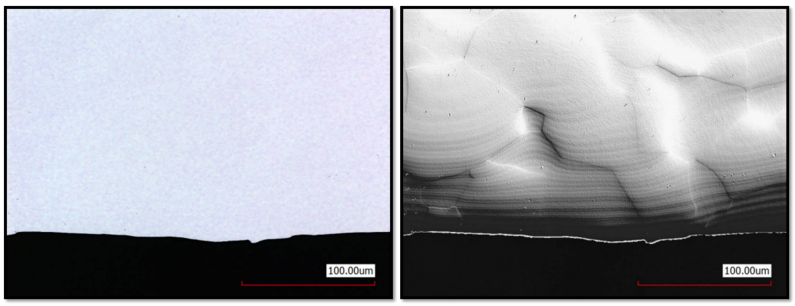

Figure A3.6: Confocal imaging of the polished cross-section in laser-optical (left) and DIC modes (right).

Appendix D

Functional Surface Parameters

In the tribology science may be used the additional parameters. For example, the functional parameters(S_k, S_{pk}, S_{vk}, S_{xp}, S_{mr1}, S_{mr2}, V_{mc},V_{mp},V_{vc},V_{mc}) define the bearing area of surface during contact with another surface due to the elimination of the certain peaks and valleys [258, 259], see the Abbott-Firestone curve (Figure A4.1). These material ratio defines the wear of the surface.

They do not give any information about directional characteristics, but they are useful to investigate the height distribution regions.

Parameter S_{pk} defines the highest peak, this place characterized by the largest contact stress due to small contact-interfaces between the surfaces. To cut this region the parameter S_{mr1}, defined in the percentages (typically 10 %), may be used. The highest points of the height profile have the fastest wear. The functional volume parameter S_{mp} represents the S_{pk}, but for volume under peak.

Parameter S_{vk} indicates the deepest valley, it is region where debris of processing is trapped. To cut this region analogical parameter to S_{mr1}, can be used, which is called as S_{mr2} (typically 80 %). The functional volume parameter V_{vv} represents the S_{vk}, but for volume above valley.

S_k represents the core height of the surface. This parameter characterizes the roughness and shows the bearing area, the place where the applied pressure will be distributed during processing between the surfaces. The functional volume parameters S_{mc} and S_{vc} represents the S_k, but for volume under and above the core line respectively.

Table D.1: Functional and functional volume parameters of 3D surface roughness.

Parameter, [Unit]	Meaning
S_k, [μm]	Core height
S_{pk}, [μm]	Reduced peak height
S_{vk}, [μm]	Reduced valley depth
S_{xp}, [μm]	Extreme peak height
S_{mr1}, [%]	Percentage of material that comprises the peak structures
S_{mr2}, [%]	Percentage of material that comprises the valleys structures
V_{vv}, [%]	Volume above valley
V_{vc}, [%]	Volume above core height
V_{mp}, [%]	Volume under peak height
V_{mc}, [%]	Volume under core height

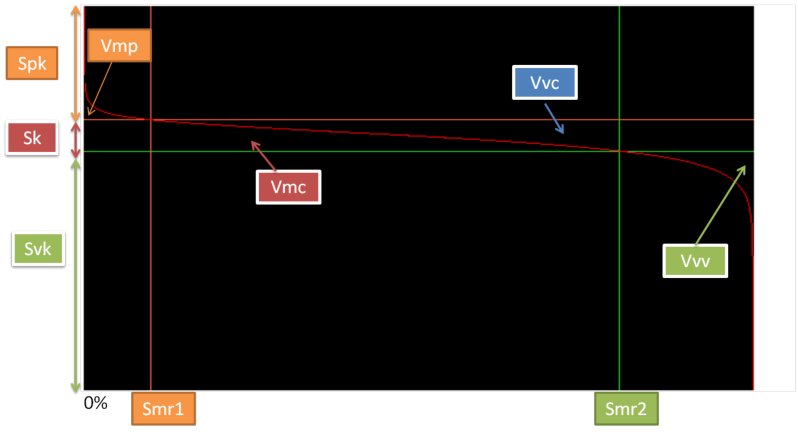

Figure A4.1: Schematic representation of the functional parameters on the height distribution (the curve called the Abbott-Firestone).

Appendix E

Examples of Metallographic Procedures

The preparation procedures for several metals (stainless steel, copper and niobium), inspired from metallographic laboratories/companies, are presented here. The preparation procedure consists from number of steps, which aims to obtain the best preparation quality (no-scratches, no-damaged layer...) with shortest period of time, hence to reduce the costs during process. Each process has a number of parameters which varies from step to step. Main parameters presented in the tables of mastered procedures.

- Disk (paper, resine, RCD, cloth...) used for grinding and polishing as carrier of abrasives
- Abrasives (SiC, diamond, silica, alumina...)
- Grain size of abrasives in μm
- Rotation speed of disk/header in RPM
- Applied pressure per sample controlled by force [N].

Complementary parameters such as the lubricant type used for lubrication (water, oil, alcohol based), the direction of rotation disk/header (either clock wise or counter clock wise) and dossing frequency of lubricant/suspension could be changed.

Table E.1: Preparation process for stainless steel samples developed by metallographic laboratory [260].

Step	Disk	Abrasive type-size	RPM disk/header	Pressure
1	Paper	SiC - 68 μm	300/150	30 kPa
2	RCD, soft	Diamond - 9 μm	150/150	35 kPa
3	Cloth, hard	Diamond - 3 μm	150/150	30 kPa
4	Cloth, soft	SiO_2 - 0.05 μm	150/150	20 kPa
5	Cloth, soft	Al_2O_3 - 0.02 μm	150/150	20 kPa

Table E.2: Preparation process for stainless steel samples developed by metallographic company Lamplan [227].

Step	Disk	Abrasive type-size	RPM disk/header	Pressure
1	Resine	Diamond - 59 μm	150/125	15 kPa
2	RCD, soft	Diamond - 6 μm	150/125	15 kPa
3	Cloth, hard	Diamond - 3 μm	150/125	12.5 kPa
4	Cloth, soft	Diamond - 1 μm	150/125	10 kPa

Table E.3: Preparation process for niobium samples developed by metallographic laboratory [261] (method C-55).

Step	Disk	Abrasive type-size	RPM disk/header	Pressure
1	Resine	Diamond - 68 μm	300/150	25-35 kPa
2	RCD, soft	Diamond - 9 μm	150/150	25-35 kPa
3	Cloth, hard	Diamond - 3 μm	150/150	35 kPa
4	Cloth, soft	SiO_2 - 0.04 μm	150/150	12.5-15 kPa

Table E.4: Preparation process for niobium samples developed by metallographic laboratory [261] (method T-55).

Step	Disk	Abrasive type-size	RPM disk/header	Pressure
1	SiC paper	SiC - 68 μm	300/150	25-35 kPa
2	SiC paper	SiC - 46 μm	300/150	25-35 kPa
3	SiC paper	SiC - 30 μm	300/150	25-35 kPa
4	SiC paper	SiC - 15 μm	300/150	25-35 kPa
5	SiC paper	SiC - 8.4 μm	150/150	25-35 kPa
6	Cloth, hard	Diamond - 3 μm	150/150	25 kPa
7	Cloth, soft	SiO_2 - 0.04 μm	150/150	25 kPa

Table E.5: Preparation process for copper samples developed by metallographic laboratory [262].

Step	Disk	Abrasive type-size	RPM disk/header	Pressure
1	Paper	SiC - 68 μm	300/150	30 kPa
2	Paper	SiC - 46 μm	300/150	30 kPa
3	Paper	SiC - 30 μm	300/150	30 kPa
4	Paper	SiC - 15 μm	300/150	30 kPa
5	Paper	SiC - 8.4 μm	300/150	30 kPa
6	Paper	SiC - 5 μm	300/150	30 kPa
7	Cloth, hard	Diamond - 3 μm	150/150	22 kPa
8	Paper	SiC - 5 μm	150/150	30 kPa
9	Cloth, soft	SiO_2 - 0.05 μm	150/150	10 kPa

Bibliography

[1] URL: http://www.ensarfp7.eu/.

[2] URL: http://irfu.cea.fr/en/.

[3] *Private communication with C.Z. Antoine.* unpublished. 2018.

[4] Claire Antoine. *Materials and surface aspects in the development of SRF Niobium cavities.* Tech. rep. 2012.

[5] Shyh-Yuan Lee. *Accelerator physics.* World scientific publishing, 2018.

[6] F Hinterberger. "Electrostatic accelerators". In: (2006).

[7] J Kockum and N Starfelt. "The response to high-energy gamma rays of a NaI (Tl) scintillation spectrometer". In: *Nuclear Instruments and Methods* 4.3 (1959), pp. 171–180.

[8] D Kostin et al. "Superconducting accelerating module tests at DESY". In: *Proceedings of SRF2009* (2009).

[9] M Aicheler et al. *A Multi-TeV linear collider based on CLIC technology: CLIC Conceptual Design Report.* Tech. rep. SLAC National Accelerator Lab., Menlo Park, CA (United States), 2014.

[10] Nan Phinney, Nobukasu Toge, and Nicholas Walker. "ILC reference design report volume 3-accelerator". In: *arXiv preprint arXiv:0712.2361* (2007).

[11] J-Luc Biarrotte et al. "High power proton/deuteron accelerators". In: *16th International Conference on RF Superconductivity (SRF2013).* 2013.

[12] Herbert Lengeler. *RF superconductivity for high energy accelerators.* Tech. rep. CM-P00061169, 1986.

[13] Jo P Turneaure and Nguyen Tuong Viet. "SUPERCONDUCTING Nb TM010 MODE ELECTRON-BEAM WELDED CAVITIES". In: *Applied Physics Letters* 16.9 (1970), pp. 333–335.

[14] JK Sekutowicz. "Superconducting elliptical cavities". In: *arXiv preprint arXiv:1201.2598* (2012).

[15] David Rice and David Rubin. “1.1 Colliding Beams at the Cornell Electron Storage Ring CESR”. In: ().

[16] J Auerhammer et al. “The S-DALINAC facility—Operational experience from the accelerator and the experimental installations”. In: *Nuclear Physics A* 553 (1993), pp. 841–844.

[17] Giovanni Bisoffi et al. “ALPI QWR and S-RFQ operating experience”. In: *Proceedings of the 13th Workshop on RF Superconductivity, Peking University, Beijin, China*. 2007.

[18] J Feldhaus. “FLASH—the first soft x-ray free electron laser (FEL) user facility”. In: *Journal of Physics B: Atomic, Molecular and Optical Physics* 43.19 (2010), p. 194002.

[19] RE Laxdal and RA Baartman. “Design Optimization of the proposed ISAC-2 Project at TRIUMF”. In: *Proceedings of the 1999 Particle Accelerator Conference (Cat. No. 99CH36366)*. Vol. 5. IEEE. 1999, pp. 3537–3539.

[20] Erich Kugler. “The ISOLDE facility”. In: *Hyperfine interactions* 129.1-4 (2000), pp. 23–42.

[21] Marion M White for the SNS Project. “Spallation neutron source (SNS)”. In: *AIP Conference Proceedings*. Vol. 613. 1. AIP. 2002, pp. 15–24.

[22] P Azzi et al. “Standard Model Physics at the HL-LHC and HE-LHC”. In: *arXiv preprint arXiv:1902.04070* (2019).

[23] Shreyasi Acharya et al. “Λc+ production in Pb–Pb collisions at sNN= 5.02 TeV”. In: *Physics Letters B* 793 (2019), pp. 212–223.

[24] Albert Puig Navarro. *First measurements of radiative B decays in LHCb*. Tech. rep. 2012.

[25] Chris Llewellyn Smith. “Genesis of the Large Hadron Collider”. In: *Philosophical Transactions of the Royal Society A: Mathematical, Physical and Engineering Sciences* 373.2032 (2015), p. 20140037.

[26] Giorgio Apollinari et al. *High-luminosity large hadron collider (HL-LHC): Preliminary design report*. Tech. rep. Fermi National Accelerator Lab.(FNAL), Batavia, IL (United States), 2015.

[27] Enrico Chiaveri. *The CERN Nb/Cu Programme for the LHC and Reduced-b Superconducting Cavities*. Tech. rep. 1999.

[28] Helen Marie McGlone. “Neural network analysis in Higgs search using ttH, H bband tag database development for ATLAS”. PhD thesis. University of Glasgow (United Kingdom), 2009.

[29] Don Lincoln. *The Large Hadron Collider: the extraordinary story of the Higgs Boson and other stuff that will blow your mind*. JHU Press, 2014.

[30] Dirk Nölle. “The Diagnostic System at the European XFEL; Commissioning and First User Operation”. In: *7\textsuperscript {th} Int. Beam Instrumentation Conf.(IBIC'18), Shanghai, China, 09-13 September 2018*. JACOW Publishing, Geneva, Switzerland. 2019, pp. 162–168.

[31] Hans Weise, Winfried Decking, et al. “Commissioning and first lasing of the European XFEL”. In: *Proc. FEL'17* (2018).

[32] Massimo Altarelli, Reinhard Brinkmann, and Majed Chergui. *The European X-ray free-electron laser. technical design report*. Tech. rep. DEsY XFEL Project Group, 2007.

[33] Sebastian Aderhold. *Study of field-limiting defects in superconducting RF cavities for electron-accelerators*. Tech. rep. Verlag Deutsches Elektronen-Synchrotron, 2015.

[34] *FCC*. URL: `https://fcc.web.cern.ch/`.

[35] *ILC*. URL: `www.linearcollider.org/`.

[36] *PIP-2*. URL: `https://pip2.fnal.gov/`.

[37] *LCLS-2*. URL: `https://lcls.slac.stanford.edu/`.

[38] *FRIB*. URL: `https://frib.msu.edu/`.

[39] *ESS*. URL: `https://europeanspallationsource.se/`.

[40] L Liu, RT Neuenschwander, and ARD Rodrigues. “Synchrotron radiation sources in Brazil”. In: *Philosophical Transactions of the Royal Society A* 377.2147 (2019), p. 20180235.

[41] Michael Benedikt and Frank Zimmermann. *Status of the future circular collider study*. Tech. rep. FCC-DRAFT-ACC-2016-030, 2016.

[42] Rama Calaga et al. “SRF for future circular colliders”. In: (2015).

[43] Michael Benedikt, Frank Zimmermann, et al. “FCC: colliders at the energy frontier”. In: *9th Int. Particle Accelerator Conf.(IPAC'18), Vancouver, BC, Canada, April 29-May 4, 2018*. JACOW Publishing, Geneva, Switzerland. 2018, pp. 2908–2913.

[44] Marc Wenskat. *Automated surface classification of SRF cavities for the investigation of the influence of surface properties onto the operational performance*. Tech. rep. 2015.

[45] Ties Behnke et al. "The International Linear Collider Technical Design Report-Volume 1: Executive Summary". In: *arXiv preprint arXiv:1306.6327* (2013).

[46] *SRF Accelerators*. 2019. URL: `https://tesla-new.desy.de`.

[47] Mario Weiss. "Introduction to RF linear accelerators". In: (1994).

[48] Frank Gerigk. "Cavity types". In: *arXiv preprint arXiv:1111.4897* (2011).

[49] A Facco et al. "Low and medium beta SC cavities". In: *Proc. EPAC*. 2004.

[50] Sergey Belomestnykh and Valery Shemelin. "High-beta Cavity Design-A Tutorial". In: *SRF International Workshop, Ithaca, New York*. 2005.

[51] Raphael Kleindienst. "Radio frequency characterization of superconductors for particle accelerators". In: (2018).

[52] PE Bernaudin et al. "Design of the low-beta, quarter-wave resonator and its cryomodule for the SPIRAL2 project". In: *EPAC*. Vol. 6. 2004, p. 1276.

[53] T Junquera et al. "Design of a Superconducting 352MHz fully jacketed double-spoke resonator for the ESS-Bilbao proton linac". In: *THP018, these proceedings* (2013).

[54] Bernard Aune et al. "Superconducting TESLA cavities". In: *Physical Review Special Topics-Accelerators and Beams* 3.9 (2000), p. 092001.

[55] Heike Kamerlingh Onnes. "The disappearance of the resistivity of mercury". In: *Comm. Leiden* 122 (1911), p. 2.

[56] Walther Meissner and Robert Ochsenfeld. "A new effect concerning the onset of superconductivity". In: *Die Naturwissenschaften* 21 (1933), p. 787.

[57] W Farrell Edwards. "Classical derivation of the London equations". In: *Physical Review Letters* 47.26 (1981), p. 1863.

[58] Harry Suhl. "Ginsburg-Landau theory of two antagonistic order parameters: Magnetism and superconductivity". In: *Journal of the Less Common Metals* 62 (1978), pp. 225–244.

[59] Philip W Anderson. "Theory of dirty superconductors". In: *Journal of Physics and Chemistry of Solids* 11.1-2 (1959), pp. 26–30.

[60] Brian David Josephson. "Possible new effects in superconductive tunnelling". In: *Physics letters* 1.7 (1962), pp. 251–253.

[61] Hyung-Woo Lee, Ki-Chan Kim, and Ju Lee. "Review of maglev train technologies". In: *IEEE transactions on magnetics* 42.7 (2006), pp. 1917–1925.

[62] H Kamerlingh Onnes. "The resistance of pure mercury at helium temperatures". In: *Commun. Phys. Lab. Univ. Leiden, b* 120 (1911).

[63] P.J. Ray Own work CC BY-SA 4.0. *title*. URL: https://commons.wikimedia.org/w/index.php?curid=46193149.

[64] Peter John Ford and George A Saunders. *The rise of the superconductors*. CRC press, 2004.

[65] P Schmüser. "Superconductivity". In: (2004). DOI: 10.5170/CERN-2004-008.1. URL: https://cds.cern.ch/record/808345.

[66] Karl-Heinz Bennemann and John B Ketterson. *Superconductivity: Volume 1: Conventional and Unconventional Superconductors Volume 2: Novel Superconductors*. Springer Science & Business Media, 2008.

[67] Jean-Luc Biarrotte. "Etude de cavités supraconductrices pour les accélérateurs de protons de forte puissance". PhD thesis. Paris 11, 2000.

[68] VL Ginzburg and LD Landau. "Phenomenological theory". In: *J. Exp. Theor. Phys. USSR* 20 (1950), p. 1064.

[69] David R Tilley. *Superfluidity and superconductivity*. Routledge, 2018.

[70] Hasan Padamsee. "RF Superconductivity: Science, Technology and Applications (v. 2)". In: (2009).

[71] Hasan Padamsee, Jens Knobloch, Tom Hays, et al. *RF superconductivity for accelerators*. Vol. 2011. Wiley Online Library, 2008.

[72] J Bardeen. "LN cooper, and JR Schrieffer". In: *Phys. Rev* 108.1175 (1957), p. 5.

[73] P Townsend and J Sutton. "Investigation by electron tunneling of the superconducting energy gaps in nb, ta, sn, and pb". In: *Physical Review* 128.2 (1962), p. 591.

[74] JP Turneaure, J Halbritter, and HA Schwettman. "The surface impedance of superconductors and normal conductors: The Mattis-Bardeen theory". In: *Journal of Superconductivity* 4.5 (1991), pp. 341–355.

[75] Thorsten Freclrick Stromberg. *THE SUPERCONDUCTING PROPERTIES OF HIGH PURITY NIOBIUM (Thesis)*. Tech. rep. Ames Lab., Iowa State Univ. of Science and Tech., 1965.

[76] I Ben-Zvi and JM Brennan. "The quarter wave resonator as a superconducting linac element". In: *Nuclear Instruments and Methods in Physics Research* 212.1-3 (1983), pp. 73–79.

[77] A Facco and V Zviagintsev. "Study on beam steering in intermediate-/spl beta/superconducting quarter wave resonators". In: *PACS2001. Proceedings of the 2001 Particle Accelerator Conference (Cat. No. 01CH37268)*. Vol. 2. IEEE. 2001, pp. 1095–1097.

[78] JR Delayen and JE Mercereau. "Cryogenic test of a superconducting half-wave resonator for the acceleration of heavy ions". In: *Nuclear Instruments and Methods in Physics Research Section A: Accelerators, Spectrometers, Detectors and Associated Equipment* 257.2 (1987), pp. 71–76.

[79] D Longuevergne. "Course on superconductivity and cryogenics for accelerators". PHENIICS doctoral school, University Paris-Saclay, France. 2016.

[80] K Hosoyama et al. *Construction and commissioning of KEKB superconducting crab cavities*. Tech. rep. 2007.

[81] P Bauer et al. "A comparison of Q-slope models and data in bulk Nb SRF cavities". In: *SRF material meetings, FNAL*. 2005.

[82] K Saito. "Basic principles of SRF". SRF 2005 Tutorials, Ithaca, USA. 2005.

[83] Pasi Yla-Oijala. "Electron multipacting in TESLA cavities and input couplers". In: *Part. Accel.* 63 (1999), pp. 105–137.

[84] T Higuchi et al. "Hydrogen Q disease and electropolishing". In: *10th Workshop on RF Superconductivity*. 2001.

[85] J Knobloch and H Padamsee. "Enhanced susceptibility of Nb cavity equator welds to the hydrogen related Q-virus". In: *8th Workshop on the RF Superconductivity, Padova, Italy*. 1998.

[86] D Longuevergne. "Vertical Test Results of Spoke Resonator at IPNO". TTC Meeting at Saclay. 2016.

[87] A Grassellino. "Pushing bulk Niobium Limits". SRF 2019 Tutorials, Dresden, Germany. 2009.

[88] B Bonin. *Field emission in RF cavities*. Tech. rep. CEA Centre d'Etudes de Saclay, 1996.

[89] W Singer et al. "Quality requirements and control of high purity niobium for superconducting RF cavities". In: *Physica C: Superconductivity* 386 (2003), pp. 379–384.

[90] S Posen et al. “Nb3Sn at FERMILAB: exploring performance”. In: *Proceedings of the 19th International Conference on RF Superconductivity*. 2019.

[91] Claire Antoine. “Materials for superconducting accelerators: beyond bulk Nb”. SRF 2019 Tutorials, Dresden, Germany. 2009.

[92] Anne-Marie Valente-Feliciano. “SRF Materials other than Niobium”. In: *Proceedings of the 13th International Conference on RF Superconductivity, Beijing, China*. 2007.

[93] A Gurevich. “Enhancement of rf breakdown field of superconductors by multilayer coating”. In: *Applied Physics Letters* 88.1 (2006), p. 012511.

[94] Richard Carter. *Reviews of Accelerator Science and Technology: Volume 5–Applications of Superconducting Technology to Accelerators, edited by Alexander W. Chao and Weiren Chou: Scope: review. Level: specialist, scientists, engineers*. 2015.

[95] Taylor Hobson and GUIDE PRECISION’S. “Exploring Surface Texture: A fundamental guide to the measurement of surface finish”. In: *Taylor Hobson Ltd, England* (2003), pp. 53–62.

[96] Bharat Bhushan. “Surface roughness analysis and measurement techniques”. In: *Modern Tribology Handbook, Two Volume Set*. CRC press, 2000, pp. 74–144.

[97] Bharat Bhushan. *Tribology and mechanics of magnetic storage devices*. Springer Science & Business Media, 2012.

[98] Ningtao Mao, Yiyi Wang, and Jianguo Qu. “SMOOTHNESS AND ROUGHNESS: CHARACTERISTICS OF FABRIC-TO-FABRIC SELF-FRICTION PROPERTIES”. In: *The Proceedings of 90th Textile Institute World Conference*. The Textile Institute. 2016.

[99] J Raja, B Muralikrishnan, and Shengyu Fu. “Recent advances in separation of roughness, waviness and form”. In: *Precision Engineering* 26.2 (2002), pp. 222–235.

[100] Sergio Manuel Oliveira Tavares. “Analysis of surface roughness and models of mechanical contacts”. PhD thesis. Ph. D. dissertation (Università di Pisa, 2005), 2005.

[101] Yann Quinsat, Laurent Sabourin, and Claire Lartigue. “Surface topography in ball end milling process: description of a 3D surface roughness parameter”. In: *Journal of materials processing technology* 195.1-3 (2008), pp. 135–143.

[102] ES Gadelmawla et al. “Roughness parameters”. In: *Journal of materials processing Technology* 123.1 (2002), pp. 133–145.

[103] DM Shivanna, MB Kiran, and SD Kavitha. “Evaluation of 3D surface roughness parameters of EDM components using vision system”. In: *Procedia Materials Science* 5 (2014), pp. 2132–2141.

[104] Liam Blunt and Xiang Jiang. *Advanced techniques for assessment surface topography: development of a basis for 3D surface texture standards” surfstand”*. Elsevier, 2003.

[105] E Jansons, J Lungevics, KA Gross, et al. “Surface roughness measure that best correlates to ease of sliding”. In: *proceedings of the international scientific conference*. Latvia University of Agriculture. 2016.

[106] Natalija Bulaha et al. “Calculations of surface roughness 3D parameters for surfaces with irregular roughness”. In: *proceedings of the international scientific conference*. [Latvijas Lauksaimniecības universitāte]. 2018.

[107] Richard Leach. *Characterisation of areal surface texture*. Springer, 2013.

[108] Harry Chandler et al. *Hardness testing*. ASM international, 1999.

[109] Konrad Herrmann et al. *Hardness testing: principles and applications*. ASM International, 2011.

[110] Giulio Barbato et al. “Influence of the indenter shape in Rockwell hardness test”. In: *Proc. of the HARDMEKO ‘98, Sept* (1998), pp. 21–23.

[111] C Hays and EG Kendall. “An analysis of Knoop microhardness”. In: *Metallography* 6.4 (1973), pp. 275–282.

[112] Robert Hill, Bertil Storåkers, and AB Zdunek. “A theoretical study of the Brinell hardness test”. In: *Proceedings of the Royal Society of London. A. Mathematical and Physical Sciences* 423.1865 (1989), pp. 301–330.

[113] John Mitchell. *Vickers Hardness Test: What it is and how it’s measured*. Ed. by Engineering clicks. 2017. URL: `https://www.engineeringclicks.com/`.

[114] JA Williams. “Analytical models of scratch hardness”. In: *Tribology international* 29.8 (1996), pp. 675–694.

[115] D Tabor. “Mohs’s hardness scale-a physical interpretation”. In: *Proceedings of the Physical Society. Section B* 67.3 (1954), p. 249.

[116] David Roylance. “Mechanical properties of materials”. In: *Massachusetts Institute of Technology* (2008), pp. 51–78.

[117] Tat Joo Teo, Guilin Yang, and I-Ming Chen. "Compliant Manipulators". In: Mar. 2014, pp. 1–64. ISBN: 978-1-4471-4976-7. DOI: 10.1007/978-1-4471-4976-7_102-1.

[118] H Jiang et al. "Mechanical properties, microstructure, and texture of electron beam butt welds in high purity Niobium". In: *Proceedings of the 2003 Particle Accelerator Conference*. Vol. 2. IEEE. 2003, pp. 1359–1361.

[119] C Antoine, M Foley, and N Dhanaraj. *Physical properties of niobium and specifications for fabrication of superconducting cavities*. Tech. rep. Fermi National Accelerator Lab.(FNAL), Batavia, IL (United States), 2011.

[120] Ronald W Armstrong. "60 years of Hall-Petch: past to present nano-scale connections". In: *Materials Transactions* 55.1 (2014), pp. 2–12.

[121] Andrii Repula and Eric Grelet. "Elementary Edge and Screw Dislocations Visualized at the Lattice Periodicity Level in the Smectic Phase of Colloidal Rods". In: *Physical review letters* 121.9 (2018), p. 097801.

[122] C Antoine et al. "Nuclear Microprobe studies of impurities segregation in Niobium used for radiofrequency cavities". In: *Proc. of 8 th SRF Workshop, Abano Terme*. 1997.

[123] Ismail C Noyan and Jerome B Cohen. *Residual stress: measurement by diffraction and interpretation*. Springer, 2013.

[124] Hans Hilgenkamp and Jochen Mannhart. "Grain boundaries in high-T c superconductors". In: *Reviews of Modern Physics* 74.2 (2002), p. 485.

[125] RL Geng, J Knobloch, and H Padamsee. "Microstructures of rf surfaces in the electron-beam-weld regions of niobium". In: *Krawcyk [36]* (1999), pp. 238–245.

[126] A Romanenko and DI Schuster. "Understanding quality factor degradation in superconducting niobium cavities at low microwave field amplitudes". In: *Physical review letters* 119.26 (2017), p. 264801.

[127] H Diepers et al. "A new method of electropolishing niobium". In: *Physics Letters A* 37.2 (1971), pp. 139–140.

[128] F Eozenou et al. *Niobium Electro-Polishing: Best EP Parameters*.

[129] K Saito et al. "Proceedings of the 4th Workshop on RF Superconductivity". In: (1990).

[130] N Steinhau-Kühl et al. *Update On The Experiences Of Electro-polishing Of Multi-cell Resonators At DESY*. Tech. rep. 2005.

[131] P Kneisel et al. “Surface characterization of bulk Nb: what has been done, what has been learnt?” In: *Proc. of the 11th Workshop on RF Superconductivity, Lübeck/Travemünde, Germany*. 2003.

[132] Jean R Delayen et al. *Alternate electrolyte composition for electropolishing of niobium surfaces*. Tech. rep. Thomas Jefferson National Accelerator Facility, Newport News, VA (US), 2001.

[133] Song Jin et al. “Niobium Sample Surface Treatment by Buffered Electropolishing”. In: *Peking University, Beijing, China* (2007).

[134] Andy T Wu et al. “Smooth Nb surfaces fabricated by buffered electropolishing”. In: *Applied Surface Science* 253.6 (2007), pp. 3041–3052.

[135] L Lilje et al. “Improved surface treatment of the superconducting TESLA cavities”. In: *Nuclear Instruments and Methods in Physics Research Section A: Accelerators, Spectrometers, Detectors and Associated Equipment* 516.2-3 (2004), pp. 213–227.

[136] Gianluigi Ciovati, Hui Tian, and Sean G Corcoran. “Buffered electrochemical polishing of niobium”. In: *Journal of Applied Electrochemistry* 41.6 (2011), pp. 721–730.

[137] Lutz Lilje et al. “State of the art SRF cavity performances”. In: *Proc. 22nd International Linear Accelerator Conference, Lübeck, Germany*. 2004, p. 518.

[138] CZ Antoine et al. “Alternative approaches for surface treatment of Nb superconducting cavities”. In: *Krawcyk [21]* (1999), pp. 109–117.

[139] Gianluigi Ciovati, Sean Corcoran, and Juergen Halbritter. *Preliminary Results on” Polarized” Buffered Chemical Polishing of a Large Grain Niobium Cavity*. Tech. rep. Thomas Jefferson National Accelerator Facility, Newport News, VA, 2008.

[140] Francois Goossens. “Modélisation du processus de polissage: identification des effets et des phénoménologies induits par l’usinage abrasif”. PhD thesis. Université de Bordeaux, 2015.

[141] Ioan D Marinescu, Eckart Uhlmann, and Toshiro Doi. *Handbook of lapping and polishing*. CrC Press, 2006.

[142] TO Mulhearn and LE Samuels. “The abrasion of metals: a model of the process”. In: *Wear* 5.6 (1962), pp. 478–498.

[143] Kay Geels et al. *Metallographic and materialographic specimen preparation, light microscopy, image analysis, and hardness testing*. Vol. 46. ASTM international West Conshohocken, 2007, pp. 87–88.

[144] K Hokkirigawa and K Kato. "An experimental and theoretical investigation of ploughing, cutting and wedge formation during abrasive wear". In: *Tribology international* 21.1 (1988), pp. 51–57.

[145] Leonard Ernest Samuels. *Metallographic polishing by mechanical methods*. Asm International, 2003.

[146] Kay Geels et al. *Metallographic and materialographic specimen preparation, light microscopy, image analysis, and hardness testing*. Vol. 46. ASTM international West Conshohocken, 2007, pp. 3–13.

[147] George F Vander Voort. *Metallography, principles and practice*. ASM International, 1999.

[148] Kay Geels et al. *Metallographic and materialographic specimen preparation, light microscopy, image analysis, and hardness testing*. Vol. 46. ASTM international West Conshohocken, 2007, pp. 82–84.

[149] Kay Geels et al. *Metallographic and materialographic specimen preparation, light microscopy, image analysis, and hardness testing*. Vol. 46. ASTM international West Conshohocken, 2007, pp. 85–87.

[150] Kay Geels et al. *Metallographic and materialographic specimen preparation, light microscopy, image analysis, and hardness testing*. Vol. 46. ASTM international West Conshohocken, 2007.

[151] Kay Geels et al. *Metallographic and materialographic specimen preparation, light microscopy, image analysis, and hardness testing*. Vol. 46. ASTM international West Conshohocken, 2007, pp. 93–94.

[152] James F Shackelford et al. *CRC materials science and engineering handbook*. CRC press, 2016.

[153] Yaw Samuel Obeng. *Method of polishing*. US Patent 5,735,963. 1998.

[154] Robert J Small et al. *Chemical mechanical polishing composition and process*. US Patent 6,117,783. 2000.

[155] Srikanth Sundararajan et al. "Two-Dimensional Wafer-Scale Chemical Mechanical Planarization Models Based on Lubrication Theory and Mass Transport". In: *Journal of the electrochemical society* 146.2 (1999), pp. 761–766.

[156] RJ Walsh and Arno H Herzog. *Process for polishing semiconductor materials*. US Patent and Trademark Office, 1965.

[157] M Sivanandini, S Dhami Sukhdeep, and BS Pabla. "Chemical mechanical polishing by colloidal silica slurry". In: *International Journal of Engineering Research and Applications (IJERA) ISSN* 6 (2013), pp. 2248–9622.

[158] Kay Geels et al. *Metallographic and materialographic specimen preparation, light microscopy, image analysis, and hardness testing*. Vol. 46. ASTM international West Conshohocken, 2007, pp. 1–12.

[159] Dewen Zhao and Xinchun Lu. "Chemical mechanical polishing: theory and experiment". In: *Friction* 1.4 (2013), pp. 306–326.

[160] T Higuchi et al. "Investigation on barrel polishing for superconducting niobium cavity". In: *Proc. 7th SRF Int. Workshop, DIST CEA, Gif-sur-Yvette*. 1995.

[161] Aliaksandr Navitski et al. "R&D on cavity treatments at DESY towards the ILC performance goal". In: *MOP053, these proceedings* (2013).

[162] Aliaksandr Navitski et al. "Surface analyses and optimization of centrifugal barrel polishing of Nb cavities". In: (2015).

[163] Alena Prudnikava et al. "R&D Activities on centrifugal barrel polishing of 1.3 GHz niobium cavities at DESY/University of hamburg". In: *Proc. Int. Conf. RF Supercond.* 2017.

[164] Ari Palczewski. *R&D progress in SRF surface preparation with centrifugal barrel polishing (CBP) for both Nb and Cu*. Tech. rep. Thomas Jefferson National Accelerator Facility, Newport News, VA (United States), 2013.

[165] Ari Palczewski, Rongli Geng, and Hui Tian. *Optimizing Centrifugal barrel polishing for mirror finish SRF Cavity and RF Tests at Jefferson Lab*. Tech. rep. Thomas Jefferson National Accelerator Facility, Newport News, VA (United States), 2012.

[166] Ari Palczewski et al. *Exploration of material removal rate of srf elliptical cavities as a function of media type and cavity shape on niobium and copper using centrifugal barrel polishing (cbp)*. Tech. rep. Thomas Jefferson National Accelerator Facility, Newport News, VA (United States), 2013.

[167] C Cooper et al. "Cavity processing research laboratory at Fermilab: SRF cavity processing R&D". In: *Proceedings of SRF*. 2011.

[168] C Cooper et al. "Centrifugal barrel polishing of cavities worldwide". In: *Proceedings of SRF*. 2011, pp. 571–575.

[169] C Cooper et al. "Recent developments in electropolishing and tumbling\& at Fermilab". In: *Presented at*. FERMILAB-CONF-09-539-AD-TD. 2009.

[170] CA Cooper and LD Cooley. *Mirror smooth superconducting rf cavities by mechanical polishing with minimal acid use*. Tech. rep. 2011.

[171] CA Cooper and LD Cooley. "Mirror-smooth surfaces and repair of defects in superconducting RF cavities by mechanical polishing". In: *Superconductor Science and Technology* 26.1 (2012), p. 015011.

[172] Sam Posen, Matthias Liepe, and Daniel Gonnella. "Recent progress in Nb3Sn SRF cavity development at Cornell". In: (2014).

[173] Prashant Khare et al. "New Technique and Results of Laser Welded SCRF Cavity Developed at RRCAT". In: *16th International Conference on RF Superconductivity(SRF2013), September*. 2013, pp. 23–27.

[174] T Higuchi, K Saito, and S Noguchi. *Application of centrifugal barrel polishing to a niobium superconducting cavity*. Tech. rep. 2001.

[175] Ari D Palczewski et al. *Detailed surface analysis of incremental centrifugal barrel polishing (CBP) of single-crystal niobium samples*. Tech. rep. Thomas Jefferson National Accelerator Facility, Newport News, VA (United States), 2011.

[176] David A Davidson. "Mass finishing processes". In: *Metal finishing* 100 (2002), pp. 104–117.

[177] Gregory S Kirkendall. *Light weight ceramic abrasive media*. US Patent 5,443,603. 1995.

[178] Eckart Uhlmann, Arne Dethlefs, and Alexander Eulitz. "Investigation of material removal and surface topography formation in vibratory finishing". In: *Procedia CIRP* 14 (2014), pp. 25–30.

[179] Jörg Hildebrand et al. "Laser beam polishing of quartz glass surfaces". In: *Physics Procedia* 12 (2011), pp. 452–461.

[180] F Laguarta, N Lupon, and J Armengol. "Optical glass polishing by controlled laser surface-heat treatment". In: *Applied optics* 33.27 (1994), pp. 6508–6513.

[181] A Lamikiz et al. "Laser polishing of parts built up by selective laser sintering". In: *International Journal of Machine Tools and Manufacture* 47.12-13 (2007), pp. 2040–2050.

[182] SM Pimenov et al. "Laser polishing of diamond plates". In: *Applied Physics A* 69.1 (1999), pp. 81–88.

[183] JA Ramos et al. “Surface roughness enhancement of indirect-SLS metal parts by laser surface polishing”. In: *Solid Freeform Fabrication Proceedings*. 2001, pp. 28–38.

[184] Mircea V Udrea, Hamdi Orun, and Ali Alacakir. “Laser polishing of optical fiber end surface”. In: *Optical Engineering* 40.9 (2001), pp. 2026–2031.

[185] K Alrbaey et al. “On optimization of surface roughness of selective laser melted stainless steel parts: A statistical study”. In: *Journal of Materials Engineering and Performance* 23.6 (2014), pp. 2139–2148.

[186] SL Campanelli et al. “Taguchi optimization of the surface finish obtained by laser ablation on selective laser molten steel parts”. In: *Procedia CIRP* 12 (2013), pp. 462–467.

[187] Benoit Rosa, Pascal Mognol, and Jean-Yves Hascoët. “Modelling and optimization of laser polishing of additive laser manufacturing surfaces”. In: *Rapid Prototyping Journal* 22.6 (2016), pp. 956–964.

[188] E Ukar et al. “Laser polishing parameter optimization for die and moulds surface finishing”. In: *ASME 2008 International Manufacturing Science and Engineering Conference collocated with the 3rd JSME/ASME International Conference on Materials and Processing*. American Society of Mechanical Engineers. 2008, pp. 197–204.

[189] E Ukar et al. “Laser polishing parameter optimisation on selective laser sintered parts”. In: *International Journal of Machining and Machinability of Materials* 8.3-4 (2010), pp. 417–432.

[190] Christian Weingarten et al. “Laser polishing and laser shape correction of optical glass”. In: *Journal of Laser Applications* 29.1 (2017), p. 011702.

[191] Benoit Rosa, Pascal Mognol, and Jean-Yves Hascoët. “Laser polishing of additive laser manufacturing surfaces”. In: *Journal of Laser Applications* 27.S2 (2015), S29102.

[192] André Temmler, E Willenborg, and K Wissenbach. “Laser polishing”. In: *Laser Applications in Microelectronic and Optoelectronic Manufacturing (LAMOM) XVII*. Vol. 8243. International Society for Optics and Photonics. 2012, 82430W.

[193] Liang Zhao et al. *Laser polishing of niobium for SRF applications*. Tech. rep. Thomas Jefferson National Accelerator Facility, Newport News, VA (United States), 2013.

[194] Vitali Porshyn et al. “Laser treatment of niobium surfaces for SRF applications”. In: *Journal of Physics: Conference Series*. Vol. 1067. 8. IOP Publishing. 2018, p. 082011.

[195] Liang Zhao et al. “Parameter Optimization for Laser Polishing of Niobium for SRF Applications”. In: (2013).

[196] RG Poulsen. “Plasma etching in integrated circuit manufacture—A review”. In: *Journal of Vacuum Science and Technology* 14.1 (1977), pp. 266–274.

[197] JH Greiner. “Josephson tunneling barriers by rf sputter etching in an oxygen plasma”. In: *Journal of Applied Physics* 42.12 (1971), pp. 5151–5155.

[198] M Gurvitch et al. “Preparation and properties of Nb Josephson junctions with thin Al layers”. In: *IEEE Transactions on Magnetics* 19.3 (1983), pp. 791–794.

[199] Akira Shoji et al. “New fabrication process for Josephson tunnel junctions with (niobium nitride, niobium) double-layered electrodes”. In: *Applied Physics Letters* 41.11 (1982), pp. 1097–1099.

[200] S Moshkalyov, C Reyes-Betanzo, and J Swart. “Anisotropic Etching of Si for Micromachining Applications Using SF6/CH4/O2/Ar Plasma”. In: *Proc. of the 16th Brazilian Congress of Mechanical Engineering*, pp. 19–3.

[201] Mehmet Ozgur and Michael Huff. “High-etch rate processes for performing deep, highly anisotropic etches in silicon carbide using inductively coupled plasma etching”. In: *Journal of Vacuum Science & Technology B, Nanotechnology and Microelectronics: Materials, Processing, Measurement, and Phenomena* 35.4 (2017), p. 042003.

[202] M Rašković et al. “Plasma treatment of bulk niobium surface for SRF cavities”. In: *Nuclear Instruments and Methods in Physics Research Section A: Accelerators, Spectrometers, Detectors and Associated Equipment* 569.3 (2006), pp. 663–670.

[203] J Upadhyay et al. “Plasma etching of a single-cell RF cavity-asymmetric electronegative discharge”. In: *Proceedings of SRF*. 2009.

[204] J Upadhyay et al. *Plasma Treatment of Niobium SRF Cavity Surfaces*. Tech. rep. Thomas Jefferson National Accelerator Facility, Newport News, VA (United States), 2010.

[205] M Rašković et al. "Plasma treatment of bulk niobium surface for superconducting rf cavities: Optimization of the experimental conditions on flat samples". In: *Physical Review Special Topics-Accelerators and Beams* 13.11 (2010), p. 112001.

[206] J Upadhyay et al. *Plasma Treatment of Single-Cell Niobium SRF Cavities*. Tech. rep. Thomas Jefferson National Accelerator Facility, Newport News, VA (United States), 2011.

[207] Janardan Upadhyay et al. "Experiment and Results on Plasma Etching of SRF cavities". In: (2015).

[208] Janardan Upadhyay et al. "Etching mechanism of niobium in coaxial Ar/Cl2 radio frequency plasma". In: *Journal of Applied Physics* 117.11 (2015), p. 113301.

[209] J Upadhyay et al. "Cryogenic rf test of the first SRF cavity etched in an rf Ar/Cl2 plasma". In: *AIP Advances* 7.12 (2017), p. 125016.

[210] Jeremy Peshl et al. "The Effect of Process Parameters on the Surface Properties of Niobium During Plasma Etching". In: (2018).

[211] VN Duradzhi, IV Bryantsev, and AK Tokarov. "Investigation of erosion of the anode under the action of an electrolytic plasma on it". In: *Elektronnaya Obrabotka Materialov* 5 (1979), pp. 15–19.

[212] Alexander Mayorov and Anna Berkovich. *Plasma-electrolytic polishing of metals products*. US Patent App. 12/691,773. 2010.

[213] Klaus Nestler et al. "Plasma Electrolytic Polishing–an Overview of Applied Technologies and Current Challenges to Extend the Polishable Material Range". In: *Procedia CIRP* 42 (2016), pp. 503–507.

[214] Matthias Cornelsen, Carolin Deutsch, and Hermann Seitz. "Electrolytic Plasma Polishing of Pipe Inner Surfaces". In: *Metals* 8.1 (2017), p. 12.

[215] EV Parfenov et al. "Towards smart electrolytic plasma technologies: An overview of methodological approaches to process modelling". In: *Surface and Coatings Technology* 269 (2015), pp. 2–22.

[216] Falko Böttger-Hiller et al. "Plasma electrolytic polishing of metalized carbon fibers". In: *AIMS Mater. Sci* 3 (2016), pp. 260–269.

[217] VN Duradji, DE Kaputkin, and AY Duradji. "Aluminum Treatment in the Electrolytic Plasma During the Anodic Process." In: *Journal of Engineering Science & Technology Review* 10.3 (2017).

[218] Wanyuan Gui et al. “Electrolytic plasma processing-an innovative treatment for surface modification of 304 stainless steel”. In: *Scientific reports* 7.1 (2017), p. 308.

[219] MK Smyslova et al. “Surface electrolytic-plasma polishing of Ti-6Al-4V alloy with ultrafine-grained structure produced by severe plastic deformation”. In: *IOP Conference Series: Materials Science and Engineering*. Vol. 461. 1. IOP Publishing. 2018, p. 012079.

[220] Talwinder Singh Bedi and Anant Kumar Singh. “Magnetorheological methods for nanofinishing–a review”. In: *Particulate Science and Technology* 34.4 (2016), pp. 412–422.

[221] N A Mutalib et al. “Magnetorheological finishing on metal surface: A review”. In: *IOP Conference Series: Materials Science and Engineering* 469 (Jan. 2019), p. 012092. DOI: 10.1088/1757-899X/469/1/012092.

[222] VK Jain et al. “Nano-finishing techniques: a review”. In: *Proceedings of the Institution of Mechanical Engineers, Part C: Journal of Mechanical Engineering Science* 226.2 (2012), pp. 327–346.

[223] Hang Du, Ci Song, and Shengyi Li. “Study on Surface Roughness of Modified Silicon Carbide Mirrors polished by Magnetorheological Finishing”. In: *IOP Conference Series: Materials Science and Engineering*. Vol. 301. 1. IOP Publishing. 2018, p. 012164.

[224] Marzena Sutowska and Paweł Sutowski. “Contemporary applications of magnetoreological fluids for finishing process”. In: *Journal of Mechanical and Energy Engineering* 1 (2017).

[225] Wm I Kordonski and SD Jacobs. “Magnetorheological finishing”. In: *International Journal of modern physics B* 10.23n24 (1996), pp. 2837–2848.

[226] Jérôme Neauport et al. “Magnetorheological finishing for removing surface and subsurface defects of fused silica optics Magnetorheological finishing for removing surface and subsurface defects of fused silica optics”. In: *Optical Engineering* 53 (2014), p. 092010.

[227] *Lamplan*. URL: http://www.lamplan.com/fr/.

[228] *ABC SwissTech*. URL: https://www.abcswisstech.com/.

[229] Edward H Tulinski. “Mass finishing”. In: *ASM International, Member/Customer Service Center, Materials Park, OH 44073-0002, USA, 1994*. (1994), pp. 118–125.

[230] Yegor Tamashevich. *Diagnostics and treatment of 1.3 GHz Nb cavities*. Tech. rep. Verlag Deutsches Elektronen-Synchrotron, 2016.

[231] F Barkov et al. "Precipitation of hydrides in high purity niobium after different treatments". In: *Journal of Applied Physics* 114.16 (2013), p. 164904.

[232] *FLIR*. URL: https://www.flir.com/.

[233] Minsky Marvin. *Microscopy apparatus*. US Patent 3,013,467. 1961.

[234] Wolfgang Zinth, Alfred Laubereau, and Wolfgang Kaiser. "The long journey to the laser and its rapid development after 1960". In: *The European Physical Journal H* 36.2 (2011), pp. 153–181.

[235] Tony Wilson et al. *Confocal microscopy*. Vol. 426. Academic press London, 1990.

[236] Kirk J. Czymmek and Tanya Dahms. "Future Directions in Advanced Mycological Microscopy". In: Oct. 2015, pp. 143–162. ISBN: 978-3-319-22436-7. DOI: 10.1007/978-3-319-22437-4_8.

[237] L Yu Ming. "Chemical enhancement effects in SIMS analysis". In: *Nuclear Instruments and Methods in Physics Research Section B: Beam Interactions with Materials and Atoms* 15.1-6 (1986), pp. 151–158.

[238] Rainer Behrisch. "Sputtering by particle bombardment I". In: *Sputtering by Particle Bombardment I: Physical Sputtering of Single-Element Solids* (1981).

[239] *Mass spectrometers for vacuum, gas, plasma and surface science*. URL: https://www.hidenanalytical.com/.

[240] ME Fitzpatrick et al. "Determination of residual stresses by X-ray diffraction". In: (2005).

[241] Shoji Nishikawa and Seishi Kikuchi. "Diffraction of cathode rays by calcite". In: *Nature* 122.3080 (1928), p. 726.

[242] JA Venables and CJ Harland. "Electron back-scattering patterns—A new technique for obtaining crystallographic information in the scanning electron microscope". In: *Philosophical Magazine* 27.5 (1973), pp. 1193–1200.

[243] J Perret et al. "EBSD, SEM and FIB characterisation of subsurface deformation during tribocorrosion of stainless steel in sulphuric acid". In: *Wear* 269.5-6 (2010), pp. 383–393.

[244] Zhong Lin Wang and Jean L Lee. "Electron microscopy techniques for imaging and analysis of nanoparticles". In: *Developments in Surface Contamination and Cleaning*. Elsevier, 2008, pp. 531–584.

[245] *Scanning Electron Microscopes (SEM)*. URL: https://www.zeiss.com/microscopy/us/products/scanning-electron-microscopes.html.

[246] Alena Prudnikava et al. "Toward Optimization of Centrifugal Barrel Polishing Procedure for Treatment of Niobium Cavities". In: *IEEE Transactions on Applied Superconductivity* 28.4 (2018), pp. 1–5.

[247] C Baumier et al. *Multilayers Activities at Saclay/Orsay*. Tech. rep. 2013.

[248] CZ Antoine and R Crooks. "Reducing Electropolishing Time with Chemical-Mechanical Polishing". In: *Proc. 14th Int. Conf. on RF Superconductivity, SRF*. 2009.

[249] W Singer. "Seamless/bonded niobium cavities". In: *Physica C: Superconductivity* 441.1-2 (2006), pp. 89–94.

[250] E Cantergiani et al. *First Results of Superconducting RF (SRF) Cavity Fabrication by Electrohydraulic Forming*. Ohio State University, 2018.

[251] *private communication with LAM PLAN*. 2018.

[252] Oleksandr Hryhorenko et al. "Metallographic Polishing Pathway to the Future of Large Scale SRF Facilities". In: *19th Int. Conf. on RF Superconductivity (SRF'19), Dresden, Germany, 30 June-05 July 2019*. JACOW Publishing, Geneva, Switzerland. 2019, pp. 828–832.

[253] G Martinet et al. "Development of a te011 cavity for thin-films study". In: (2010).

[254] Paul Welander, Matt Franzi, and Sami Tantawi. "Cryogenic RF characterization of superconducting materials at SLAC with hemispherical cavities". In: (2015).

[255] Jiquan Guo et al. "Cryogenic RF material testing at SLAC". In: *Conf. Proc. C110328: 1030-1032, 2011*. SLAC-PUB-16689. SLAC National Accelerator Lab., Menlo Park, CA (United States). 2016.

[256] Said Atieh et al. "First results of SRF cavity fabrication by electro-hydraulic forming at CERN". In: (2015).

[257] URL: https://soft-matter.github.io/trackpy/v0.3.2/.

[258] Minodora Rîpă et al. "Tribological characterisation of surface topography using Abbott-Firestone curve". In: *Annals of University Dunărea de Jos of Galati, Fascicle VIII, Tribology* (2003), pp. 208–212.

[259] J Schmähling and FA Hamprecht. "Generalizing the Abbott–Firestone curve by two new surface descriptors". In: *Wear* 262.11-12 (2007), pp. 1360–1371.

[260] Kay Geels et al. *Metallographic and materialographic specimen preparation, light microscopy, image analysis, and hardness testing*. Vol. 46. ASTM international West Conshohocken, 2007, pp. 328–331.

[261] Kay Geels et al. *Metallographic and materialographic specimen preparation, light microscopy, image analysis, and hardness testing*. Vol. 46. ASTM international West Conshohocken, 2007, pp. 398–401.

[262] Kay Geels et al. *Metallographic and materialographic specimen preparation, light microscopy, image analysis, and hardness testing*. Vol. 46. ASTM international West Conshohocken, 2007, pp. 376–379.